# Design, Synthesis and Magnetism of Single-Molecule Magnets with Large Anisotropic Barriers

**Po-Heng Lin**

PhD. thesis submitted to the Faculty of Graduate and Postdoctoral Studies

In partial fulfillment of the requirements

For the PhD. Degree in the Faculty of Science, Department of Chemistry

Supervisor: Dr. Muralee Murugesu

Department of Chemistry

Faculty of Science

University of Ottawa

**Abstract**

This thesis will present the synthesis, characterization and magnetic measurements of lanthanide complexes with varying nuclearities (Ln, $Ln_2$, $Ln_3$ and $Ln_4$). $Eu^{III}$, $Gd^{III}$, $Tb^{III}$, $Dy^{III}$, $Ho^{III}$ and $Yb^{III}$ have been selected as the metal centers. Eight polydentate Schiff-base ligands have been synthesized with N- and mostly O-based coordination environments which chelate 7-, 8- or 9-coordinate lanthanide ions. The molecular structures were characterized by single crystal X-ray crystallography and the magnetic properties were measured using a SQUID magnetometer.

Each chapter consists of crystal structures and magnetic measurements for complexes with the same nuclearity. There are eight $Dy^{III}$ SMMs in this thesis which are discrete molecules that act as magnets below a certain temperature called their blocking temperature. This phenomenon results from an appreciable spin ground state (*S*) as well as negative uni-axial anisotropy (*D*), both present in lanthanide ions owing to their *f* electron shell, generating an effective energy barrier for the reversal of the magnetization ($U_{eff}$). The *ab initio* calculations are also included for the SMMs with high anisotropic energy barriers to understand the mechanisms of slow magnetic relaxation in these systems.

**Acknowledgements and Contributions**

There are many people who deserve a special mention for their invaluable help with this research project:

First and foremost my supervisor Prof. Muralee Murugesu who taught me inorganic chemistry and molecular magnetism. Thanks for all your patience over the years and spent a lot of time on correcting my English. Thanks for the skating and snowboarding lessons, whiskey tastings, rum tastings and philosophy education. I would like to say if you did not push me so hard in these five years, I would not have this many results and publications.

Wan-Jou Hsu for waiting for me in Taiwan for five years. You are my best support when I feel frustrated. Thanks for giving up your high salary job, marrying me and staying with me in my PhD. last year. Love you forever.

Fatemah Habib for all the help with anything and everything not only in chemistry. Thanks for all your patience for correcting my writing and listening to my practices again and again. Thanks for letting me know that "women's rights" are so important.

Dr. Jérôme Long for all his help with theoretical aspects of molecular magnetism and teaching me how to use the SQUID. Moreover, I will never forget the awesome conference memories, especially the wheelchair.

Dr. Ilia Korobkov and Dr. Tara J. Burchell for all the crystal structures presented in this thesis and for always finding that one crystal that worked.

Dr. Cyril Cook for all his help with organic chemistry.

Prof. Rodolphe Clérac for SQUID measurements and Dr. Wolfgang Wernsdorfer for micro-SQUID measurements.

Prof. Liviu Chibtaru and Dr. Liviu Ungur in Belgium for all the *ab initio* calculations.

Jennifer Le Roy for "some" beers and wonderful Canadian experience.

Last but certainly not least, thanks to all the lab members, past and present, for making time in the lab enjoyable and fun.

Table of Contents

# List of Figures and Tables

# Chapter 1

## Introduction

Single-Molecule Magnets (SMMs) are a new class of magnetic materials that exhibit superparamagnetic-like behavior below their blocking temperature, slow relaxation of their magnetization and display magnetic hysteresis at low temperatures. The first and most studied family of SMMs are the dodecanuclear complexes with the formula, $[Mn_{12}O_{12}(O_2CR)_{16}(H_2O)_4]$, abbreviated as $\{Mn_{12}\}$, which were synthesized in 1980 but the SMM properties were not discovered until 1993. Since discovering the SMM properties of $\{Mn_{12}\}$, synthesizing SMMs with high anisotropic energy barriers ($U$) has become the main target in this field in order to apply these materials to memory storage devices and quantum computers. This energy barrier is given by $U = S^2|D|$ for integer or $(S^2\text{-}1/4)\ |D|$ for half-integer spin where $S$ is the high spin ground state and $D$ is the significant negative zero-field splitting parameter. Many researchers are focused on either making bigger metal clusters or introducing more anisotropy into the molecules. With this in mind, my research focused on the synthesis of lanthanide SMMs with Schiff-base ligands. Strong spin–orbit coupling and many unpaired electrons are commonly observed

in 4*f* systems which have the potential to generate a high energy barrier. In this thesis, mononuclear, dinuclear, trinuclear and tetranuclear complexes have been synthesized and studied both structurally and magnetically. A variety of lanthanide-based SMMs with different geometries will be presented. Additionally, the basic principles governing the magnetic properties of molecules will be discussed in this chapter as well as the techniques and measurements used to study the SMM behavior.

## 1.1 Magnetic properties of materials

When materials are under a magnetic field, their properties will relate to the electron configurations of atoms and ions. All electrons are spin-paired in a diamagnetic material whereas a paramagnetic material contains one or more unpaired electrons. When the paramagnetic centers are close to each other, the interactions between the metal centers also need to be considered. We can further classify these behaviors into three types: ferromagnetism, anti-ferromagnetism and ferrimagnetism.

### 1.1.1 Diamagnetism

In diamagnetic materials, the all eelectron are paired electrons are oriented in opposite directions causing their magnetic fields to cancel. All materials containing

paired electrons exhibite some diamagnetism, even paramagnetic or ferromagnetic materials. The magnetic moments always oppose the applied field and the resulting negative magnetic susceptibility is very weak and will not be retained when the applied field is removed. Therefore it may be negligible when we consider paramagnetism or ferromagnetism. In the magnetic measurements, the diamagnetic contribution of the sample holder will be considered to adjust the magnetic susceptibility. This will be described in more detail in subsequent sections.

### 1.1.2 Paramagnetism

Paramagnetism is another type of magnetism which is defined as small, positive susceptibility to applied magnetic field.[1] Paramagnetic materials will be slightly attracted to each other when a magnetic field is applied due to the presence of unpaired electrons, but will not retain their magnetization when the field is removed. Moreover, only a small induced magnetization will be detected since not all spins will be oriented parallel to the applied field.

---

[1] Boudreaux, E. A.; Mulay, L. N. *Theory and Applications of Molecular Paramagnetism*, J. Wiley & Sons, New York, **1976**.

When the interactions between the spins are strong enough, the electrons in the material will be aligned. These magnetic properties will disappear when the applied magnetic field is removed. Three dimensional ordering can arise from the interaction of the spins in different materials as shown in Figure 1-1.

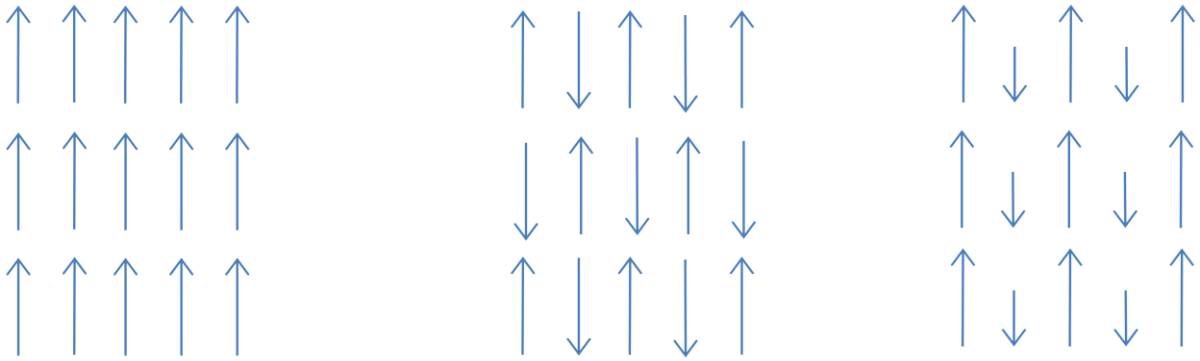

**Figure 1-1.** Magnetic ordering of a ferromagnetic (left), anti-ferromagnetic (center) and ferrimagnetic (right) nature.

## 1.1.3 Ferromagnetism

Ferromagnetism resembles paramagnetism with spins that tend to align in a parallel fashion. The spins in the material can be aligned by the external magnetic field and they will keep their alignment even when the applied field is removed. Ferromagnetic materials exhibit a net magnetic moment which is due to all unpaired electrons being aligned in the same direction; a refrigerator magnet is a simple example. We can also find magnetic materials in memory storage devices. The magnetic surface in the hard-disk is

divided into many small magnetic regions and each region can represent one bit of information.

### 1.1.4 Anti-ferromagnetism

Antiferromagnetism is the most commonly observed type of magnetism in bulk materials where the unpaired electron spins are aligned in opposite directions to their neighboring spins. Because of the reversed direction of the spins, the magnetic moments of the atoms or molecules will cancel and subsequently lead to diamagnetic behavior at absolute 0 K.

### 1.1.5 Ferrimagnetism

The interactions between spins of ferrimagnetic materials are anti-ferromagnetic in nature with a net magnetic moment different from zero. These phenomena happen when the molecule or crystal lattices consist of different materials or ions (such as $Fe^{2+}$ and $Fe^{3+}$). These materials can be magnetized by an external magnetic field and can maintain their magnetic moment when the field is removed below a certain temperature.

The ferromagnetic, anti-ferromagnetic or ferrimagnetic properties can be lost due to thermal agitation. The thermal energy above a certain temperature is large enough to render the magnetic ordering random. This temperature is called the Curie temperature

for ferro- and ferri-magnetic materials and the Néel temperature for anti-ferromagnetic material. At high enough temperatures, the material will become paramagnetic.

## 1.2 Basic principles of magnetism

### 1.2.1 Fundamental Physical Constants

When a material is placed in an applied magnetic field, the measured response is called magnetization and can be written as:

$$M = \chi * H \qquad \text{(eq. 1)}$$

where $M$ is the magnetization, $\chi$ is the magnetic susceptibility and $H$ is the auxiliary magnetic field. The definition of the magnetic susceptibility is the degree of magnetization of a material in an applied magnetic field. The unit that will be used in this thesis is $\chi$ or $\chi_m$ which is the molar magnetic susceptibility.[2] Although the International System of Unites (SI unit) should be used theoretically, the centimeter-gram-second system (cgs system) is more commonly employed in this field. Moreover, the

[2] Kittel, C. *Introduction to Solid State Physics*, 7th Ed., J. Wiley and Sons, New York, **1995**.

diamagnetic contribution to the overall susceptibility of a sample is additive as well as independent of the temperature and the strength of the applied field. We can correct the diamagnetic susceptibility by adding the diamagnetic contributions of atoms, ligands and sample holders. The molar magnetic susceptibility is presented in unit of $cm^3.mol^{-1}$ while the unit of $H$ is Oe. The magnetic susceptibility measurements in this thesis are presented as $\chi T$ which is expressed in $cm^3.K.mol^{-1}$. The molar magnetization $M$ is expressed in $cm^3.Oe.mol^{-1}$ according to equation 1 as well as in the electronic Bohr magneton unit ($\mu_B$) where 1 $\mu_B$ is equal to 5585 $cm^3.Oe.mol^{-1}$.

## 1.2.2 Curie Law and Curie-Weiss Law

The molar magnetic susceptibility of paramagnetic materials can be described by Curie's Law:

$$\chi = \frac{C}{T} \qquad (eq.\ 2)$$

where $C$ is the Curie constant and depends on the spin multiplicity of the ground state while $T$ is the temperature. This correlation was discovered by Pierre Curie in 1910 after the analysis of experimental data. Moreover, the magnetic susceptibility of a material

with ferromagnetic or anti-ferromagnetic interactions could be described by the Curie-Weiss Law:[3]

$$\chi = \frac{C}{T-\theta} \qquad \text{(eq. 3)}$$

where $C$ is the Curie constant, $T$ is the temperature and $\theta$ is the Weiss temperature or Weiss constant. A positive $\theta$ indicates ferromagnetic interaction while negative θ indicates anti-ferromagnetic interactions between the metal centers either intra- or inter-molecularly.

### 1.2.3 Van Vleck equation

When a magnetic field $H$ is applied, the magnetization will be related to the energy variation.

$$M = \frac{-\partial E}{-\partial H} \qquad \text{(eq. 4)}$$

According to the Boltzmann distribution law, the formula can be written as:

$$M = \frac{N \sum_n (\frac{\partial E_n}{\partial H}) \exp(-\frac{E_n}{kT})}{\sum_n \exp(-\frac{E_n}{kT})} \qquad \text{(eq. 5)}$$

[3] Trainer, M. *Eur. J. Phys.*, **2000**, *21*, 459.

where $T$ is the temperature, $N$ is the total number of molecules in the system, $E_n$ is the energy level of microstate and $k$ is the Boltzmann constant ( 0.685039 $cm^{-1}K^{-1}$).

In order to apply this equation, we need to consider the energies of different states, $E_n$ (energy of state n). Van Vleck expressed $E_n$ of the state n as a power series in $H_0$:

$$E_n = E_n^{(0)} + E_n^{(1)}H_0 + E_n^{(2)}H_0^2 + \cdots \quad \text{(eq. 6)}$$

where $E_n^{(0)}$ is the energy of level n in zero field. $E_n^{(1)}$ and $E_n^{(2)}$ are the 1st and 2nd Zeeman coefficients, respectively. Moreover, under zero field the magnetization will be zero.

$$\sum_n E_n^{(1)} \exp\left(-\frac{E_n^{(0)}}{kT}\right) = 0 \quad \text{(eq. 7)}$$

The magnetization can be written as:

$$M = \frac{NH\sum_n (\frac{E_n^{(1)^2}}{kT} - 2E_n^{(2)})\exp(-\frac{E_n^{(0)}}{kT})}{\sum_n \exp(-\frac{E_n^{(0)}}{kT})} \quad \text{(eq. 8)}$$

As the magnetic susceptibility ($\chi$) is equal to $M/H$, the magnetic susceptibility can be written as:[4]

$$\chi = \frac{N\sum_n (\frac{E_n^{(1)^2}}{kT} - 2E_n^{(2)})\exp(-\frac{E_n^{(0)}}{kT})}{\sum_n \exp(-\frac{E_n^{(0)}}{kT})} \quad \text{(eq. 9)}$$

[4] Bleaney, B.; Bowers, K. D. *Proc. R. Soc. London, Ser. A,* **1952**, *214*, 451

### 1.2.4 Derivation of the magnetic susceptibility from the van Vleck equation

For a paramagnetic material, the 2S+1 spins are degenerate without the presence of an external magnetic field. When a field is applied, the energies can be presented as:

$$E_n = M_s g \beta H \qquad \text{(eq. 10)}$$

where $M_s$ is varying by an integer value from $-S$ to $+S$ ($-S$, $-S+1$, ……, $S-1$, $S$), $g$ is gyromagnetic ratio and $\beta$ is the Bohr constant. The $E_n^{(0)}$ is equal to 0 since the energy of the $M_s$ in zero field is 0. The energies $E_n$ are in a linear relationship with $H$ so $E_n^{(2)}$ can be simplified to 0.

Now, the van Vleck equation can be written as:

$$\chi = \frac{Ng^2\beta^2}{3kT} S(S+1) \qquad \text{(eq. 11)}$$

This is the same equation as the Curie law. The constant $C$ depends on the spin multiplicity of the ground state and the molar magnetic susceptibility varies as $C/T$.

Experimentally, the magnetic susceptibility is measured as a function of temperature ($\chi$ *vs. T*). The data can be plotted as $\chi$ *vs. T,* $\chi T$ *vs. T* and $\chi^{-1}$ *vs. T*.[5]

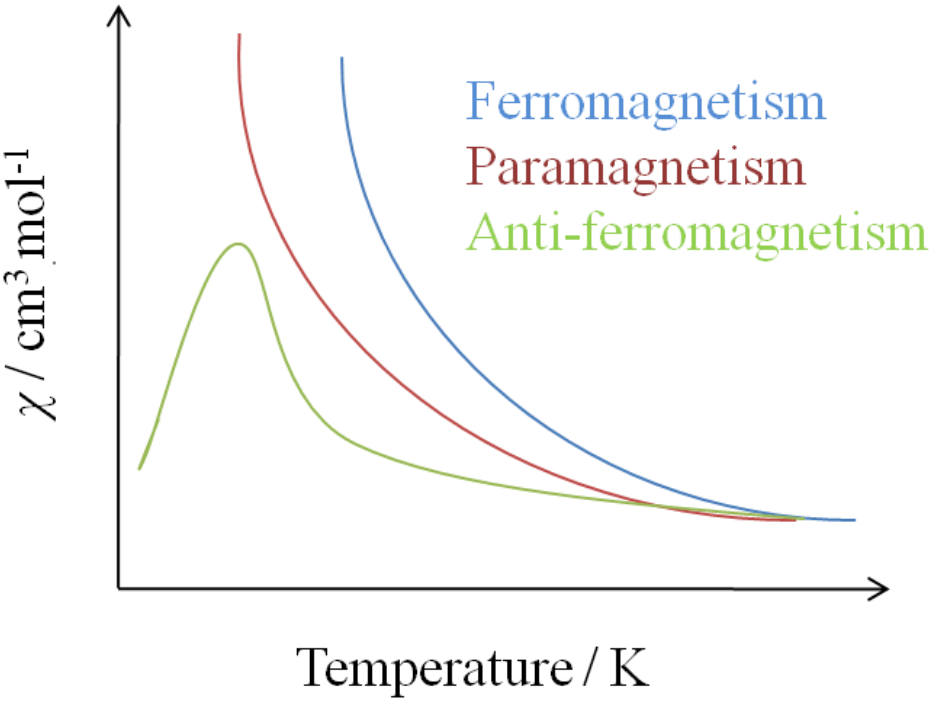


**Figure 1-2.** Magnetic susceptibility as a function of temperature.

Figure 1-2 shows the $\chi$ *vs. T* plot which is very useful for measuring the effect of field on the material. This plot is widely used in physics research. The temperatures at which a ferromagnetic and anti-ferromagnetic material become paramagnetic are called Curie temperature ($T_c$) and Néel temperature ($T_N$), respectively. However, when we look

[5] Carlin, R. L. *Magnetochemistry*, Springer-Verlag, **1986**.

for interactions between the atoms, magnetic susceptibilities will increase as the temperature decreases in all three types of magnetism. Since the slopes of the magnetic susceptibility for ferromagnetic and paramagnetic compounds are different, it is very hard to distinguish one from the other.

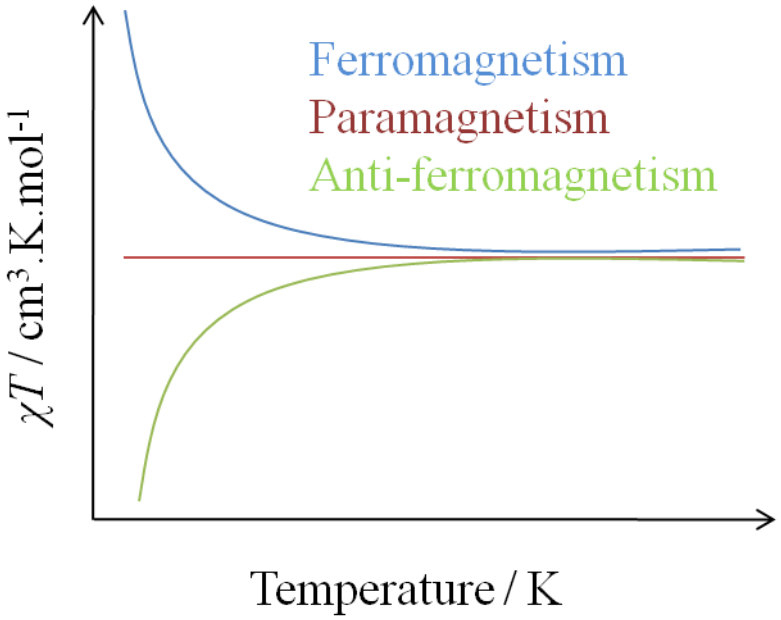


**Figure 1-3.** Magnetic susceptibility multiplied by temperature as a function of temperature.

One useful way to present the magnetic susceptibility data is $\chi T$ *vs.* $T$ (Figure 1-3). A horizontal straight line in this plot indicates paramagnetic material where the $\chi T$ value is equal to the Curie constant. Ferromagnetic and antiferromagnetic interactions can be recognized very easily by the increase or decrease, respectively, of the $\chi T$ value with

decreasing temperatures. In order to fit the curve to the Curie-Weiss Law, a plot of $\chi^{-1}$ *vs.* *T* could be practical where the slope indicates $C^{-1}$ (Figure 1-4). The constant, θ, can be obtained from the temperature intercept which can signify ferromagnetic or antiferromagnetic interactions between the metal centers for positive or negative values, respectively.

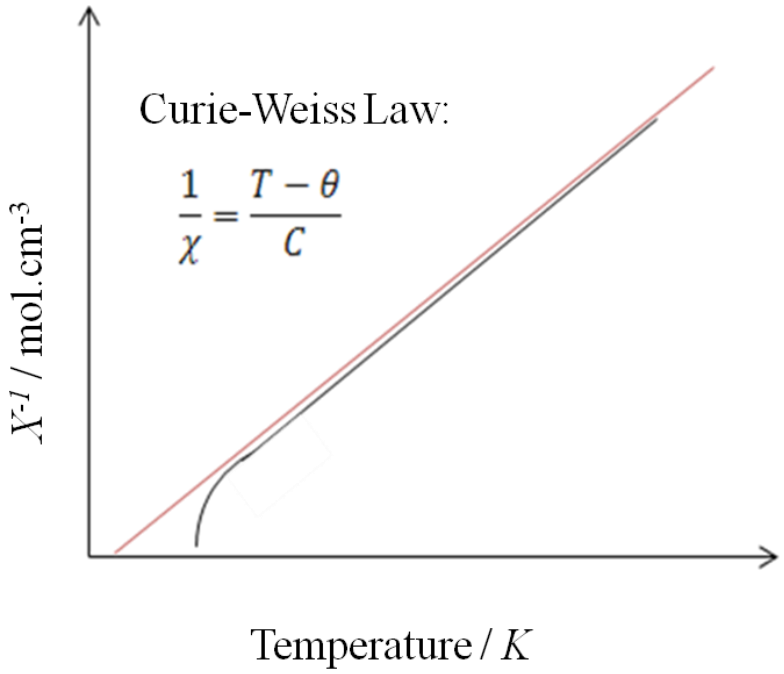


**Figure 1-4.** The inverse of the magnetic susceptibility as a function of temperature.

## 1.2.5 Magnetic anisotropy.

Magnetic anisotropy is an important factor of a material's magnetic properties where the magnetic susceptibility is no longer following the Curie Law. For an isotropic material without an applied external field, the magnetic moment does not align in any certain direction. The spins will align in a random direction and the magnetic properties will be similar to paramagnetic materials. When the magnetic materials exhibit magnetic anisotropy, the magnetic moment will prefer to align in a certain direction known as the easy axis or anisotropic axis. Additionally, the plane perpendicular to the easy axis is known as the hard plane. For molecular magnets, the magnetic anisotropy mainly results from the metal centers in the molecule. This is the key component when synthesizing a Single-Molecule Magnet. Spin-orbital coupling and/or zero-field splitting are the main contributors of magnetic anisotropy.

Spin-orbital coupling (or spin-orbital interaction) is a coupling of spin angular momentum and orbital angular momentum. The total angular momentum quantum number, $J$, can take the values of $(L+S)$, $(L+S-1)\ldots.\left|L-S\right|$ where $L$ is the orbital angular momentum and $S$ is spin angular momentum. Different values of $J$ indicate different energy levels. This mechanism may be operative for removing the degeneracy of the energy level which will result in high anisotropy. Zero-field splitting (zfs) is the removal

of $M_s$ state degeneracy for systems with S > 1/2 in the absence of an applied field. In other words, the energies of the (2S+1) spin levels of the S multiplet are split. The Jahn-Teller distortions and the spin-orbital coupling may result in zero-field splitting but not necessarily. The case for high-spin $d^5$ ions with cubic environment might also result in anisotropy but it is relatively rare.[6]

### 1.2.6 Magnetometery

In order to understand the magnetic properties of a material, we need to first measure the magnetic moment using a magnetometer. Traditionally, a sample was placed in a magnetic field and magnetized. A diamagnetic material was repelled by the applied magnetic field whereas a paramagnetic material was attracted to it. The movement between zero field and applied field could be measured. The magnetic susceptibility can be calculated from these movements.

More frequently, a Superconducting Quantum Interference Device (SQUID) (Figure 1-5) is used nowadays for magnetic measurements as it is more sensitive and accurate. Instead of directly measuring a sample the coils are inductively coupled to a

---

[6] Dunbar, K. R.; Schelter, E. J.; Tsukerblat, B. S.; Ostrovsky, S. M.; Mirovitsky, V. Y.; Palii, A. V. Polyhedron, **2003**, *22*, 2545.

superconducting loop which can detect tiny magnetic flux. There are two types of SQUIDs: dc-SQUID and ac-SQUID which are operated by direct and alternating currents, respectively. In this thesis, the magnetic susceptibility measurements were obtained using a Quantum Design SQUID magnetometer MPMS-XL operating between 1.8 and 300 K for dc applied fields ranging from -7 to 7 T.

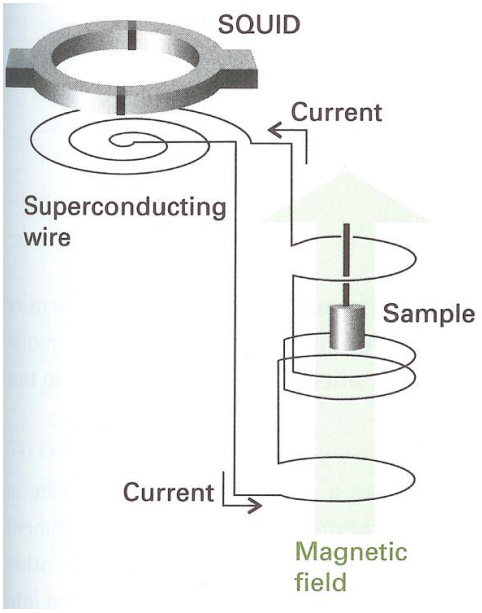


**Figure 1-5.** The arrangement used to measure the magnetic susceptibility using a SQUID[7].

The micro-SQUID is a homemade setup which can measure the magnetization of a single crystal. Dr. Wernsdorfer at the L. Néel Laboratory in Grenoble built the first

[7] Atkins, P. W. *Physical Chemistry*, W H Freeman and Co: New York, **2006**.

micro-SQUID.[8] A superconductive ring is placed on the array of SQUID device. This equipment is highly sensitive and can detect magnetic moments as small as $10^{-17}$ emu. It allows the study of magnetic properties on one micro crystal. Moreover, it is capable of measuring high sweep rates and very low temperatures (0.04 K) which makes it very useful for the investigation of molecular nanomagnets.

## 1.3 Single-Molecule Magnets (SMMs)

Magnets are widely used in a large number of applications, including refrigerator magnets and compasses. Magnets can also be applied in information storage devices such as hard discs. Each magnetic region is referred to as a magnetic domain which can save one bit of information. The more information we need to save on a disk of a certain size, the smaller the magnetic region must be. However, when the magnetic domains are lower than 10-100 nm, the material will become superparamagnetic meaning the magnet will become paramagnetic and the information will be lost as the magnetic moment

[8] Wernsdorfer,W. *Supercond. Sci. Technol.*, **2009**, *22*, 064013

disappears. Single-Molecule Magnets (SMMs)[9] are new materials with magnetic properties that depend on each molecule rather than a region, making it possible to save information in each molecule.[10] Moreover, SMMs can also be candidates for use in quantum computers due to the quantum mechanisms present in the molecule, such as quantum tunneling.[11]

SMMs are metal cluster molecules composed exclusively of metal ions and organic molecules. These polynuclear metal complexes exhibiting superparamagnetic-like properties show magnet-like behavior below their blocking temperature. There are two requirements that must be present in a complex in order for it to exhibit SMM behavior: Large spin ground state (*S*) and negative uniaxial anisotropy (*D*). These two factors generate the energy barrier *U* for the reversal of the magnetization vector, given by

---

[9] a) Christou,G.; Gatteschi, D.; Hendrickson, D. N.; Sessoli, R. *MRS Bull.*, **2000**, *25*, 66; b) Thomas, L.; Lionti, L.; Ballou, R.; Gatteschi, D.; Sessoli, R.; Barbara, B. *Nature*, **1996**, *383*, 145;

[10] a) Bogani, L.; Wernsdorfer, W. *Nat. Mater.*, **2008**, *7*, 179; b) Coronado, E., Day, P. *Chem. Rev.*, **2004**, *104*, 5419.

[11] Milios, C. J.; Piligkos, S.; Berchin, E. K. *Dalron Trans.*, **2008**, 1809.

$S^2 \left| D \right|$ and $(S^2 - 1/4) \left| D \right|$, for integer and half-integer $S$ values, respectively. Herein, the famous $\{Mn_{12}\}$[12] complex will be used as an example of an SMM.

$[Mn_{12}O_{12}(O_2CMe)_{16}(H_2O)_4]$ was first synthesized in 1980 by Lis[13] whereas the SMM property was only discovered in the early 90's by R. Sessoli et. al.[5] The $\{Mn_{12}\}$ complex is comprised of four $Mn^{IV}$ ions in the cubic center and eight $Mn^{III}$ ions in the outer shell with $Mn^{IV}$ and $Mn^{III}$ ions contributing spin of 3/2 and 2, respectively. The top view and the side view of $\{Mn_{12}\}$ are presented in Figure 1-6. In addition, there are 16 acetate and 4 water ligands in a $\{Mn_{12}\}$ cluster. Within the cubic center, $Mn^{IV}$ ions are ferromagnetically coupled to one another while in the outer shell, all $Mn^{III}$ ions are ferromagnetically coupled. The overall interaction between these two sets of Mn ions leads to an anti-ferromagnetic coupling and a net spin ground state of $S_T = 10$ which satisfies the first requirement: Large spin ground state. Moreover, the magnetic anisotropy in this complex arises from the near parallel alignment of the $Mn^{III}$ Jahn-Teller axes. This leads to significant zero field splitting this molecule. In addition to being the

---

[12] Caneschi, A.; Gatteschi, D.; Sessoli, R.; Barra, A. L.; Brunel, L. C.; Guillot, M. *J. Am. Chem. Soc.*, **1991**, *113,* 5873

[13] Lis, T. *Acta. Cryst.*, **1980**, *B36,* 2042.

most studied SMM to date, {$Mn_{12}$} held the record for the highest energy barrier (around 60 K) for an SMM for more than 15 years.

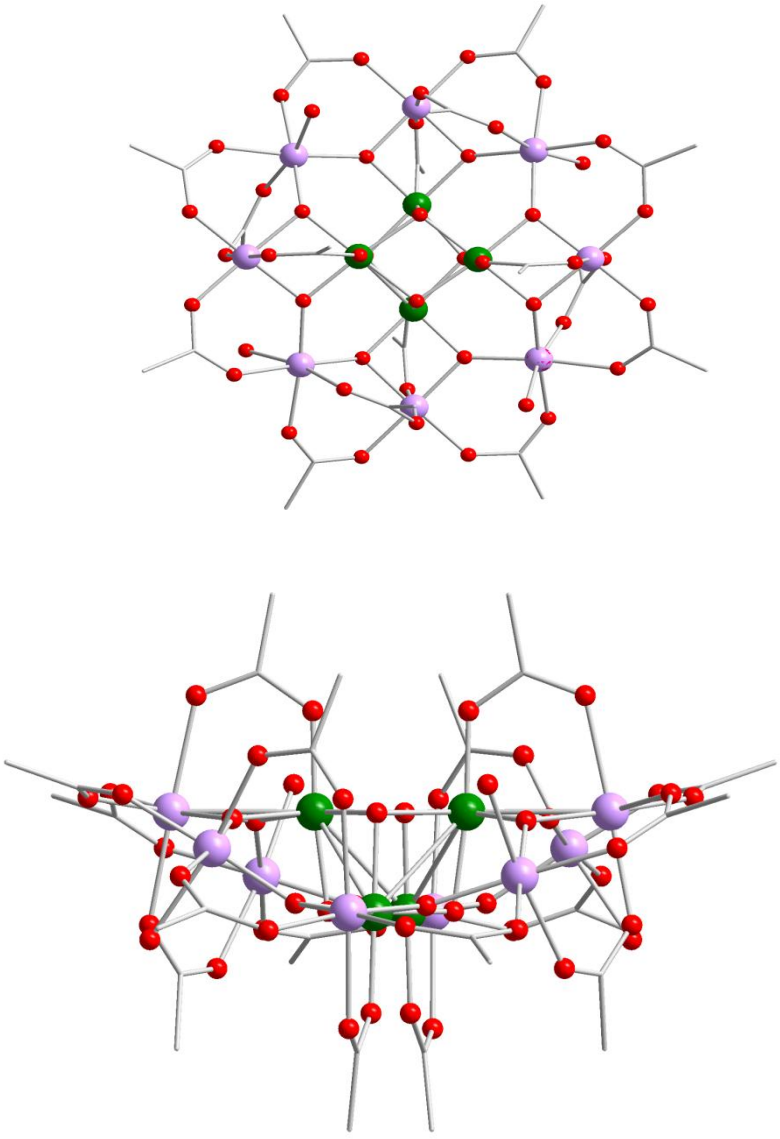

**Figure 1-6.** Top: The molecular structure of {$Mn_{12}$}. Bottom: The side view of {$Mn_{12}$}. Hydrogen atoms have been omitted for clarity. Purple ($Mn^{III}$), dark green ($Mn^{IV}$), red (O) and grey(C).

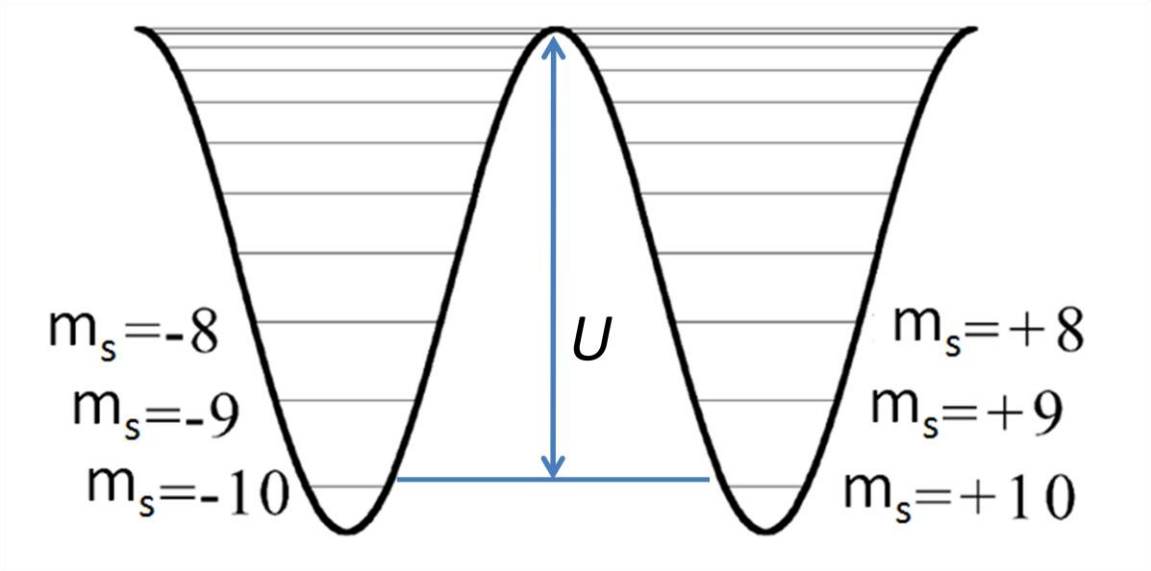


**Figure 1-7.** The energy barrier, *U* ,for the reversal of the spins between the spin 'up' ($m_s$ = 10) and 'down' ($m_s$ = -10) state for {$Mn_{12}$}.

The energy barrier which is approximately $|D| S^2$ will separate the two sub levels ($m_s$ = 10 and -10 for spin up and spin down, respectively) (Figure 1-7). The potential applications of SMMs in information storage arise from the difference in the orientations of the spins. Due to thermal agitation, the thermal energy will be higher than the energy barrier between the two states when the temperature is increased. The molecule will become paramagnetic above the blocking temperature and will no longer act as a magnet. This limits its application in information storage as the spins will randomize and the information will disappear. Therefore, synthesizing SMMs with high energy barriers is

the main target for this field using strategies that increase the total spin ground state of a molecule or increase the magnetic anisotropy.

## 1.4 Magnetic measurements for SMMs

In order to confirm the SMM properties in a complex, there are two critical measurements that can be carried out: hysteresis loop measurement and ac susceptibility measurement. Hysteresis loops are a physical phenomenon present in all magnetic materials where a magnetization lag occurs when the applied field is removed.

When an external magnetic field is applied to a paramagnetic material, the spins will align with this external field and the magnetic moment will reach saturation at high field (Figure 1-8A). Even when the external field is removed, the magnetic moment will be retained and the material will keep the magnetization. A reverse external field which can be called coercive field is necessary to remove the magnetization (Figure 1-8B). The spins will be reversed and the other saturated magnetic moment will again saturate when the negative field is increased (Figure 1-8C).

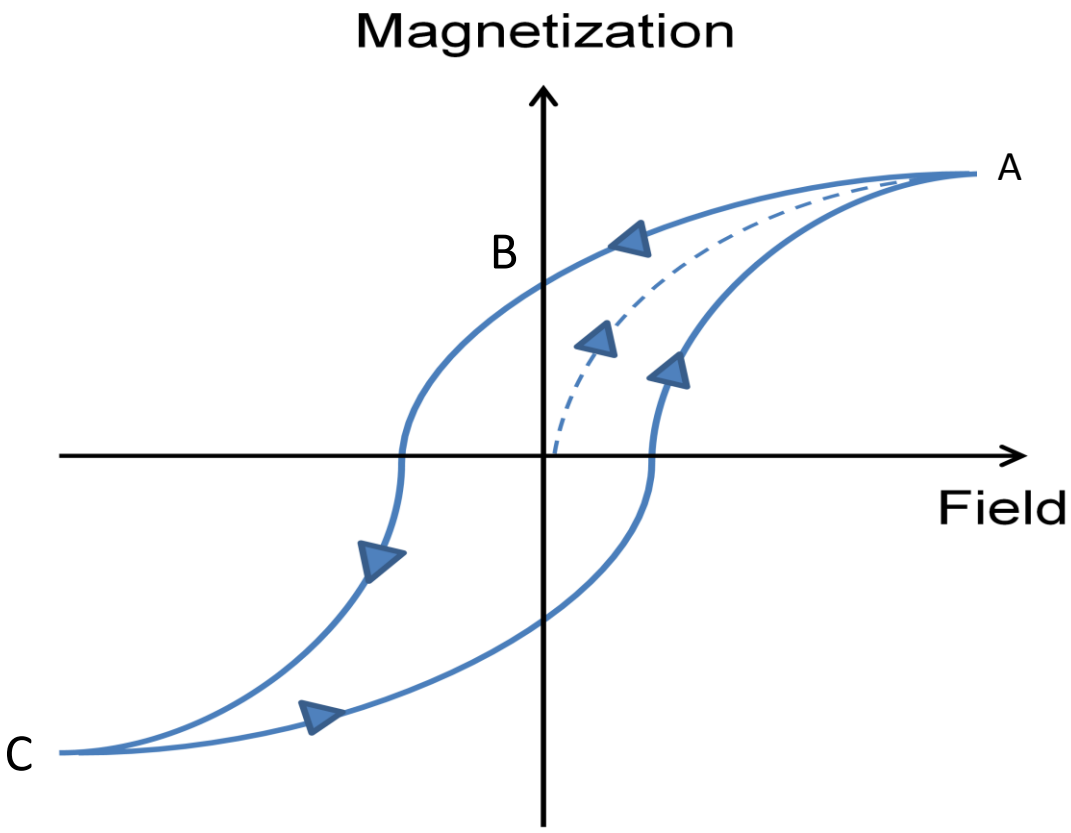


**Figure 1-8.** Plot of the magnetization *vs*. applied dc field showing an example of a hysteresis loop.

The goal is to obtain an open hysteresis loop or coercivity at high temperatures which indicates that the magnet-like property will be present at higher temperatures. However, the hysteresis loops of SMMs are only present at very low temperatures due to superparamagnetism. The micro-SQUID is key for measuring hysteresis loops of SMMs which can br observed at temperatures as low as 0.04 K.

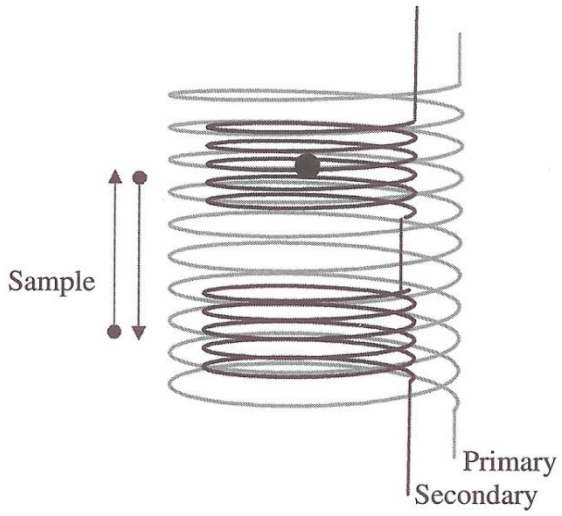


**Figure 1-9.** The coils surrounding the sample holder of an ac-SQUID.

Instead of a precision instrument, there is a very simple technique that can confirm the SMM properties of a complex known as ac susceptometry. The sample chamber is surrounded by a small wire coil and an alternating current goes through this copper coil with a small oscillating magnetic field (*H*) of less than 10 Oe generated inside the coil. The main purpose of the primary coil is to induce a magnetic moment in the sample by an alternating field. A secondary coil lies inside the primary coil and is involved in detecting the magnetic properties. This secondary coil is wrapped in two different directions (Figure 1-9).[14] If a sample is not inserted, the voltage induced in the secondary coil is

[14] Gatteschi, D.; Sessoli, R.; Villain, J. *Molecular Nanomagnets*; Oxford University Press: New York, **2006**

zero. When a sample is inserted and a magnetic field is induced by the alternating field, its oscillating magnetic moment will generate a voltage which can be detected easily in amplitude and phase by the secondary coil. Moreover, a static field $H_0$ can also be applied in the ac measurements. The total applied magnetic field becomes:

$$H = H_0 + hcos\omega t \qquad \text{(eq. 12)}$$

where $H_0$ is the applied field, $h$ is the oscillating field, $\omega$ is the angular frequency of the ac current and $t$ is elapsed time.

In a dc measurement, the magnetic susceptibility ($\chi$) is equal to $M/H$ while in an ac measurement, the magnetic susceptibility ($\chi_{ac}$) corresponds to $dM/dH$. There are two advantages arising from the latter: firstly, only a small field needs to be applied without lowering the sensitivity and secondly, the dynamics of the magnetization can be easily investigated by varying the angular frequency ($\omega$). The slow relaxation can be measured directly by ac susceptometry.

The ac susceptibility is presented as:

$$\chi(\omega) = \chi_S + \frac{\chi_T - \chi_S}{1 + i\omega\tau} \qquad \text{(eq. 13)}$$

where $\tau$ is the relaxation time which means the time it takes for the thermal equilibrium to be established, $\chi_T$ is the isothermal susceptibility when the frequency $\omega$ of the ac field is very low and $\chi_S$ is the adiabatic susceptibility when the frequency $\omega$ of the ac field is very high. The real and imaginary components of the susceptibility are given by:[15]

$$\chi'(\omega) = \chi_S + \frac{(\chi_T - \chi_S)}{1+\omega^2\tau^2} \quad \text{(eq. 14)}$$

$$\chi''(\omega) = \frac{(\chi_T - \chi_S)\omega\tau}{1+\omega^2\tau^2} \quad \text{(eq. 15)}$$

The maximum of $\chi''$ will occur when $\omega\tau$ is equal to 1, so the relaxation time can be calculated by the frequency $\omega$.

Moreover, because $\chi_{ac}$ corresponds to *dM/dH*, the magnetization can be defined by:

$$M(t) = M_0 + Re[(\chi' - i\chi'')he^{i\omega t}] = M_0 + (\chi' \cos\omega t + \chi'' \sin\omega t)h \quad \text{(eq. 16)}$$

where $M_0$ is the magnetization of the static field, $h$ is the oscillating field, $\omega$ is the angular frequency of the ac current and $t$ is elapsed time. Eq. 16 also explains why real and imaginary susceptibility are called in-phase and out-of-phase susceptibility, respectively.

---

[15] Domingo, N.; Luis, F.; Nakano, M.; Munto, M.; Gomez, J.; Chaboy, J.; Ventosa, N.; Campo, J.; Veciana, J.; Ruiz-Molina, D. *Phys. Rev. B*, **2009**, 79.

When a relaxation process is not characterized by a single $\tau$, the ac susceptibility can be described by:[16]

$$\chi(\omega) = \chi_S + \frac{\chi_T - \chi_S}{1+(i\omega\tau)^{1-\alpha}} \quad \text{(eq. 17)}$$

where,

$$\chi'(\omega) = \chi_S + \frac{(\chi_T - \chi_S)\left[1+(\omega\tau)^{1-\alpha}\sin{}^{1}\!/_{2}\alpha\pi\right]}{1+2(\omega\tau)^{1-\alpha}\sin{}^{1}\!/_{2}\alpha\pi+(\omega\tau)^{2(1-\alpha)}} \quad \text{(eq. 18)}$$

$$\chi''(\omega) = \frac{(\chi_T - \chi_S)(\omega\tau)^{1-\alpha}\cos{}^{1}\!/_{2}\alpha\pi}{1+2(\omega\tau)^{1-\alpha}\sin{}^{1}\!/_{2}\alpha\pi+(\omega\tau)^{2(1-\alpha)}} \quad \text{(eq. 19)}$$

with the α factor describing the distribution of the relaxation times in a sample. When α is zero, the formula will be the same as eq. 13 which means there is only one relaxation process in the molecule.

Because all paramagnetic materials will exhibit a $\chi'$ signal at low temperature, the out-of-phase susceptibility signal ($\chi''$) is more commonly used to detected SMM properties in the ac measurement. The frequency for common measurements ranges from 1 Hz to 1500 Hz which can be corrected to the spin-spin relaxation time of the paramagnetic materials. The temperature range for these measurements is around 1.8-50

---

[16] Cole, K. S.; Cole, R. H. *J. Chem. Phys.*, **1941**,*9*, 341.

K since the SMM properties are only present at low temperatures. If the material is behaving as an SMM, we would observe a maximum value of $\chi''$ which is temperature and frequency dependent. Figure 1-10 shows an example of an analogue of $\{Mn_{12}\}$ behaving as an SMM.[17]

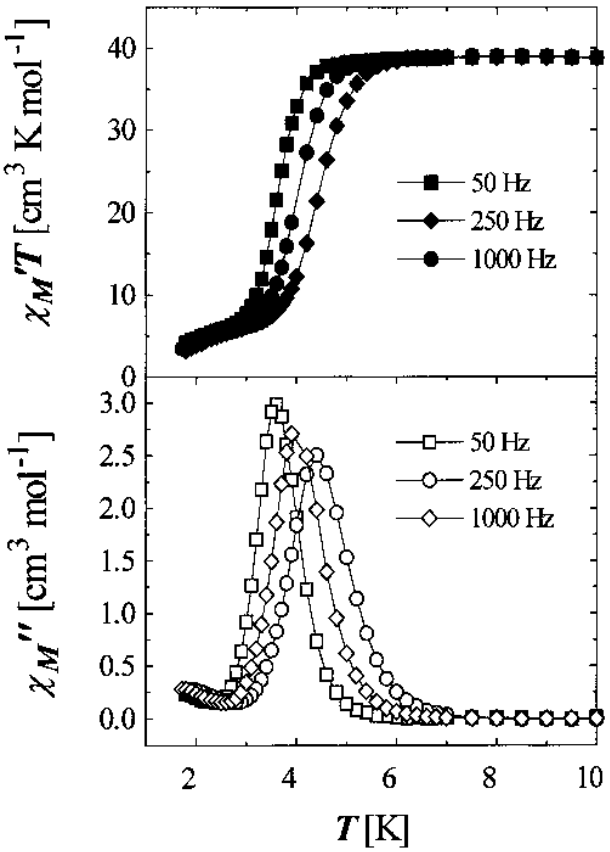


**Figure 1-10.** Temperature dependence of the in-phase and out-of-phase ac susceptibility of $(PPh_4)[Mn_{12}O_{12}(O_2CPh)_{16}(H_2O)_4]$.

[17] Aubin, S. M. J.; Sun, Z.; Pardi, L.; Krzystek, J.; Folting, K.; Brunel, L.-C.; Rheingold, A. L.; Christou, G.; Hendrickson, D. N. *Inorg. Chem.*, **1999**, *38*, 5329.

This phenomenon is related to the slow relaxation characteristic of SMMs. When an alternating field is applied to a paramagnetic material, the direction of the spins will follow the alternating field and $\chi''$ would be close to zero. For SMMs, the spin ground state of the molecule exhibits bistability through the presence of two sub levels ($m_s$) at the same energy. These two $m_s$ levels are separated by an energy barrier and we can assume that the spins in these levels are oriented in opposite directions. (Figure 1-7) When an alternating field is applied to an SMM, the spin will follow the direction of the field but the sweep rate of the spins will be slower than the rate of the field. This difference is attributed to an energy barrier between the two $m_s$ levels.

The peak shifting in the $\chi''$ *vs. T* or $\chi''$ *vs.* $\upsilon$ plots is characteristic of SMM behavior. The maximum of $\chi''$ will be observed when the frequency satisfies the relation $\omega = \tau^{-1}$ and the relaxation time can be calculated using:

$$\tau = \omega^{-1} = (2 * \pi * \upsilon)^{-1} \qquad \text{(eq. 20)}$$

The temperatures and frequencies at the peak positions of each curve are determined by fitting the $\chi''$ *vs. T* or $\chi''$ *vs.* $\upsilon$ data using a Gaussian function. The relaxation time will decrease as the temperature increases obeying the Arrhenius equation which means the effective energy barrier ($U_{eff}$) can be determined by fitting the experimental data to:

$$\tau = \tau_0 e^{\frac{U_{eff}}{kT}} \text{ or } \ln(\tau) = \ln(\tau_0) + \frac{U_{eff}}{kT} \qquad \text{(eq. 21)}$$

where $k$ is the Boltzmann constant, $T$ is the temperature and $\tau_0$ is the pre-exponential factor. When we plot ln(τ) as a function of $1/T$, the slope of the straight line region obtained is $U_{\text{eff}}$.

## 1.5 Lanthanide chemistry

Lanthanide elements are a set of fifteen chemical elements at the bottom of the periodic table. Although they are known as rare earth elements, the abundance of the lanthanides in the earth's crust is not all relatively low. The elements are typically dispersed; they are not in concentrated ores and are economically inexploitable.

The electron configurations of lanthanide metals are presented in Table 1-1. The 5*d* subshell is lower in energy than the 4*f* orbital so the configuration of La is [Xe]5$d^1$6$s^2$. As the atomic number increases, more protons are added to the nucleus and the 4*f* orbitals contract becoming more stable than the 5*d* orbitals. The electron configurations can be presented by [Xe]4$f^n$6$s^2$ (n=3-14 for Pr-Yb except Gd).

The physical and chemical properties of lanthanides are different from the *d*-block metals due to the 4*f* orbitals. The 4*f* electrons are shielded by the 5*s* and 5*p* electrons and

are core-like in their behaviors. 4*f* orbitals cannot overlap with ligand orbitals and do not participate in bonding. The spectroscopic and magnetic properties are independent of the environment since the buried 4*f* orbitals are not influenced by the ligand field. Moreover, ligand sterics become more important than crystal field effects. Crystal-field splitting of lanthanide coordination complexes is smaller than that for *d*-block metal and the electronic spectra are very sharp. Lanthanide elements also span a wider range of coordination numbers than the transition metals (generally 6-12).

**Table 1-1**. Electron configurations of the lanthanide metals and the corresponding ions.

| | **La** | **Ce** | **Pr** | **Nd** | **Pm** |
|---|---|---|---|---|---|
| Atom | $[Xe]5d^16s^2$ | $[Xe]4f^15d^16s^2$ | $[Xe]4f^36s^2$ | $[Xe]4f^46s^2$ | $[Xe]4f^56s^2$ |
| $Ln^{III}$ | [Xe] | $[Xe]4f^1$ | $[Xe]4f^2$ | $[Xe]4f^3$ | $[Xe]4f^4$ |
| | **Sm** | **Eu** | **Gd** | **Tb** | **Dy** |
| Atom | $[Xe]4f^66s^2$ | $[Xe]4f^76s^2$ | $[Xe]4f^75d^16s^2$ | $[Xe]4f^96s^2$ | $[Xe]4f^{10}6s^2$ |
| $Ln^{III}$ | $[Xe]4f^5$ | $[Xe]4f^6$ | $[Xe]4f^7$ | $[Xe]4f^8$ | $[Xe]4f^9$ |
| | **Ho** | **Er** | **Tm** | **Yb** | **Lu** |
| Atom | $[Xe]4f^{11}6s^2$ | $[Xe]4f^{12}6s^2$ | $[Xe]4f^{13}6s^2$ | $[Xe]4f^{14}6s^2$ | $[Xe]4f^{14}5d^16s^2$ |
| $Ln^{III}$ | $[Xe]4f^{10}$ | $[Xe]4f^{11}$ | $[Xe]4f^{12}$ | $[Xe]4f^{13}$ | $[Xe]4f^{14}$ |

## 1.6 Magnetic properties of $Ln^{III}$ ions

Because the 4*f* electrons are shielded by the filled 5*s* and 5*p* orbitals, the ligand field will not affect the ground state of lanthanide ions, resulting in weak crystal field splittings. In these cases, the spin-orbit coupling becomes more important. This interaction occurs between *S* (spin quantum number) and *L* (orbital angular momentum) which is described by the total angular momentum and the quantum number *J*. *J* can have values ranging between (*L*+*S*)……(*L*-*S*). For shells that are less than half-filled, *J* for the ground state takes the lowest value (*L*-*S*). When the shell is more than half-filled, the ground state will be the highest value of *J* (*L*+*S*). The ground state terms and magnetic moments of $Ln^{III}$ ions are presented in Table 1-2. Moreover, an example of energy levels seen for $Ln^{III}$ ions is presented in Figure 1-11.[18]

[18] Ishikawa, N.; Sugita, M.; Ishikawa, T.; Koshihara, S-Y.; Kaizu, Y. *J. Phys. Chem. B,* **2004,** *108,* 11265.

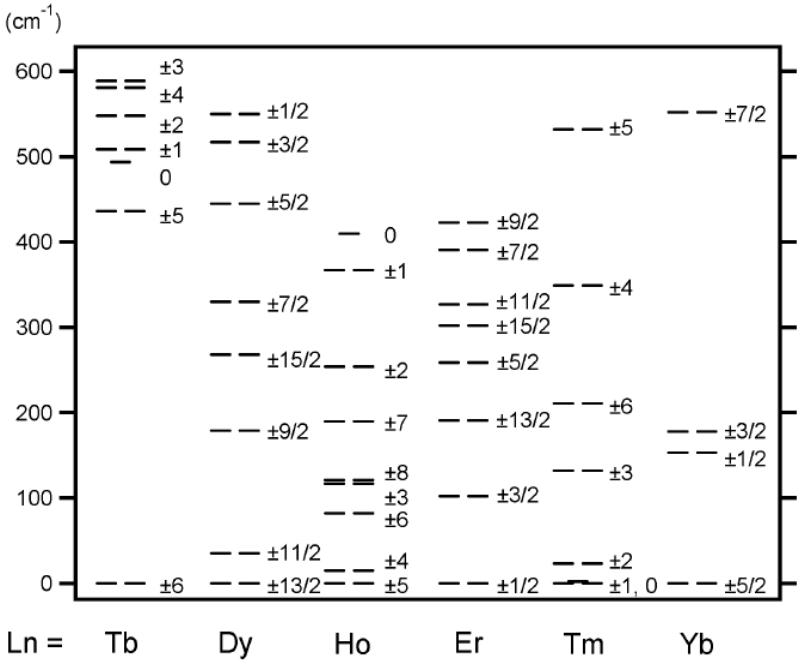


**Figure 1-11.** Energy diagram of the substates of the ground state multiplets of $[Pc_2Ln]^-TBA^+$ (Ln : Tb, Dy, Ho, Er, Tm, or Yb)

**Table 1-2**. Ground state terms and magnetic moments of $Ln^{III}$ ions.

| | Ce | Pr | Nd | Pm | Sm | Eu | Gd |
|---|---|---|---|---|---|---|---|
| Unpaired electrons | 1 | 2 | 3 | 4 | 5 | 6 | 7 |
| Ground state term | $^2F_{5/2}$ | $^3H_4$ | $^4I_{9/2}$ | $^5I_4$ | $^6H_{5/2}$ | $^7F_0$ | $^8S_{7/2}$ |
| $g_J$ | 6/7 | 4/5 | 8/11 | 3/5 | 2/7 | 5 | 2 |
| $\chi T$ ($cm^3Kmol^{-1}$) | 0.80 | 1.60 | 1.64 | 0.90 | 0.09 | 0 | 7.88 |

| | Tb | Dy | Ho | Er | Tm | Yb |
|---|---|---|---|---|---|---|
| Unpaired electrons | 6 | 5 | 4 | 3 | 2 | 1 |
| Ground state term | $^7F_6$ | $^6H_{15/2}$ | $^5I_8$ | $^4I_{15/2}$ | $^3H_6$ | $^3F_{7/2}$ |
| $g_J$ | 3/2 | 4/3 | 5/4 | 6/5 | 7/6 | 8/7 |
| $\chi T$ ($cm^3Kmol^{-1}$) | 11.82 | 14.17 | 14.07 | 11.48 | 7.15 | 2.57 |

$Ln^{III}$ ions all contain unpaired electrons and are paramagnetic with the exception of $La^{III}$ and $Lu^{III}$. The magnetic moments of the $Ln^{III}$ ions are essentially independent of the environment and are given by the equations:

$$\mu_{\text{eff}} = g_J\sqrt{J(J+1)} \qquad \text{(eq. 21)}$$

or

$$\chi T = \frac{g_J^2 * J * (J+1)}{8} \qquad \text{(eq. 22)}$$

and $g_J$ can be described as:

$$g_J = [S(S+1) - L(L+1) + 3J(J+1)]/2J(J+1) \qquad \text{(eq. 23)}$$

$J$ is the total angular momentum of quantum number. The spin ground state and the values of $g_J$ and $\chi T$ for lanthanide ions are presented in Table 1-2.

## 1.7 Lanthanide SMMs

Single-Molecule Magnets (SMMs) are discrete molecules which exhibit slow relaxation of the magnetization at low temperatures. Due to their nano-size, SMMs are often seen as the ultimate elementary magnetic unit that could be used in future electronic devices and high density storage systems. Recently, rare-earth metal systems, such as Tb, Dy, Ho and Er, have sparked increasing interest in the area of molecular magnetism due to their large spin ground states and uni-axial anisotropy.[19] Ishikawa and co-workers published the first lanthanide SMM.[20] Double-decker phthalocyanine mononuclear complexes with Tb, Dy, Ho, Er, Tm, or Yb ions were synthesized. The Tb and Dy compexes showed slow magnetization relaxation as a single-molecular entity where the temperature ranges in which the behavior was observed were far higher than those of transition-metal-cluster SMMs. It has been proven that lanthanide elements are

---

[19] Bertaina,S,; Gambarelli, S.; Tkachuk, A.; Kurkin, I. N.; Malkin, B.; Stepanov, A.; Barbara, B. *Nat. Nanotechnol.,* **2007**, *2*, 39; b) Benelli, C.; Gatteschi, D. *Chem. Rev.*, **2002**, *102*, 2369.

[20] Ishikawa, N.; Sugita, M.; Ishikawa, T.; Koshihara, S.; Kaizu, Y. *J. Am. Chem. Soc.*, **2003**, *125*, 8694.

good candiates for SMMs even as mononuclear complexes. Large spin ground state (*S*) and uni-axial anisotropy (*D*) are the two factors that generate the energy barrier (*U*). The large number of unpaired electrons in lanthanide ions result in large *S* values. Large intrinsic *D* values can be attributed to large spin-orbital coupling characteristic of lanthanide ions except for $Gd^{III}$ which has half-filled *f* orbitals.

It is difficult to promote magnetic interactions between the lanthanide ions because the 4*f* orbitals are well shielded by 5*s* and 5*p* orbitals. However, it is still a challenge to induce interactions between $Ln^{III}$ centers. One of the approaches involves the synthesis of lanthanide-only complexes with the right super-exchange pathways. Pure lanthanide SMMs require overlapping orbitals which would enhance magnetic interactions between the metal centers. This pathway could be obtained using bridging ligands. Pure lanthanide SMMs are relatively rare; however they have become increasingly popular and widely studied in the past five years. Dinuclear[21], trinuclear[22],

---

[21] a) Aguilà, D.; Barrios, L. A.; Luis, F.; Repollés, A.; Roubeau, O.; Teat, S. J.; Aromí, G. *Inorg. Chem.*, **2010**, *49*, 6784; b) Bernot, K.; Pointillart, F.; Rosa, P.; Etienne, M.; Sessoli, R.; Gatteschi, D. *Chem. Commun.*, **2010**, *46*, 6458; c) Chakraborty, J.; Ray, A.; Pilet, G.; Chastanet, G.; Luneau, D.; Ziessel, R. F.; Charbonniere, L. J.; Carrella, L.; Rentschler, E.;

tetranuclear[23], pentanuclear[24], hexanuclear[25] to polynuclear[26] dysposium clusters with

---

El Fallah, M. S.; Mitra, S. *Dalton Trans.*, **2009**, 10263; d) Layfield, R.; McDouall, J. J.; Sulway, S.; Tuna, F.; Collison, D.; Winpenny, R. E. *Chem. Eur. J.*, **2010**, *16*, 4442; e) Xu, G.-F.; Wang, Q.-L.; Gamez, P.; Ma, Y.; Clerac, R.; Tang, J.; Yan, S.-P.; Cheng, P.; Liao, D.-Z. *Chem. Commun.*, **2010**, *46*, 1506.

[22] a) Tang, J.; Hewitt, I.; Madhu, N. T.; Chastanet, G.; Wernsdorfer, W.; Anson, C. E.; Benelli, C.; Sessoli, R.; Powell, A. K. *Angew. Chem. Int. Ed.*, **2006**, *45*, 1729; b) Hewitt, I. J.; Lan, Y.; Anson, C. E.; Luzon, J.; Sessoli, R.; Powell, A. K. *Chem. Commun.*, **2009**, 6765.

[23] a) Abbas, G.; Lan, Y.; Kostakis, G. E.; Wernsdorfer, W.; Anson, C. E.; Powell, A. K. *Inorg. Chem.*, **2010**, *49*, 8067; b) Bi, Y.; Wang, X.-T.; Liao, W.; Wang, X.; Deng, R.; Zhang, H.; Gao, S. *Inorg. Chem.*, **2009**, *48*, 11743; c) Gao, Y.; Xu, G.-F.; Zhao, L.; Tang, J.; Liu, Z. *Inorg. Chem.*, **2009**, *48*, 11495; d) Guo, Y.-N.; Xu, G.-F.; Gamez, P.; Zhao, L.; Lin, S.-Y.; Deng, R.; Tang, J.; Zhang, H.-J. *J. Am. Chem. Soc.*, **2010**, *132*, 8538; e) Ke, H.; Gamez, P.; Zhao, L.; Xu, G.-F.; Xue, S.; Tang, J. *Inorg. Chem.* **2010**, *49*, 7549; f) Ke, H.; Xu, G.-F.; Guo, Y.-N.; Gamez, P.; Beavers, C. M.; Teat, S. J.; Tang, J. *Chem. Commun.*, **2010**, *46*, 6057; g) Wang, Y.; Li, X.-L.; Wang, T.-W., Song, Y., You, X.-Z.

SMM properties have emerged with high energy barriers.

---

*Inorg. Chem.*, **2009**, *49*, 969; h) Zheng, Y.-Z.; Lan, Y.; Anson, C. E.; Powell, A. K. *Inorg. Chem.*, **2008**, *47*, 10813.

[24] Gamer, M. T.; Lan, Y.; Roesky, P. W.; Powell, A. K.; Clérac, R. *Inorg. Chem.*, **2008**, *47*, 6581.

[25] a) Hussain, B.; Savard, D.; Burchell, T. J.; Wernsdorfer, W.; Murugesu, M. *Chem. Commun.*, **2009**, 1100; b) Langley, S. K.; Moubaraki, B.; Forsyth, C. M.; Gass, I. A.; Murray, K. S. *Dalton Trans.* **2010**, *39*, 1705.

[26] a) Feng, X.; Liu, B.; Wang, L.-Y.; Zhao, J.-S.; Wang, J. G.; Weng, N. S.; Shi, X.-G. *Dalton Trans.*, **2010**, *39*, 8038; b) Feng, X.; Wang, L.-Y.; Wang, J.-G.; Xie, C.-Z.; Zhao, J.-S.; Sun, Q. *CrystEngComm*, **2010**, *12*, 3476; c) Gu, X., Clérac, R.; Houri, A.; Xue, D. *Inorg. Chim. Acta.*, **2008**, *361*, 3873; d) Gu, X., Xue, D. *Inorg. Chem.*, **2007**, *46*, 3212; e) Liu, R.; Li, L.; Wang, X.; Yang, P.; Wang, C.; Liao, D.; Sutter, J.-P. *Chem. Commun.*, **2010**, *46*, 2566; f) Plabst, M.; Bein, T. *Inorg. Chem.*, **2009**, *48*, 4331; g) Zheng, Y. Z.; Lan, Y.; Wernsdorfer, W.; Anson, C.; Powell, A. *Chem. Eur. J.*, **2009**, *15*, 12566; h) Ke, H.; Xu, G. F.; Zhao, L.; Tang, J.; Zhang, X. Y.; Zhang, H. J. *Chem. Eur. J.*, **2009**, *15*, 10335; i) Westin, L. G.; Kritikos, M.; Caneschi, A. *Chem. Commun.* **2003**, 1012.

Quantum tunneling of the magnetization (QTM) occurs when energy levels of two sub-states coincide under an appropriate magnetic field and the states are brought to resonance.[27] This results in an experimental energy barrier ($U_{eff}$) lower than the value from $U = S^2|D|$ due to tunneling promoting an overall relaxation process. In lanthanide SMMs, the pure quantum regime could be observed at low temperatures. The peaks in the of out-of-phase ac susceptbility plot become temperature independent resulting in a plateau in the Arrhenius plot. The relaxation becomes thermally activated (Arrhenius-like behavior) when thermal relaxation becomes faster than quantum relaxation. In order to reduce the occurring QTM and confirm the pure thermal relaxation regime, a static dc field can be applied in the ac measurement which might lift the degeneracy and result in an energy barrier unaffected by quantum tunnelling.

Moreover, the packing arrangements of the complexes will be directly related to their magnetic properties.[28] Although modifying counter ions and/or co-solvents in the

---

[27] Ishikawa, N.; Sugita, M.; Wernsdorfer, W. *Angew. Chem. Int. Ed.* **2005**, *44*, 2931

[28] a) Aakeroy, C. B.; Champness, N. R.; Janiak, C. *CrystEngComm*, **2010**, *12*, 22; b) Feng, P. L.; Koo, C.; Henderson, J. J.; Nakano, M.; Hill, S.; del Barco, E.; Hendrickson,

reaction can tune the organization of the SMM units, modified ligands with specific functional groups can more effectively predict the packing arrangements. Here, a series of Schiff-base ligands have been applied in the synthesis of pure lanthanide complexes with nuclearities ranging from one to four.

## 1.8 Ligand design

In the isolation of molecular magnetic systems, ligands play an important role by stabilizing and encapsulating metal ions as well as promoting intramolecular interactions *via* super-exchange pathways. Therefore, along with appropriate metal systems, careful ligand design is essential. As part of our research efforts towards new preparative routes to SMMs, we turned our attention to polydentate Schiff-base ligands in lanthanide chemistry.

The Schiff-base ligands are characterized by a carbon double bonded to a nitrogen atom and can be synthesized from the reaction of a primary amine with an aldehyde

---

D. N. *Inorg. Chem.* **2008**, *47*, 8610; c) Inglis, R.; Katsenis, A. D.; Collins, A.; White, F.; Milios, C. J.; Papaefstathiou, G. S.; Brechin, E. K. *CrystEngComm*, **2010**, *12*, 2064.

starting material.[29] The mechanism is presented in Scheme 1-1. A moderate acid will help the protonation of the hydroxyl intermediate to allow for the removal of water.

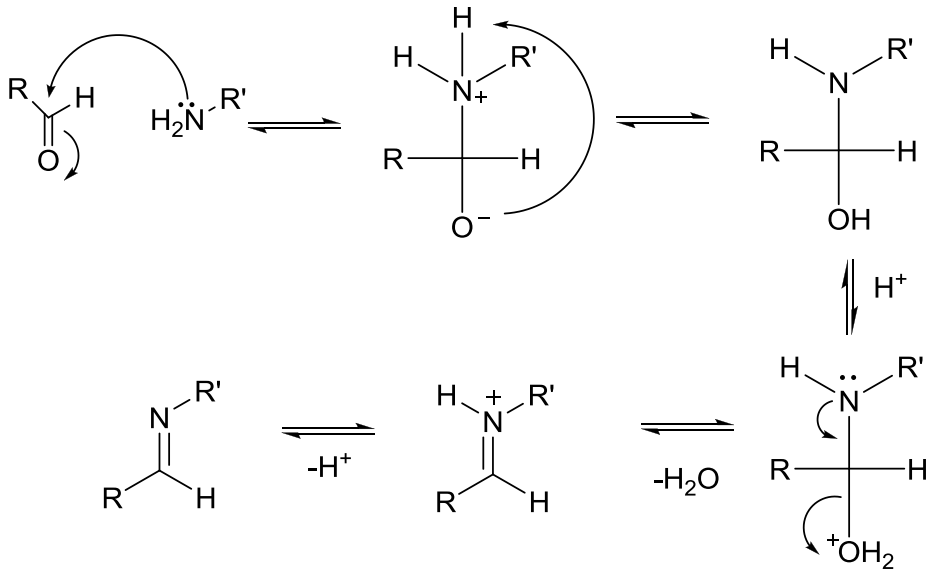


**Scheme 1-1.** The mechanism of a Schiff-base reaction.

The *o*-vanillin molecule has been applied in the synthesis of trinuclear $Dy^{III}$ complexes with novel magnetic properties.[15a] The deprotonated phenoxy atoms act as bridges creating a super-exchange pathway between the metal centers. In this thesis, various Schiff-base ligands are investigated which are based on the *o*-vanillin moiety including hydrazine-based molecules which provide an O,N,N,O multichelating coordination pocket (Table 1-3). It is well known that N- and mostly O-based

[29] Yang, D.-S. *J. Chem. Cryst.*, **2007**, *37*, 343.

coordination environments favor the encapsulation of lanthanide ions which can accommodate most commonly 8 or 9 coordination sites. Possible coordination modes of the ligands are presented in Scheme 1-2.

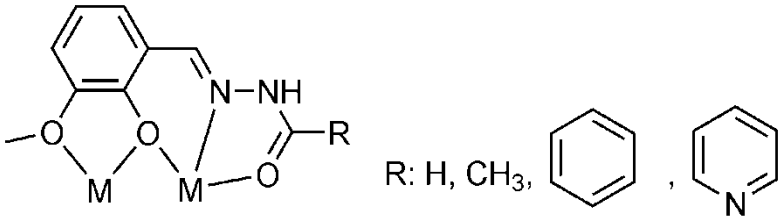


**Scheme 1-2**. Possible coordination modes of the ligands.

A series of ligands with the same coordinating pocket and different R groups were synthesized to diversify the lanthanide complexes. Comparing different complexes with similar core structures will allow us to probe the interaction mechanisms between metal centers. Moreover, the R groups can also bridge the metal units forming extended structures. For example, the ligand with a pyridine group provides an avenue for the formation of organized extended coordination networks; using terephthalohydrazide to react with *o*-vanillin will form two pockets at each site of the ligand.

It is noteworthy that the ligands can exist in various tautomeric forms.[30] This

---

[30] Lin, P.-H.; Gorelsky, S.; Savard, D.; Burchell, T. J.; Wernsdorfer, W.; Clérac, R.; Murugesu, M. *Dalton Trans*., **2010**, *39*, 7650.

provides rich and versatile coordination chemistry with metal centers. An example of a ligand with different tautomeric forms is presented in Scheme 1-3. The charges on the ligand could vary between neutral, -1 and -2 depending on the charge balance of the whole molecule and the number of deprotonated atoms.

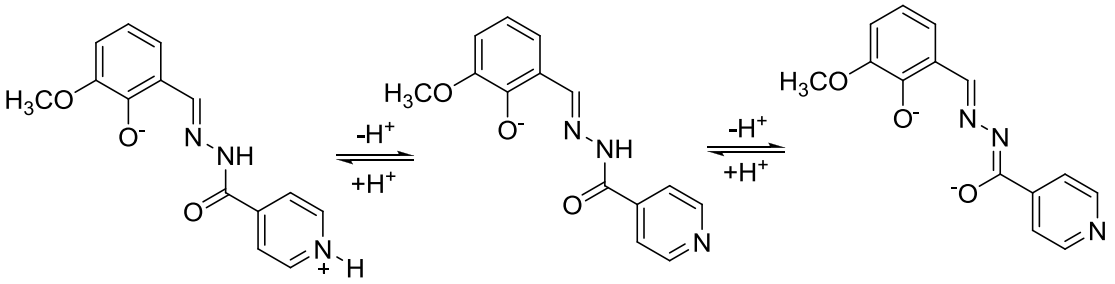

**Scheme 1-3**. Different tautomeric forms of the ligand.

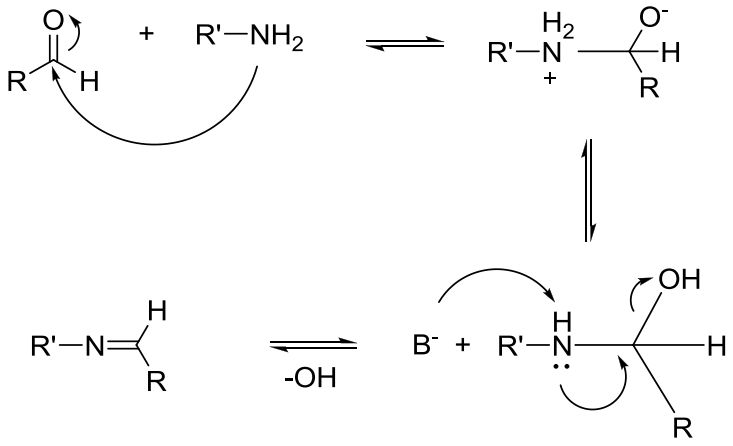

**Scheme 1-4**. The mechanism involved in a Schiff-base reaction under basic conditions.

In addition to the synthesis of Schiff-base ligands, this *in situ* strategy is also applied in the synthesis of inorganic complexes where base is a key component in the reaction. The Schiff-base reaction under basic conditions is presented in Scheme 1-4. Because the $OH^-$ group is not a good leaving group, the reaction rate is much slower than the reaction under acidic or neutral conditions (Scheme 1-2). However, Schiff-base ligands can be synthesized under basic conditions where metal ions in the reaction can form $M(OH)^{n+}$ to help remove the $OH^-$ group,

**Table 1-3.** Starting materials for the ligands.

| Starting material | | Ligand |
|---|---|---|
| 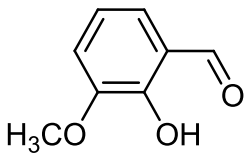 | 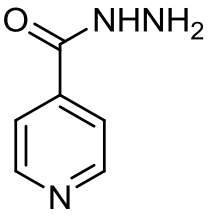 | 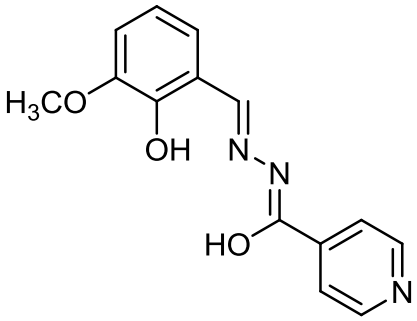 (2-hydroxy-3-methoxyphenyl) methylene-(isonicotino)hydrazine ($H_2$hmi) |

| | | |
|---|---|---|
| | 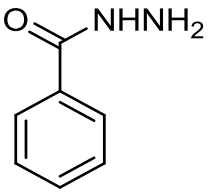 | 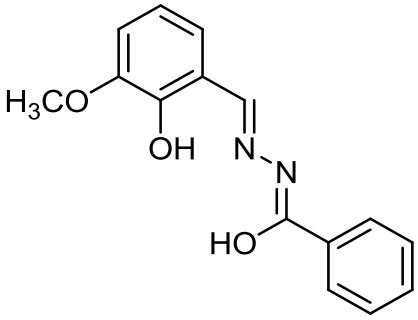 <br>(2-hydroxy-3-methoxyphenyl)methylene-<br>benzohydrazine ($H_2$hmb) |
| | 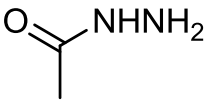 | 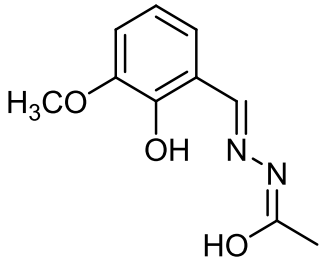 <br>(2-hydroxy-3-methoxyphenyl)methylene-<br>(aceto) hydrazine ($H_2$hma) |
| | 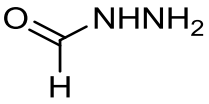 | 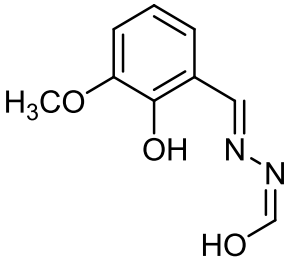 <br>[(2-hydroxy-3-methoxyphenyl)methylene]<br>Formylhydrazine ($H_2$hmf) |

| | | |
|---|---|---|
| | $NH_2NH_2$ | 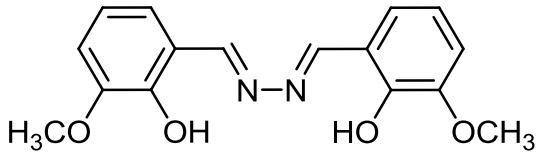 <br>1,2-bis(2-hydroxy-3-methoxybenzylidene)-hydrazone ($H_2$bmh)<br> 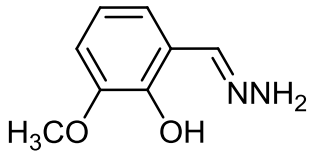 <br>3-methoxysalicylaldehyde hydrazone (Hmsh) |
| | 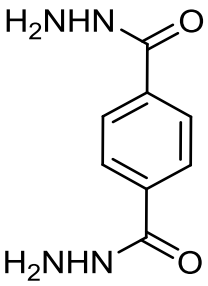 | 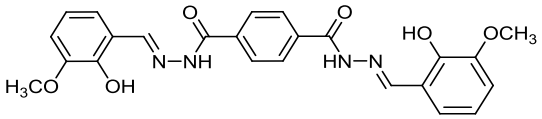 <br>*N,N'*-bi(2-hydroxy-3-methoxybenzylidene)-terephthalohydrazide ($H_4$hmt) |
| 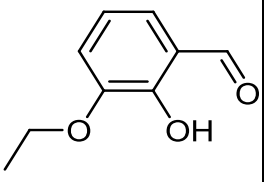 | 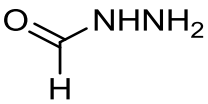 | 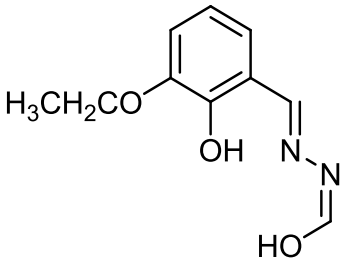 <br>[(2-hydroxy-3-ethoxyphenyl)methylene]-formylhydrazine ($H_2$hef) |

| | | |
|---|---|---|
| 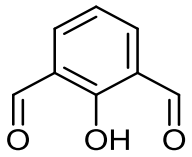 | 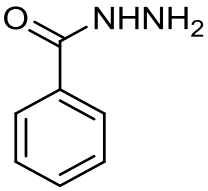 | 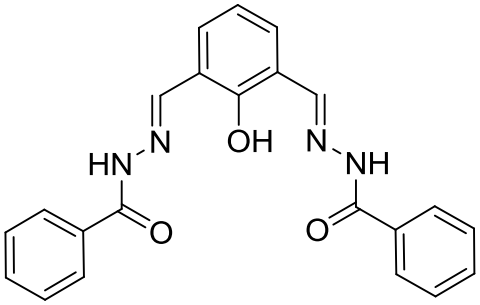 (2-hydroxyphenyl)-1,3-bis(methylene-(benzonicotino) hydrazine) ($H_3$hbb) |

## 1.9 Thesis overview

Lanthanide complexes with different nuclearities (Ln, $Ln_2$, $Ln_3$ and $Ln_4$) are presented in the following chapters by increasing number of metal centers. This thesis will demonstrate a systematic approach to the synthesis and development of multi-nuclear lanthanide complexes. Each chapter consists of crystal structures for complexes with the same nuclearity as well as magnetic measurements performed if their magnetic properties are interesting. *ab initio* calculations are also included for the SMMs with high anisotropic energy barriers which give insight into understanding the mechanisms of slow magnetic relaxation in these systems.

# Chapter 2

## Mononuclear Lanthanide Complexes

In this chapter, ten mononuclear lanthanide complexes with $Tb^{III}$, $Dy^{III}$ or $Yb^{III}$ centers will be discussed in detail with regards to their structural features. The rigid pocket of the ligand we designed can form stable five- and six- membered rings when metal ions are coordinated. All mononuclear complexes have lanthanide metal centers that are seven, eight or nine coordinate with some coordination sites occupied by solvents or counter ions depending on the reaction conditions. Moreover, secondary ligands can replace these terminal solvents or ions. Furthermore, two lanthanide ions can be well isolated in one molecule when the designed ligand has two isolated pockets (complex **2-10**). The magnetic properties of mononuclear lanthanide complexes are well-known in the literature and therefore magnetic measurements were not performed. Only the magnetic measurements of complex **2-10** are presented. Herein, we mainly focus on how to modify the different geometries of lanthanide centers. Complex **2-10** exhibits a tail of a peak in the out-of-phase ac magnetic susceptibility indicating potential SMM properties which were verified when a static dc field was applied.

## 2.1 Molecular structure of [Tb(Hhmi)$(NO_3)_2(MeOH)_2$] (2-1)

[Tb(Hhmi)$(NO_3)_2(MeOH)_2$], (**2-1**) was obtained through the reaction of $H_2$hmi (1 equiv.) and pyridine (4 equiv.) with $Tb(NO_3)_3{\cdot}6H_2O$ (1 equiv.) in MeOH. Single crystal X-ray diffraction reveals that [Tb(Hhmi)$(NO_3)_2(MeOH)_2$] crystallizes in the triclinic *P-1* space group. The structure of [Tb(Hhmi)$(NO_3)_2(MeOH)_2$] is shown in Figure 2.1 with selected bond lengths in Table 2.1. The Tb center of the mononuclear complex is nine-coordinate where the coordination sites are occupied by one ligand, two nitrate molecules and two methanol molecules. The Tb center is in a distorted pentagonal, interpenetrating tetrahedral arrangement where O12, O13, O21 and O22 form a distorted tetrahedron which is interpenetrated by the pentagonal plane of N1, O2, O3 from the ligand and O30, O31 from MeOH. The O2 atom of the ligand is deprotonated whereas the C9-O3 distance (1.25 Å) indicates a double bond. The ligand coordinates to the Tb center *via* two O atoms (O2 and O3) and one N atom (N1). The two closest $Tb^{III}$ ions are separated by an intermolecular distance of 7.31 Å.

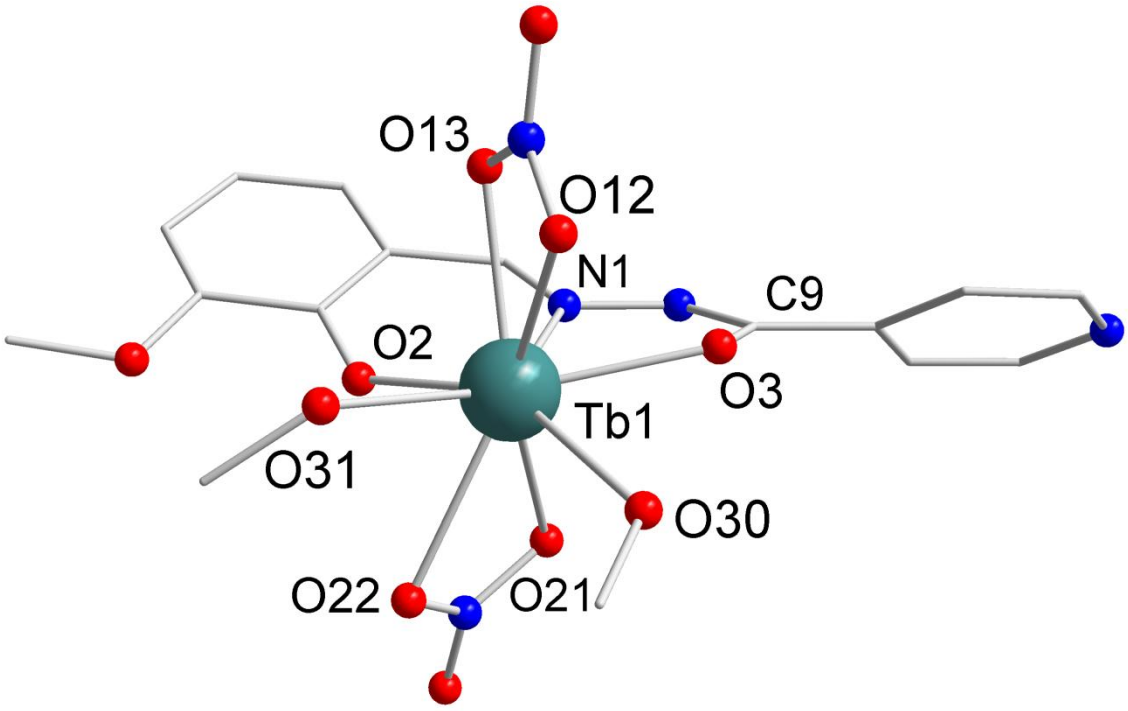


**Figure 2.1** Partially labeled molecular structure of mononuclear complex **2-1**.

**Table 2.1** Selected bond distances (Å ) for complex **2-1**.

| | | | |
|---|---|---|---|
| Tb1-O2 | 2.174(6) | Tb1-O12 | 2.526(5) |
| Tb1-O3 | 2.400(6) | Tb1-O13 | 2.460(4) |
| Tb1-N1 | 2.525(6) | Tb1-O21 | 2.538(8) |
| Tb1-O30 | 2.235(18) | Tb1-O22 | 2.535(9) |
| Tb1-O31 | 2.349(18) | Tb1---Tb1 | 7.341(6) |

## 2.2 Molecular structure of $[Ln(H_2hmi)(DMF)_2Cl_2]Cl\cdot 2(CH_3CN)$ (Ln: Tb(2-2) and Yb(2-3))

The trivalent lanthanides mostly form ionic salts with the most common complexes being 8- or 9-coordinate. Here we present two new 7-coordinate complexes. $[Ln(H_2hmi)(DMF)_2Cl_2]Cl\cdot 2(CH_3CN)$ (Ln: Tb (**2-2**) and Yb (**2-3**)) was obtained through the reaction of $H_2hmi$ (1 equiv.) and pyridine (4 equiv.) with $TbCl_3\cdot 6H_2O$ or $YbCl_3\cdot 6H_2O$ (1 equiv.) in MeOH. In contrast with the reaction conditions used for complex **2-1**, the counter ion selected was $Cl^-$ instead of $NO_3^-$ which have potential to decrease the coordination numbers. The structure of **2-2** is shown in Figure 2.2 and selected bond lengths of **2-2** and **2-3** are in Table 2.2. The Tb center of the mononuclear complex is seven-coordinate with the coordination sites occupied by one ligand, two chloride molecules and two DMF molecules. The Tb center is in a pentagonal bipyramidal arrangement where Cl1 and Cl2 are in axial positions and N1, O2, O3 from the ligand and O4, O5 from the DMF are in equatorial positions. Compared with the core geometry of complex **2-1**, the same rigid pocket of the ligands is coordinated to the metal centers and the pentagonal planes of both complexes are

formed by the ligand and the terminal solvent molecules. The geometry of the lanthanide centers was successfully modified by utilizing different counter ions. Since the O2 atom of the ligand is deprotonated, the C9-O3 bond is a double bond with 1.22 Å for both complexes and the pyridine is protonated to form pyridinium (H3), making the ligand neutral in the molecule. This simply suggested the ligands can easily undergo various tautomeric forms as was mentioned in the introduction. The ligand coordinates to the Tb center via O2, O3 and N1. The two closest $Tb^{III}$ and $Yb^{III}$ ions are separated by intermolecular distances of 9.62 and 9.59 Å, respectively.

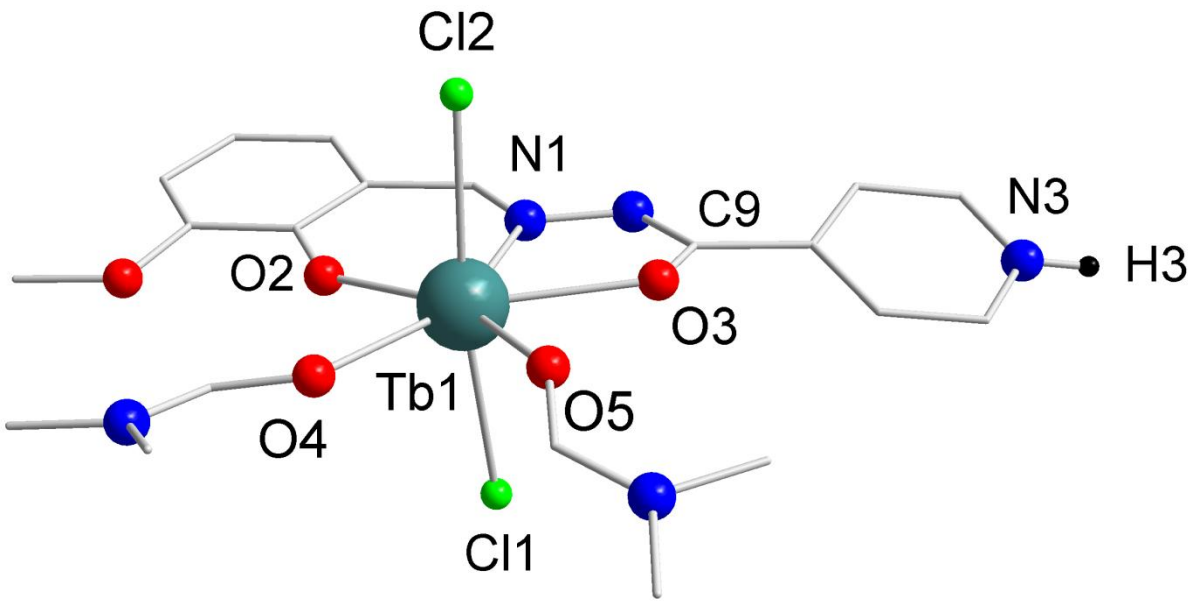


**Figure 2.2** Partially labeled molecular structure of mononuclear complex **2-2**.

**Table 2.2** Selected bond distances (Å ) for complexes **2-2** and **2-3**.

| | | | |
|---|---|---|---|
| Tb1-O2 | 2.207(6) | Tb1-O4 | 2.355(5) |
| Tb1-O5 | 2.328(6) | Tb1-O3 | 2.418(5) |
| Tb1-N1 | 2.536(7) | Tb1-Cl1 | 2.640(2) |
| Tb1-Cl2 | 2.658(2) | Tb1---Tb1a | 9.617(2) |
| Yb1-O2 | 2.349(18) | Yb1-O4 | 2.278(6) |
| Yb1-O5 | 2.288(6) | Yb1-O3 | 2.372(6) |
| Yb1-N1 | 2.465(8) | Yb1-Cl1 | 2.602(3) |
| Yb1-Cl2 | 2.593(3) | Yb1---Yb1 | 9.594(1) |

## 2.3 Molecular structure of $[Dy(Hhmb)(DMF)_2Cl_2]$ (2-4)

In order to study the effect of different tautomeric forms of the ligand, we exchange the pyridine group for the phenol group. The pyridine group of the ligand in complexes **2-2** and **2-3** is protonated to pyridinium. Here the metal is dysprosium instead of terbium or ytterbium. $[Dy(Hhmb)(DMF)_2Cl_2]$ (**2-4**) was obtained through the reaction of $H_2$hmb (1 equiv.) and $DyCl_3{\cdot}6H_2O$ (1 equiv.) in MeCN and DMF. The structure of complex **2-4** is shown in Figure 2.3 with selected bond lengths in Table 2.3.

**Table 2.3** Selected bond distances (Å ) for complex **2-4**

| | | | |
|---|---|---|---|
| Dy1-O2 | 2.199(6) | Dy1-Cl2 | 2.619(3) |
| Dy1-O5 | 2.331(7) | Dy1-O3 | 2.382(6) |
| Dy1-O4 | 2.332(7) | Dy1-N1 | 2.485(8) |
| Dy1-Cl1 | 2.689(3) | Dy1---Dy1 | 7.170(3) |

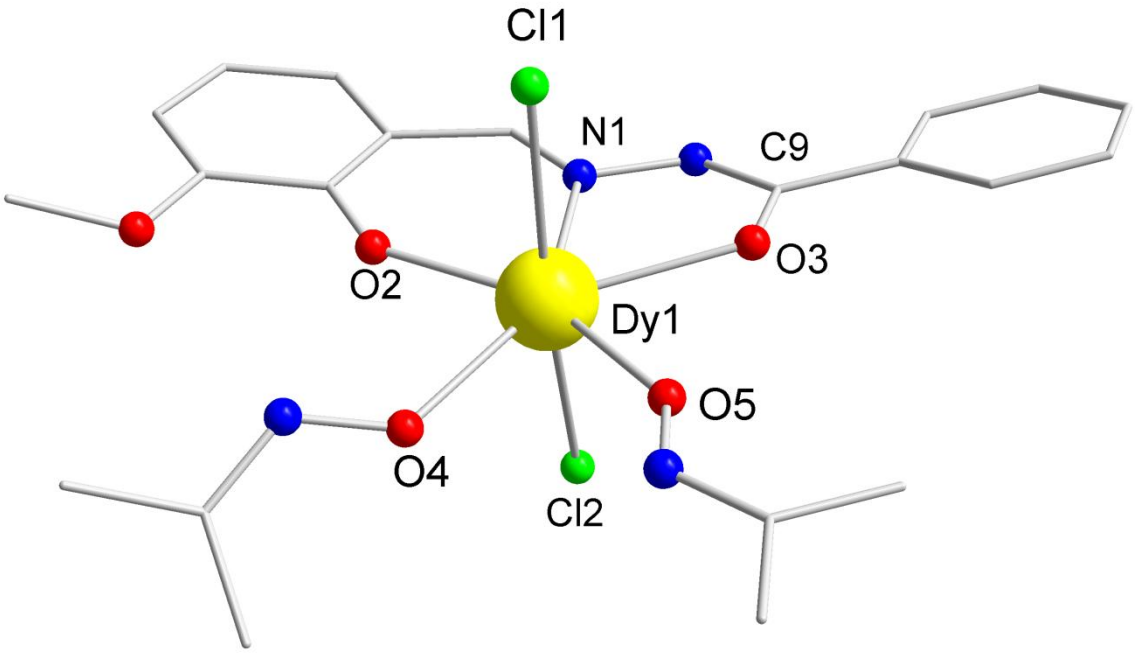


**Figure 2.3** Partially labeled molecular structure of mononuclear complex **2-4**.

The Dy center of the mononuclear complex is seven-coordinate where the coordination sites are occupied by one ligand *via* O2, O3 and N1, two chloride molecules and two DMF molecules. The Dy center is in a pentagonal bipyramidal arrangement where Cl1 and Cl2 are occupy the axial positions and N1, O2, O3 from the ligand and O4, O5 from the DMF occupy the equatorial positions. The coordination environments of complexes **2-3** and **2-4** are similar to complex **2-2**. Charge balance considerations for the

molecule indicate that the ligand must have one negative charge resulting from one deprotonated O2 atom and one double bond between C9 and O3 (1.24 Å) which has a similar bond distance to those in complexes **2-3** and **2-4**. Comparing the two different ligands of $H_2$hmb and $H_2$hmi, the phenyl group which replaces the pyridyl group will not be protonated and there is no counter ion in the lattice thus confirming that the charge of the ligand and Dy ion are -1 and +3, respectively. The two closest $Dy^{III}$ ions are separated by an intermolecular distance of 7.17 Å. The role of the counter ions is to exclusively balance the charge. The coordination environment of the rigid pocket was not changed as a result of ligand modification. We can modify different ligands with the same rigid pocket in order to obtain various mononuclear complexes.

## 2.4 Molecular structure of [Dy(Hhma)$(DMF)_2Cl_2$] (2-5)

We selected $H_2$hma as the ligand for the synthesis of a dysprosium complex where $-CH_3$ groups replaced the phenol or pyridine groups. [Dy(Hhma)$(DMF)_2Cl_2$] (**2-5**) was obtained through the reaction of $H_2$hma (1 equiv.) and $DyCl_3{\cdot}6H_2O$ (1 equiv.) in THF and DMF. The structure of complex **2-5** is shown in Figure 2.4 with selected bond lengths in Table 2.4. The Dy center of the mononuclear complex is seven-coordinate where the

coordination sites are occupied by one ligand, two chloride molecules and two DMF molecules. The Dy center is in a pentagonal bipyramidal arrangement with the Cl1 and Cl2 are in axial positions and N1, O2, O3 from the ligand and O4, O5 from the DMF are in equatorial positions. The coordination environment of the Dy center is similar to that in complexes **2-2** and **2-4** since the same rigid pockets are utilized in this series of ligands. This ligand exhibits the same tautomeric form in complex **2-4** which has one negative charge resulting from one deprotonated O2 atom and one double bond between C9 and O3. Two chloride atoms are present in each molecule and the oxidation state of Dy center ion is 3+. The two closest $Dy^{III}$ ions are separated by an intermolecular distance of 7.00 Å. For now, we can conclude that the rigid pocket of our ligand can coordinate with lanthanides and form stable mononuclear complexes. The modified functional groups on the ligands did not change the geometry of the metal center in the mononuclear complexes and only the packing arrangements were affected by these substitutions.

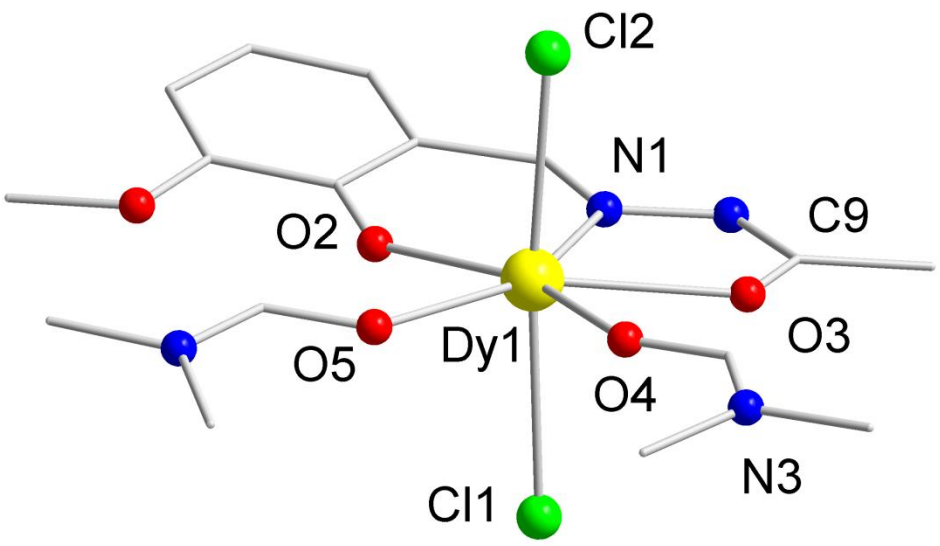


**Figure 2.4** Partially labeled molecular structure of mononuclear complex **2-5**.

**Table 2.4** Selected bond distances (Å ) for complex **2-5**.

| | | | |
|---|---|---|---|
| Dy1-O2 | 2.182(4) | Dy1-O4 | 2.325(5) |
| Dy1-O5 | 2.337(5) | Dy1-O3 | 2.395(5) |
| Dy1-N1 | 2.544(6) | Dy1-Cl1 | 2.690(2) |
| Dy1-Cl2 | 2.608(2) | Dy1---Dy1 | 6.995(8) |

## 2.5 Molecular structure of $[Ln(Hhmb)(bpy)_2(NO_3)_2]$•MeOH (Ln: Tb(2-6) Dy(2-7) and Ho(2-8))

Different counter ions have been employed to adjust the coordination environment of the metal center. Secondary ligands are introduced in this chapter in order to modify the geometry of the mononuclear complex. $[Ln(Hhmb)(bpy)(NO_3)_2]\cdot MeCN$ (Ln: Tb (**2-6**), Dy (**2-7**) and Ho (**2-8**)) was obtained through the reaction of $H_2hmb$ (1 equiv.), 2,2'-bipyridine (bpy) (3 equiv.) and pyridine (4 equiv.) with $Tb(NO_3)_3{\cdot}6H_2O$ / $Dy(NO_3)_3{\cdot}6H_2O$ / $Ho(NO_3)_3{\cdot}6H_2O$ (1 equiv.) in MeCN and MeOH. The structure of complex **2-7** is shown in Figure 2.5 with selected bond lengths in Table 2.5.

**Table 2.5** Selected bond distances (Å ) for complexes **2-6**, **2-7** and **2-8**.

| | | | |
|---|---|---|---|
| Tb1-O2 | 2.199(5) | Tb1-O4 | 2.445(5) |
| Tb1-O3 | 2.387(4) | Tb1-O6 | 2.493(6) |
| Tb1-N1 | 2.516 (5) | Tb1-O7 | 2.444(6) |
| Tb1-N3 | 2.535(5) | Tb1-O9 | 2.529(5) |
| Tb1-N4 | 2.480(6) | Tb1---Tb1a | 8.372(8) |
| Dy1-O2 | 2.187(4) | Dy1-O4 | 2.481(5) |
| Dy1-O3 | 2.374(4) | Dy1-O6 | 2.466(5) |

| | | | |
|---|---|---|---|
| Dy1-N1 | 2.491(5) | Dy1-O7 | 2.425(5) |
| Dy1-N3 | 2.526(5) | Dy1-O9 | 2.506(5) |
| Dy1-N4 | 2.522(6) | Dy1---Dy1a | 8.862(11) |
| Ho1-O2 | 2.170(6) | Ho1-O4 | 2.453(8) |
| Ho1-O3 | 2.361(6) | Ho1-O6 | 2.414(6) |
| Ho1-N1 | 2.484(7) | Ho1-O7 | 2.453(8) |
| Ho1-N3 | 2.514(6) | Ho1-O9 | 2.478(6) |
| Ho1-N4 | 2.521(7) | Ho1---Ho1 | 8.991(12) |

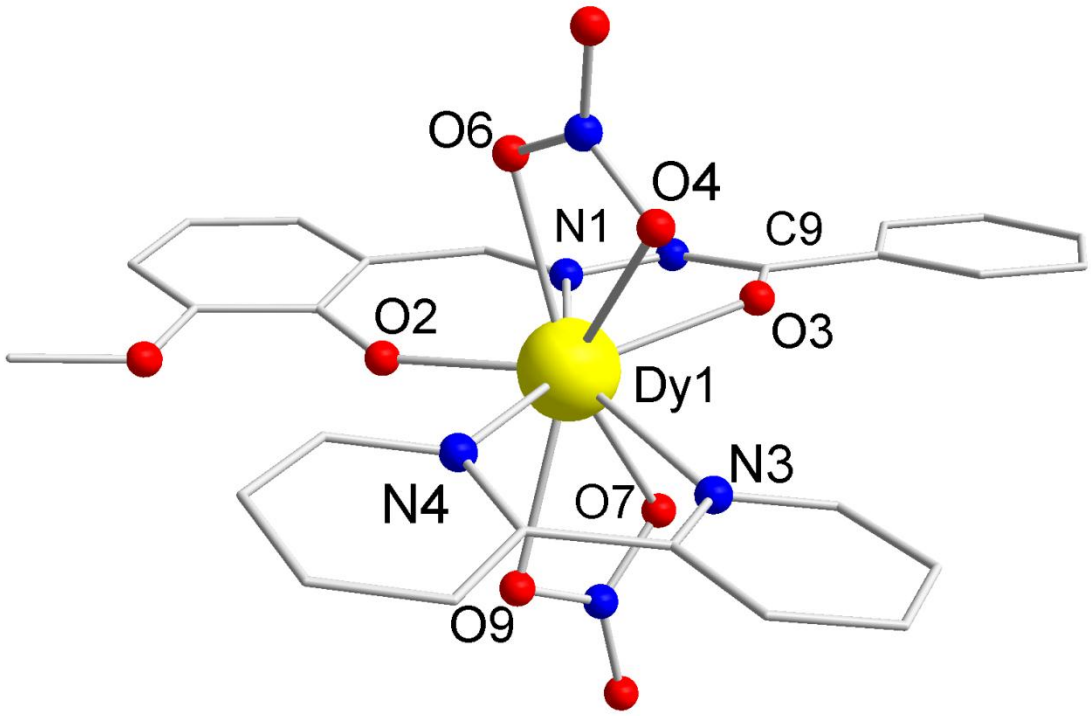


**Figure 2.5** Partially labeled molecular structure of mononuclear complex **2-7**.

The Dy center of the mononuclear complex is nine-coordinate where the coordination sites are occupied by one ligand, two nitrates and one bpy molecule. The Dy center is in a distorted pentagonal interpenetrating tetrahedral arrangement where O4, O6, O7 and O9 form a distorted tetrahedron which is interpenetrated by the pentagonal plane of N1, O2, O3 from the ligand and N3, N4 from the pyridine. It is interesting to note that the Dy center has similar geometry to complex **2-1** where the bpy molecule replaces two MeOH groups and the angle of N3-Dy-N4 (64.3°) is smaller than O31-Dy-O30 (77.4°) of complex **2-1**. The oxidation state of Dy center ion is 3+ and the positive charge is balanced by two chloride atoms and one hmb ligand which has one negative charge resulting from one deprotonated O2 atom. The bpy ligand replacement of the terminal solvent molecule rather than counter ions may be due to the neutral bpy ligand and the bite angle of two N atoms on bpy ligand. The two closest ions of $Tb^{III}$, $Dy^{III}$ and $Ho^{III}$ complexes are separated by an intermolecular distance of 8.7, 8.3 and 9.0 Å , respectively. The synthetic strategy of employing the multifunctional ligands enabled us to create various coordinating on geometries. Different secondary ligands can be designed with different functional groups such as pyridine and carboxylate in the future in order to extend the mononuclear centers to network structures.

## 2.6 Molecular structure of $[Dy(hmf)(DETA)_2]Cl \cdot 2CH_2Cl_2 \cdot MeOH$ (2-9)

In section 2-5, secondary ligands were used to fine tune the coordination environment of the metal center where two terminal solvent molecules are replaced by 2,2'-bipyridine. Here we selected diethylenetriamine (DETA) to be the secondary ligand where the three N atoms of the ligand have the potential to coordinate with the metal center and afford new coordination geometry. $[Dy(hmf)(DETA)_2]Cl \cdot 2CH_2Cl_2 \cdot MeOH$ (**2-9**) was obtained through the reaction of DETA (4 equiv.), $H_2hmf$ (1 equiv.) and $DyCl_3 \cdot 6H_2O$ (1 equiv.) in $CH_2Cl_2$ and MeOH. Although $Cl^-$ did not coordinate to the $Dy^{III}$ center, $DyCl_3 \cdot 6H_2O$ is necessary for the synthesis to provide required charge as $Cl^-$ is present in the structure for charge balance. The structure of complex **2-9** is shown in Figure 2.6 (top) with selected bond lengths in Table 2.6. The Dy center of the mononuclear complex is nine-coordinate where the coordination sites are occupied by one ligand and two DETA. Since both O2 and O3 atoms of the ligand are deprotonated, the overall charge of the ligand is -2 which is different from the complexes in previous sections of this chapter. The two closest $Dy^{III}$ ions are separated by an intermolecular distance of 8.71 Å. In contrast to the previous other nine coordinate complexes, the

geometry of the Dy center of complex **2-9** is a distorted monocapped square anti-prism. The coordination polyhedron of the $Dy^{III}$ ion is shown in Figure 2.6, right. The set of N4, N5, N7, and N8 and the set of O2, O3, N3, and N6 around the $Dy^{III}$ center form two near parallel squares. The N1 atom, as the capping atom, lies above the top plane of O2, O3, N3, and N6. In both seven- and nine- coordinate complexes, the counter ions are in the axial positions and the ligand or solvent molecules occupy equatorial positions. DETA ligand has enabled a change in the geometry around the lanthanide center, which could potentially to modify the direction of the anisotropic axis of the lanthanide ion. Recently, mononuclear dysprosium complex with monocapped square anti-prism arrangements have shown very interesting SMM properties.[31] Further magnetic investigations are necessary.

**Table 2.6** Selected bond distances (Å ) for complex **2-9**.

| | | | |
|---|---|---|---|
| Dy1-O2 | 2.246(8) | Dy1-O3 | 2.363(8) |
| Dy1-N1 | 2.337(5) | Dy1-N3 | 2.395(5) |
| Dy1-N4 | 2.544(6) | Dy1-N5 | 2.690(2) |

[31] Cucinotta, G.; Perfetti, M.; Luzon, J.; Etienne, M.; Car, P.-E.; Caneschi, A,; Calvez, G.; Bernot, K.; Sessoli, R. *Angew. Chem. Int. Ed.*, **2012**, *51*, 1606

| | | | |
|---|---|---|---|
| Dy1-N6 | 2.608(2) | Dy1-N7 | 2.613(10) |
| Dy1-N8 | 2.601(9) | Dy1---Dy1 | 8.714(2) |

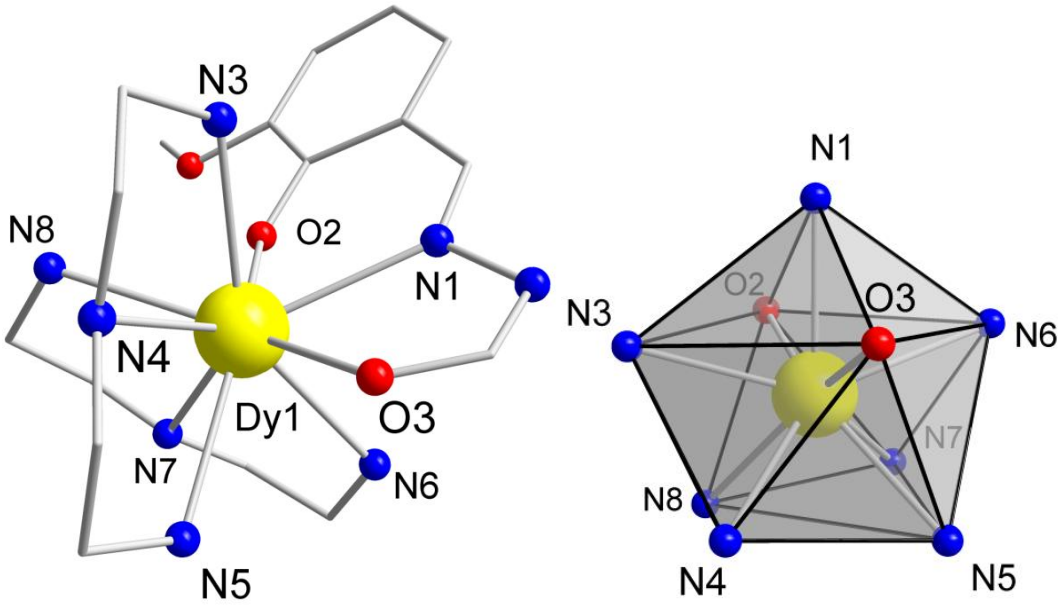


**Figure 2.6** Left: Partially labeled molecular structure of mononuclear complex **2-9**. Right: Distorted monocapped square anti-prism arrangement of the $Dy^{III}$ ion.

## 2.7 Molecular structure and magnetism of $[Dy_2(H_2hmt)(NO_3)_4(DMF)_4]$ (2-10)

In section 2-1, nine mononuclear complexes have been synthesized where all ligands were coordinated to metal centers using rigid pockets. Here we design a new ligand with two separated rigid pockets in order to dimerize complex **2-1** to create a centrosymmetric dinuclear complex. $[Dy_2(H_2hmt)(NO_3)_4(DMF)_4]$ (**2-10**) was isolated using the similar synthetic strategy as complex **2-1** with different solvent system and obtained through the reaction of $H_4hmt$ (1 equiv.), $Dy(NO_3)_3{\cdot}6H_2O$ (2 equiv.) and pyridine (8 equiv.) in THF and DMF. The X-ray molecular structure of complex **2-10** is shown in Figure 2.7 with the selected bond distances (Å) in Table 2.7. The two symmetrical $Dy^{III}$ ions are well-isolated in the molecule by an intramolecular distance of 12.00 Å (Figure 2.8). This complex could be described as two mononuclear units bridged by the phenyl ring of the ligand. As complex **2-10** is centrosymmetric and the two $Dy^{III}$ ions are well-separated, the magnetic properties will be similar to single ion complexes. Therefore, the magnetism of complex **2-10** will be discussed in this chapter.

Here we successfully dimerized the Dy unit of complex **2-1** where the differences of coordination environments are two DMF molecules instead of two methanol molecules.

The Dy center is also in a distorted pentagonal interpenetrating tetrahedral arrangement. The two closest $Dy^{III}$ ions are separated by an intermolecular distance of 8.15 Å. Our study of complex **2-10** can be extended to modify the orientation of mononuclear lanthanide cores. This in turn influences the supramolecular chemistry which involves macromolecules that originate from the self-assembly of smaller subunits or components.

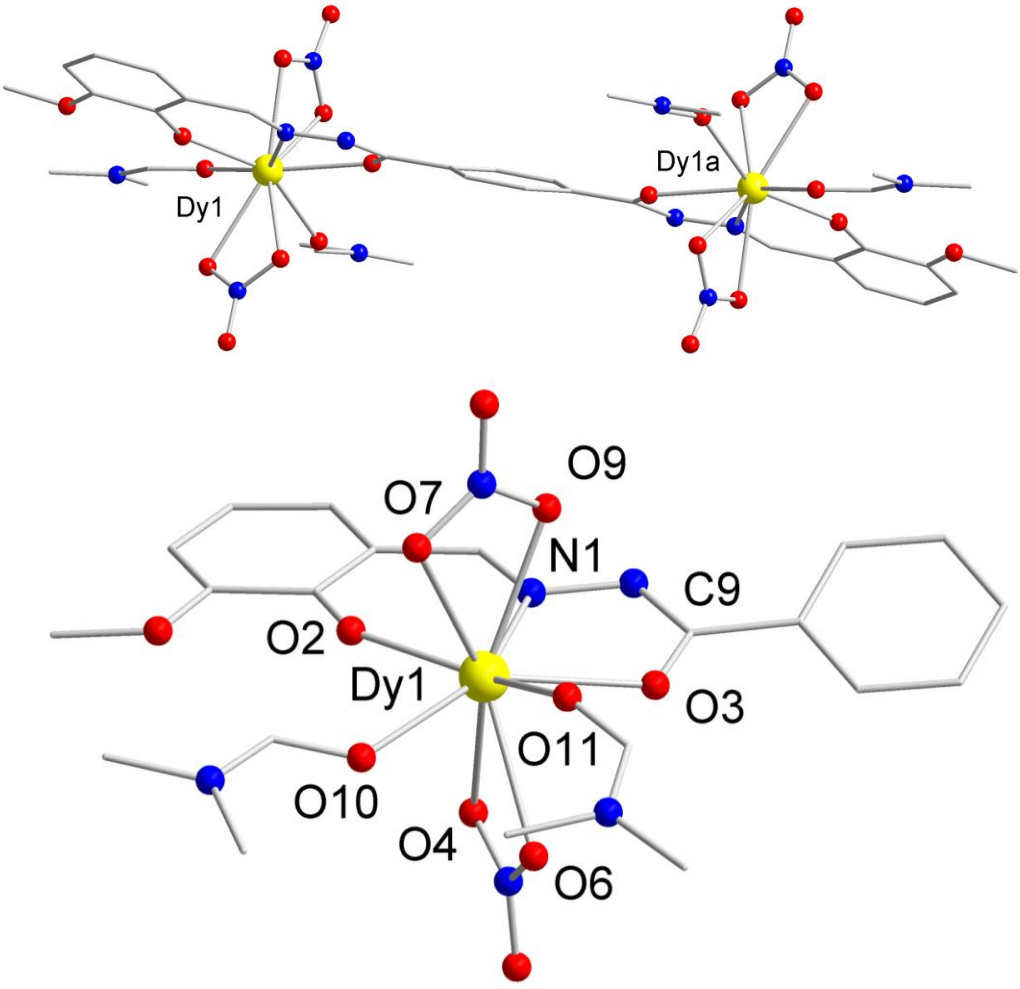


**Figure 2.7** Top: Partially labeled molecular structure of mononuclear complex **2-10**. Bottom: Detailed structure of the mononuclear Dy unit of complex **2-10**.

**Table 2.7** Selected bond distances (Å ) for complex **2-10**.

| | | | |
|---|---|---|---|
| Dy1-O2 | 2.203(3) | Dy1-O4 | 2.468(4) |
| Dy1-O3 | 2.409(3) | Dy1-O6 | 2.515(4) |
| Dy1-N1 | 2.555(4) | Dy1-O7 | 2.498(4) |
| Dy1-O9 | 2.461(4) | Dy1-O10 | 2.361(4) |
| Dy1-O11 | 2.346(4) | Dy1---Dy1a | 12.00(2) |

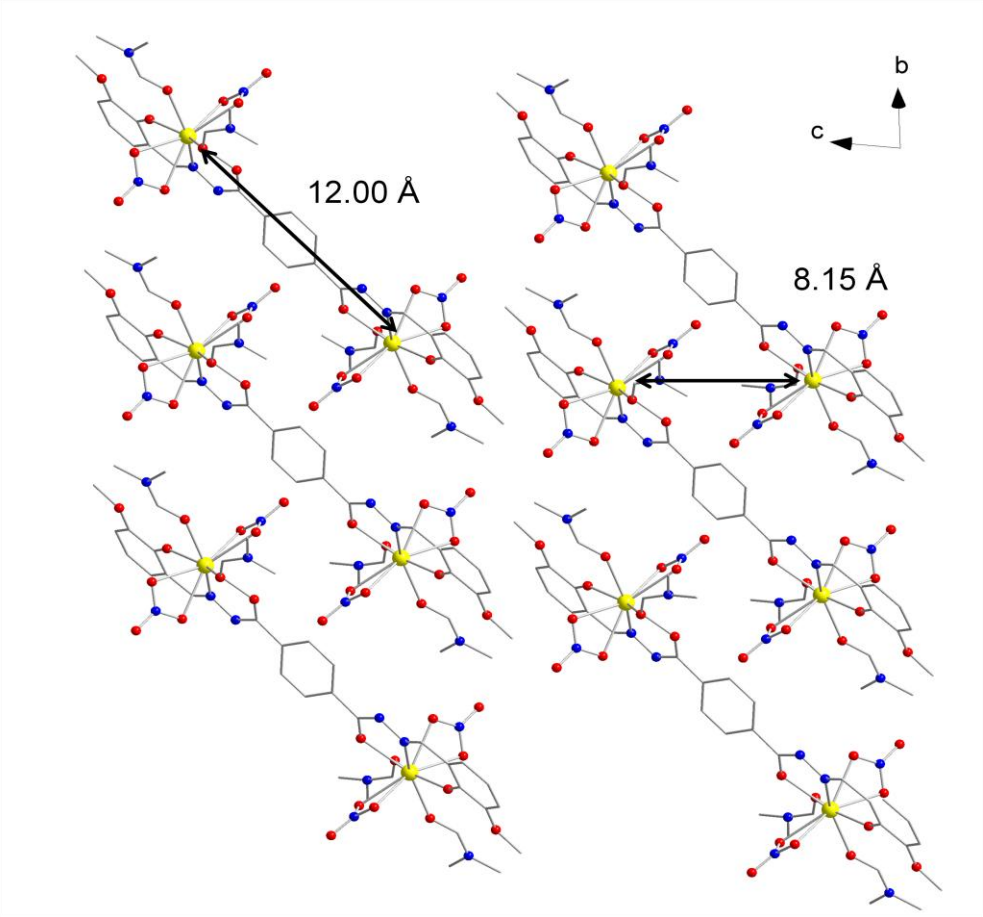


**Figure 2.8** Packing arrangement of complex **2-10** along the crystallographic *a* axis with hydrogen atoms omitted for clarity. Yellow (Dy), Red (O), Blue (N), Grey (C).

The packing arrangement along the *a* axis of complex **2-10** is presented in Figure 2.8. Close inspection reveals that all dinuclear complexes are well isolated along the *a* axis. The closest intermolecular Dy···Dy distance of 8.15 Å is shorter than the intramolecular Dy1···Dy1a distance of 12.00 Å.

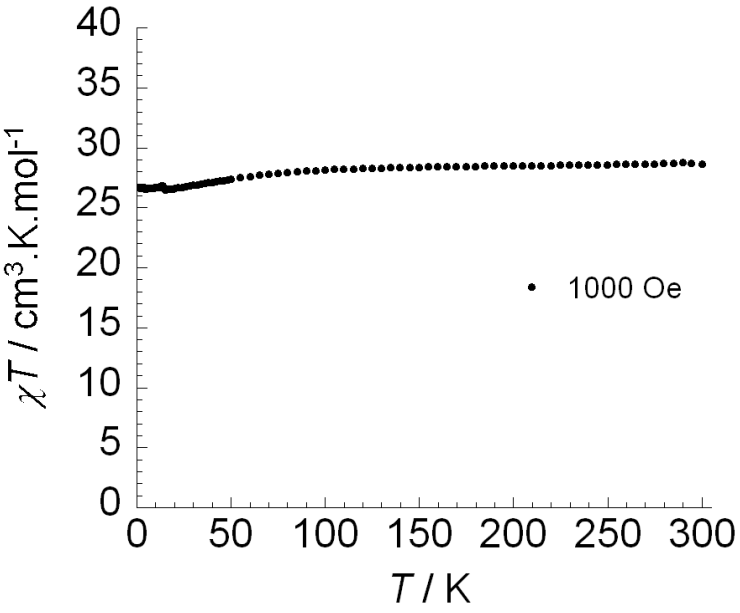


**Figure 2.9.** Temperature dependence of the $\chi T$ product at 1000 Oe for complex **2-10** (with $\chi = M/H$ normalized per mol).

The magnetic susceptibility for complex **2-10** was measured in an applied dc field of 1000 Oe in the range of 1.8 K to 300 K on crushed polycrystalline samples. The $\chi T$ *vs. T* plot is shown in Figure 2.9. At room temperature, the $\chi T$ value for **2-10** is 28.62 $cm^3.K.mol^{-1}$ which is in good agreement with the expected value of 28.34 $cm^3.K.mol^{-1}$ for

two uncoupled $Dy^{III}$ ions ($S$ = 5/2, $L$ = 5, $^6H_{15/2}$, $g$ = 4/3). The $\chi T$ product remains relatively constant above 60 K and decreases at lower temperatures reaching 26.63 $cm^3.K.mol^{-1}$ for **2-10** at 1.8 K. This behavior is generally indicative of weak antiferromagnetic coupling of the metal centers. However, due to the large separations of the $Dy^{III}$ ions, this decrease is most likely due to the thermal depopulation of the Stark sub-levels and/or the presence of large anisotropy in the system.

Field dependence of the magnetization, *M*, measurements show non-saturation at low temperatures (1.8 K) and high magnetic fields (up to 7 T) (Figure 2.10). Additionally, the reduced magnetization plot, *M vs. H/T*, (Figure 2.11) at different temperatures shows magnetization curves that are not superimposable on a single master curve. These two figures are indicative of the presence of significant magnetoanisotropy and/or low-lying excited states in the molecule.

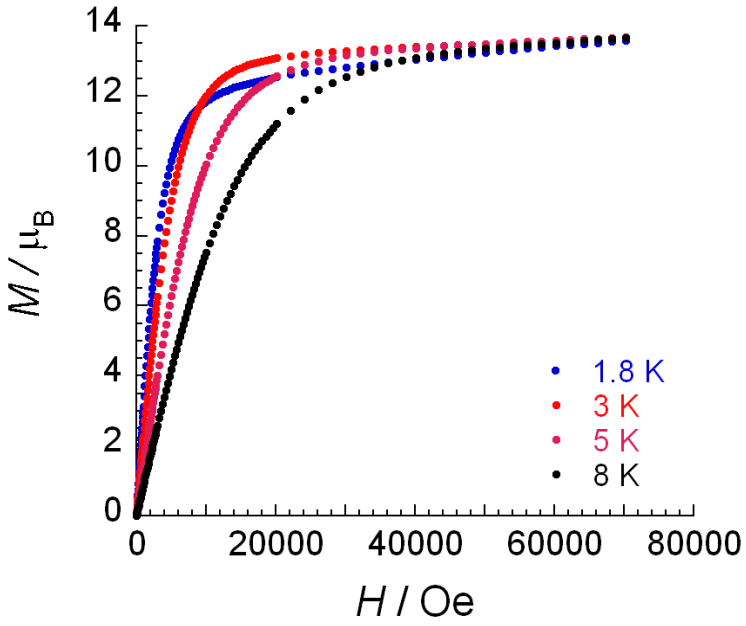


**Figure 2.10.** Field dependence of the magnetization, *M*, at 1.8, 3, 5 and 8 K for complex **2-10**.

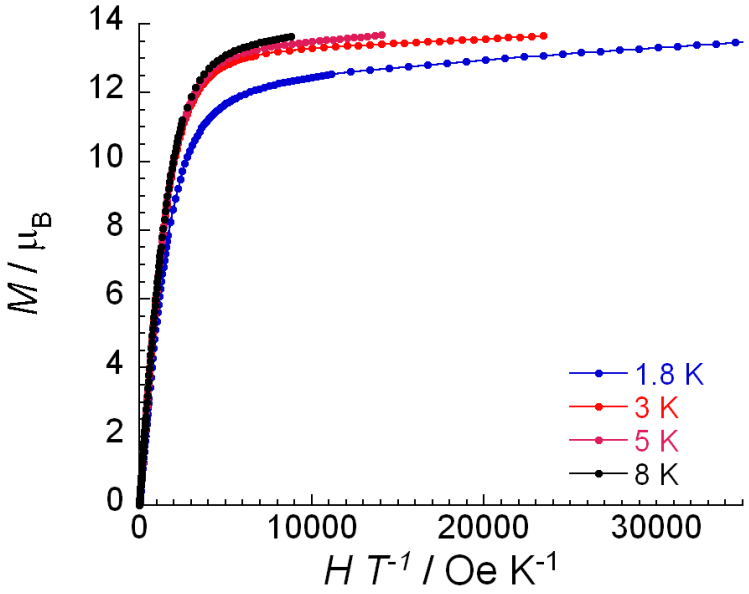


**Figure 2.11.** The reduced magnetization plot for **2-10** measured at 1.8, 3, 5 and 8 K.

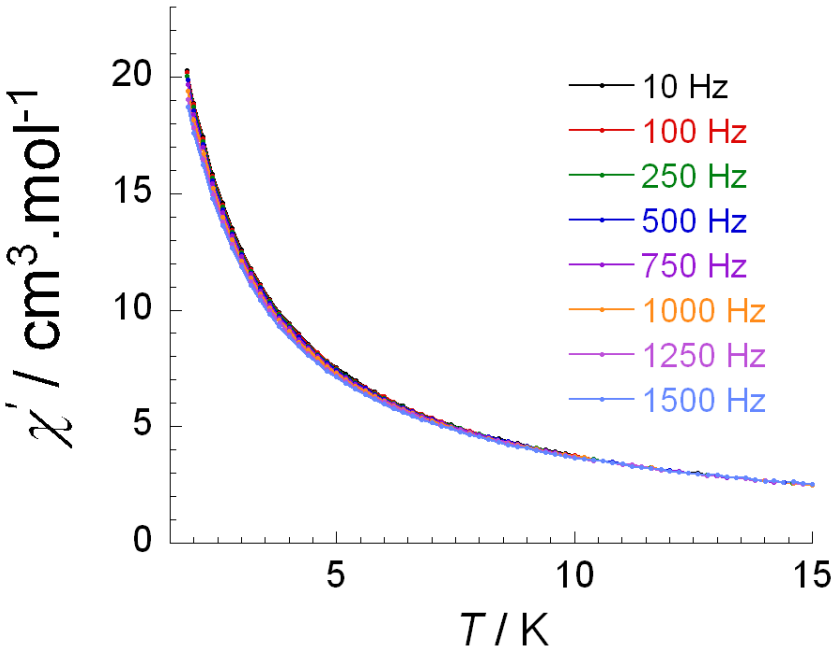


**Figure 2.12** In-phase magnetic susceptibility, $\chi'$, *vs*. temperature, *T*, in the frequency range of 10 - 1500 Hz under zero dc field for **2-10**.

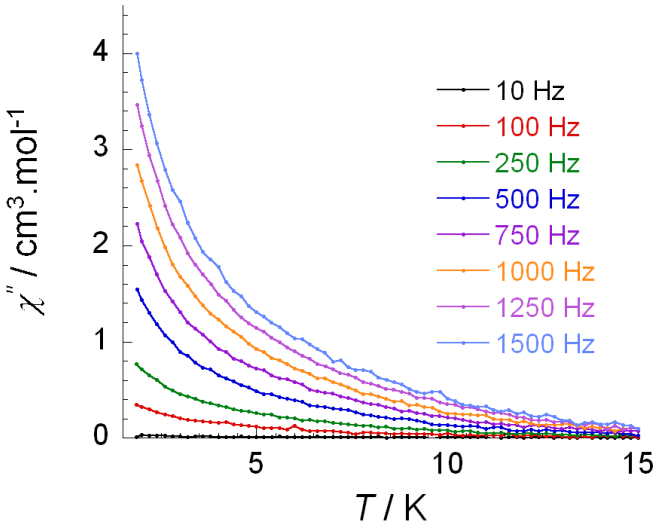


**Figure 2.13** Out-of-phase magnetic susceptibility, $\chi''$, *vs*. temperature, *T*, in the frequency range of 10 - 1500 Hz under zero dc field for **2-10**.

In order to investigate the possibility of SMM behavior, ac magnetic susceptibility measurements were carried out under zero dc field (Figure 2.12 and 2.13). A frequency dependent tail of a peak is observed in the out-of-phase, $\chi''$, measurement below 15 K for **2-10** indicating potential SMM behavior at very low temperature; however, it is difficult to quantify the energy barrier without a full peak with maxima. Such behavior generally indicates that the slow relaxation of the magnetization is highly influenced by the quantum tunneling of the magnetization (QTM) through the spin reversal barrier which is very common in mononuclear SMMs[32]

Moreover, in order to shortcut the QTM which is commonly observed in lanthanide systems, ac measurements need to be carried out under an optimum dc field. Therefore, we initially carried out ac measurements while varying the applied fields to determine the

[32]a) Lin, P.-H.; Smythe, N C.; Gorelsky, S.; Maguire, S.; Henson, N. J.; Korobkov, I.; Scott, B. L.; Gordon, J. C.; Baker, R. T.; Murugesu, M. *J. Am. Chem. Soc.*, **2011**, *133*, 15806.; b) Harman, W. H.; Harris, T. D.; Freedman, D.E.; Fong, H.; Chang, A.; Rinehart, J. D.; Ozarowski, A.; Sougrati, M. T.; Grandjean, F., Long, G. J.; Long, J. R.; Chang, C. J. , *J. Am. Chem. Soc.,* **2010**, *132*, 18115.

optimum field for which the QTM will be reduced or suppressed (Figure 2.14). This was found to be 1800 Oe for **2-10** where the quantum relaxation is minimized.

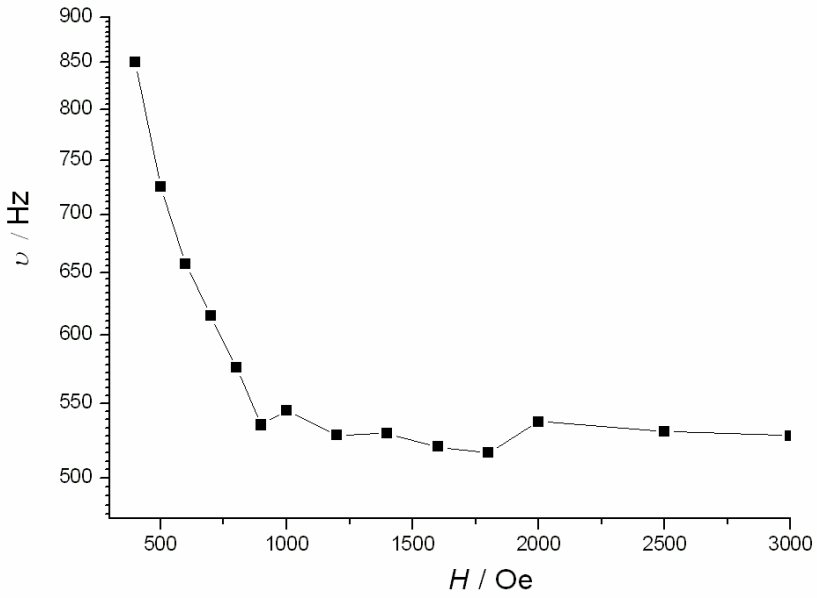


**Figure 2.14** Field dependence of the characteristic frequency (maximum of $\chi''$) as a function of the applied dc field for **2-10** at 8K. Line is guide for the eyes and the optimum field is observed at 1800 Oe.

Ac measurements under the applied optimum field of 1800 Oe (Figure 2.15 and 2.16) reveal a frequency dependent signal with a clear out-of-phase ($\chi''$) peak. Such behavior is indicative of superparamagnet-like slow magnetization relaxation of a SMM. The thermally activated relaxation follows an Arrhenius-like behavior ($\tau = \tau_0 \exp(U_{eff}/kT)$) where the anisotropic energy barrier is calculated to be $U_{eff}$ = 36 K ($\tau_0 = 3 \times 10^{-6}$ s) (Figure 2.17).

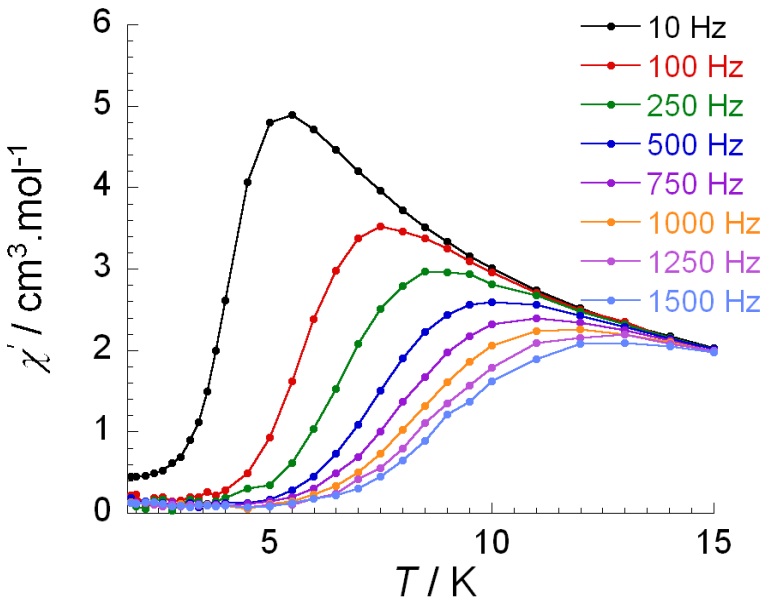


**Figure 2.15** In-phase magnetic susceptibility, $\chi'$, *vs.* *T* in the frequency range of 10 - 1500 Hz under an applied field of 1800 Oe for **2-10**.

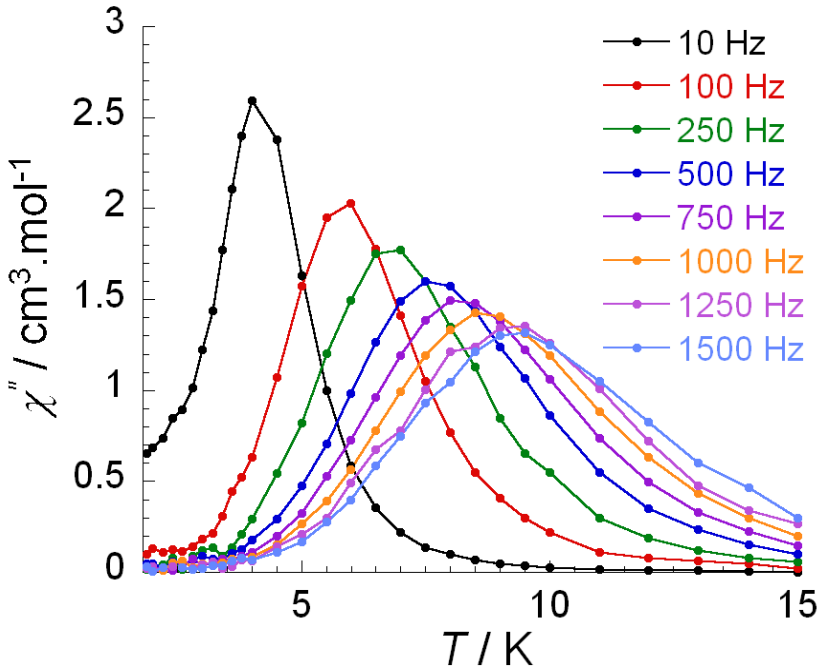


**Figure 2.16** Out-of-phase susceptibility $\chi''$ *vs.* *T* in the frequency range of 10 - 1500 Hz under an applied field of 1800 Oe for **2-10**.

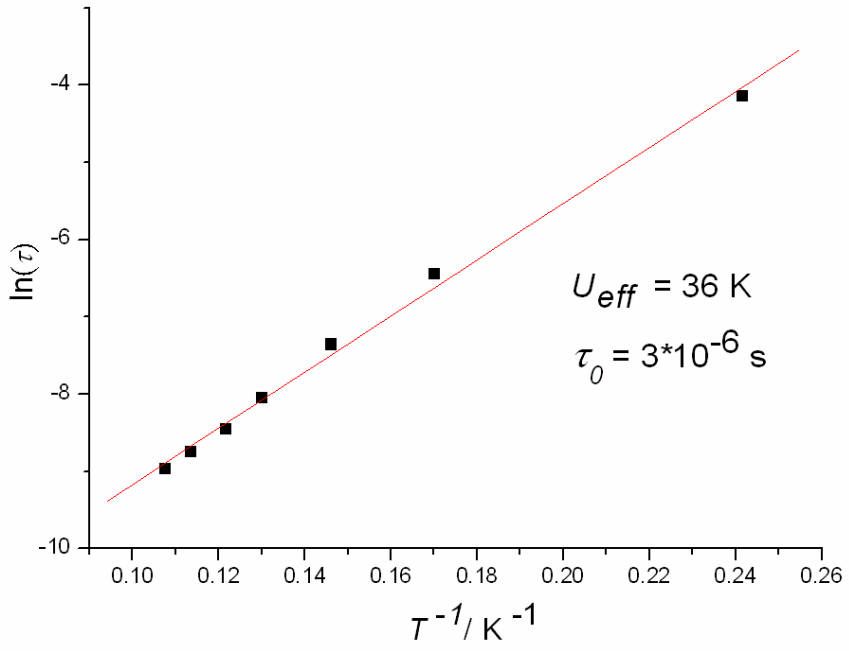


**Figure 2.17** Relaxation time of the magnetization ln($\tau$) *vs.* $T^{-1}$ (Arrhenius Plot using temperature-dependent ac data). The solid line corresponds to the fit.

# Conclusion

In this chapter, ten mononuclear $Ln^{III}$ complexes were reported to exhibit seven and nine coordination numbers. The rigid pockets created by the ligands we designed can form stable six-membered rings when coordinated to metal ions. Various tautomeric forms of the ligands are present in the mononuclear complexes. The secondary ligands can be solvent molecules such as MeOH or DMF or organic ligands such as bipyridine and diethylenetriamine. Three different geometries of lanthanide centers have been

synthesized. Of these geometries, a pentagonal bipyramidal arrangement and distorted pentagonal interpenetrating tetrahedron arrangement are rare for lanthanide coordination compounds. Although the 4*f* electrons are shielded by the 5*s* and 5*p* electrons and are core-like in their behaviors, any given set of ligand field parameters can be still be related to the energies of the *f*-orbitals of the rare earth ion in the complex.[33] These various geometries will be useful for further studies.

The magnetic properties of rare earth ions are unique due to the unquenched orbital momentum. The magnetic properties of complexes **2-1** to **2-9** were not investigated because mononuclear lanthanide SMMs had previously been reported, such as double decker[34] and polyoxometalate complexes[35] and were not interesting to the field at that time. The recent interest in SMMs has shifted toward Single Ion Magnets (SIMs), especially high anisotropic systems. The magnetic properties are correlated to the

---

[33] Gerloch, M.; Mackey, D. J. *J. Chem. Soc. A*, **1970**, 3030

[34] Ishikawa, N.; Sugita, M.; Ishikawa, T.; Koshihara, S.-ya.; Kaizu, Y. *J. Am. Chem. Soc.*, **2003**, *125*, 8694

[35] AlDamen, M. A.; Clemente-Juan, J. M.; Coronado, E.; Marti-Gastaldo, C.; Gaita-Arino, A. *J. Am. Chem. Soc.*, **2008**, *130*, 8874

geometry and orientation of the anisotropic axis on lanthanide centers as well as the energy gap between the spin ground state and first excited state. It may be advantageous to study the magnetic properties of these compounds in the future to identify possible magneto-structural correlations. The anisotropic axes of mononuclear complexes should also be determined by *ab initio* calculations in the future.

Complex **2-10** is shown to have two lanthanide ions in the same molecule which are well-separated by coordinating to two isolated pockets. Complex **2-10** opens a new synthetic strategy for organizing SMM units within their crystal structures using ligand modification, while maintaining the same coordination pocket. Complex **2-10** was shown to exhibit SMM behavior with $U_{eff}$ = 36 K under a static field of 1600 Oe. In order to improve SMM properties and obtain higher energy barriers, we will investigate multi-nuclear lanthanide complexes in the later chapters.

# Chapter 3

## Dinuclear Lanthanide Complexes

In this chapter, eleven dinuclear lanthanide complexes will be discussed in detail with regards to their structural features. The magnetic properties have been measured and three complexes reveal SMM properties. In chapter 2, the rigid pockets of the ligand were shown to form stable five and six membered rings when metal ions are coordinated. Reaction conditions will be modified for the multi-nuclear metal complexes synthesized. The dinuclear complexes are synthesized successfully with ligands containing the same pockets by tuning reaction conditions carefully.

All dinuclear complexes have two lanthanide metal centers that are eight or nine coordinate with some coordination sites occupied by solvents or counter ions depending on the reaction conditions. Moreover, secondary ligands can replace these terminal solvents or counter ions. The super-exchange pathway which is the bridge between metal centers may also be modified by secondary ligands. The dinuclear units can also be linked by the pyridine moiety of the coordinating ligands ($H_2$hmi), forming a 2-D network system. SQUID measurements are used to investigate the dc and ac magnetic properties of all the dinuclear complexes. SMM properties have been observed for

complexes **3-6**, **3-9** and **3-11**. The detailed magnetic studies are investigated and further discussed in this chapter.

## 3.1 Molecular structure and magnetism of $[Dy_2(Hhmb)_2(NO_3)_4]\cdot MeCN$

$[Dy_2(Hhmb)_2(NO_3)_4]\cdot MeCN$ (**3-1**) was obtained through the reaction of $H_2hmb$ (1 equiv.), pyridine (4 equiv.) and $Dy(NO_3)_3\cdot 6H_2O$ (1 equiv.) in MeCN and MeOH. The molecular structure of complex **3-1** is shown in Figure 3.1. In the dinuclear unit, the tetradentate ligand coordinates to the Ln centers *via* three O atoms (O1, O2 and O3) and one N atom. The metal centers are bridged by the phenoxide groups of two ligands with a Dy1-O2-Dy1a angle of 104.7(2)° The Dy1-Dy1a distances is 3.69 Å. The bridges between the metal centers which can be named in super-exchange pathways are an important role for magnetic properties. The remaining four coordination sites of each lanthanide ion are filled by two nitrate anion molecules. Charge balance considerations indicated that O2 was deprotonated and C9-O3 remains a double bond (1.230(11) Å) such that the ligand is monoanionic and exhibits the same tautomeric form as complexes **2-4** and **2-7**. Selected bond distances (Å) and angles (°) are presented in Table 3.1. The Dy center is in a distorted pentagonal, interpenetrating tetrahedral arrangement which has

been shown in complex **2-1**. In comparing the two coordination environments, the distorted tetrahedrons of both complexes are formed by two nitrate molecules whereas the pentagonal plane in complex **3-1** is formed by N and O atoms from two ligands instead of the one ligand and two solvent molecules in complex **2-1**.

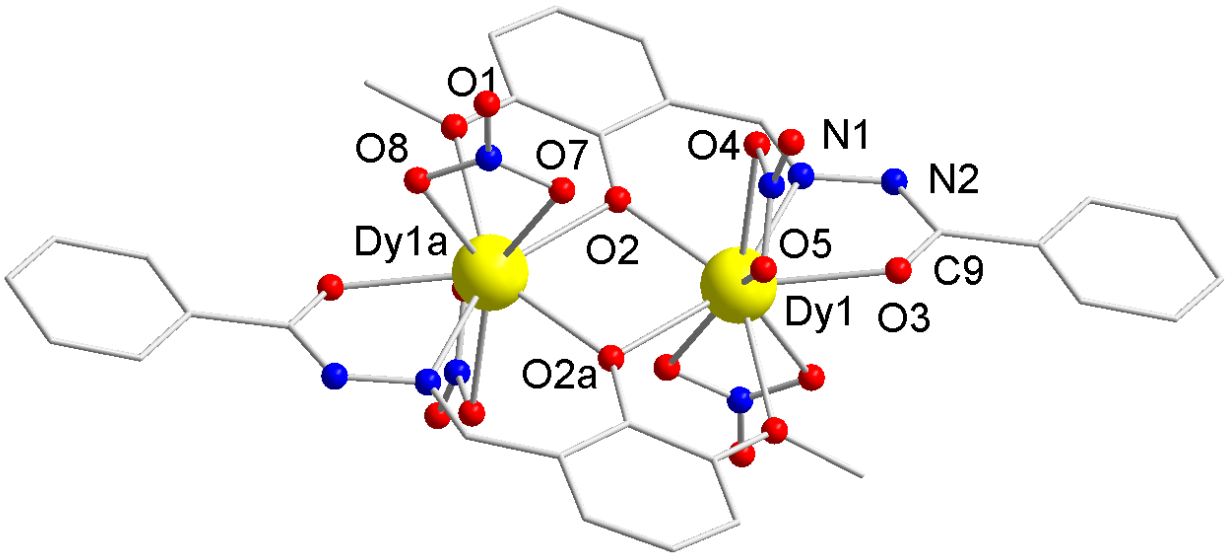


**Figure 3.1.** Partially labeled molecular structure of mononuclear complex **3-1**.

**Table 3.1.** Selected bond distances (Å) for complex **3-1**.

| | | | |
|---|---|---|---|
| Dy1-O1a | 2.417(7) | Dy1-O2 | 2.362(6) |
| Dy1-O3 | 2.372(7) | Dy1-O4 | 2.461(8) |
| Dy1-O5 | 2.445(7) | Dy1-O7 | 2.491(8) |
| Dy1-O8 | 2.460(8) | Dy1-N1 | 2.459(8) |
| Dy1-O2a | 2.293(7) | Dy1---Dy1a | 3.6881(11) |
| Dy1-O2-Dy1a | 104.7(2) | | |

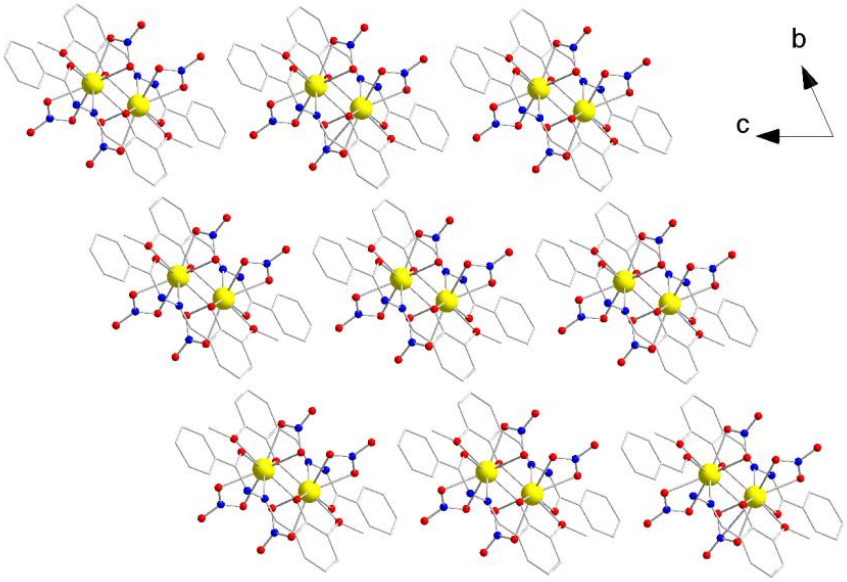


**Figure 3.2.** Packing arrangement along the crystallographic *a* axis with hydrogen atoms omitted for clarity. Yellow (Dy), Red (O), Blue (N), Grey (C).

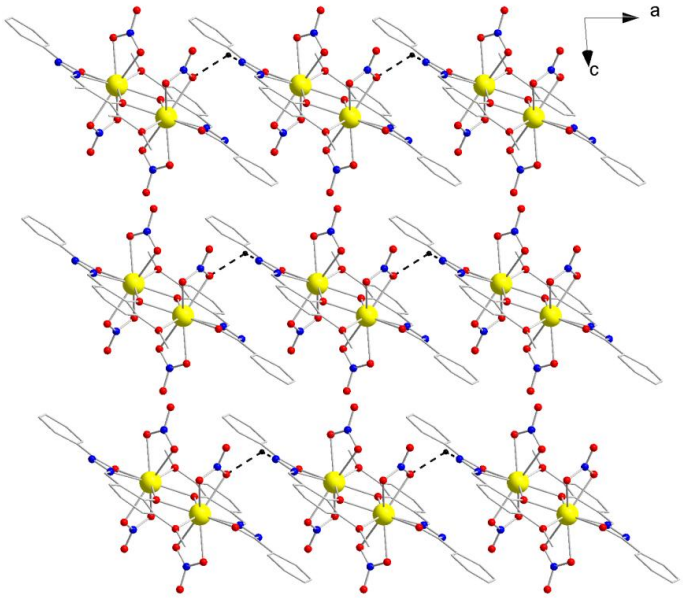


**Figure 3.3.** Packing arrangement along the crystallographic *b* axis with hydrogen atoms omitted for clarity. The black dotted lines represent hydrogen bonds between the molecules along the *b* axis. Yellow (Dy), Red (O), Blue (N), Grey (C).

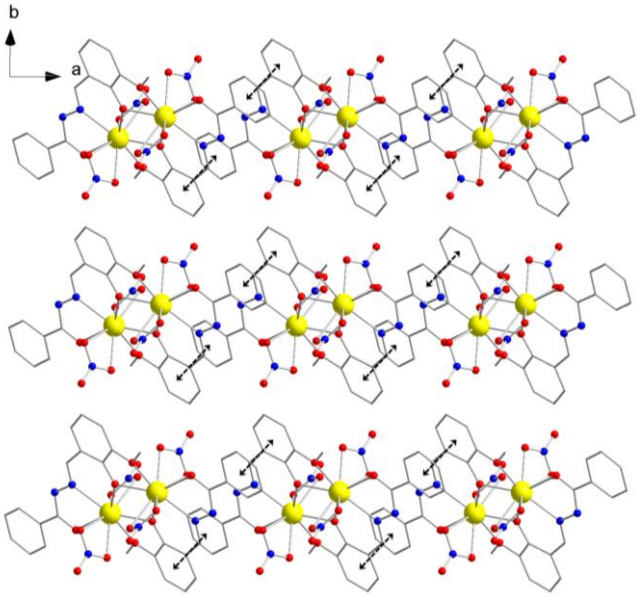


**Figure 3.4.** Packing arrangement along the crystallographic *c* axis with hydrogen atoms omitted for clarity. Yellow (Dy), Red (O), Blue (N), Grey (C). The phenyl rings participating in π-π stacking are shown in arrows.

The packing arrangements along the *a*, *b* and *c* axes of complex **3-1** are presented in Figure 3.2, 3.3 and 3.4, respectively. Close inspection of the packing arrangements reveals that all dinuclear complexes are well isolated along the *a* and *b* axes. One hydrogen bond is present between N2 and O4 [N2···O4 = 2.895 Å , N2···H-O4 = 124.65°] (Figure 3.3). Along the *c* axis, all the phenyl rings of one layer are participating in π-π stacking with a distance of 3.82 Å between two phenyl rings.

The magnetic susceptibility for complex **3-1** was measured in an applied dc field of 1000 Oe in the range of 1.8 K to 300 K on polycrystalline samples. The $\chi T$ *vs.* $T$ plot is

shown in Figure 3.5. At room temperature, the $\chi T$ value for **3-1** is 27.4 $cm^3.K.mol^{-1}$ which is slightly lower than the expected value of 28.3 $cm^3.K.mol^{-1}$ for two uncoupled $Dy^{III}$ ions ($S$ = 5/2, $L$ = 5, $^6H_{15/2}$, $g$ = 4/3). At lower temperature, the $\chi T$ product decreases significantly to a minimum value at 1.8 K of 10.2 $cm^3.K.mol^{-1}$.

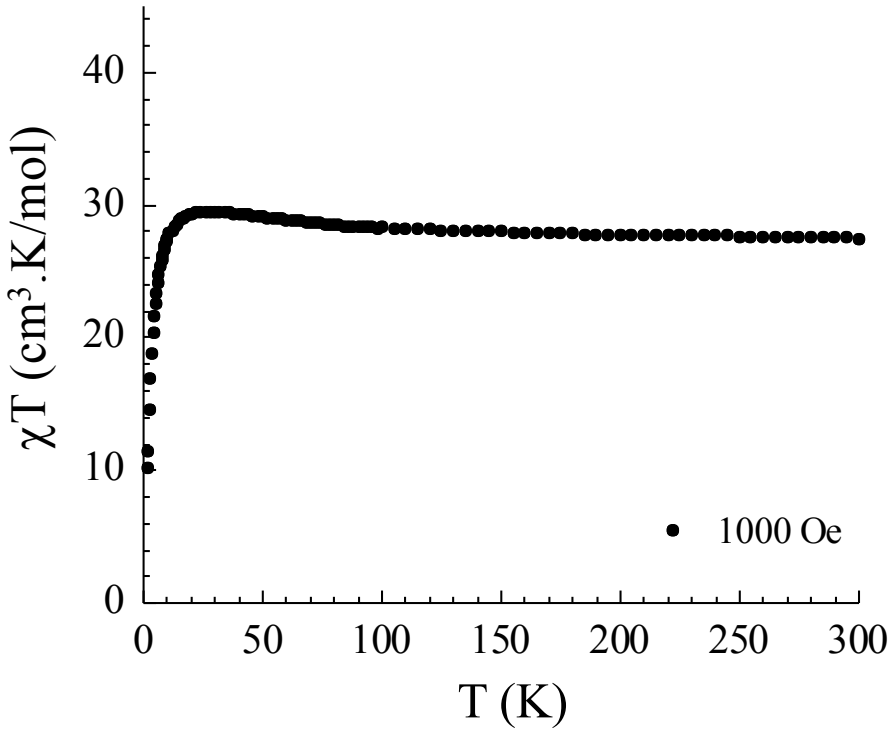


**Figure 3.5.** Temperature dependence of the $\chi T$ product at 1000 Oe for complex **3-1** (with $\chi = M/H$ normalized per mol).

This behavior is generally indicative of weak intra-molecular antiferromagnetic coupling of the metal centers. This behavior may also be due to the thermal depopulation of the Stark sub-levels and/or the presence of large anisotropy in the system. Field

dependence of the magnetization, *M*, measurements show non-saturation at low temperatures (1.8 K) and high magnetic fields (up to 7 T) (Figure 3.6). Additionally, the reduced magnetization plot, *M vs. H/T*, (Figure 3.7) at different temperatures shows magnetization curves that are not superimposable on a single master curve. These two figures are indicative of the presence of significant magnetoanisotropy and/or low-lying excited states in the molecule. In addition, there is no observable hysteresis in the *M vs. H* data above 1.8 K with sweep-rates used in a traditional SQUID magnetometer (100 – 200 Oe/min) nor an out-of phase signal of the ac susceptibility for complex **3-1** in zero dc field. The structure and magnetic properties of complex **3-1** are studied and it is not a SMM.

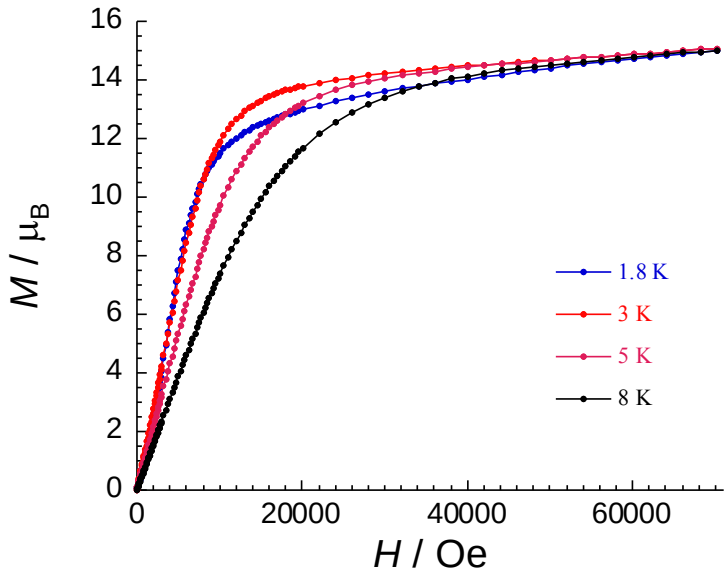


**Figure 3.6.** Field dependence of the magnetization, *M*, at 1.8, 3, 5 and 8 K for complex **3-1**.

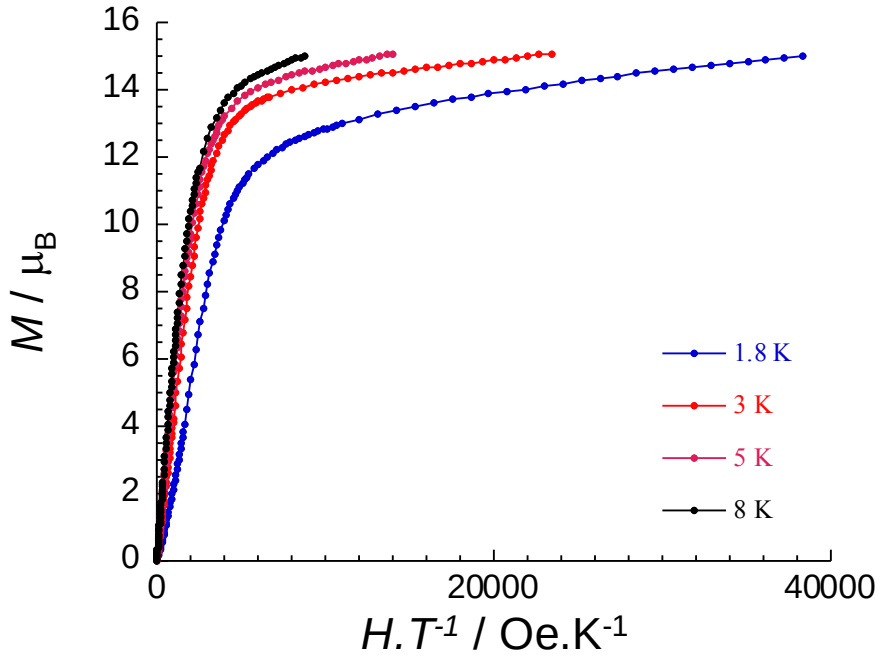


**Figure 3.7.** The reduced magnetization plot for **3-1** measured at 1.8, 3, 5 and 8 K.

## 3.2 Molecular structure and magnetism of $[Dy_2(Hhmb)_2(NO_3)_2(N_3)_2(MeOH)]\cdot 2MeOH$

Magnetic exchange pathways have become of interest recently in regards to SMMs. Both ferro- and antiferro- interactions between transition metal centers strongly depend on the different intermediary of bridging ligands.[36] The end-on azides are known to lead the

[36] Ribas, J.; Escuer, A.; Monfort, M.; Vicente, R.; Cortes, R.; Lezama, L.; Rojo, T. *Coord. Chem. Rev.*, **1999**, *193-195*, 1027.

ferromagnetic interaction between transition metal centers which has been well used in the construction of magnetic molecule materials.[37] Although this has not been clearly domenstrated in lanthanide systems, we investigated the effect of azide bridge.

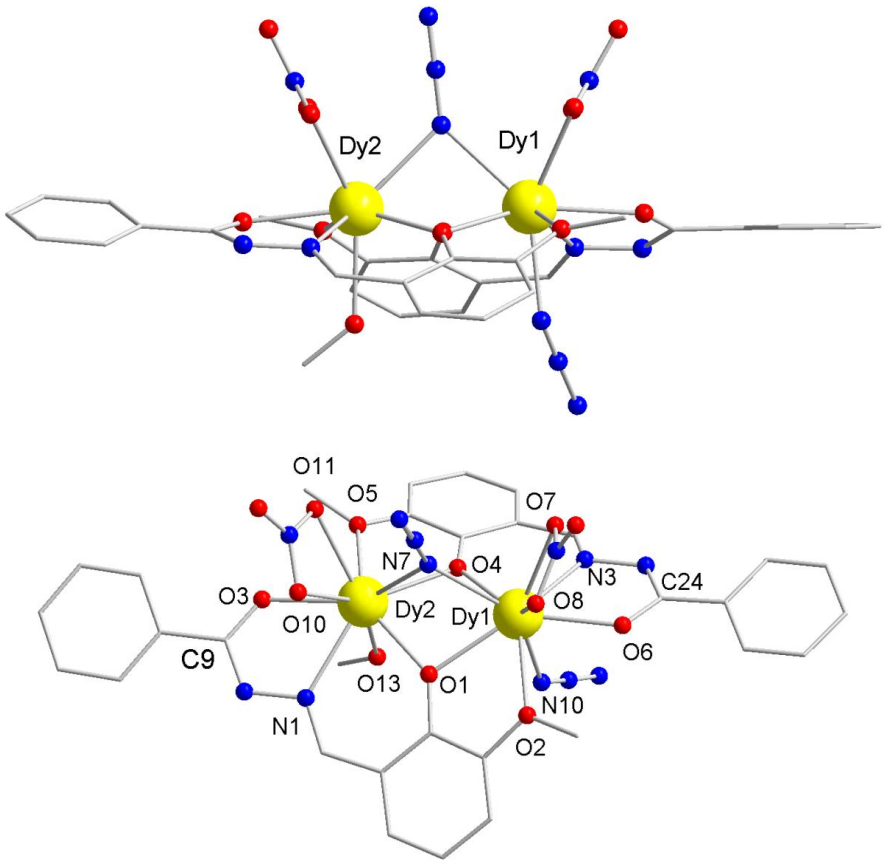


**Figure 3.8.** The side view (top) and the top view (bottom) of partially labeled molecular structure of mononuclear complex **3-2.**

---

[37] Zeng, Y.-F.; Hu, X.; Liu, F.-C.; Bu, X.-H. *Chem. Soc. Rev.*, **2009**, *38*, 469.

Sodium azide was selected in the reaction of complex **3-2**. $[Dy_2(Hhmb)_2(NO_3)_2(N_3)_2$**(**$MeOH)] \cdot 2MeOH$ (**3-2**) was obtained through the reaction of $H_2$hmb (1 equiv.), $NaN_3$ (3 equiv.), pyridine (4 equiv.) and $Dy(NO_3)_3 \cdot 6H_2O$ (1 equiv.) in MeOH. The molecular structure of **3-2** is shown in Figure 3.8.

Complex **3-2** is a dinuclear compound composed of two unsymmetrical nine-coordinate $Dy^{III}$ ions. Two unsymmetrical tetradentate ligands coordinate to the Ln centers in the dinuclear unit *via* three O atoms and one N atom (O1, O2, O3, N1 and O4, O5, O6, N3). The metal centers are bridged by the phenoxide groups of two ligands (Dy1-O-Dy2) and one nitrogen atom of the azide group (Dy1-N-Dy2). The Dy1-Dy2 distance is 3.58 Å and the Dy1-O1-Dy2, Dy1-O4-Dy2 and Dy1-N7-Dy2 angles are 98.9°, 99.4° and 92.5°, respectively. The remaining four coordination sites of Dy1 are filled by one nitrate anion and one terminal azide molecule which is different from Dy2. One nitrate anion and one methanol molecule fill the remaining four coordination sites of Dy2. The charge of the ligand is monoanionic which is the same tautomeric form as complex **3-1**. Selected bond distances (Å) and angles (°) are presented in Table 3.2. In contrast with complex **3-1**, the extra super-exchange pathway (end-on azido bridge) was successfully inserted between $Dy^{III}$ centers and one terminal nitrate on Dy1 and exchanged by a terminal azide group. Moreover, two $Dy^{III}$ and two phenoxides are

located in the same plane in complex **3-1** whereas it was bent in complex **3-2** (the angle between plane Dy1, O1, Dy2 and Dy1, O4, Dy2 is 39.0°).

**Table 3.2.** Selected bond distances (Å) for complex **3-2**.

| | | | |
|---|---|---|---|
| Dy1-O1 | 2.399(2) | Dy1-O2 | 2.478(2) |
| Dy1-O4 | 2.325(2) | Dy1-O6 | 2.374(3) |
| Dy1-O7 | 2.493(3) | Dy1-O8 | 2.477(3) |
| Dy1-N3 | 2.508(3) | Dy1-N7 | 2.493(3) |
| Dy1-N10 | 2.369(4) | Dy2-O1 | 2.311(2) |
| Dy2-O3 | 2.373(3) | Dy2-O4 | 2.366(2) |
| Dy2-O5 | 2.450(2) | Dy2-O10 | 2.489(3) |
| Dy2-O11 | 2.506(3) | Dy2-O13 | 2.384(3) |
| Dy2-N1 | 2.502(3) | Dy2-N7 | 2.462(3) |
| Dy1---Dy2 | 3.5779(2) | Dy1-O1-Dy2 | 98.86(8) |
| Dy1-O4-Dy2 | 99.38(8) | Dy1-N7-Dy2 | 92.47(12) |

The packing arrangements along the *a* and *b* axes of complex **3-2** are presented in Figures 3.9 and 3.10. The packing arrangements reveal that all dinuclear complexes are well isolated along the *a* and *b* axes. Close inspection reveals that the dinuclear units are alternating along the *a* axis in an abab fashion where the molecules in layer a and b are oriented in opposite directions.

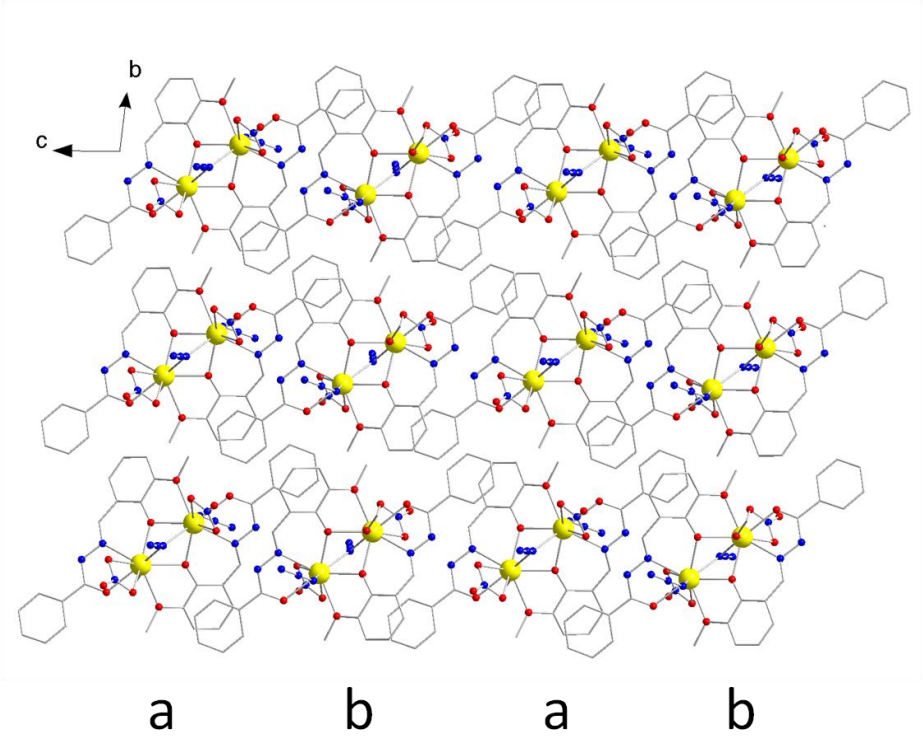


**Figure 3.9.** Packing arrangement along the crystallographic *a* axis with hydrogen atoms omitted for clarity. Yellow (Dy), Red (O), Blue (N), Grey (C). Layer a and b are shown two different layers of molecules.

Along the *c* axis, the hydrogen bond between the first and second layer is present between N2, O10 [N2···O10 = 2.871 Å, N2···H-O10 = 148.89°] and that between second and third layers is present between N4, O7 [N4···O7 = 3.076 Å, N4···H-O7 = 131.12°]. (Figure 3.10).

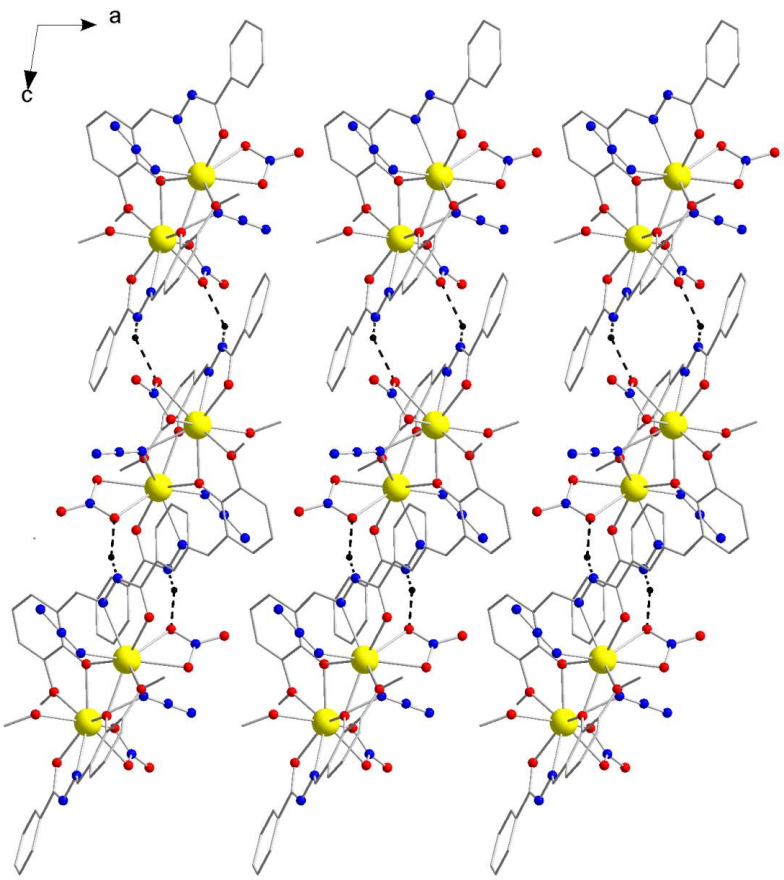


**Figure 3.10.** Packing arrangement along the crystallographic *b* axis with hydrogen atoms omitted for clarity. The black dotted lines represent hydrogen bonds between the molecules along the *b* axis. Yellow (Dy), Red (O), Blue (N), Grey (C).

The magnetic susceptibility for complex **3-2** was measured in an applied dc field of 1000 Oe in the range of 1.8 K to 300 K on polycrystalline samples. The $\chi T$ *vs.* $T$ plot is shown in Figure 3.11. The $\chi T$ product is 27.4 $cm^3.K.mol^{-1}$ which is in good agreement with the expected value (28.34 $cm^3.K/mol$) for two non-interacting $Dy^{III}$ metal ions ($S$ = 5/2, $L$ = 5, $^6H_{15/2}$ g = 4/3: $\chi T$ = 14.17 $cm^3.K.mol^{-1}$). At lower temperature, the $\chi T$ product

at 1000 Oe decreases significantly to a minimum value at 2.5 K of 24.2 $cm^3.K.mol^{-1}$. This behavior is generally indicative of weak intra-molecular antiferromagnetic coupling of the metal centers. The $\chi T$ product increases slightly below 2.5 K due to weak inter-molecular ferromagnetic coupling between the molecules. This behavior may also be due to the thermal depopulation of the Stark sub-levels and/or the presence of large anisotropy in the system.

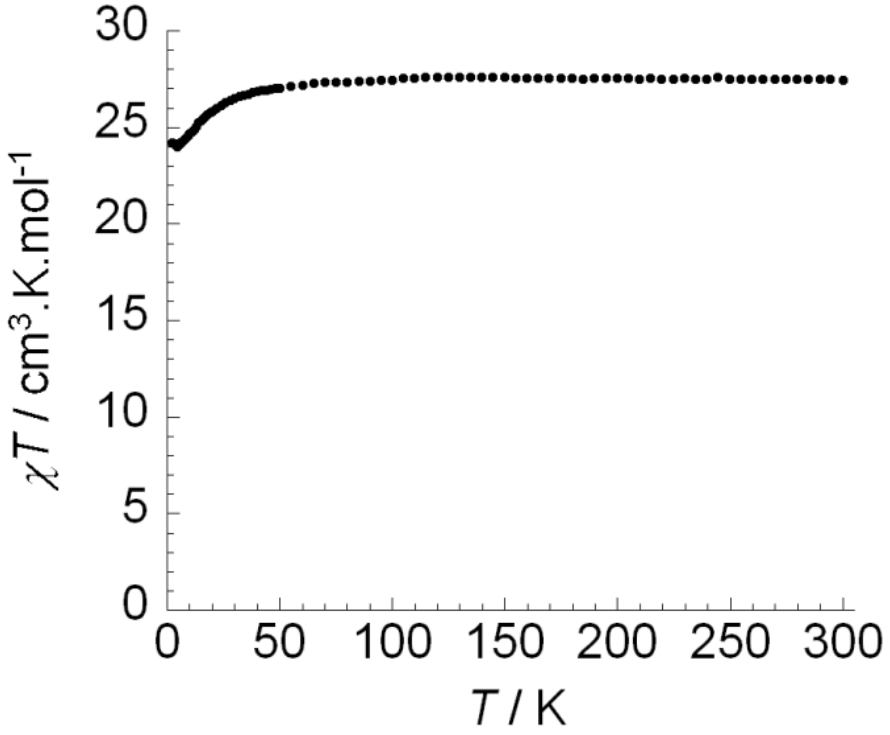


**Figure 3.11.** Temperature dependence of the $\chi T$ product at 1000 Oe for complex **3-2** (with $\chi = M/H$ normalized per mol).

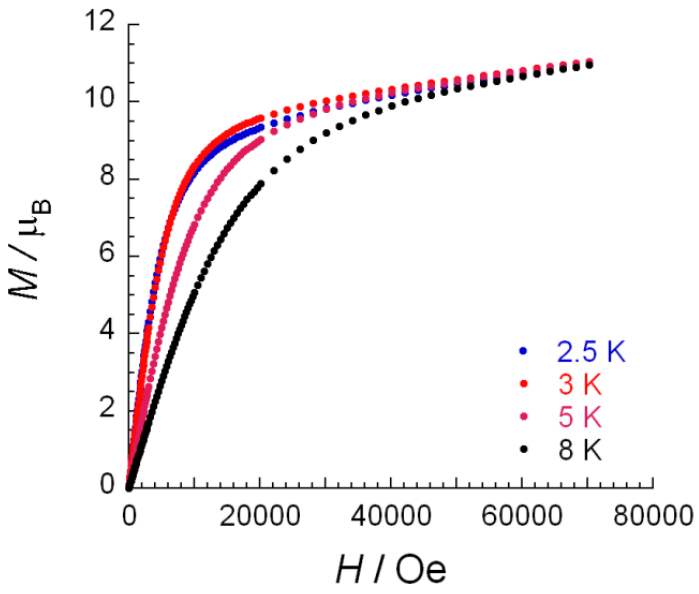


**Figure 3.12.** Field dependence of the magnetization, *M*, at 2.5, 3, 5 and 8 K for complex **3-2**.

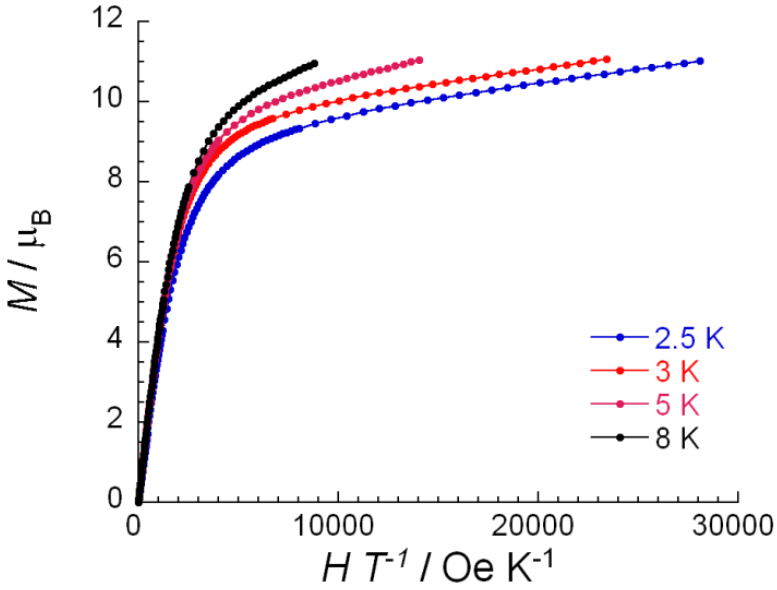


**Figure 3.13.** The reduced magnetization plot for **3-2** measured at 2.5, 3, 5 and 8 K.

Field dependence of the magnetization, *M*, does not saturate at low temperatures (2.5 K) and high magnetic fields (up to 7 T)(Figure 3.12) and the measurements of different temperatures in reduced magnetization plot, *M vs. H/T* (Figure 3.13) are not superimposed. These two figures are indicating the presence of significant magnetoanisotropy or low-lying excited states in the molecule. Moreover, there is no out-of phase signal of the ac susceptibility for complex **3-2** in zero dc field. It was thus not possible to compare the role of the extra azido super-exchange pathway by comparing the molecular structures and magnetic properties between complexes **3-1** and **3-2**. Different exchange pathways with similar $Dy^{III}$ core geometries will be necessary in the future in order to understand the role of bridging ligands. Calculation may also provide additional information on the super-exchage pathway of end-on azide bridge molecules in the future.

## 3.3 Molecular structure and magnetism of $[Dy_2(hma)_3(NO_3)_3]\cdot CH_3CN\cdot 2CH_3OH$

The observed slow relaxation in polynuclear lanthanide SMMs has been reported to be due to single ion relaxation mechanisms.[38] Therefore, understanding the relaxation mechanism in polynuclear lanthanide SMMs is key. Careful investigations of coordinatively unsymmetrical dinuclear SMMs have sparked increasing interest in the area of molecular magnetism.[39] Here we report a dinuclear complex with two unsymmetrical $Dy^{III}$ centers. Synthetically speaking $[Dy_2(hma)_3(NO_3)_3]\cdot CH_3CN\cdot 2CH_3OH$ (**3-3**) was obtained through the reaction of $H_2hma$ (1 equiv.), triethylamine (4 equiv.) and $Dy(NO_3)_3\cdot 6H_2O$ (1 equiv.) in MeOH and MeCN.

[38] Blagg, R. J.; Muryn, C. A.; McInnes, E. J. L.; Tuna, F.; Winpenny, R. E. P. *Angew. Chem. Int. Ed.*, **2011**, *50*, 6530.

[39] (a) Lin, P.-H.; Sun, W.-B.; Yu, M.-F.; Li, G.-M.; Yan, P.-F.; Murugesu, M. *Chem. Commun.*, **2011**, *47*, 10993; (b) Guo, Y.-N.; Xu, G.-F.; Wernsdorfer, W.; Ungur, L.; Guo, Y.; Tang, J.; Zhang, H.-J.; Chibotaru, L. F.; Powell, A. K. *J. Am. Chem. Soc.*, **2011**, *133*, 13948.

The structure of complex **3-3** is shown in Figure 3.14 with selected bond lengths in Table 3.3. Although $Dy^{III}$ ions are both nine-coordinate, the coordination geometries of metal centers varied significantly, for example, Dy1 contains a bidental nitrate while Dy2 has a monodentate nitrate. There are three ligands coordinated to the Ln centers in the dinuclear unit *via* two O atoms and one N atom. The metal centers are bridged by the phenoxide groups of three ligands with Dy1-O-Dy2 angles of 101.3, 97.3 and 97.6° and a Dy1---Dy2 intramolecular distance of 3.55 Å. The remaining six coordination sites of Dy1 are filled by two nitrogen (N1, N3) and two oxygen (O3, O6) atoms from two ligands and one nitrate ion (O10, O12). One methoxy (O1), one nitrogen (N5) and one oxygen (O9) atom from the other ligand coordinate to Dy2. The remaining three coordination sites of Dy2 are filled by one monodentate (O16) and one bidentate (O13, O15) nitrate ions. Charge balance considerations indicated only bridged deprotonated phenoxides (O2, O5 and O8) whereas C9-O3, C19-O6 and C29-O9 of the ligands with bond distances 1.21, 1.27 and 1.22 Å, respectively, are double bonds and the ligands are monoanionic. Selected bond distances (Å) and angles (°) are presented in Table 3.3. The $Dy^{III}$ ions in both complexes **3-2** and **3-3** are asymmetric. If the terminal ligands on $Dy^{III}$ are not considered in complex **3-2**, the $Dy^{III}$ ions showed similar arrangement. The anisotropic axes are unpredictable but strongly correlated to the geometry of $Dy^{III}$ center.

Complex **3-3** thus has more potential to obtain two non-parallel anisotropic axes and to observe more than one relaxation mode in ac magnetic susceptibility measurements.

**Table 3.3** Selected bond distances (Å ) and angles (°) for complex **3-3**

| | | | |
|---|---|---|---|
| Dy1-O2 | 2.298(10) | Dy1-O5 | 2.322(10) |
| Dy1-O6 | 2.386(11) | Dy1-O3 | 2.406(11) |
| Dy1-O8 | 2.426(11) | Dy1-O10 | 2.582(13) |
| Dy1-O12 | 2.446(10) | Dy1-N1 | 2.577(12) |
| Dy1-N3 | 2.582(13) | Dy2-O1 | 2.693(10) |
| Dy2-O2 | 2.297(10) | Dy2-O5 | 2.412(10) |
| Dy2-O8 | 2.297(11) | Dy2-O9 | 2.406(11) |
| Dy2-O13 | 2.477(11) | Dy2-O16 | 2.407(11) |
| Dy2-N5 | 2.556(12) | Dy1---Dy2 | 3.5536(12) |
| Dy1-O2-Dy2 | 101.3(4) | Dy1-O5-Dy2 | 97.3(4) |
| Dy1-O8-Dy2 | 97.6(4) | | |

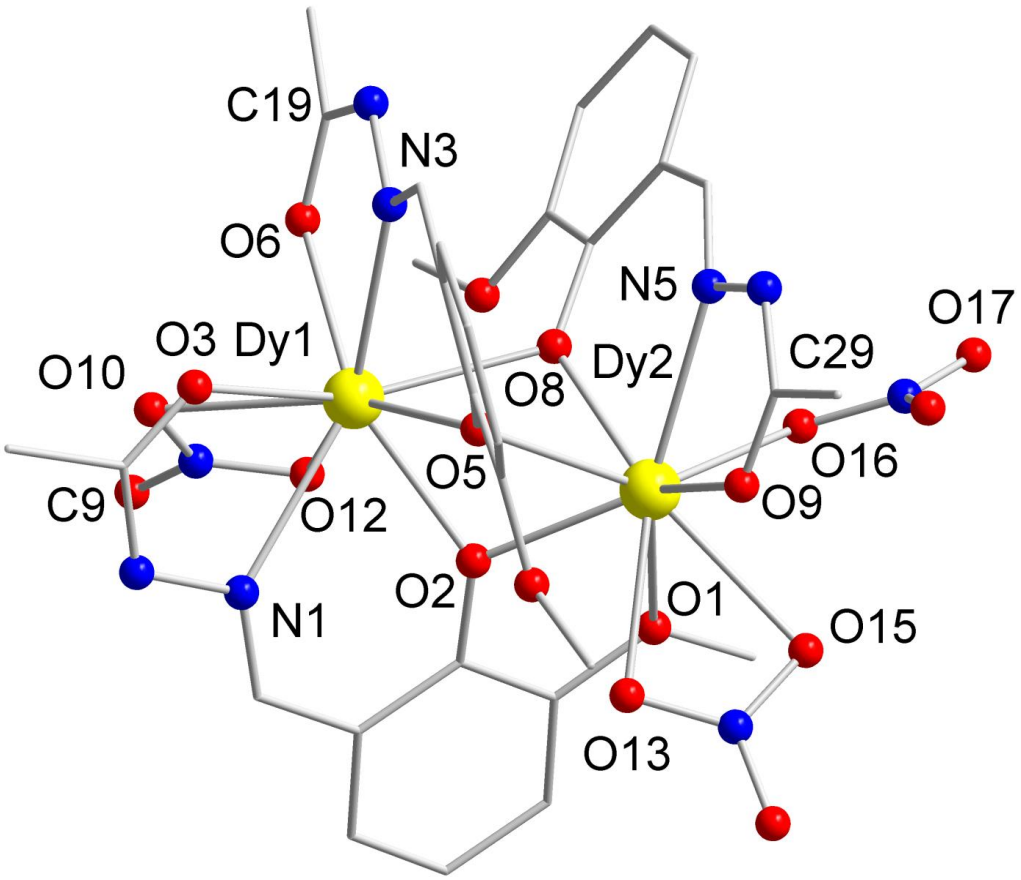


**Figure 3.14.** Partially labeled molecular structure of mononuclear complex **3-3.**

The packing arrangements along the *a* and *b* axes of $[Dy_2(hma)_3(NO_3)_3]\cdot CH_3CN\cdot 2CH_3OH$ are presented in Figures 3.15 and 3.16. Close inspection reveals that the dinuclear units are alternating along the *c* axis in an aba'b' fashion and extend to 1-D chain structures by two types of hydrogen bonds. The black dotted lines in Figure 3.15 represent hydrogen bonds through N2 and O4 [N2···O4 = 2.895 Å, N2···H-O4 = 169.04°] between a and b layers as well as through N5 and O17 [N5···O17 = 2.918 Å, N5···H-O17 = 160.29°] between a' and b layers.

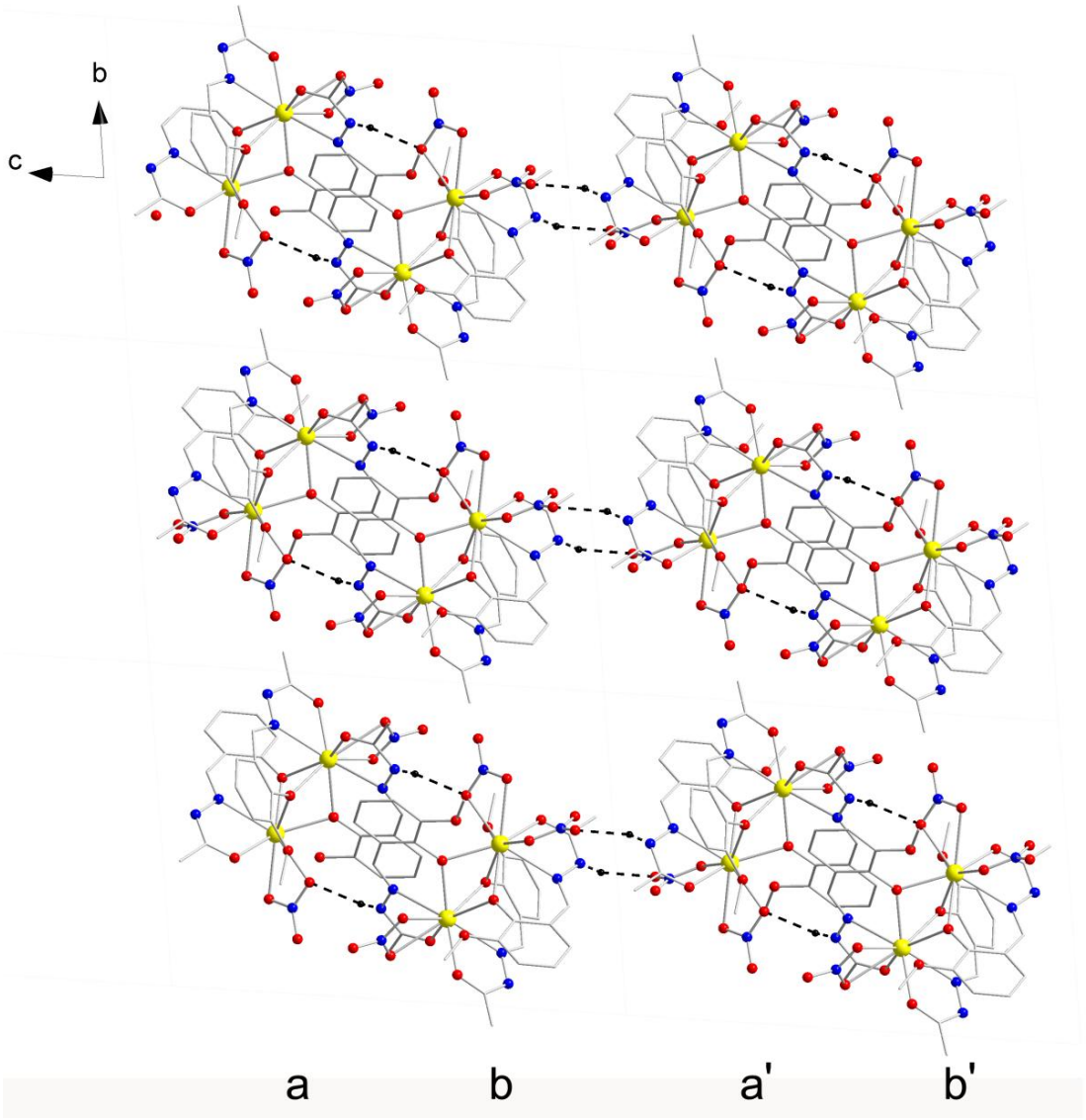


**Figure 3.15** Packing arrangement along the crystallographic *c* axis of **3-3** with hydrogen atoms omitted for clarity. The black dotted lines represent hydrogen bonds between the molecules. Yellow (Dy), Red (O), Blue (N), Grey (C). Layer a and b are shown two different layers of molecules.

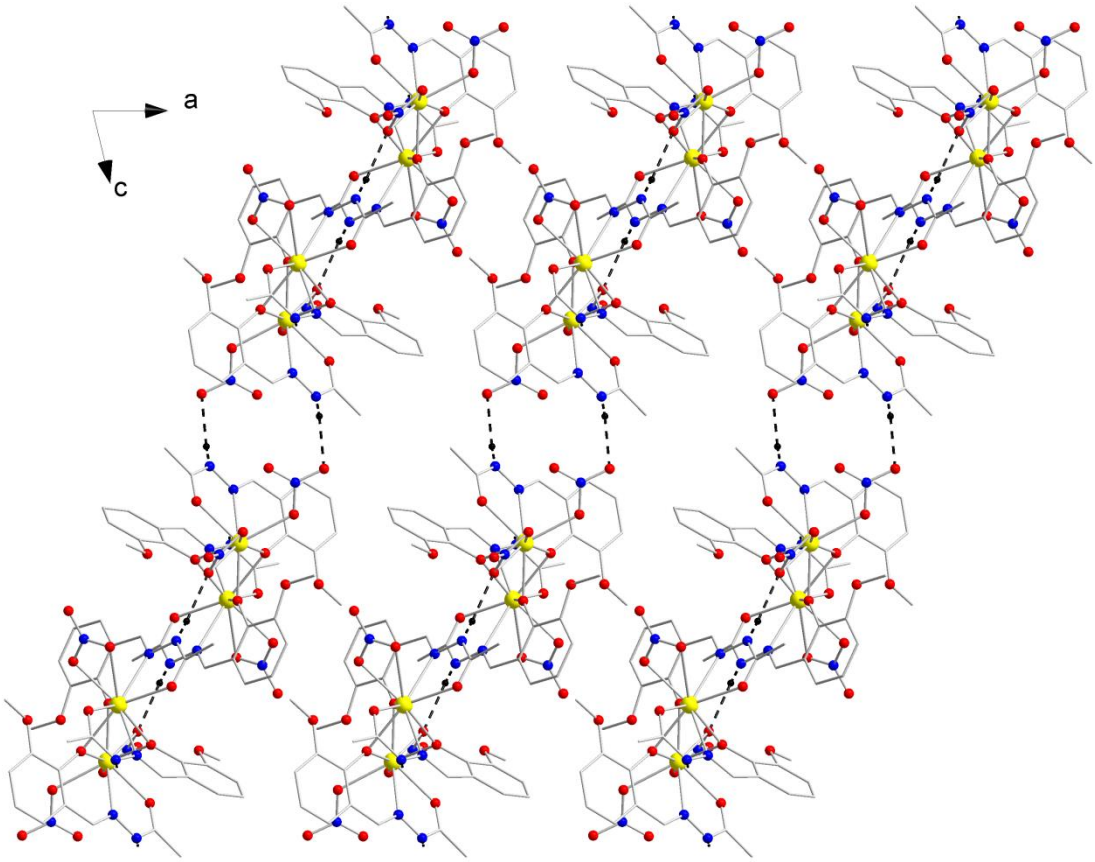


**Figure 3.16.** Packing arrangement along the crystallographic *b* axis of **3-3** with hydrogen atoms omitted for clarity. The black dotted lines represent hydrogen bonds between the molecules. Yellow (Dy), Red (O), Blue (N), Grey (C).

There were no magnetic measurements performed on complex **3-3**. It may be advantageous to correlate the structure, magnetic properties and anisotropic axes on $Dy^{III}$ centers in the future in order to explore the possibility of different relaxation processes in one molecule.

## 3.4 Molecular structure of $[Ln_2(hmi)_2(NO_3)_x(MeOH)_y]$ (Ln: Eu, Gd, Tb and Dy, x = 2 and y = 2 or 4)

A series of lanthanide metals (Eu, Gd, Tb and Dy) have been chosen. Three isolated dinuclear complexes, ($[Eu_2(hmi)_2(NO_3)_2(MeOH)_4]$ (**3-4**), $[Tb_2(hmi)_2(NO_3)_2(MeOH)_4]$ (**3-5**) and $[Dy_2(hmi)_2(NO_3)_2(MeOH)_2]$ (**3-6**)) as well as five 2-D network systems, ($[Eu_2(hmi)_2(NO_3)_2(MeOH)_2]_\infty \cdot MeCN$ (**3-7**·MeCN), $[Gd_2(hmi)_2(NO_3)_2(H_2O)_2]_\infty \cdot MeOH$ (**3-10**·MeOH), $[Tb_2(hmi)_2(NO_3)_2(MeOH)_2]_\infty \cdot MeCN$ (**3-8**·MeCN), $[Dy_2(hmi)_2(NO_3)_2(MeOH)_2]_\infty \cdot MeCN$ (**3-9**·MeCN) and $[Dy_2(hmi)_2(N_3)_2(MeOH)_2]_\infty \cdot 2MeOH$ (**3-11**·2MeOH)) were synthesized by carefully controlling the reaction conditions.

The general procedure for the synthesis of dinuclear complexes is the addition of $Ln(NO_3)_3 \cdot 6H_2O$, ligand ($H_2hmi$) and base ($Et_3N$, pyridine or $NaN_3$) to a solution of MeOH and/or MeCN. The $Ln(NO_3)_3 \cdot 6H_2O$ was chosen due to the potential eight or nine coordination sites of the metal center. Furthermore, the base plays an important role by promoting the deprotonation of $H_2hmi$. The absence of base from the reaction results in a mononuclear complex. Reaction of $H_2hmi$ with 4 equivalents of $Et_3N$ and 1.5 equivalents of $Ln(NO_3)_3 \cdot 6H_2O$ (Ln = Eu, Tb and Dy) in MeOH gave the isolated

dinuclear complexes, $[Eu_2(hmi)_2(NO_3)_2(MeOH)_4]$ (**3-4**), $[Tb_2(hmi)_2(NO_3)_2(MeOH)_4]$ (**3-5**) and $[Dy_2(hmi)_2(NO_3)_2(MeOH)_2]$ (**3-6**). The extended 2-D network systems were obtained using the reaction of $H_2hmi$ with 4 equivalents of pyridine and 1 equivalent of $Ln(NO_3)_3 \cdot 6H_2O$ (Ln = Eu, Tb and Dy) in a MeOH/MeCN (1:3) mixture. A variety of solvents were used in an attempt to alter the packing arrangement of the molecules; MeCN was found to be essential for obtaining extended 2-D networks which are observed in the crystal structures of $[Eu_2(hmi)_2(NO_3)_2(MeOH)_2]_\infty \cdot MeCN$ (**3-7**·MeCN), $[Tb_2(hmi)_2(NO_3)_2(MeOH)_2]_\infty \cdot MeCN$ (**3-8**·MeCN) and $[Dy_2(hmi)_2(NO_3)_2(MeOH)_2]_\infty \cdot MeCN$ (**3-9**·MeCN).

We obtained the same extended 2-D network complex using Gd, $[Gd_2(hmi)_2(NO_3)_2(H_2O)_2]_\infty \cdot MeOH$ (**3-10**·MeOH); both reaction conditions were treated with $Gd(NO_3)_3 \cdot 6H_2O$. Compared with the other network complexes, MeCN is not necessary to form the 2-D network in the case of Gd. MeOH is the co-solvent in the structure regardless of the presence of MeCN.

In order to replace the terminal ligand and compare the magnetic properties, 1 equivalent of $DyCl_3 \cdot 6H_2O$ was reacted with 1 equivalent of $H_2hmi$ in MeOH yielding complex **3-11**. Sodium azide was chosen instead of pyridine or $Et_3N$ due to its role as a ligand as well as a mild base which would deprotonate the $H_2hmi$ ligand and

potentially act as a terminal or bridging entity simultaneously.

*Isolated Dinuclear Complexes* (**3-4**, **3-5** and **3-6**): Complexes **3-4** and **3-5** (Figure 1, top) are dinuclear complexes composed of two nine-coordinate $Eu^{III}$ and $Tb^{III}$ ions, respectively.

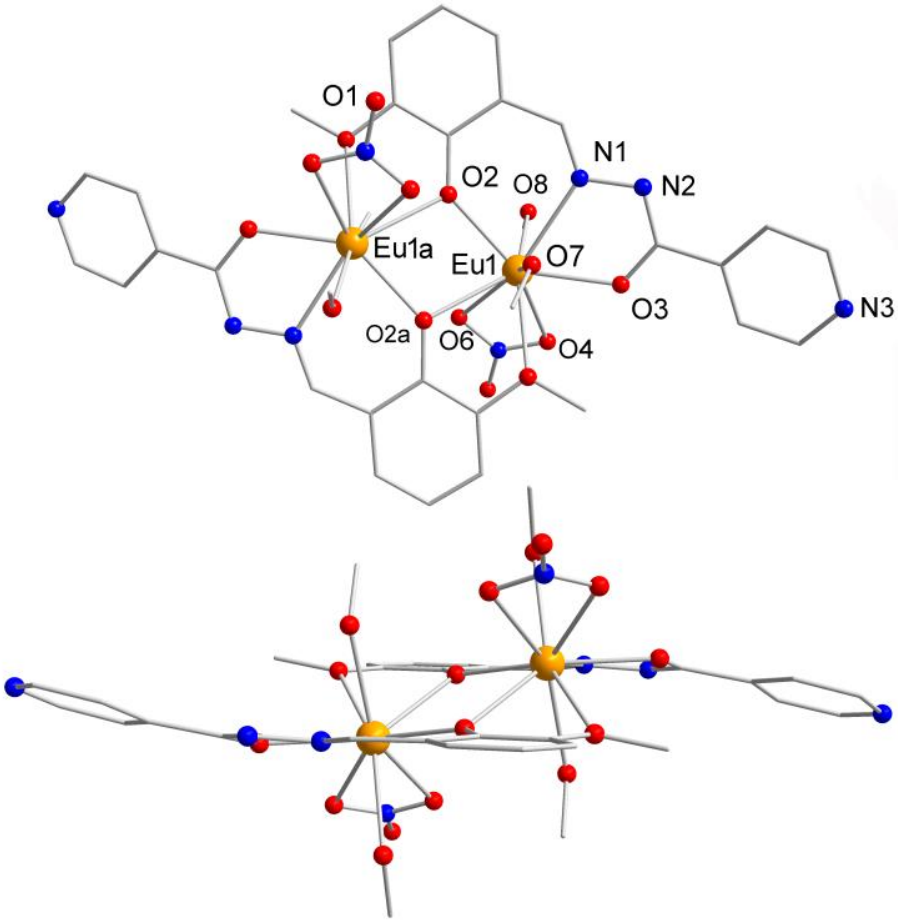


**Figure 3.17.** Top: The molecular structure of complex **3-4** (Eu) and complex **3-5** (Tb)**.** Bottom: The side view of complexes **3-4** and **3-5.** Hydrogen atoms are omitted from both figures for clarity. Orange (Eu or Tb), Red (O), Blue (N), Grey (C).

The pentadentate $hmi^{2-}$ ligand coordinates to the Ln centers in the dinuclear unit *via* three O atoms (from hydroxide, $\mu$-phenoxide and methoxy group) and one N atom. The metal centers are bridged by the phenoxide groups of two ligands with Ln1-O-Ln1a. The Ln-Ln distances of **3-4** and **3-5** are 3.87 and 3.82 Å, respectively. The Ln1-O-Ln1a angles of **3-4** and **3-5** are 106.8° and 107.4°, respectively. The remaining four coordination sites of each lanthanide ion are filled by one nitrate anion and two methanol molecules. Selected bond distances (Å) and angles (°) are presented in Table 3.4.

The side view of complexes **3-4** and **3-5** (Figure 3.17, bottom) shows the two ligands nearly parallel to each other. The dihedral plane angle between the two phenyl rings is 0.18° and 180.00°, respectively. The pyridine plane of the ligand is on an angle of 18.62° to the phenyl plane for **3-4** and 17.63° for **3-5**. The dihedral angle between the phenyl ring of the ligand and the Ln1, O2, Ln1a plane is 49.47° for **3-4** and 48.76° for **3-5**. Two terminal methanol molecules are coordinated to each Ln atom above and below the plane of the ligand. The two terminal nitrate molecules occupy the remaining axial positions.

The structure of complex **3-6** (Figure 3.18, top) consists of two pentadentate $hmi^{2-}$ ligands and two $Dy^{III}$ centers bridged by the phenoxide groups of the ligands. The $Dy^{III}$

ions are eight coordinate due to the presence of only one terminal methanol on each metal center. It can be described as a distorted square anti-prism for complex **3-6** which is well-known in octacoordinated lanthanide. This, however, does not have a significant effect on the Dy-O distances and Dy-O-Dy angle (Table 3.4) of the core and unit cell.

**Table 3.4.** Selected bond distances (Å), angles (°) and coordination number of the lanthanide centers for complexes **3-4** (Eu)**, 3-5** (Tb) and **3-6** (Dy).

| | **3-4** | **3-5** | **3-6** |
|---|---|---|---|
| Ln1-O2 | 2.329(4) | 2.309(7) | 2.312(6) |
| Ln1a-O2 | 2.494(4) | 2.463(8) | 2.372(6) |
| Ln1-N1 | 2.537(5) | 2.498(10) | 2.429(7) |
| Ln1-O3 | 2.325(4) | 2.283(8) | 2.260(6) |
| Ln1-O1a | 2.494(4) | 2.463(8) | 2.422(6) |
| Ln1-O4 | 2.549(4) | 2.547(8) | 2.430(8) |
| Ln1-O6 | 2.540(5) | 2.502(9) | 2.459(8) |
| Ln1-O7 | 2.493(5) | 2.471(9) | 2.335(7) |
| Ln1-O8 | 2.445(5) | 2.410(8) | N.A. |
| Ln1-Ln1a | 3.873(1) | 3.8469(11) | 3.7500(8) |
| Ln1-O2-Ln1a | 106.80(14) | 107.4(3) | 106.4(2) |
| Coordination number | 9 | 9 | 8 |

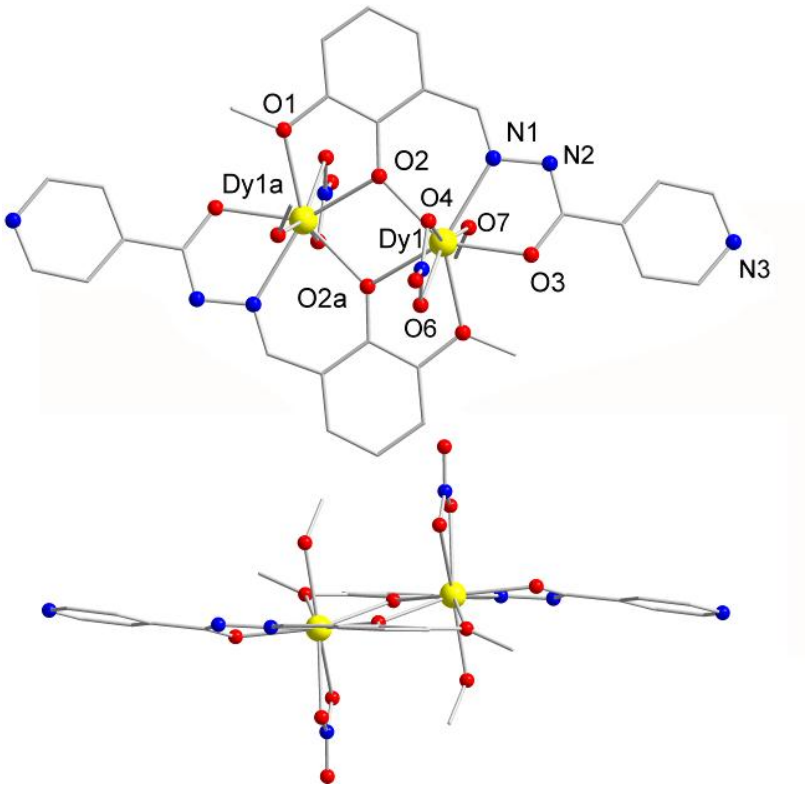


**Figure 3.18.** Top: The molecular structure of complex **3-6**. Bottom: The side view of complex **3-6**. Hydrogen atoms are omitted from both figures for clarity. Yellow (Dy), Red (O), Blue (N), Grey (C).

The side view of complex **3-6** (Figure 3.18, bottom) shows geometrical differences between **3-4** and **3-5**. The two ligands remain nearly parallel (0.13° between the phenyl rings of the $hmi^{2-}$ ligands). Moreover, the angle between the pyridine plane of the ligand and the phenyl plane, as well as the dihedral angle between the phenyl ring of the ligand and the Dy1, O2, Dy1a plane are significantly less than those of **3-4** and **3-5**, 9.65° and 31.74°, respectively. Only one terminal methanol is coordinated to each Dy atom, and

nitrate groups occupy the remaining axial positions of the metal centers.

Three packing arrangements along the *a*, *b* and *c* axes of complexes **3-4** and **3-5** are presented in figure 3.19. Close inspection of the packing arrangements reveals that all dinuclear complexes are well isolated along the *a* and *b* axes. Two hydrogen bonds are present in complexes **3-4** and **3-5** between N3 and O7 [N3···O7 = 2.773, 2.767 Å, N3···H-O7 = 152.16, 141.89°] and between N2 and O8 [N2···O8 = 2.779, 2.796 Å, N2···H-O8 = 162.28, 161.48°] (Figure 3.19, center), respectively; which contribute to the close proximity of the two molecules. π-stacking appears clearly between the phenyl and pyridine rings of $hmi^{2-}$ ligands of different molecular entities with a distance between the mean planes of 3.67 Å along the *c* axis.

The packing arrangement along the *a* axis of **3-6** is similar to that of **3-4** and **3-5** with all lanthanide dinuclear units well separated (Figure 3.20, top). The difference can be observed when we compare the molecules horizontally along the *b* axis (Figure 3.20, center). The dinuclear $Dy^{III}$ cores are arranged with a slight angle due to the octacoordinate $Dy^{III}$ centers. Only one terminal methanol is coordinated to each $Dy^{III}$ ion, resulting in one type of hydrogen bond between N3 and O7 [N3···O7 = 2.634 Å, N3···H-O7 = 164.29°]. Compared to **3-4** and **3-5**, there is no π-stacking between the phenyl and pyridine rings of $hmi^{2-}$ ligands along the *c* axis in compound **3-6**.

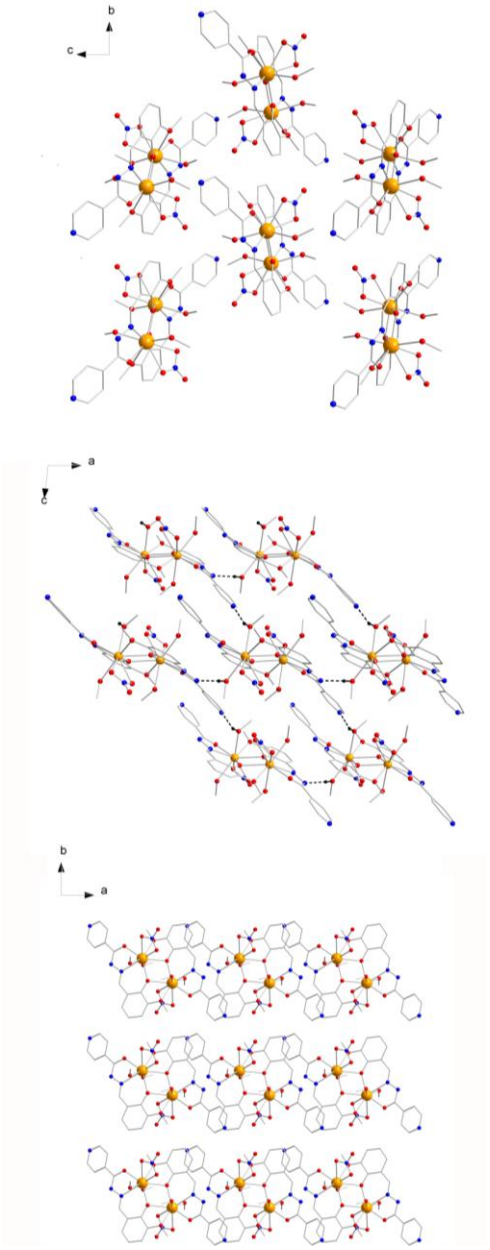


**Figure 3.19.** Packing arrangements of **3-4** and **3-5** along the crystallographic *a* (top), *b* (center) and *c* (bottom) axes with hydrogen atoms omitted for clarity. The black dotted lines represent hydrogen bonds between the molecules along the *b* axis. Orange (Tb or Eu), Red (O), Blue (N), Grey (C).

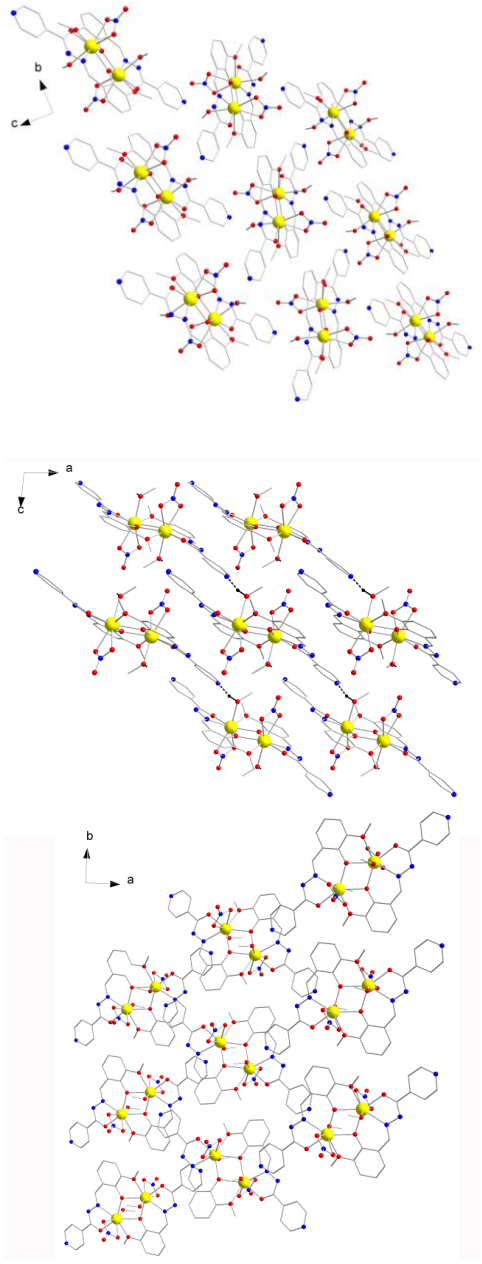


**Figure 3.20.** Packing arrangement of **3-6** along the crystallographic a (top), b (center) and *c* (bottom) axis with hydrogen atoms omitted for clarity. The black dotted lines represent hydrogen bonds between the molecules. Yellow (Dy), Red (O), Blue (N), Grey (C).

*2-D Network Complexes*: Single crystal X-ray diffraction reveals that complexes **3-7**, **3-8** and **3-9** are isostructural. A labelled X-ray structure of the centrosymmetric dinuclear complexes is presented in figure 3.21.

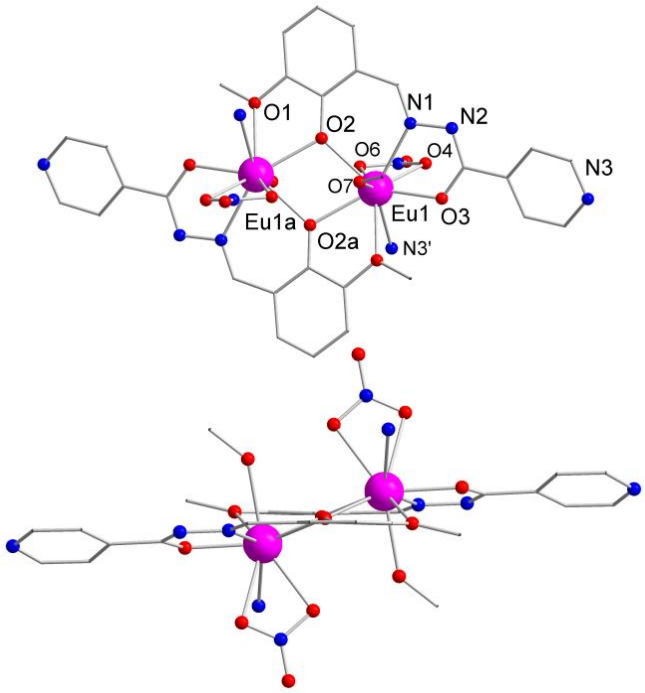


**Figure 3.21.** Top: The molecular structure of complexes **3-7**, **3-8** and **3-9**. Bottom: The side view of complexes **3-7**, **3-8** and **3-9**. Hydrogen atoms are omitted from both figures for clarity. Pink (Eu, Tb and Dy for **3-7**, **3-8** and **3-9**, respectively), Red (O), Blue (N), Grey (C).

The coordination environments of the metal centers and $hmi^{2-}$ ligands are identical to the isolated dinuclear complexes. Two $Ln^{III}$ ions are bridged by phenoxide groups of two ligands. The Ln-Ln distances of **3-7**, **3-8** and **3-9** are 3.84, 3.81 and 3.80 Å,

respectively. The Ln-O-Ln angles of **3-7**, **3-8** and **3-9** are 106.7°, 107.3° and 107.7°, respectively. Selected bond distances (Å) and angles (°) are presented in Table 3.5.

**Table 3.5.** Selected bond distances (Å), angles (°) and coordination number of the lanthanide centers for complexes **3-7**, **3-8** and **3-9.**

| | **3-7** | **3-8** | **3-9** |
|---|---|---|---|
| Ln1-O2 | 2.411(3) | 2.383(4) | 2.367(4) |
| Ln1a-O2 | 2.367(3) | 2.345(4) | 2.340(4) |
| Ln1-N1 | 2.502(4) | 2.471(5) | 2.470(5) |
| Ln1-O3 | 2.274(3) | 2.248(4) | 2.238(4) |
| Ln1-O1a | 2.557(3) | 2.535(4) | 2.530(4) |
| Ln1-O4 | 2.519(4) | 2.486(5) | 2.567(5) |
| Ln1-O6 | 2.582(4) | 2.565(5) | 2.484(5) |
| Ln1-O7 | 2.511(4) | 2.484(5) | 2.490(5) |
| Ln1-N3’ | 2.274(3) | 2.560(5) | 2.554(5) |
| Ln1-Ln1a | 3.8345(5) | 3.8081(6) | 3.801(0) |
| Ln1-O2-Ln1a | 106.72°(12) | 107.32(15) | 107.69°(15) |
| Coordination number | 9 | 9 | 9 |

Ln: Eu, Tb, and Dy for complexes **3-7**, **3-8** and **3-9**, respectively.

Two pentadentate ligands coordinate with the metal centers. The remaining coordination sites of the nine-coordinate lanthanide ions are filled by one terminal $NO_3^-$, methanol and the pyridyl N atom (N3') from neighboring complexes resulting in a two-dimensional network of the dinuclear units. One MeCN solvent molecule is present in the crystal structure.

In the case of complex **3-10**, the main structure is similar to those described above with MeOH as the solvent molecule and two terminal water molecules (Figure 3.22, top). The Gd-Gd distance in complex **3-10** is 3.83 Å, whereas, the Gd-O-Gd angle is 106.7°, both are similar to complexes **3-7**, **3-8** and **3-9**.

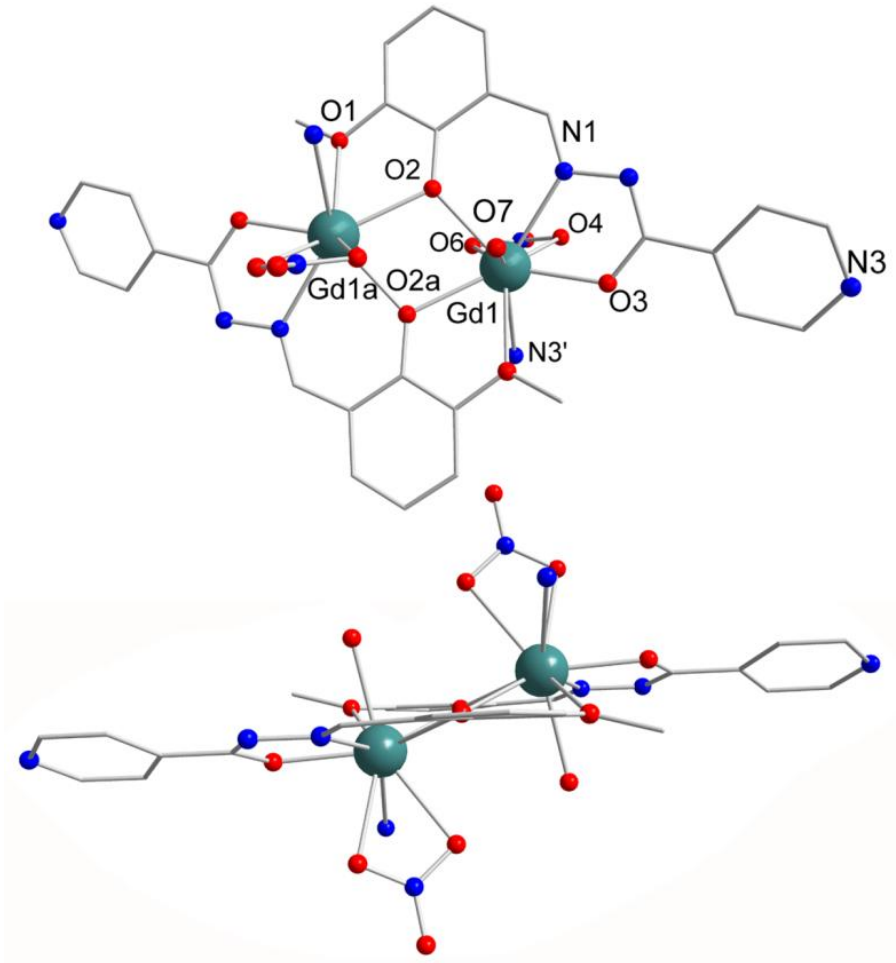


**Figure 3.22.** Top: The molecular X-ray structure of complex **3-10**. Bottom: The side view of complex **3-10**. Both figures omit hydrogen atoms for clarity. Dark cyan (Gd), Red (O), Blue (N), Grey (C).

The reaction conditions are slightly different for complex **3-11**, as mentioned previously. Two azide groups replace the terminal nitrate groups (Figure 3.23). The structure and packing arrangement are very similar to the other 2-D network complexes with the dinuclear unit being extended by $Dy^{III}$ centers and neighboring N of pyridine

groups. The Dy-Dy distance in **8** is 3.80 Å and the Dy-O-Dy angle is 108.9°. The only difference is the terminal azide instead of $NO_3^-$ resulting in an eight-coordinate metal center in **3-11**. Selected bond distances (Å) and angles (°) for complexes **3-10** and **3-11** are presented in Table 3.6.

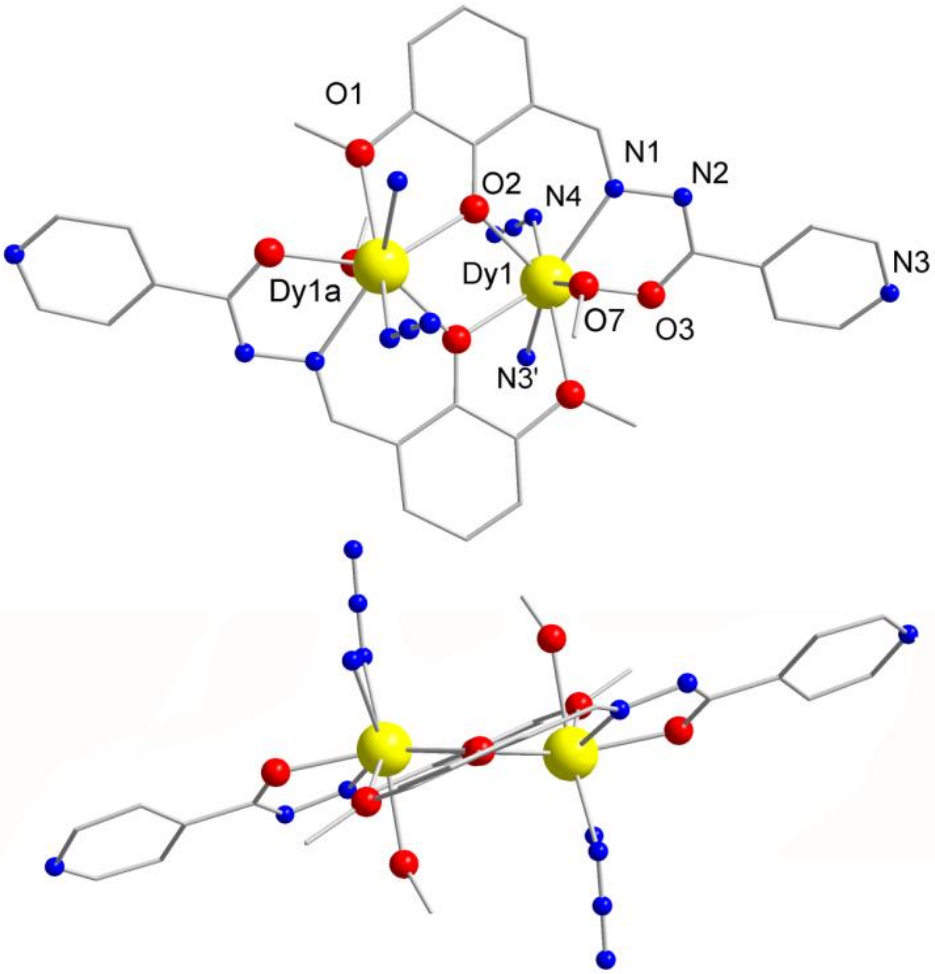


**Figure 3.23.** Top: The molecular X-ray structure of complex **3-11**. Bottom: The side view of complex **3-11**. Both figures omit hydrogen atoms for clarity. Yellow (Dy), Red (O), Blue (N), Grey (C).

**Table 3.6.** Selected bond distances (Å), angles (°) and coordination number of the lanthanide centers for complexes **3-10** and **3-11.**

| | **3-10** | **3-11** |
|---|---|---|
| Ln1-O2 | 2.407(4) | 2.353(8) |
| Ln1a-O2 | 2.352(4) | 2.318(8) |
| Ln1-N1 | 2.475(5) | 2.432(12) |
| Ln1-O3 | 2.281(4) | 2.267(9) |
| Ln1-O1a | 2.550(5) | 2.474(9) |
| Ln1-O4 | 2.549(6) | N.A. |
| Ln1-O6 | 2.567(7) | N.A. |
| Ln1-O7 | 2.464(5) | 2.411(10) |
| Dy1-N4 | N.A. | 2.395(12) |
| Ln1-N3’ | 2.587(5) | 2.561(11) |
| Ln1-Ln1a | 3.8266(5) | 3.8002(15) |
| Ln1-O2-Ln1a | 107.04(15) | 108.9(3) |
| Coordination number | 9 | 8 |

Ln: Gd and Dy for complexes **3-10** and **3-11**, respectively.

The side view of complexes **3-7**, **3-8** and **3-9** is shown in figure 3.21 (bottom), while those of complexes **3-10** and **3-11** are presented in figure 3.22 (bottom) and 3.23

(bottom), respectively. In **3-7**, **3-8** and **3-9**, one terminal group of each methanol and nitrate are coordinated with each Ln atom. Methanol and nitrate groups on each $Ln^{III}$ ion are located on the same axis, in opposing directions. The pyridine rings of neighbouring ligands coordinate on the same side as the terminal nitrate. A similar side view is observed for complex **3-10** (Figure 3.22, bottom). The only difference in **3-10** is a terminal water instead of terminal MeOH.The two ligands remain nearly parallel (0.57° (**3-7**), 180.00° (**3-10**), 1.51° (**3-8**), 180.00° (**3-9**) and 1.22°(**3-11**) between the phenyl rings of the $hmi^{2-}$ ligands. Moreover, the pyridine plane of the ligand is on an angle of 22.04°, 23.23°, 21.83°, 22.88° and 28.75° to the phenyl plane, respectively. The dihedral angle between the phenyl of the ligand and the Ln1, O2, Ln1a plane is 24.65°, 24.62°, 25.66°, 24.13° and 25.83°, respectively. Only one terminal methanol is coordinated with each Ln atom. Methanol and nitrate groups occupy the axial positions of the metal centers.

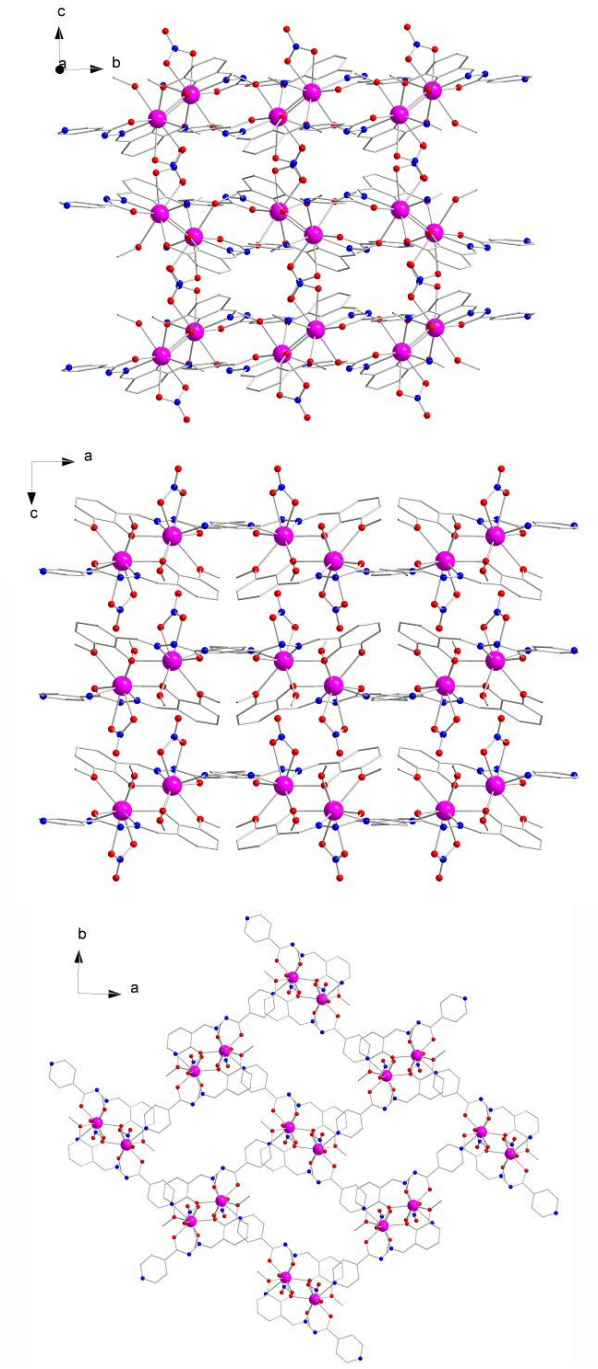


**Figure 3.24.** Packing arrangements of **3-7** (Eu), **3-8** (Tb) and **3-9** (Dy) along the crystallographic *a* (top), *b* (center) and *c* (bottom) axes with hydrogen atoms omitted for clarity. Pink (Eu, Tb or Dy), Red (O), Blue (N), Grey (C).

Packing arrangements of complexes **3-7**, **3-8** and **3-9** along the crystallographic *a*, *b* and *c* axes are shown in Figure 3.24. The 2-D network of the dinuclear lanthanide complexes is shown in the packing arrangement along the *c* axis. The pyridyl N atoms further coordinate to the lanthanide atoms of neighboring complexes. The packing arrangements along the *a* and *b* axes present well seperated units in the horizontal direction which confirms the 2-D network. The dinuclear units show parallel orientation along the *a* axis, but a zigzag arrangement of molecules along the *b* axis.

Packing arrangements of complexes **3-10** and **3-11** along the crystallographic *a*, *b* and *c* axes are shown in Figure 3.25 and 3.26, respectively. Since the dinuclear centers of both complexes are connected by the neighboring pyridine groups and hold the same geometry, these two complexes, regardless of the different terminal ligands, still show similar packing arrangements as the other 2-D network complexes.

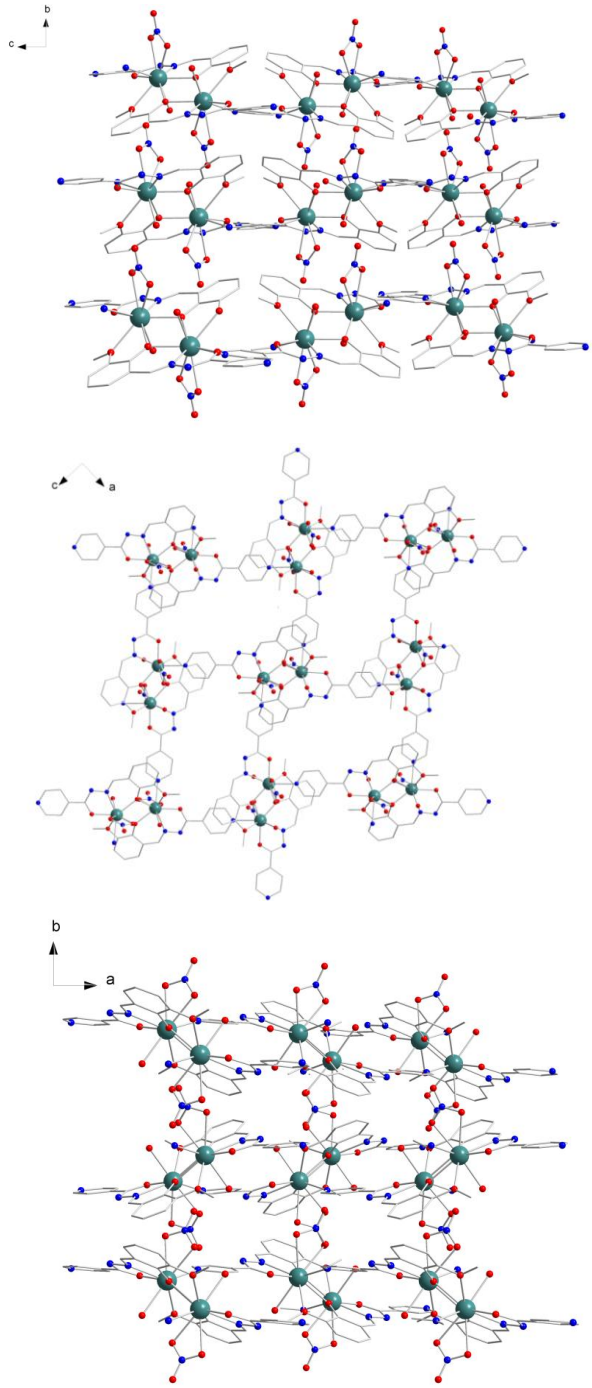


**Figure 3.25.** Packing arrangements of **3-10** (Gd) along the crystallographic *a* (top), *b* (center) and *c* (bottom) axes with hydrogen atoms omitted for clarity. Dark cyan (Gd), Red (O), Blue (N), Grey (C).

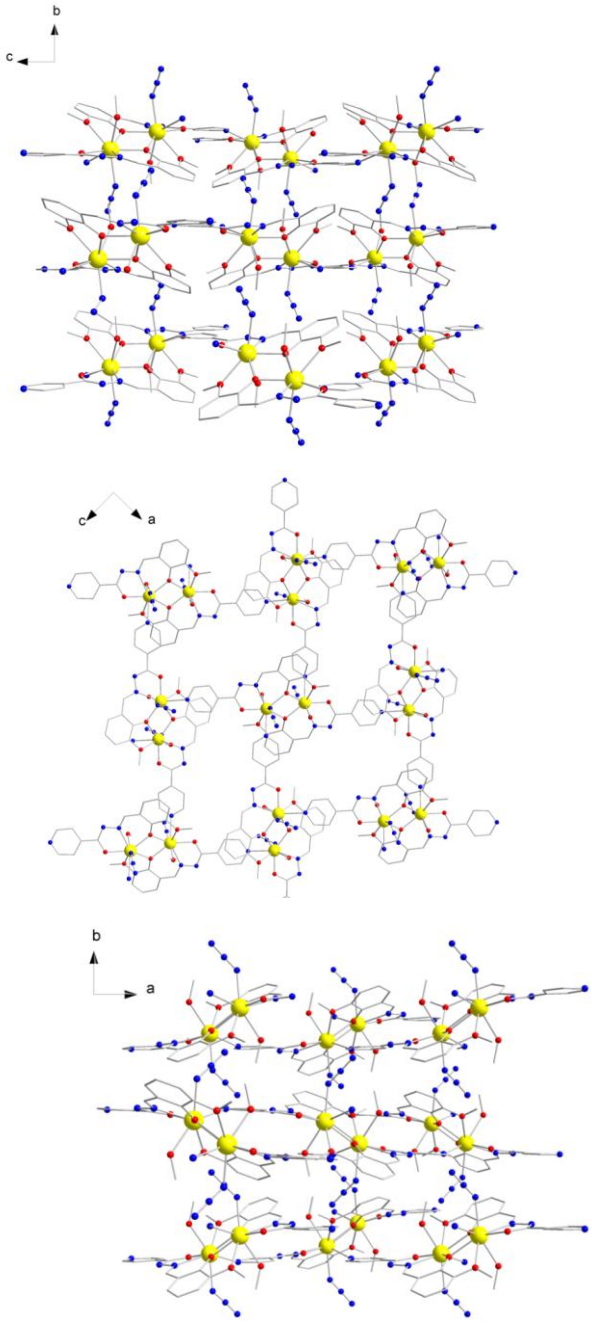


**Figure 3.26.** Packing arrangements of **3-11** (Dy) along the crystallographic *a* (top), *b* (center) and *c* (bottom) axes with hydrogen atoms omitted for clarity. Yellow (Dy), Red (O), Blue (N), Grey (C).

## 3.5 Magnetic measurements of complexes 3-4 – 3-11

### 3.9.1 DC Measurement

The magnetic susceptibilities for all eight complexes were measured in an applied dc field of 1000 Oe in the range of 1.8 K to 300 K on polycrystalline samples. The $\chi T$ *vs.* $T$ plots are shown in Figure 3.27.

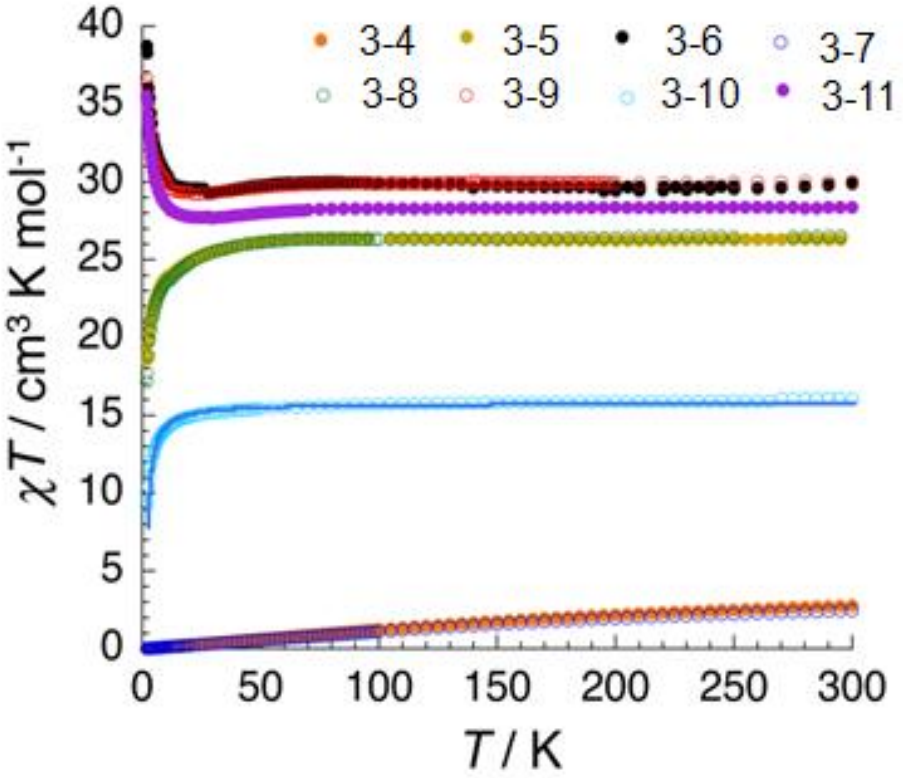


**Figure 3.27.** Temperature dependence of the $\chi T$ product at 1000 Oe for **3-4** – **3-11** (with $\chi = M/H$ normalized per mol); the solid blue line corresponds to the best fit of complex **3-10** using an $S_{Gd} = 7/2$ dinuclear model described in the text.

Due to the presence of thermally populated excited states, the magnetic properties of the europium analogues **3-4** and **3-7** remain difficult to interpret even at room temperature. The $\chi T$ values of complexes **3-4** and **3-7** are 2.8 and 2.5 $cm^3.K.mol^{-1}$, respectively. However, the typical diamagnetic ground state ($^7F_0$) is observed at low temperatures as suggested by the $\chi T$ value of 0.02 $cm^3.K.mol^{-1}$ at 1.8 K.

For compound **3-10**, the $\chi T$ value is 16.1 $cm^3.K.mol^{-1}$ which is close to the theoretical value (15.76 $cm^3.K.mol^{-1}$) for two non-interacting lanthanide ions: $Gd^{III}$ ($^8S_{7/2}$, $S = 7/2$, $L = 0$, $g = 2$, $\chi T = 7.88$ $cm^3.K.mol^{-1}$). The product remains roughly constant between 25 - 300 K and then decreases when lowering the temperature for the $Gd^{III}$ ion. It is possible to quantitatively study the interaction between the two lanthanide centers in the dinuclear $Gd^{III}$ complex due to the absence of spin-orbit coupling at the first-order. The decrease of the $\chi T$ as temperature decreases is clearly indicative of an antiferromagnetic interaction between the $Gd^{III}$ ions. Using the isotropic spin Hamiltonian $\boldsymbol{H} = -2J\boldsymbol{S}_a\boldsymbol{S}_b$ with $\boldsymbol{S}_a = \boldsymbol{S}_b = 7/2$, it is possible to reproduce the variation of $\chi T$ *vs.* $T$ with the following equation, where $x = J/k_BT$:

$$\chi T = \frac{2N\beta}{k}\frac{e^{2x} + 5e^{6x} + 14e^{12x} + 30e^{20x} + 55e^{30x} + 91e^{42x} + 140e^{56x}}{1 + 3e^{2x} + 5e^{6x} + 7e^{12x} + 9e^{20x} + 11e^{30x} + 13e^{42x} + 15e^{56x}}$$

The best fit parameters obtained are $g$ = 2.00(2) and $J/k_B$ = – 0.084(7) K which indicates weak antiferromagnetic coupling between the two gadolinium ions. This phenomenon is common in centrosymmetric complexes, especially the phenoxide-bridged $Gd^{III}$ systems, which may induce an overlap between the 4*f* orbitals leading to an antiferromagnetic interaction.

For the $Tb^{III}$ compounds **3-5** and **3-8**, the $\chi T$ values are 26.2 and 26.6 $cm^3.K.mol^{-1}$, respectively. These values are slightly higher but close to the theoretical value (23.6 $cm^3.K.mol^{-1}$) for two non-interacting lanthanide ions: $Tb^{III}$ ($^7F_6$, S = 3, L = 3, g = 3/2, $\chi T$ = 11.815 $cm^3.K.mol^{-1}$). The product remains roughly constant between 100 - 300 K and then decreases when lowering the temperature. This behavior can be attributed to several causes such as: i) the thermal depopulation of the Stark sub-levels, ii) the presence of significant anisotropy, iii) an antiferromagnetic interaction between the lanthanide ions. It is therefore difficult to establish the nature and the strength of the interactions between the metal centers.

For $Dy^{III}$ compounds **3-6**, **3-9**, and **3-11**, the $\chi T$ values of the complexes are 30.4, 30.0 and 28.4 $cm^3.K.mol^{-1}$, respectively, which are close to the theoretical value (28.16 $cm^3.K.mol^{-1}$) for two non-interacting $Dy^{III}$ ions. ($^6H_{15/2}$, $S$ = 5/2, $L$ = 5, $g$ = 4/3, $\chi T$ = 14.17 $cm^3.K.mol^{-1}$). For complexes **3-6** and **3-9**, the $\chi T$ product remains roughly

constant before reaching a minimum value of 29.3 $cm^3.K.mol^{-1}$ at 23 K. For both complexes, $\chi T$ then increases sharply to a maximum value of 38.4 $cm^3.K.mol^{-1}$ (**3-6**) and 36.6 $cm^3.K.mol^{-1}$ (**3-9**) at 1.8 K. The $\chi T$ product of **3-11** is roughly constant down to 75 K before exhibiting a slow decrease reaching a minimum of 27.7 $cm^3.K.mol^{-1}$ at 28 K. At lower temperatures, the $\chi T$ product at 1000 Oe increases to a maximum value of 35.7 $cm^3.K.mol^{-1}$ at 1.8 K. The increase in $\chi T$ at low temperature suggests the presence of intramolecular ferromagnetic interactions between the metal centers. At higher temperatures, these interactions are masked by the thermal population of the excited states of the $Dy^{III}$ ions as is often observed in $Dy^{III}$ complexes.

As shown in Figure 3.28, complex **3-10** shows almost saturated magnetization at 1.8 K under 7 T with the value of 13.9 $\mu_B$ corresponding well to the binuclear $S = 7/2$. The *M vs. H* of complex **3-10** was numerically simulated using MAGPACK program[40] and it confirms $g = 2.00(5)$ and $J/k_B = -0.085(5)$ K which are in good agreement with those obtained from the calculation of susceptibility (Figure 3.28 and 3.29).

---

[40] a) Borrás-Almenar, J. J.; Clemente-Juan, J. M.; Coronado, E.; Tsukerblat. B. S. *Inorg. Chem.* 1999, **38**, 6081.; b) Borrás-Almenar, J. J.; Clemente-Juan, J. M.; Coronado, E.; Tsukerblat. B. S. *J. Comput. Chem.*, 2001, 22, 985.

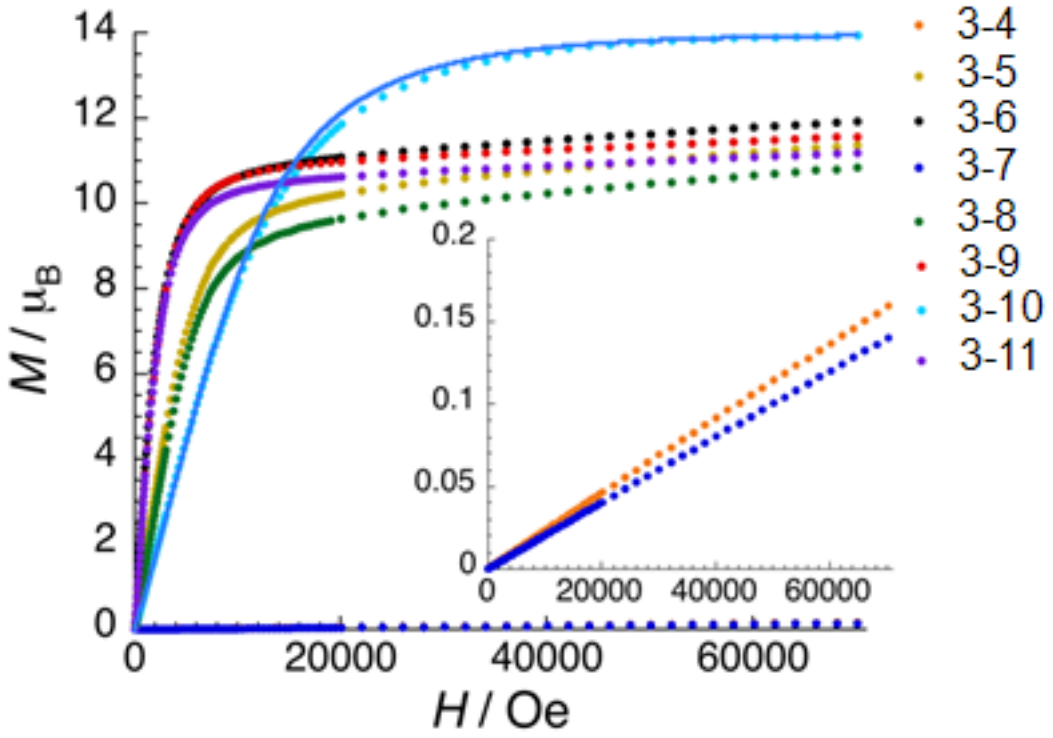


**Figure 3.28** Field dependence of the magnetization, *M*, at 1.8 K for complexes **3-4** – **3-11**. Solid blue line corresponds to the best fit of the complex **3-10**. Inset represents the enlarged plots for **3-4** and **3-5**.

The field dependence of the magnetizations at 1.8 K for **3-5** and **3-8** show relatively slow increase of magnetization at low field compared to those of **3-6**, **3-9** and **3–8** that show rapid increase due to the dinuclear ferromagnetic interaction (Figure 3.28). All these five complexes (**3-5**, **3-6**, **3-8**, **3-9** and **3-11**) exhibit slow linear increase at higher field up to 10.4, 10.5, 11.9, 11.6 and 11.2 $\mu_B$, respectively, without clear saturation. This high-field variation and the non-superposition on a

single mastercurve of the *M vs H/T* data for complexes **3-5**, **3-6**, **3-8**, **3-9** and **3-11** (Figure 3.30 to Figure 3.34) suggest the presence of significant magnetic anisotropy and/or low lying excited states. The thermally populated diamagnetic ground state of the europium analogues **3-4** and **3-7** leads to a value of the magnetization close to zero even at 7 T.

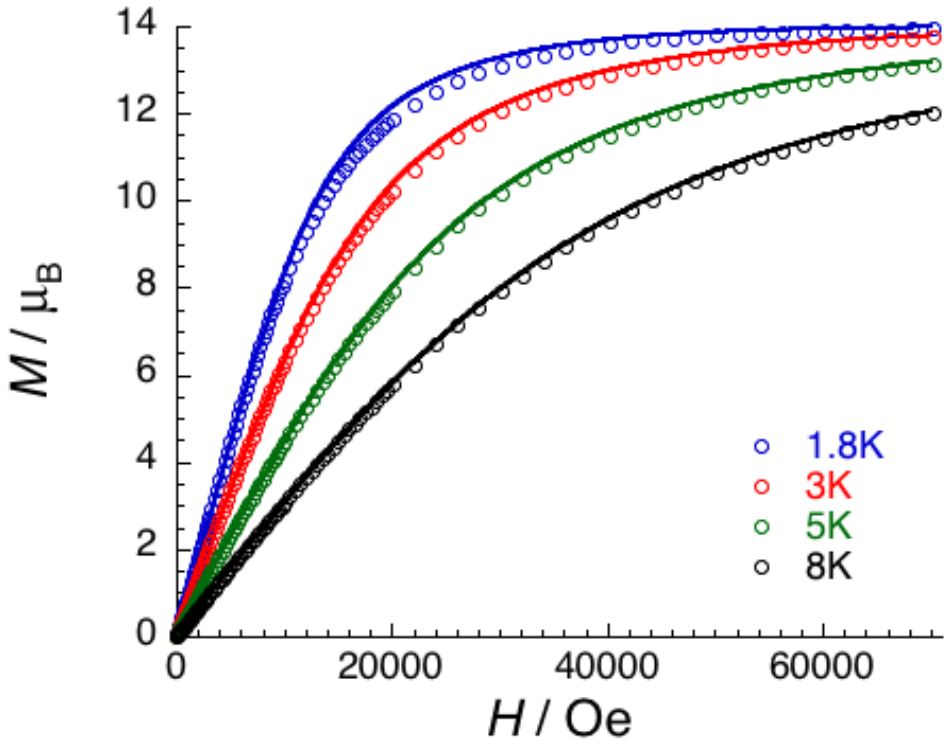


**Figure 3.29** *M vs H* plot for complex **3-10** measured at 1.8, 3, 5, and 8 K, and the solid lines for the best simulations with an Heisenberg $S = 7/2$ dinuclear model.

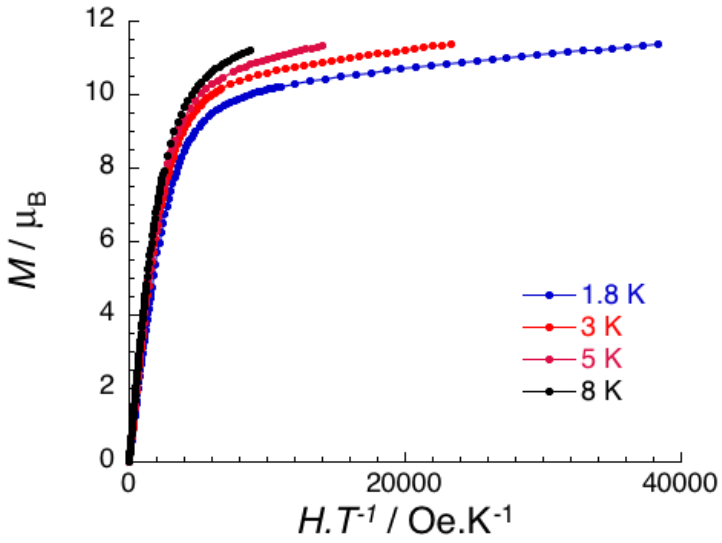


**Figure 3.30** *M vs H*/*T* plot for complex **3-5** measured at 1.8, 3, 5, and 8 K. Solid lines are guide for the eyes.

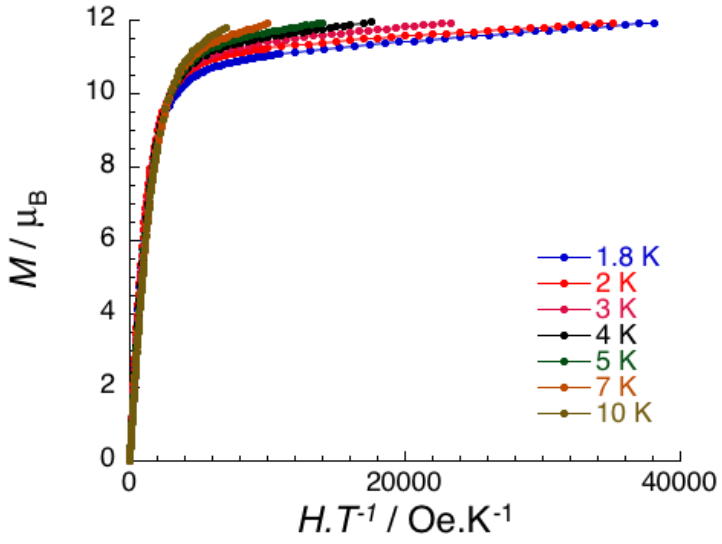


**Figure 3.31** *M vs H*/*T* plot for complex **3-6** measured at 1.8, 2, 3, 4, 5, 7 and 10 K. Solid lines are guide for the eyes.

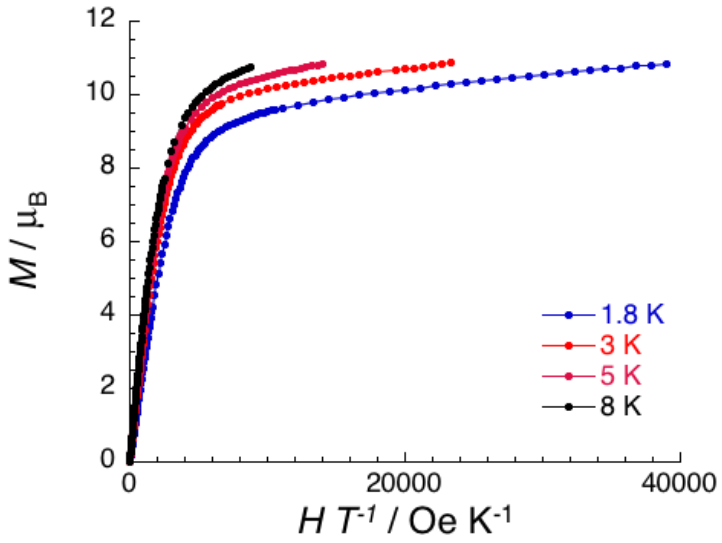


**Figure 3.32** *M vs H*/*T* plot for complex **3-8** measured at 1.8, 3, 5, and 8 K. Solid lines are guide for the eyes.

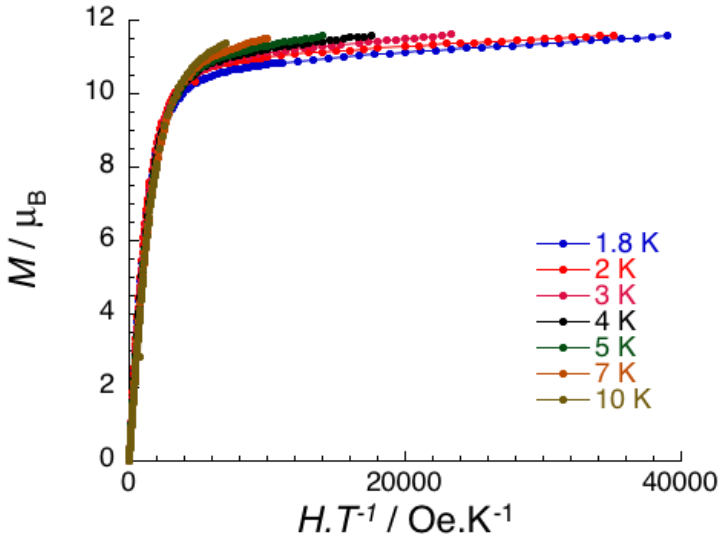


**Figure 3.33** *M vs H*/*T* plot for complex **3-9** measured at 1.8, 2, 3, 4, 5, 7 and 10 K. Solid lines are guide for the eyes.

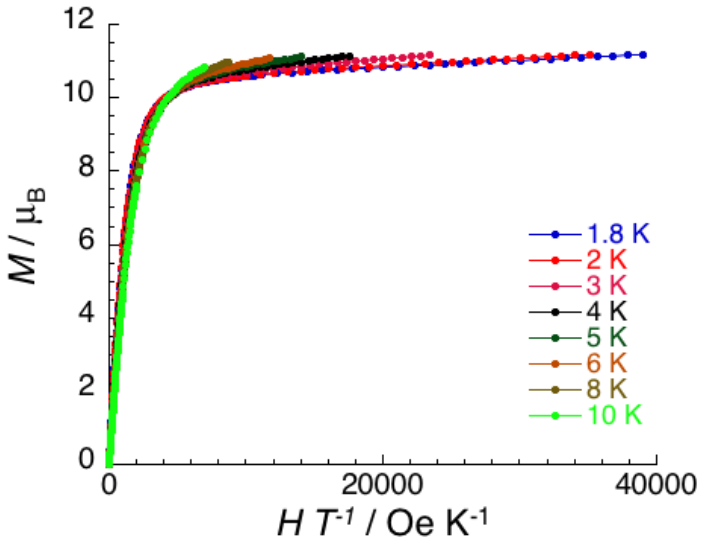


**Figure 3.34** *M vs H*/*T* plot for complex **3-11** measured at 1.8, 2, 3, 4, 5, 7 and 10 K. Solid lines are guide for the eyes.

### 3.9.2 AC measurement

The frequency-dependent ac susceptibility was measured for complexes **3-6**, **3-9** and **3-11** under an oscillating ac field of 1 Oe with frequencies ranging between 1 and 1000 Hz. For complexes **3-4**, **3-5**, **3-7**, **3-8** and **3-10**, no noticeable out-of-phase susceptibility is observed above 1.8 K. The shape and frequency dependence of the ac susceptibility signal indicate the SMM nature of complexes **3-6**, **3-9** and **3-11** in Figures 3.35, 3.36 and 3.37, respectively.

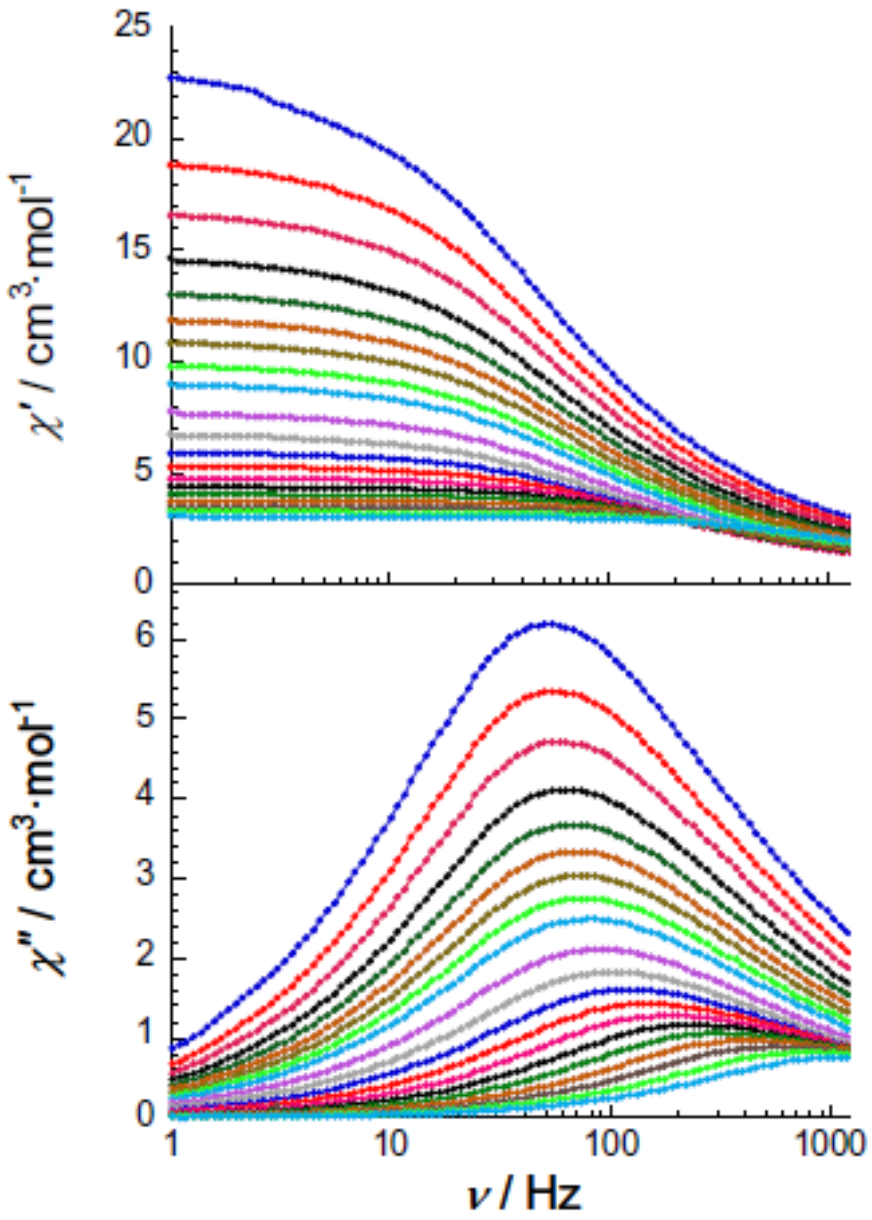


**Figure 3.35** In-phase ($\chi'$)and Out-of-phase ($\chi''$) susceptibility versus frequency ($\nu$) from 1.8 to 5.2 K with an interval of 0.2 K and from 5.5 to 13 K with an interval of 0.5 K under zero dc field for complex **3-6**.

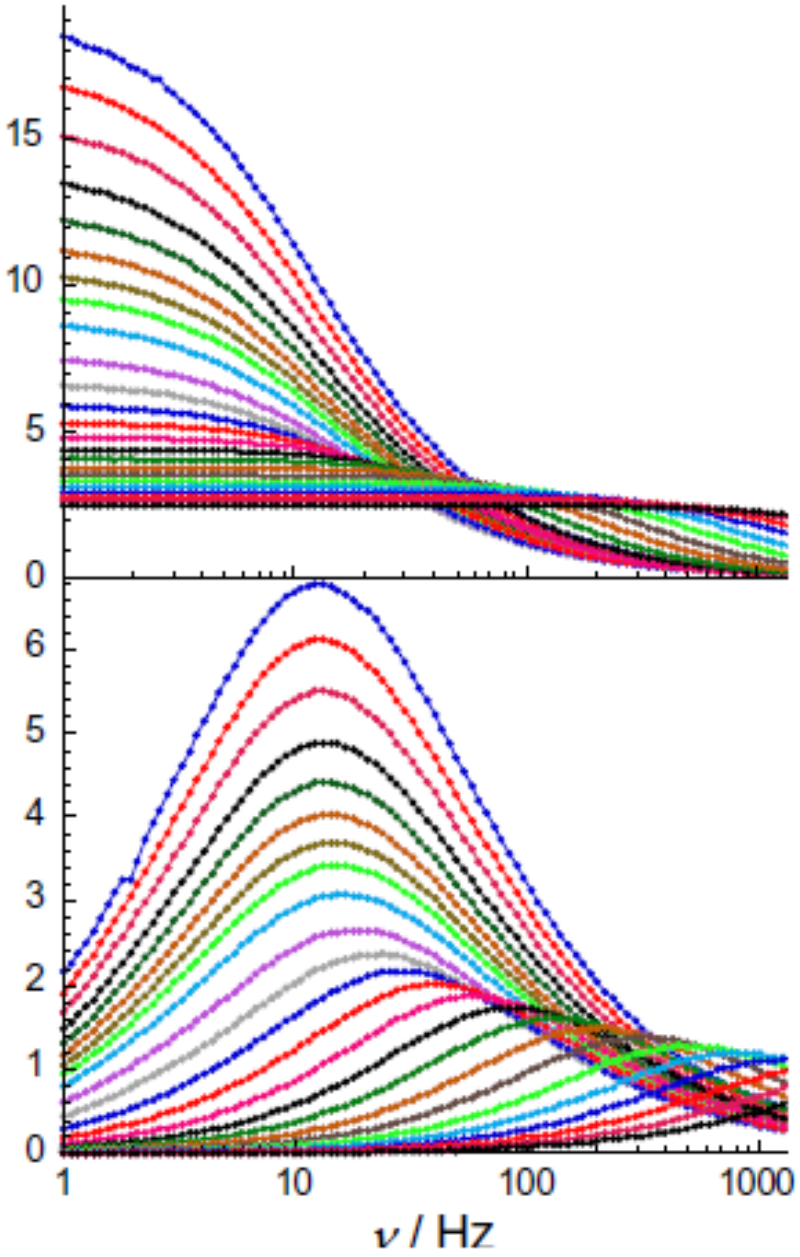


**Figure 3.36** In-phase ($\chi'$)and Out-of-phase ($\chi''$) susceptibility versus frequency ($\nu$) from 1.8 to 5.2 K with an interval of 0.2 K and from 5.5 to 13 K with an interval of 0.5 K under zero dc field for complex **3-9**.

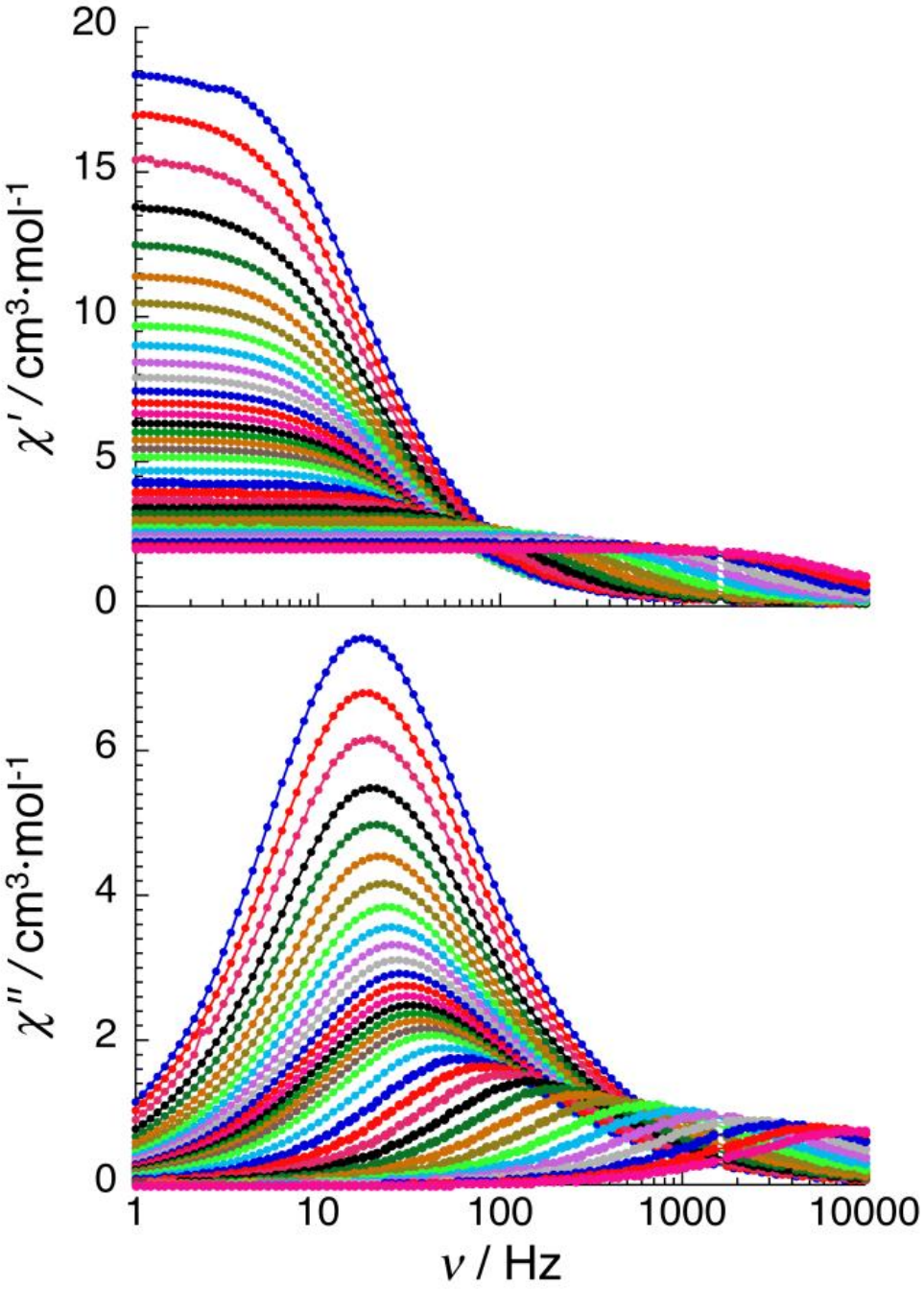


**Figure 3.37** In-phase ($\chi'$)and Out-of-phase ($\chi''$) susceptibility versus frequency ($\nu$) from 1.8 to 5.2 K with an interval of 0.2 K and from 5.5 to 13 K with an interval of 0.5 K under zero dc field for complex **3-11**.

The magnetization relaxation time ($\tau$) is derived from the frequency-dependence measurements and is plotted as a function of *1/T* (between 1.8 and 10 K) in Figure 3.38. The dynamics of complexes **3-6**, **3-9** and **3-11** become temperature independent as expected in a pure quantum regime with a $\tau$ value of $0.3\times10^{-2}$ s for complex **3-6**, $1.2\times10^{-2}$ s for complex **3-9** below 2 K and $9.0\times10^{-3}$ for complex **3-11** below 2.5 K. The relaxation becomes thermally activated (Arrhenius-like behavior) when thermal relaxation becomes faster than quantum relaxation as the temperature increases. Based on the data above 8 K, remarkably large energy barriers are observed at 56 K (complex **3-6**) and 71 K (complex **3-9**), and the pre-exponential factors of the Arrhenius laws ($\tau_0$) are $3\times10^{-7}$ s for complex **3-6** and $7\times10^{-8}$ s for complex **3-9**. Furthermore, the measurements for complex **3-11** seem to be dominated by the thermal pathway above 11 K which allow us to determine the energy gap of the thermally activated regime at 130 K while the pre-exponential factor of the the Arrhenius law ($\tau_0$) is $8.4 \times 10^{-10}$ s. The energy gap is significantly higher than complexes **3-6** and **3-9** when the two azide groups replace the terminal nitrate groups.

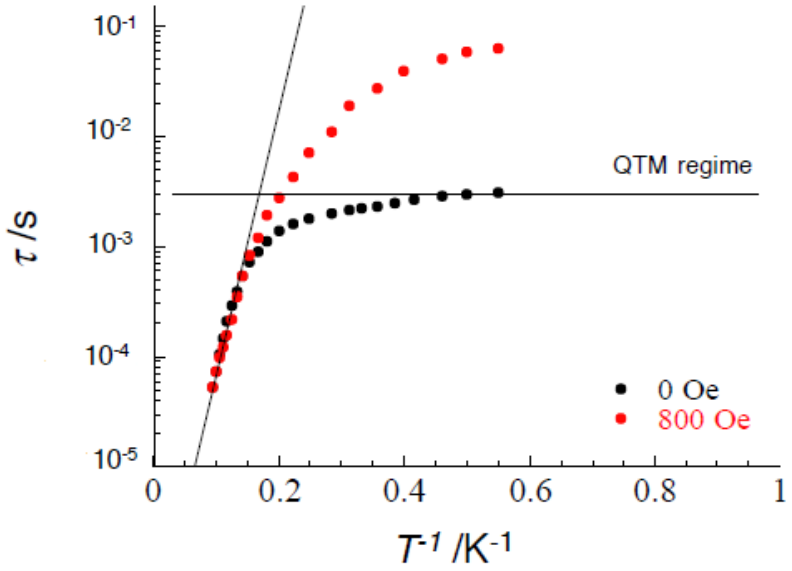


**Figure 3.38** Magnetization relaxation time ($\tau$) versus $T^{-1}$ plot for complex **3-6** under zero dc field (black) and 800 Oe (red). The solid line corresponds to the Arrhenius law

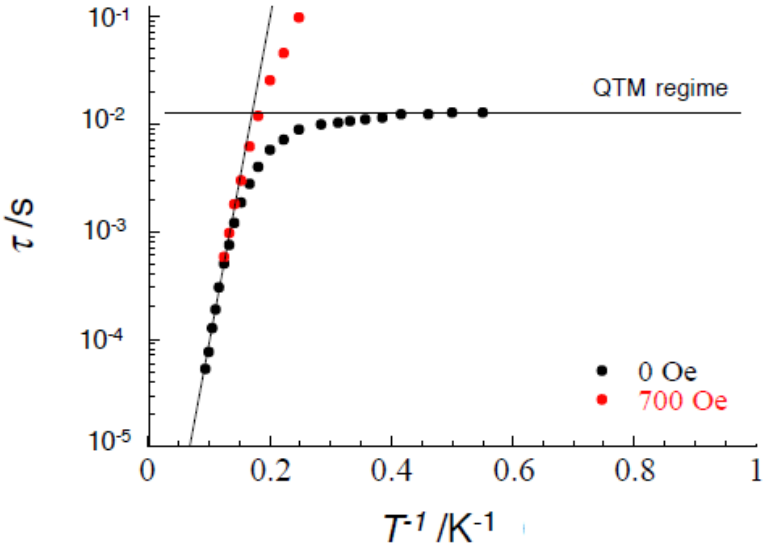


**Figure 3.39** Magnetization relaxation time ($\tau$) versus $T^{-1}$ plot for complex **3-9** under zero dc field (black) and 800 Oe (red). The solid line corresponds to the Arrhenius law

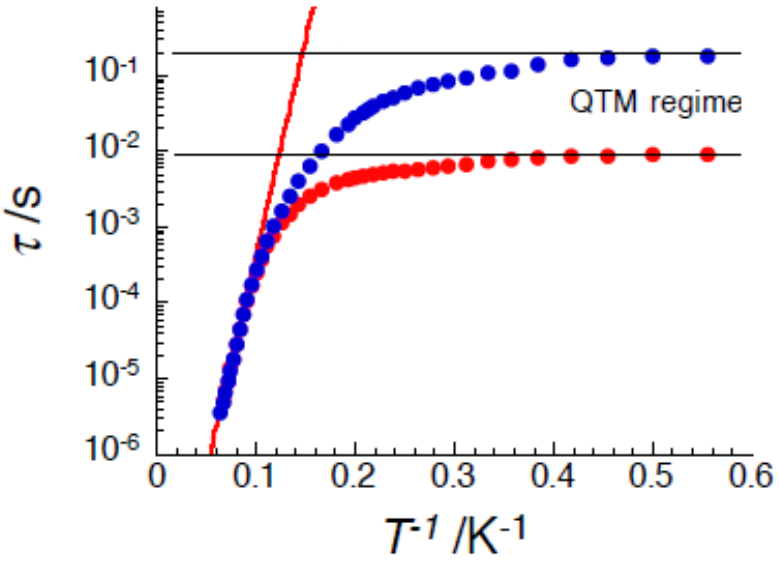


**Figure 3.40** Magnetization relaxation time ($\tau$) versus $T^{-1}$ plot for complex **3-11** under zero dc field (filled circles) and 800 Oe (empty circles). The solid line corresponds to the Arrhenius law

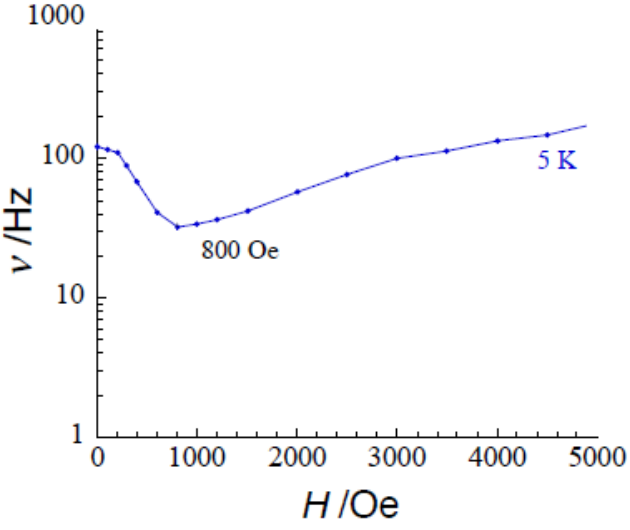


**Figure 3.41** Field dependence of the characteristic frequency as a function of the applied dc field for complex **3-6** at 5 K.

In order to minimize quantum relaxation, it was necessary to measure the ac susceptibility under an optimum dc field to shortcut the quantum tunneling. The optimum fields were chosen by a function of the applied dc field where the minimum of the characteristic frequency was observed. (Figure 3.41 (**3-6**), 3.42 (**3-9**) and 3.43 (**3-11**))

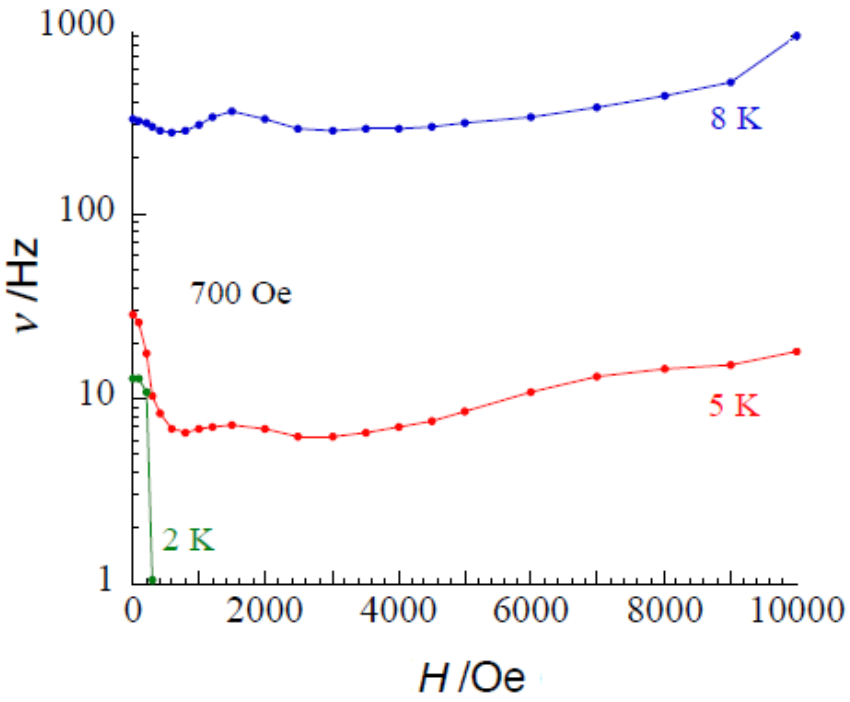


**Figure 3.42** Field dependence of the characteristic frequency as a function of the applied dc field for complex **3-9** at 2 (green), 5 (red) and 8 (blue) K.

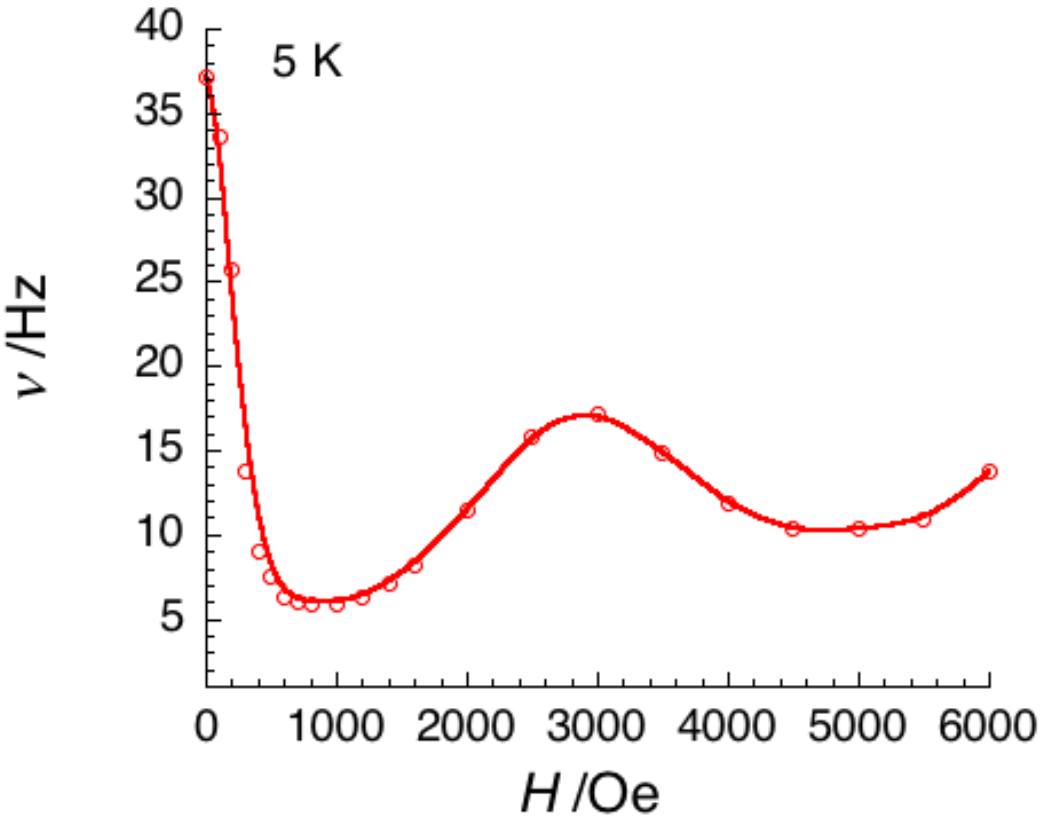


**Figure 3.43** Field dependence of the characteristic frequency as a function of the applied dc field for complex **3-11** at 5 K.

The ac susceptibility has been measured at those optimum fields (800 Oe for **3-6** and **3-11** as well as 700 Oe for **3-9**) to follow the thermally activated regime at lower temperatures (Figures 3.44, 3.45 and 3.46 for **3-6, 3-9** and **3-11**, respecitvely). The data under a small or zero dc-field are superimposable indicating a negligible effect of the quantum pathway of relaxation. This also supports the conclusion that in this

temperature region, the relaxation of the magnetization is thermally activated above 7 K for **3-6** and **3-9** and 10 K for **3-11**. The previous estimates of the energy gaps are also confirmed in this temperature region. The applied field influenced significantly the quantum relaxation process of these three complexes as the temperature decreases. For **3-11**, however, a magnetic field of 800 Oe seems to have less influence on the quantum relaxation compared to **3-6** and **3-9** since the QTM regime is still present in complex **3-11** under the optimum dc field while the quantum relaxation time was significantly increased to 0.2 s. According to the ac measurements we presented, the magnetic properties have clearly changed as the coordination environment of the metal center was modified.

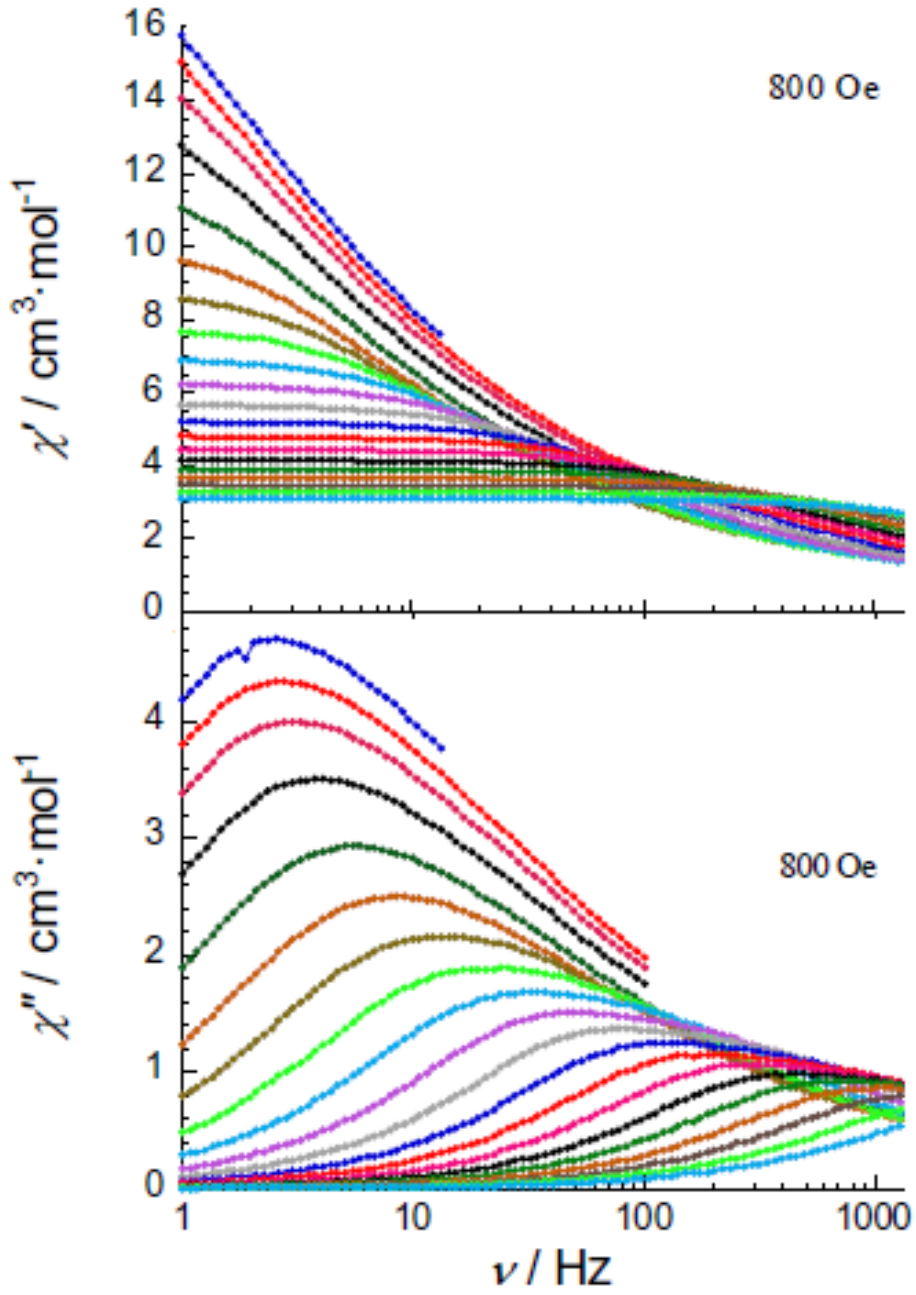


**Figure 3.44** In-phase ($\chi'$) and Out-of-phase ($\chi''$) susceptibility versus frequency ($\nu$) from 2 to 10.5 K with an interval of 0.5 K under 800 Oe for complex **3-6**.

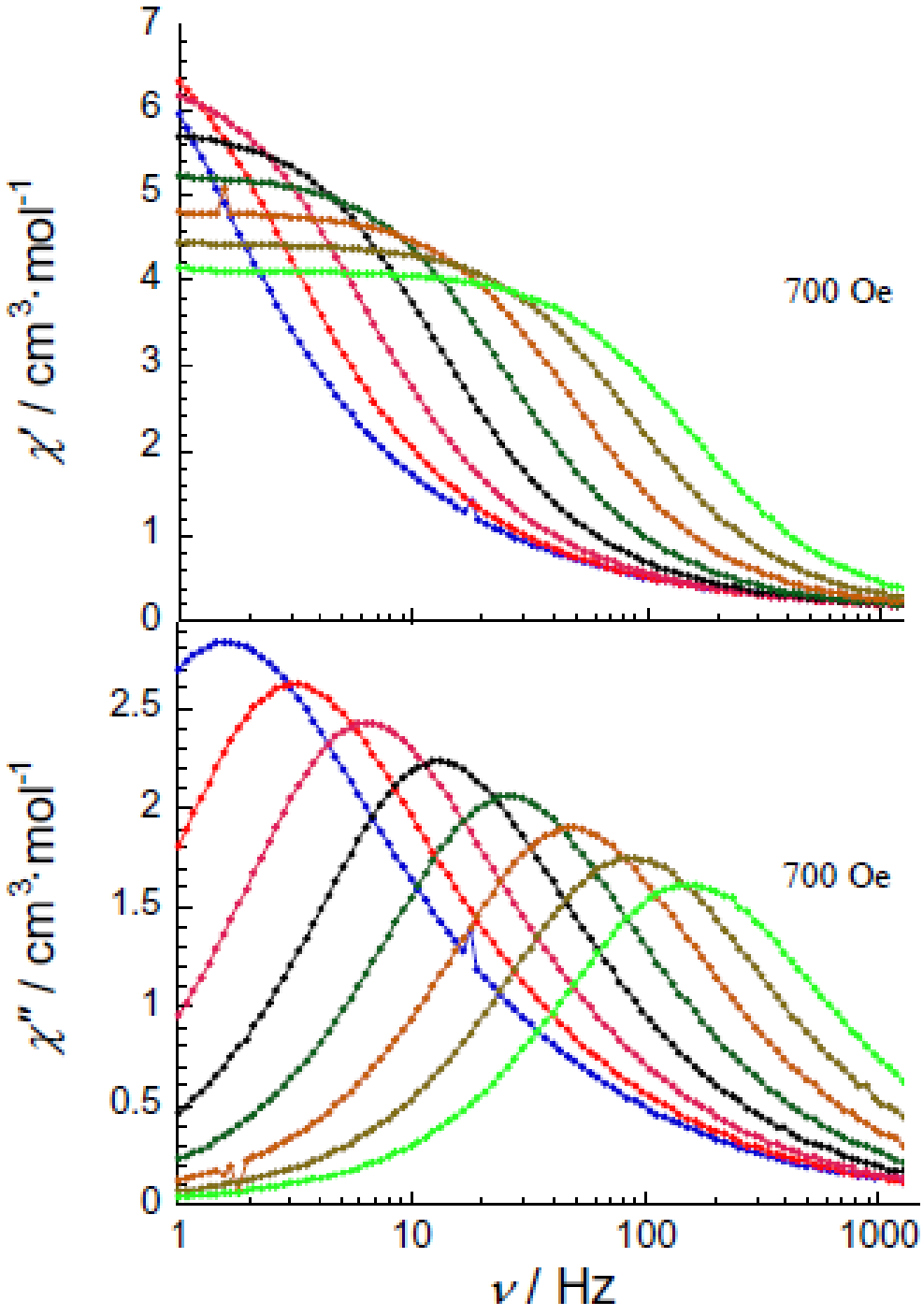


**Figure 3.45** In-phase ($\chi'$) and Out-of-phase ($\chi''$) susceptibility versus frequency ($\nu$) from 4.5 to 7.5 K with an interval of 0.5 K under 800 Oe for complex **3-9**.

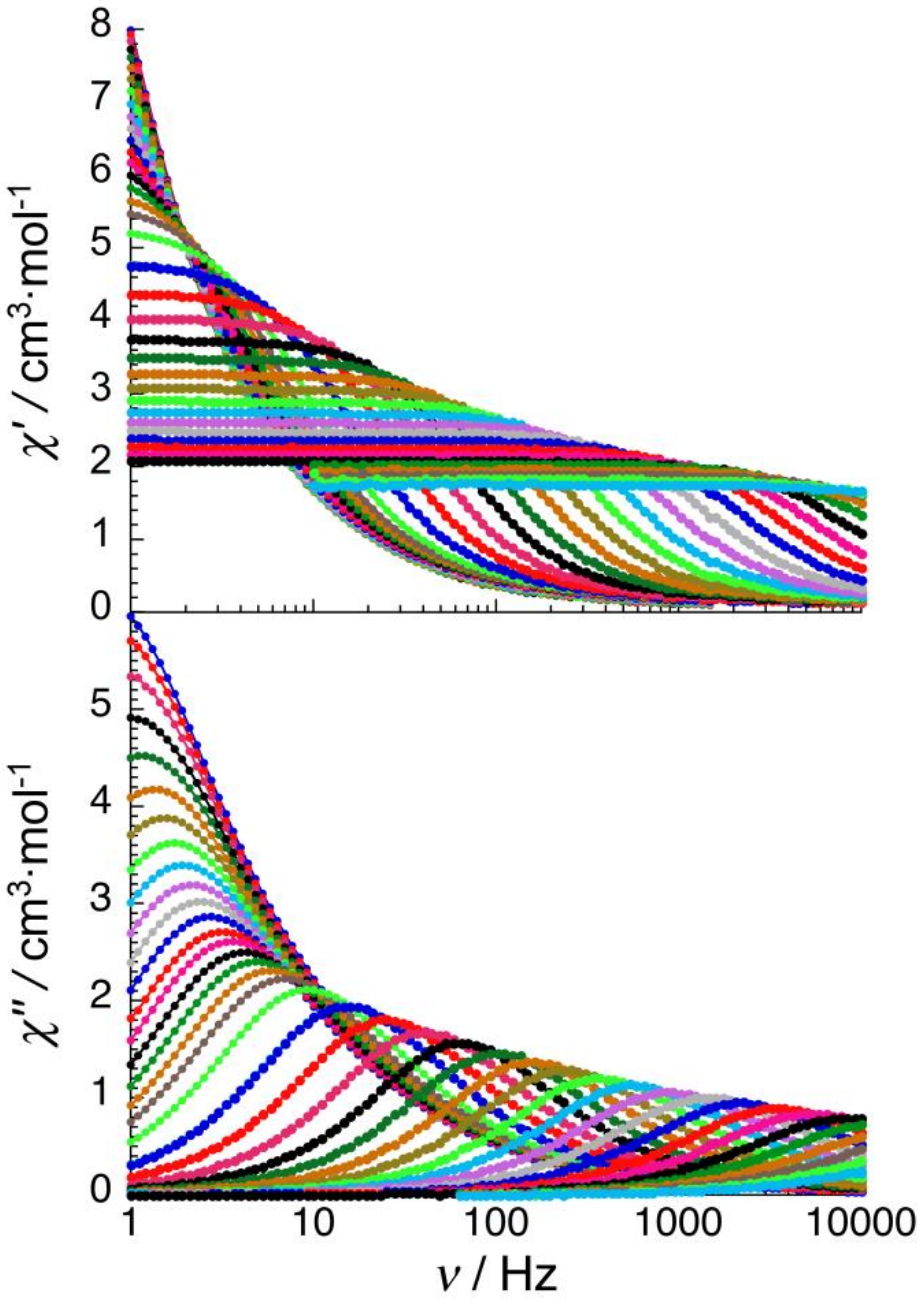


**Figure 3.46** In-phase ($\chi'$) and Out-of-phase ($\chi''$) susceptibility versus frequency ($\nu$) from 1.8 to 5.2 K with an interval of 0.2 K and from 5.5 to 15.5 K with an interval of 0.5 K under 800 Oe for complex **3-11**.

# Conclusion

In chapter 3, eleven dinuclear $Ln^{III}$ complexes were characterized, both structurally and magnetically. The dinuclear complexes were successfully synthesized with the same types of ligands by carefully tuning the reaction conditions. Two super-exchange pathways, mediated by phenoxide or $N_3^-$, are shown in these dinuclear complexes. Additionally, in complexes **3-7** to **3-11**, the dinuclear units were linked by a pyridine moiety of the coordinating ligand, $H_2$hmi, forming 2-D network systems. The dc magnetic properties of all dinuclear complexes were measured, with the exception of complex **3-3.** A series of dinuclear lanthanide analogs of $Eu^{III}$, $Gd^{III}$, $Tb^{III}$ and $Dy^{III}$ (complexes **3-4** to **3-11**) were successfully synthesized using the $H_2$hmi ligand with a similar lanthanide core structure. These complexes will be a good reference for dc magnetic properties of lanthanide analogues. The strength of the magnetic interaction between the two lanthanide ions in the dinuclear complexes was also successfully quantified with the gadolinium analogue ($J$ = 0.08 K). Even though the interaction is weak between the lanthanide ions; the slow magnetic relaxation is influenced by this

interaction.[41] Complexes **3-6, 3-9** and **3-11** present slow relaxation of the magnetization associated with SMM behavior displaying anisotropic barriers of $U_{eff}$ = 56, 71 and 130 K, respectively, which is one of the record anisotropic energy barriers for dinuclear SMMs. Complexes **3-6, 3-9** and **3-11** exhibit similar core structures, however, they display different $Dy^{III}$ geometries (square antiprism or monocapped square anti-prism for eight- or nine- coordinations, respectively) and counter ions ($NO_3^-$ or $N_3^-$). These minor changes in complex geometries and ions altered the magnetic properties, which is apparent in the presented ac measurements.

However, there are still some questions which need to be investigated. Ferromagnetic interactions were only observed between $Dy^{III}$ ions of complexes **3-6, 3-9** and **3-11**, with anti-ferromagnetic interactions being observed between $Tb^{III}$ and $Gd^{III}$ ions of the other analogues. Moreover, it can be noted when comparing the molecular structures between complexes **3-1** and **3-6**, that complex **3-1** also exhibits the same $\mu$-phenoxide bridge as complex **3-6** where the difference of Dy-O-Dy angle is only two degrees. It is worthy to consider whether this angle might exchange ferromagnetic

---

[41] Habib, F.; Lin, P.-H.; Long, J.; Korobkov, I.; Wernsdorfer, W.; Murugesu, M. *J. Am. Chem. Soc.*, **2011**, *133*, 8830.

interactions to anti-ferromagnetic interaction, as well as the question of it being associated with the SMM properties, which are only observed in complex **3-6**. It will be necessary to perform *ab-initio* calculations in the future in order to find out the correlations between molecular structure and SMM behavior.

# Chapter 4

## Trinuclear Lanthanide Complexes

Recently, trinuclear metal clusters with a triangle core which exhibit antiferromagneic interaction between the metal centers have attracted increasing interest due to spin frustration effects. Such systems can be potentially used for quantum computation. The low-energy spin states of the molecule with spin frustration can be efficiently manipulated with an external magnetic field. Since the first dysprosium triangle complex was synthesized by Powell and co-workers[42], this complex has been used for *ab initio* calculations to investigate the role of the local anisotropy of each dysprosium[43]. In order to study possible correlations between this triangular geometry and magnetic properties, new trinuclear lanthanide complexes should be investigated.

---

[42] Tang, J.; Hewitt, I.; Madhu, N. T.; Chastanet, G.; Wernsdorfer, W.; Anson, C. E.; Benelli, C.; Sessoli, R.; Powell, A. K. *Angew. Chem. Int. Ed.*, **2006**, *45*, 1729.

[43] a) Chibotaru, L. F.; Ungur, L.; Soncini, A. *Angew. Chem. Int. Ed.*, **2008**, *47*, 4126; b) Luzon, J.; Bernot, K.; Hewitt, I. J.; Anson, C. E.; Powell, A. K.; Sessoli, R. *PRL.*, **2008**, *100*, 247205.

With this in mind, we have synthesized a series of trinuclear complexes in order to investigate their magnetic properties. In this chapter, five trinuclear lanthanide complexes will be discussed in detail with regards to their structural features. All trinuclear complexes have three lanthanide metal centers arranged in triangular fashion. Metal ions in complexes **4-1**, **4-2**, **4-3** and **4-5** exhibit an eight coordinate environment while the metal center in complex **4-4** is nine coordinate with some coordination sites occupied by solvents or counter ions depending on the reaction conditions. The conformational chirality of complexes **4-1**, **4-2**, **4-3** and **4-4** is induced where two different isomers are in their respective crystal structures. SQUID measurements were carried out to investigate the dc and ac magnetic properties. Complexes **4-4** and **4-5** were found to exhibit SMM behavior. Detailed magnetic studies were conducted and are further discussed in this chapter.

## 4.1 Molecular structure and magnetism of $(N(CH_3)_4)_3[Ln_3(hmf)_6]\cdot 2CH_3OH\cdot H_2O$ (Ln: Dy(4-1), Tb(4-2))

The ligand ([(2-hydroxy-3-methoxyphenyl)methylene] formylhydrazine, $H_2hmf$) was formed *in situ* by the reaction of *o*-vanillin and formic acid hydrazine. $(N(CH_3)_4)_3[Ln_3(hmf)_6]\cdot 2CH_3OH\cdot H_2O$, (Ln: Dy(**4-1**), Tb(**4-2**)) were obtained through the

reaction of formic acid hydrazine (1 equiv.), o-vanillin (1 equiv.), tetramethylammonium hydroxide (4 equiv.) and $Dy(NO_3)_3 \cdot 6H_2O$/$Tb(NO_3)_3 \cdot 6H_2O$ (0.5 equiv.) in MeOH and $CH_2Cl_2$. The structure of complex **4-1** is shown in Figure 4.1 with selected bond distances and angles in Table 4.1. Complexes **4-1** and **4-2** are isostructural where the Dy ions are replaced with Tb ions in **4-2**.

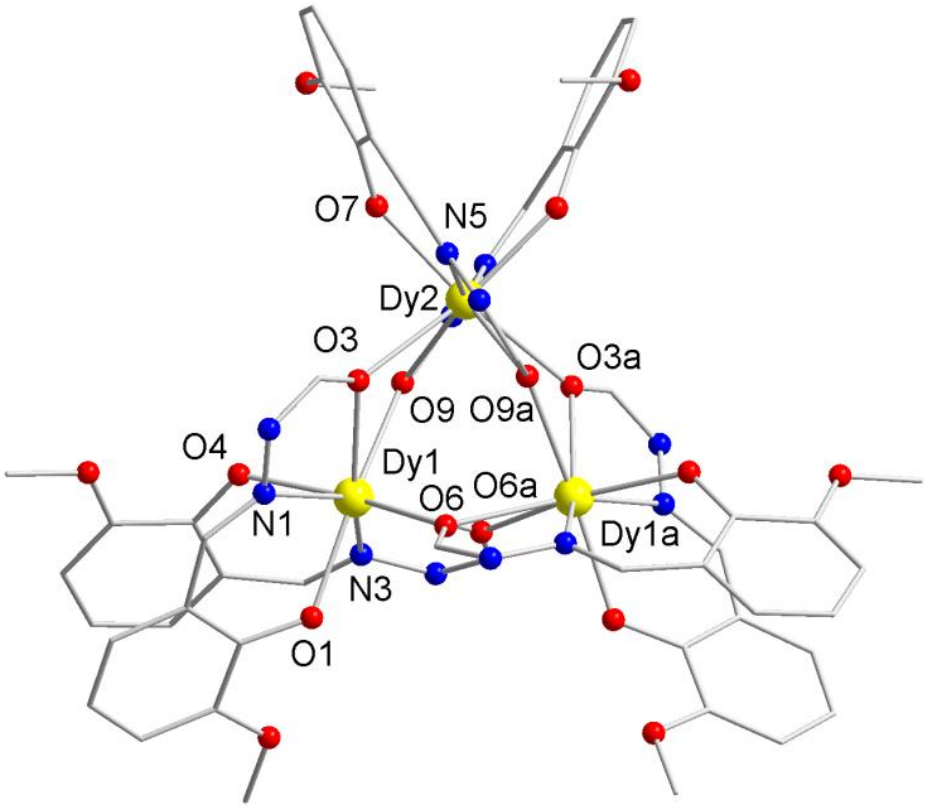


**Figure 4.1** Partially labeled molecular structure of mononuclear complex **4-1**. Yellow (Dy), Red (O), Blue (N) and Grey (C).

**Table 4.1** Selected bond distances (Å ) and angles (°) for complexes **4-1** and **4-2**.

| | | | |
|---|---|---|---|
| Dy1-O1 | 2.221(3) | Dy1-O3 | 2.386(3) |
| Dy1-O4 | 2.242(3) | Dy1-O6 | 2.386 (3) |
| Dy1-O6a | 2.434(3) | Dy1-O9 | 2.452(3) |
| Dy1-N1 | 2.478(4) | Dy1-N3 | 2.476(4) |
| Dy2-O3 | 2.488(3) | Dy2-O7 | 2.218(3) |
| Dy2-O9 | 2.374(3) | Dy2-N5 | 2.510(4) |
| Dy1---Dy1a | 3.9144(5) | Dy1---Dy2 | 3.9240(4) |
| Tb1-O1 | 2.227(7) | Tb1-O3 | 2.405(7) |
| Tb1-O4 | 2.257(7) | Tb1-O6 | 2.393(7) |
| Tb1-O6a | 2.438(7) | Tb1-O9 | 2.449(7) |
| Tb1-N1 | 2.449(7) | Tb1-N3 | 2.483(9) |
| Tb2-O3 | 2.408(7) | Tb2-O7 | 2.232(7) |
| Tb2-O9 | 2.496(7) | Tb2-N5 | 2.534(8) |
| Tb1---Tb1a | 3.9364(11) | Tb1---Tb2 | 3.9469(9) |
| Dy1-O3-Dy2 | 107.21(12) | Dy1-O9-Dy2 | 108.79(11) |
| Dy1-O6-Dy1a | 108.61(12) | Dy1-Dy1a-Dy2 | 60.079(4) |
| Dy1-Dy2-Dy1a | 59.839(9) | Tb1-O3-Tb2 | 107.3(3) |
| Tb1-O9-Tb2 | 108.7(3) | Tb1-O6-Tb1a | 109.1(3) |
| Tb1-Tb1a-Tb2 | 60.088(10) | Tb1-Tb2-Tb1a | 59.82(2) |

Complexes **4-1** and **4-2** are mainly composed of $Dy_3$ and $Tb_3$ triangles in which the coordination environment of two $Ln^{III}$ ions (Ln1 and Ln1a) is symmetric and they are linked *via* two $\mu$-alkoxide atoms (O6, O6a). A *C2* axis passes through Ln2 where the metal center forms an isosceles triangle. Each metal center is bridged with the other two $Ln^{III}$ ions by two alkoxide groups of two ligands with Ln-O-Ln. The angles of Ln2-O3-Ln1, Ln2-O6-Ln1 and Ln1-O9-Ln1a are 107.2°, 108.8° and 108.6° for **4-1** and 107.3°, 108.7° and 109.1° for **4-2**, respectively. The remaining four coordination sites of each lanthanide ion are filled by two imino nitrogens and two hydroxide molecules from two ligands. There is no $\mu_3$-O bridging the Ln atoms which is rare in Ln trinuclear complexes. Three tetramethylammonium ions are present in the structure for charge balance. Three methanol and one water molecules are present in the crystal lattice from solvent used for crystallization. Although structurally speaking the trinuclear metal center is an isosceles triangle, the bond distances and the angles can be simplified to an equilateral triangle. The distances of Ln1-Ln2 and Ln1-Ln1a are 3.92 and 3.91 Å for complex **4-1** and 3.94 and 3.95 Å for complex **4-2** and the angles of Ln1-Ln2-Ln1a and Ln2-Ln1-Ln1a are 59.7° and 60.1° for **4-1** and 59.8° and 60.1° for **4-2**, respectively. There are two stereoisomers present as a racemic mixture in both structures (Figure 4.2) where the chirality of the molecular unit is induced by the coordination of the ligands.

The Ln trinuclear complexes are well isolated along the *c* axis, and the triangular molecule is reversed from the neighboring four trinuclear units which are also enantiomers between the center and surrounded units. (Figure 4.3) The arrow shows the closet intramolecular contact between Dy1···Dy1a at 10.7 Å. The packing arrangement along the *a* axis shows the same isomers are packed in the same layer. (Figure 4.4) and the packing arrangement along the *b* axis also reveals that all trinuclear complexes are well isolated. (Figure 4.5)

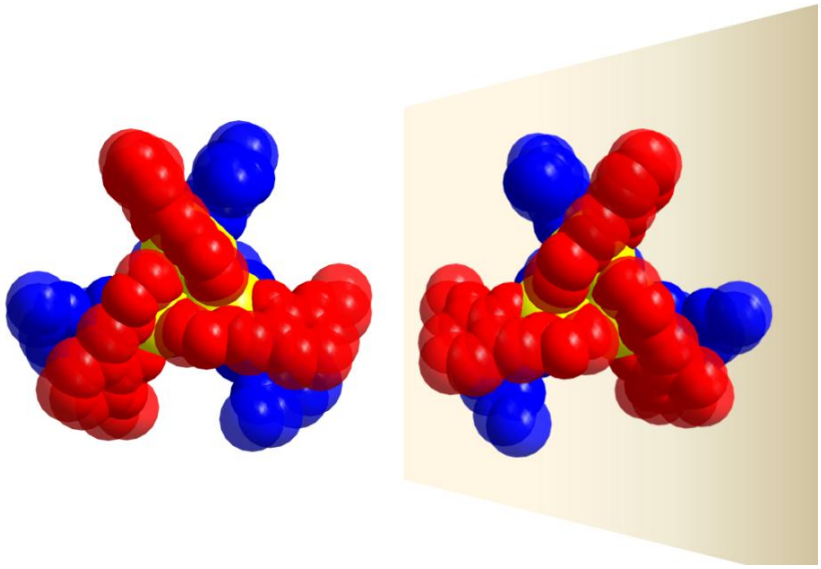

**Figure 4.2** The two enantiomers of complex **4-1**. The red ligands are out of the plane and the blue ligands are in the plane.

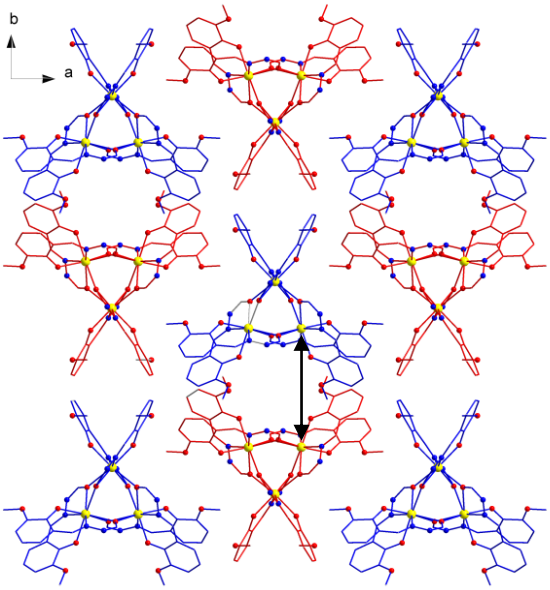


**Figure 4.3** Crystal packing diagram of complex **4-1** along the crystallographic *c* axis showing the different stereoisomers in red and blue. The arrow shows the closest intramolecular contact between Dy1···Dy1a.

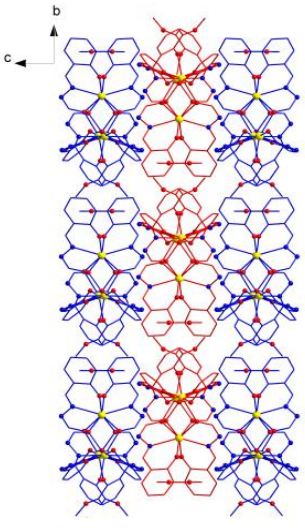


**Figure 4.4** Crystal packing diagram of complex **4-1** along the crystallographic *a* axis showing the different stereoisomers in red and blue.

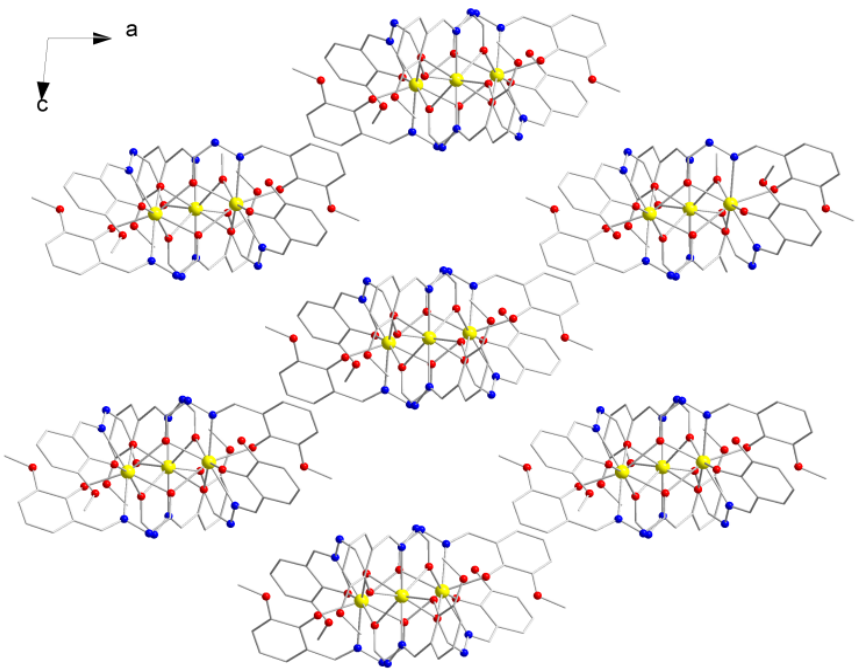


**Figure 4.5** Crystal packing diagram of complex **4-1** along the crystallographic *b* axis. Yellow (Dy), Red (O), Blue (N) and Grey (C).

The magnetic susceptibility for complexes **4-1** and **4-2** was measured in an applied dc field of 1000 Oe in the range of 1.8 K to 300 K on polycrystalline samples. The $\chi T$ *vs. T* plots are shown in Figure 4.6. At room temperature, the $\chi T$ values for **4-1** and **4-2** are 41.76 and 34.62 $cm^3.K.mol^{-1}$, respectively. They are both close to the expected value of 42.51 and 35.46 $cm^3.K.mol^{-1}$ for three uncoupled $Dy^{III}$ ions ($S$ = 5/2, $L$ = 5, $^6H_{15/2}$, $g$ = 4/3) and $Tb^{III}$ ions ($S$ = 3, $L$ = 3, $^7F_6$, $g$ = 3/2). The $\chi T$ product remains relatively constant above 40 K and decreases at lower temperatures reaching 32.59 and 19.95 $cm^3.K.mol^{-1}$

for **4-1** and **4-2** at 1.8 K, respectively. This behavior is generally indicative of weak intra-molecular antiferromagnetic coupling of the metal centers. The behavior may also be due to the thermal depopulation of the Stark sub-levels and/or the presence of large anisotropy in the system.

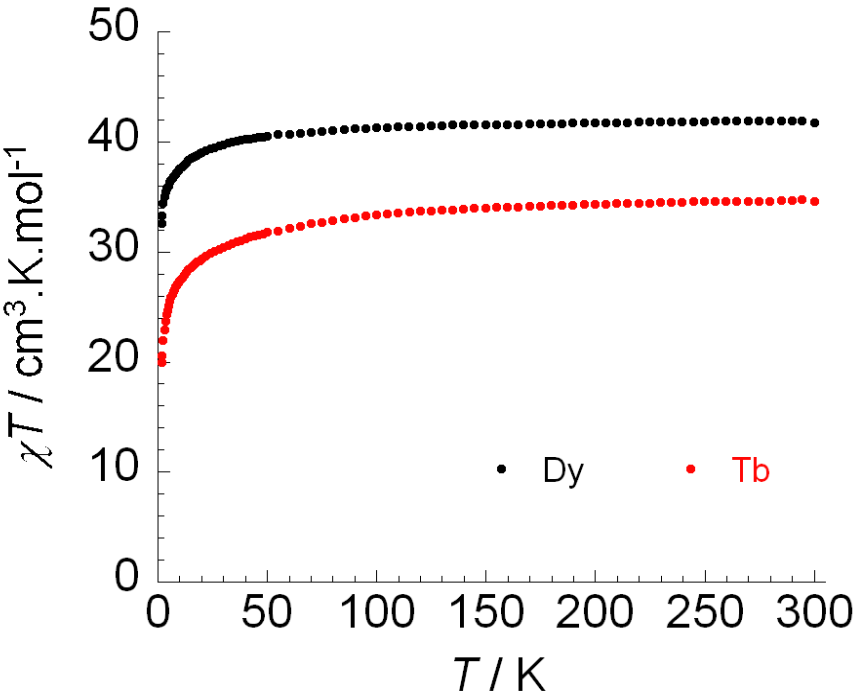


**Figure 4.6** Temperature dependence of the $\chi T$ product at 1000 Oe for complexes **4-1** (black) and **4-2** (red) (with $\chi = M/H$ normalized per mol).

Field dependence of the magnetization, *M*, measurements show non-saturation at low temperatures (1.8 K) and high magnetic fields (up to 7 T) (Figure 4.7 (complex **4-1**) and 4.9 (complex **4-2**)). Additionally, the reduced magnetization plot, *M vs. H/T*, (Figure 4.8(complex **4-1**) and 4.10 (complex **4-2**)) at different temperatures shows magnetization

curves that are not superimposable on a single master curve. These two figures are indicative of the presence of significant magnetoanisotropy or low-lying excited states in the molecule. In order to investigate the presence of slow relaxation of the magnetization which may originate from SMM behavior, ac measurements were performed on both complexes in the temperature range 1.8-10 K with zero dc field and a 3 Oe ac field at frequencies between 50 and 1500 Hz. However, both complexes did not exhibit such signals.

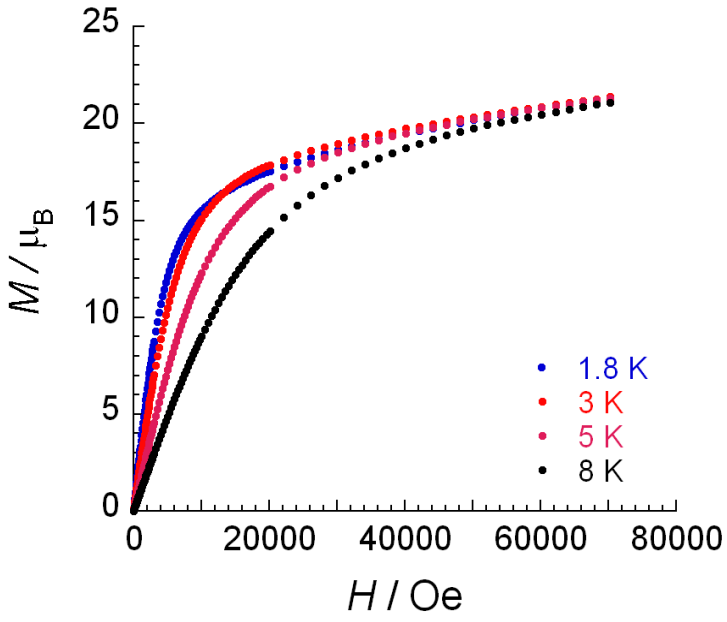


**Figure 4.7** Field dependence of the magnetization, *M*, at 1.8, 3, 5 and 8 K for complex **4-1**.

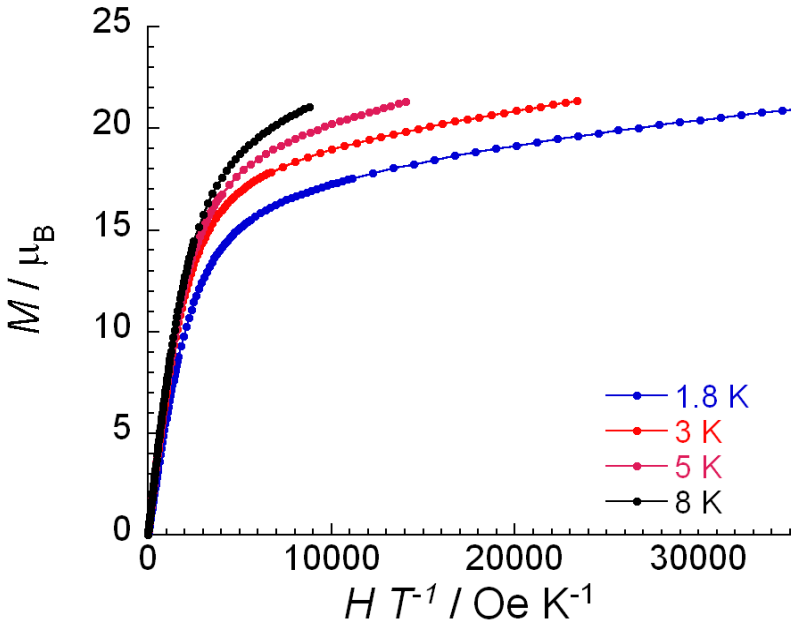


**Figure 4.8** The reduced magnetization of complex **4-1** measured at 1.8, 3, 5 and 8 K.

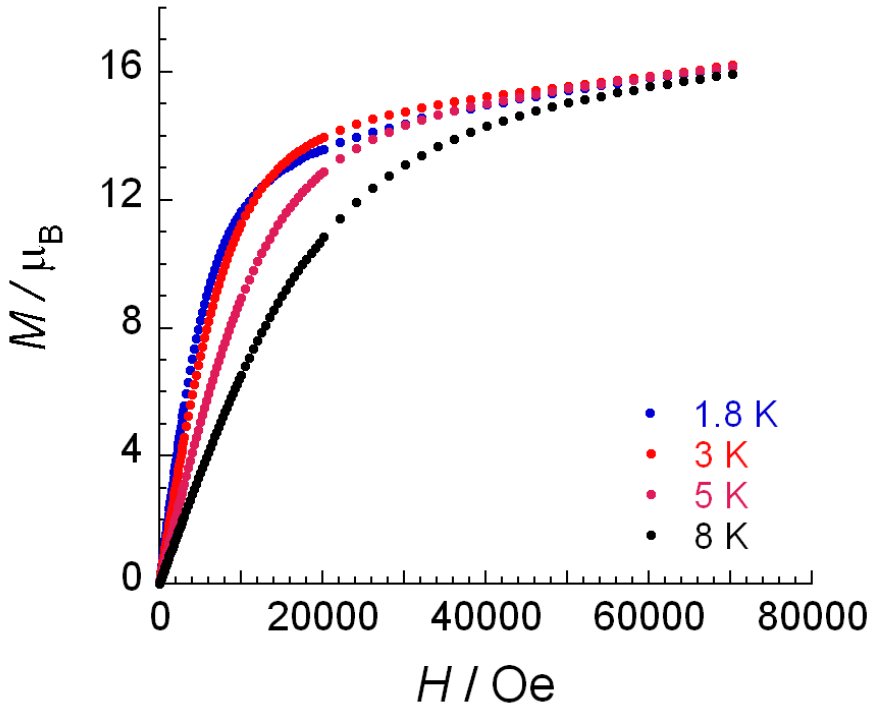


**Figure 4.9** Field dependence of the magnetization, *M*, at 1.8, 3, 5 and 8 K for complex **4-2**.

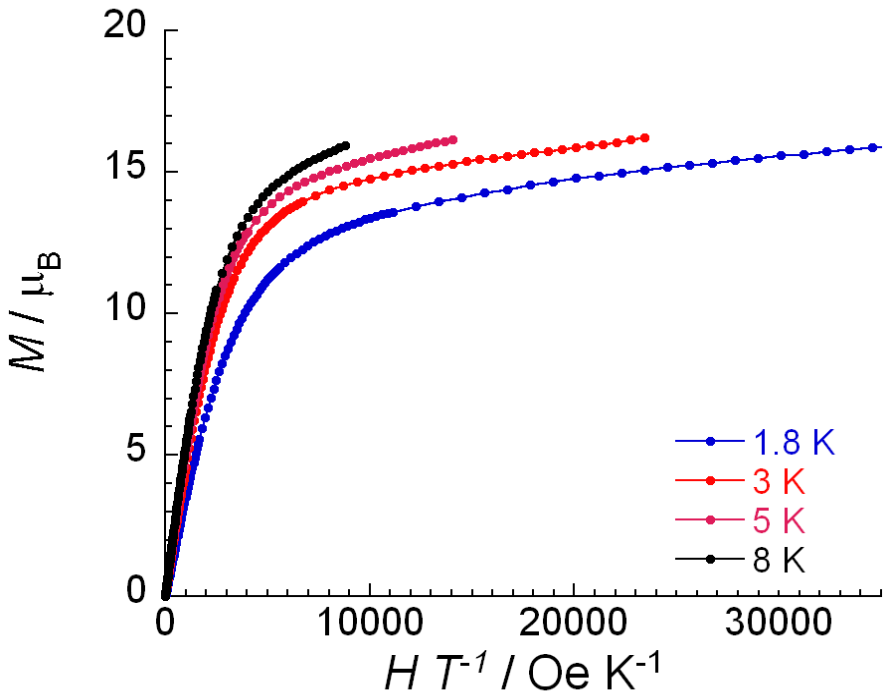


**Figure 4.10** The reduced magnetization of complex **4-2** measured at 1.8, 3, 5 and 8 K.

## 4.2 Molecular structure and magnetism of $(N(CH_3)_4)_3[Dy_3(hef)_6]\cdot 2CH_3OH\cdot H_2O$ (4-3)

Modifying different R- groups on the ligands may change the core structure of metal clusters. Comparison of this minor change will help to understand the relationship between the structure and magnetic behavior.[44] Here we synthesized a new ligand ([(2-hydroxy-3-ethoxyphenyl)methylene] formylhydrazine, $H_2$hef) which is similar to the

[44] Inglis, R.; Taylor, S. M.; Jones, L. F.; Papaefstathiou, G. S.; Perlepes, S. P.; Datta, S.; Hill, S.; Wernsdorfer, W.; Brechin, E. K. *Dalton Trans.*, **2009**, 9157.

ligand used for complex **4-2** but a methyl group has been changed by an ethyl group. The structure of complex **4-3** is shown in Figure 4.11 with selected bond distances (Å) and angles (°) in Table 4.2.

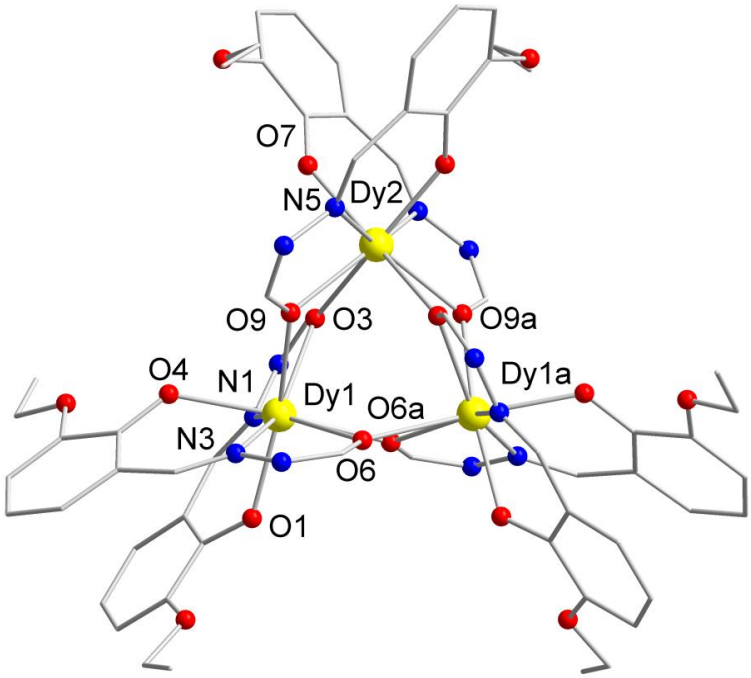


**Figure 4.11** Partially labeled molecular structure of mononuclear complex **4-3**. Yellow (Dy), Red (O), Blue (N) and Grey (C).

**Table 4.2** Selected bond distances (Å) and angles (°) for complex **4-3**.

| | | | |
|---|---|---|---|
| Dy1-O1 | 2.214(7) | Dy1-O3 | 2.404(7) |
| Dy1-O4 | 2.242(7) | Dy1-O6 | 2.407(7) |
| Dy1-O6a | 2.444(7) | Dy1-O9 | 2.434(7) |
| Dy1-N1 | 2.490(8) | Dy1-N3 | 2.495(9) |

| | | | |
|---|---|---|---|
| Dy2-O3 | 2.490(7) | Dy2-O7 | 2.222(7) |
| Dy2-O9 | 2.383(7) | Dy2-N5 | 2.504(9) |
| Dy1-Dy1a | 3.9691(12) | Dy1-Dy2 | 3.9424(10) |
| Dy1-O3-Dy2 | 107.3(3) | Dy1-O9-Dy2 | 109.8(3) |
| Dy1-O6-Dy1a | 109.8(3) | Dy1-Dy1a-Dy2 | 59.776(11) |
| Dy1-Dy2-Dy1a | 60.45(2) | | |

The core structure of complex **4-3** is similar to that of complexes **4-1** and **4-2**. The distances of Dy1-Dy2 and Dy1-Dy1a are 3.97 and 3.94 Å respectively for **4-3**. The angles of Dy2-O3-Dy1, Dy2-O6-Dy1 and Dy1-O9-Dy1a are 107.3°, 109.8° and 109.8°, respectively, for **4-3**. The Dy trinuclear cores are arranged in isosceles triangles in which Dy1-Dy2-Dy1a and Dy2-Dy1-Dy1a angles are 60.5° and 59.8°, respectively, for **4-3**. There are two stereoisomers also present as a racemic mixture in the same crystal. (Figure 4.12) The core structure is similar to complex **4-1** as well as the packing arrangement. The Dy trinuclear complexes are well isolated along *c* and *b* axes, (Figure 4.13, left and Figure 4.14) and the packing arrangement along the *a* axis also shows the same isomers are packed in the same layer similar to complex **4-1**(Figure 4.13, right).

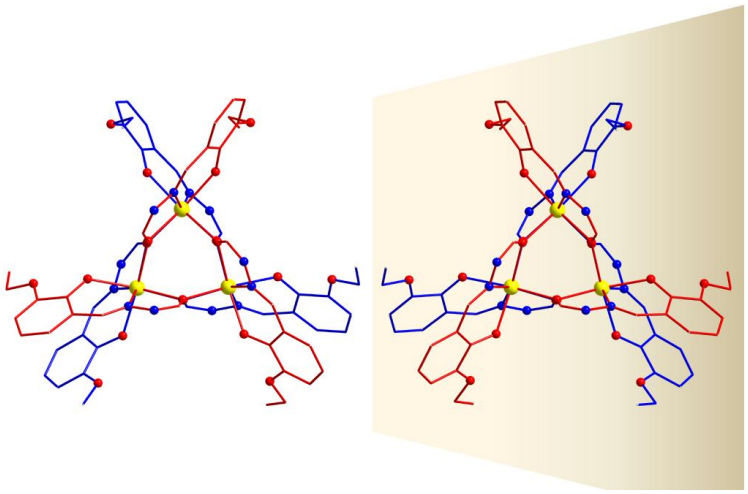

**Figure 4.12** The two enantiomers of complex **4-3**. The red ligands are out of the plane and the blue ligands are in the plane.

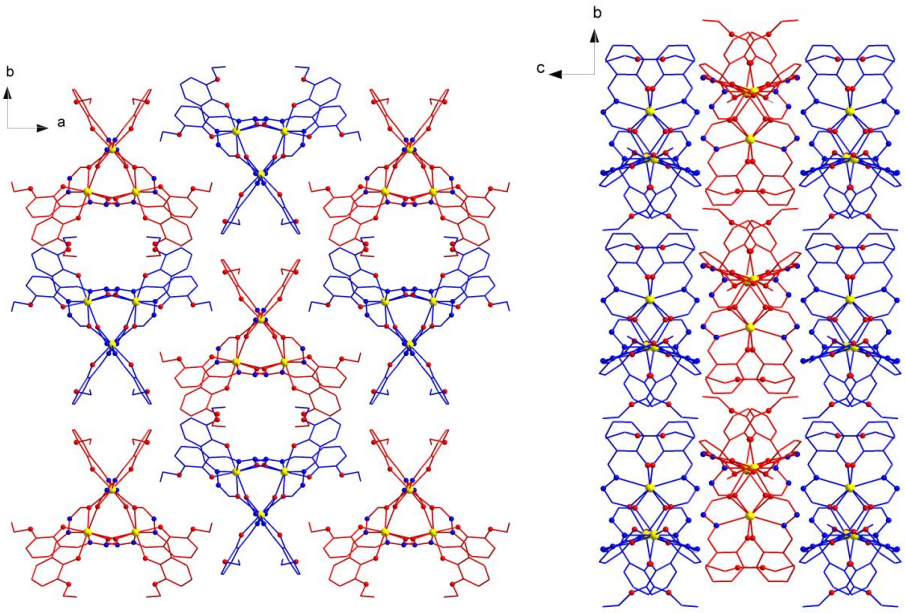


**Figure 4.13** Crystal packing diagram of complex **4-3** the along the crystallographic *a* (right) and *c* (left) axes.

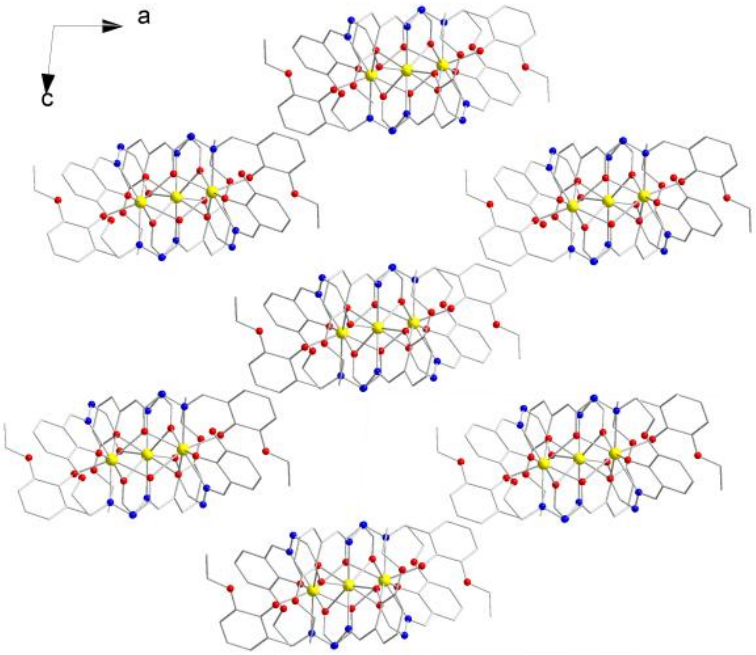


**Figure 4.14** Crystal packing diagram of complex **4-3** along the crystallographic *b* axis.

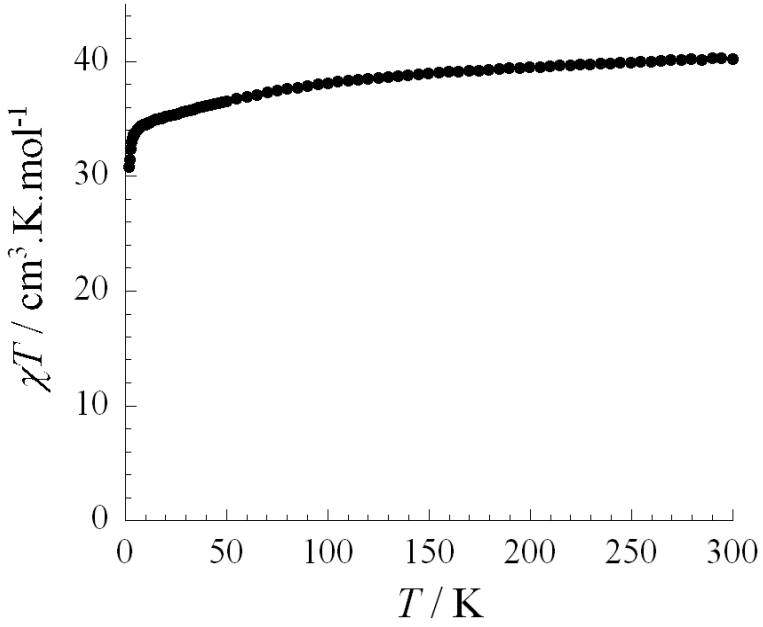


**Figure 4.15** Temperature dependence of the $\chi T$ product at 1000 Oe for complex **4-3** (with $\chi = M/H$ normalized per mol).

The magnetic susceptibility for complex **4-3** was measured in an applied dc field of 1000 Oe in the range of 1.8 K to 300 K on polycrystalline samples which were prepared in grease to prevent a physical torquing effect. The $\chi T$ *vs. T* plot is shown in Figure 4.15. At room temperature, the $\chi T$ value for **4-3** is 40.24 $cm^3.K.mol^{-1}$. It is close to the expected value of 42.51 $cm^3.K.mol^{-1}$ for three uncoupled $Dy^{III}$ ions ($S = 5/2$, $L = 5$, $^6H_{15/2}$, $g = 4/3$). The $\chi T$ product remains relatively constant above 100 K and slightly decreases at lower temperature. The $\chi T$ drops dramatically under 10 K and reaches 30.84 $cm^3.K.mol^{-1}$ for **4-3** at 1.8 K. This behavior is generally indicative of weak intra-molecular antiferromagnetic coupling of the metal centers. The behavior may also be due to the thermal depopulation of the Stark sub-levels and/or the presence of large anisotropy in the system.

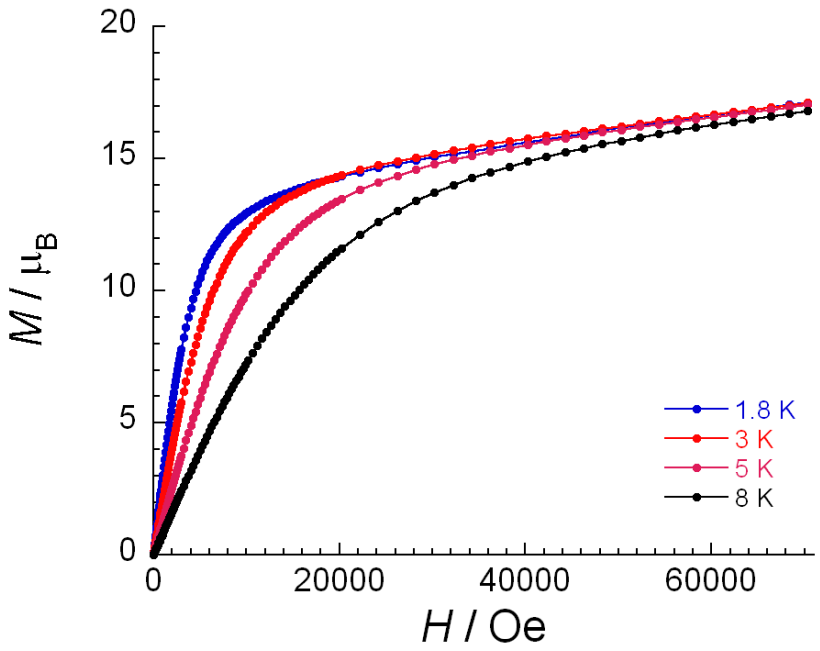


**Figure 4.16** Field dependence of the magnetization, *M*, at 1.8, 3, 5 and 8 K for complex **4-3**.

Field dependence of the magnetization, *M*, measurements shows non-saturation at low temperatures (1.8 K) and high magnetic fields (up to 7 T) (Figure 4.16). Additionally, the reduced magnetization plot, *M vs. H/T*, (Figure 4.17) at different temperatures shows magnetization curves that are not superimposable on a single master curve. These two figures are indicative of the presence of significant magnetoanisotropy or low-lying excited states in the molecule. Compared with the dc magnetic measurements of complexes **4-2** and **4-3**, there is no obvious difference which can be correlated to the similar core structures of the two complexes. Surprisingly, complex **4-3** exhibits a tail of

a peak in the out-of-phase ac magnetic susceptibility indicating potential SMM properties which will be discussed below.

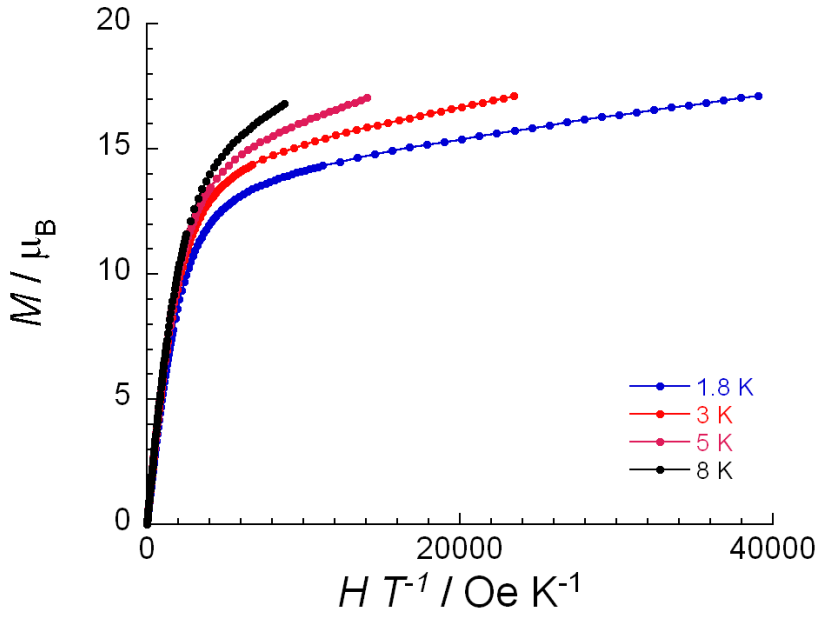


**Figure 4.17** The reduced magnetization plot for complex **4-3** measured at 1.8, 3, 5 and 8 K.

The ac measurements were performed on complex **4-3** in the temperature range of 1.8-5 K with zero dc field and a 3 Oe ac field at frequencies between 50 and 1500 Hz. (Figure 4.18). In the out-of-phase component $\chi''$ measurement, a tail of a peak is observed at very low temperature and frequencies ranging from 10- 1500 Hz. Generally, such behavior indicates slow relaxation of the magnetization which is characteristic of SMMs; however, it is difficult to quantify the energy barrier without a full peak. Moreover, when

the magnetic properties show quantum tunneling of the magnetization, the curves will also show a tail at low temperature but the complex is not considered an SMM.

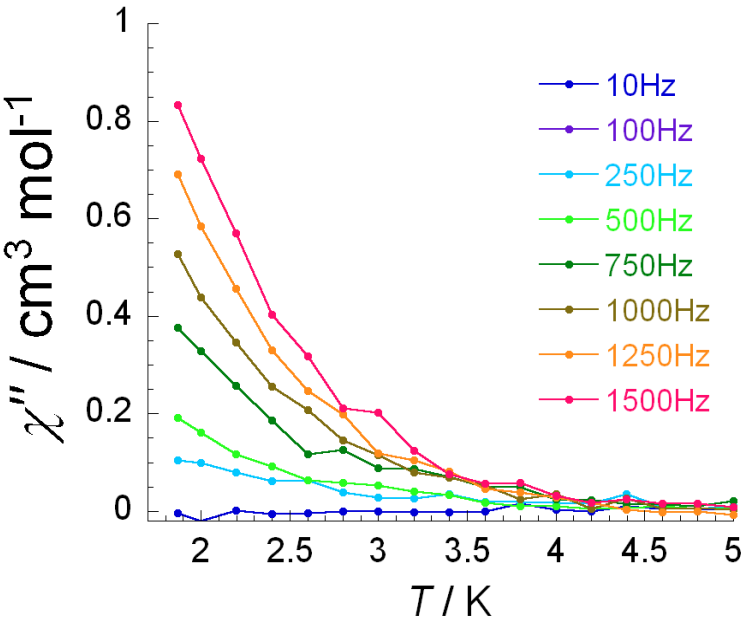


**Figure 4.18** Out-of-phase susceptibility $\chi''$ *vs.* temperature *T* in the frequency range 10 - 1500 Hz for complex **4-3**.

Low-temperature, single-crystal dc magnetization measurements of **4-3** were carried out on a micro-SQUID magnetometer between 0.04 and 5 K to confirm that the tail is due to the SMMs properties (Figure 4.19). The *M vs. H* data did not exhibit coercivity of hysteresis loops measurement even at 0.04 K with sweep rates 0.035 T/s. The few steps we observed in 0.04 K are generally due to the resonant quantum tunneling mechanism. Therefore, this molecule cannot be considered a SMM. Correlating the ac susceptibility

measurement and micro-SQUID measurement, the tail in figure 4.18 may be due to the intermolecular interaction between each molecule. Although the ethyl group instead of methyl group did not change radically of the core geometries we presumed that minute structural differences of complex **4-3** may lead to the tail in ac measurement.

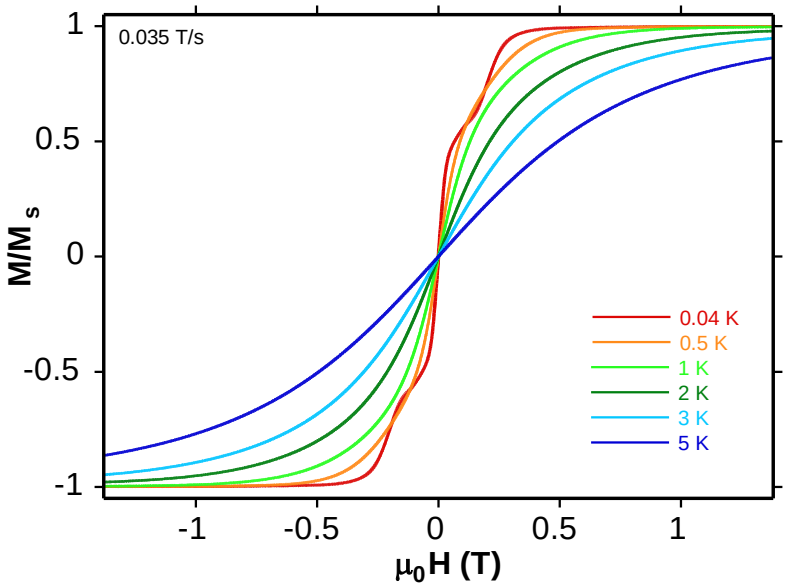


**Figure 4.19** Magnetization (*M*) *vs.* applied dc field sweeps at the indicated sweep rate and temperatures for complex **4-3**.

## 4.3 Molecular structure and magnetism of $[Dy_3(\mu_3\text{-}OMe)_2(hbb)_3(NO_3)(CH_3OH)_2]\cdot 3(NO_3)\cdot 5(CH_3OH)$ (4-4)

The ligand ([(2-hydroxy-3-methoxyphenyl)methylene] formylhydrazine, Hhbb) is formed *in situ* where two aldehyde groups both reacted with hydrazide. Two symmetrically rigid pockets were formed in the ligand.

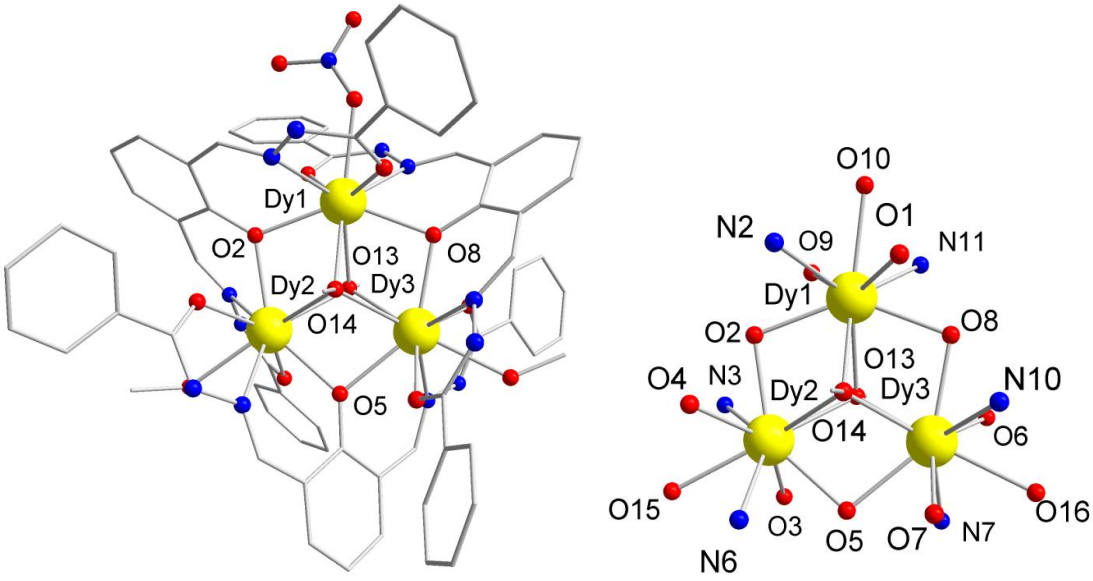


**Figure 4.20** The molecular X-ray structure (left) and the molecular core of the molecular (right) of complexes **4-4**. Yellow (Dy), Red (O), Blue (N) and Grey (C).

The $[Dy_3(\mu_3\text{-}OMe)_2(hbb)_3(NO_3)(CH_3OH)_2]\cdot 3(NO_3)\cdot 5(CH_3OH)$ (**4-4**) was obtained through the reaction of benzohydrazide (1 equiv.), 2-hydroxyisophthaldehyde (0.5 equiv.), tetraethylammonium hydroxide (1 equiv.) and $Dy(NO_3)_3\cdot 6H_2O$ (1 equiv.) in

MeOH. The structure of complex **4-4** is shown in Figure 4.20 with selected bond distances (Å ) and angles (°) in Table 4.3.

**Table 4.3** Selected bond distances (Å ) and angles (°) for complex **4-4**.

| | | | |
|---|---|---|---|
| Dy1-O1 | 2.402(6) | Dy1-O2 | 2.321(5) |
| Dy1-O8 | 2.321(6) | Dy1-O9 | 2.382(6) |
| Dy1-O10 | 2.457(7) | Dy1-O13 | 2.452(5) |
| Dy1-O14 | 2.415(5) | Dy1-N2 | 2.556(7) |
| Dy1-N11 | 2.608(7) | Dy2-O2 | 2.335(5) |
| Dy2-O3 | 2.417(6) | Dy2-O4 | 2.395(6) |
| Dy2-O13 | 2.395(5) | Dy2-O5 | 2.332(6) |
| Dy2-O15 | 2.499(19) | Dy2-O14 | 2.433(5) |
| Dy2-N6 | 2.604(7) | Dy2-N3 | 2.557(7) |
| Dy3-O6 | 2.403(6) | Dy3-O13 | 2.403(5) |
| Dy3-O7 | 2.379(6) | Dy3-O8 | 2.347(5) |
| Dy3-O5 | 2.392(6) | Dy3-O14 | 2.409(5) |
| Dy3-O16 | 2.493(6) | Dy3-N7 | 2.569(7) |
| Dy3-N10 | 2.583(7) | Dy2-Dy3 | 3.6128(8) |
| Dy1-Dy2 | 3.6168(7) | Dy1-Dy3 | 3.5925(7) |
| Dy1-O2-Dy2 | 101.9(2) | Dy1-O8-Dy3 | 100.64(19) |
| Dy2-O5-Dy3 | 99.8(2) | Dy2-O13-Dy3 | 97.71(19) |

| | | | |
|---|---|---|---|
| Dy2-O13-Dy1 | 96.52(18) | Dy3-O13-Dy1 | 95.46(18) |
| Dy3-O14-Dy1 | 96.25(18) | Dy3-O14-Dy2 | 96.50(18) |
| Dy1-O14-Dy2 | 96.48(18) | Dy3-Dy2-Dy1 | 59.593(11) |
| Dy3-Dy1-Dy2 | 60.149(14) | Dy1-Dy3-Dy2 | 60.258(14) |

Complex **4-4** is composed of $Dy_3$ triangles in which all three $Dy^{III}$ ions are nine-coordinate. The distances of Dy1-Dy2, Dy1-Dy3 and Dy2-Dy3 are 3.62 Å, 3.59 Å and 3.61 Å and the angles of Dy1-Dy2-Dy3, Dy1-Dy3-Dy2 and Dy2-Dy1-Dy3 are 59.6°, 60.3° and 60.2°, respectively. The three $Dy^{III}$ ions are bridged by the two $\mu_3$-methoxy groups (O13,O14) above and below the centroid of the plane (Dy1, Dy2, Dy3) and the distances between O (O13,O14) atoms and the centroid are both 1.23 Å. This $\mu_3$-O bridge is common for trinuclear Dy SMMs.[16a] Each $Dy^{III}$ ion is bridged by one deprotonated $\mu$-phenoxide from the ligand with the angles of 101.9°, 100.6° and 99.8° for Dy1-O2-Dy2, Dy1-O8-Dy3 and Dy2-O5-Dy3, repectively. Each pentadentate $hbb^{1-}$ ligand binds two $Dy^{III}$ ions with two different rigid pockets (O, N, and O). The remaining coordination site of each $Dy^{III}$ ion is filled by a nitrate group for Dy1 and methanol molecules for Dy2 and Dy3. The coordination environments of the three $Dy^{III}$ ions are not symmetrical where there are no C3 or C2 axes in the molecule. Three nitrate ions are found to be present in the crystal lattice for charge balance. Considering the charge for the molecule indicates

that the ligand must have only one negative charge resulting from one deprotonated phenoxide (O2, O5 and O8 on each ligand) and one double bond between C and O (O1, O3, O4, O6, O7 and O9). Five methanol molecules are also present in each molecule.

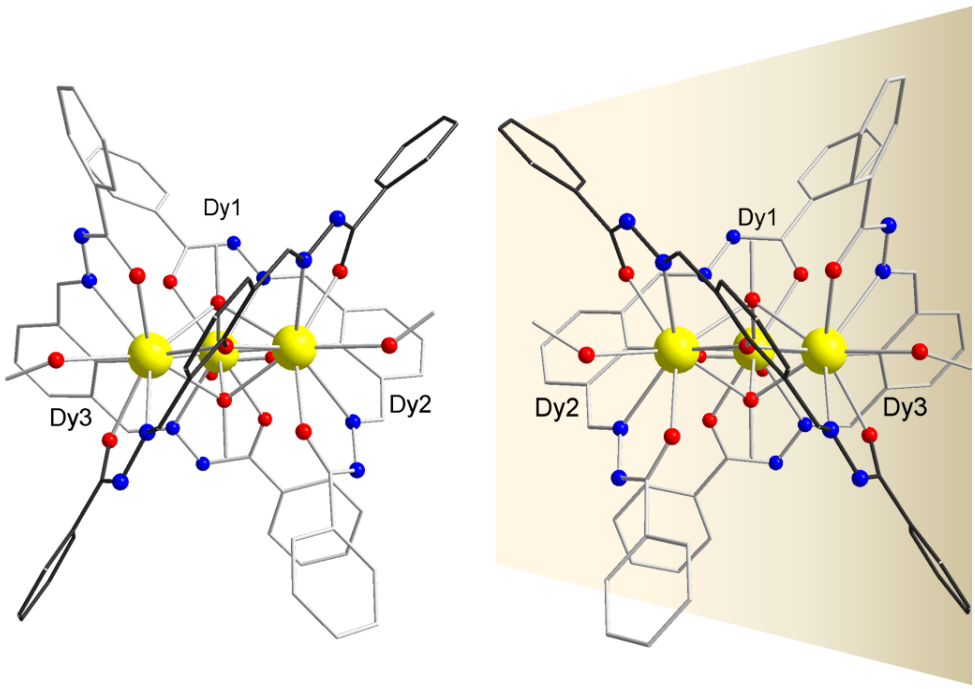


**Figure 4.21** The side views of two isomers (Δ (left) and Λ (right)) of complex **4-4**. The ligands linking Dy2 and Dy3 are in black. Yellow (Dy), Red (O), Blue (N) and Grey (C).

There are two stereoisomers present in complex **4-4**. Figure 4.21 shows the side views of the isomers where the Dy1 is in the back and the ligand bridging to Dy2 and Dy3 is presented in black which is pointed into the reverse direction. The two stereoisomers are enantiomers which are labeled by Δ and Λ (Figure 4.22) depending on the three ligands in each isomer.

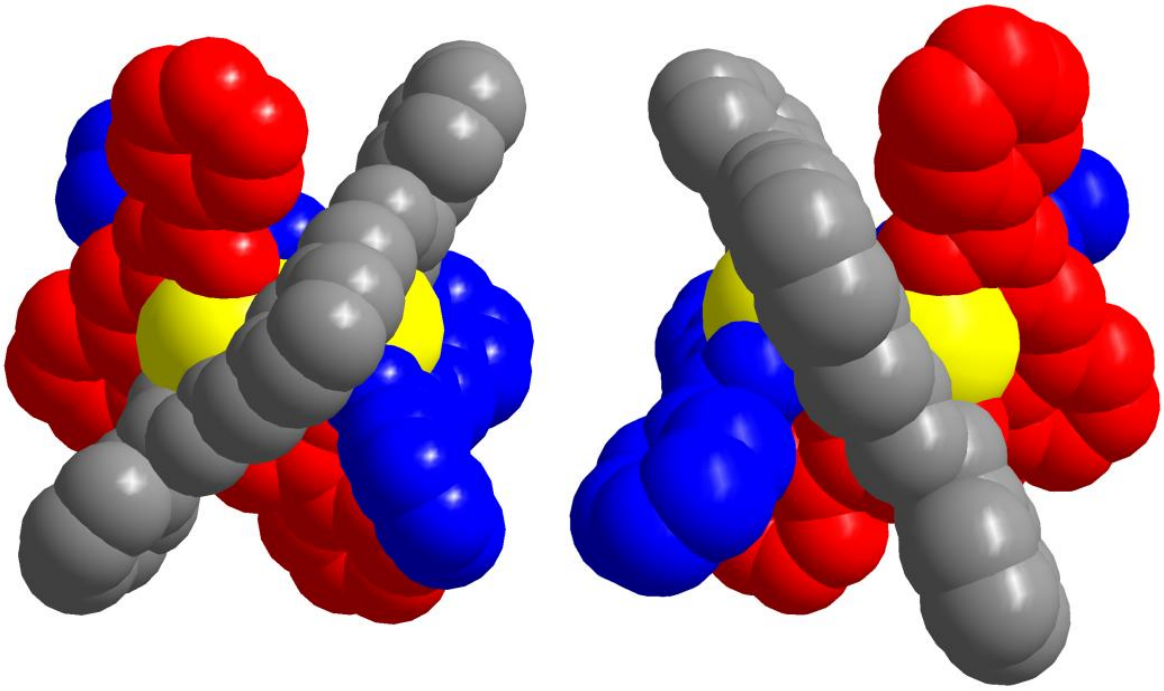

**Figure 4.22** The space-filling of two isomers (Δ (left) and Λ (right)) of complex **4-4**. Yellow (Dy), Grey, Blue and Red (ligands)

The Dy trinuclear complexes are well isolated along the *a* axis, and the same isomers are packed in the same layer (Figure 4.23). The triangle is reversed between two types of the enantiomers. The same configuration is presented along the *b* axis (Figure 4.24). It confirmed each isomer is packed on the same plane. One type of isomers is shown in the packing arrangement along the *c* axis where all the molecules are oriented in the same direction. (Figure 4.25)

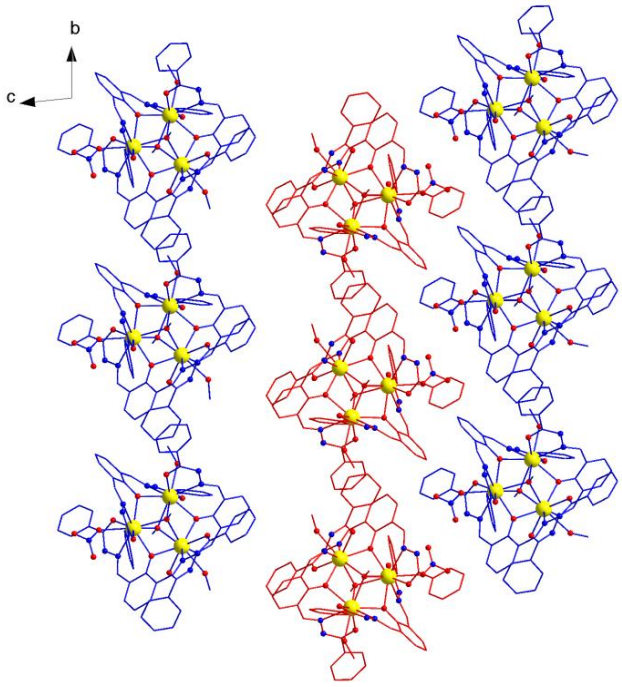


**Figure 4.23** Crystal packing diagram of complex **4-4** the along the crystallographic *a* axis showing the enantiomers Δ (blue) and Λ (red).

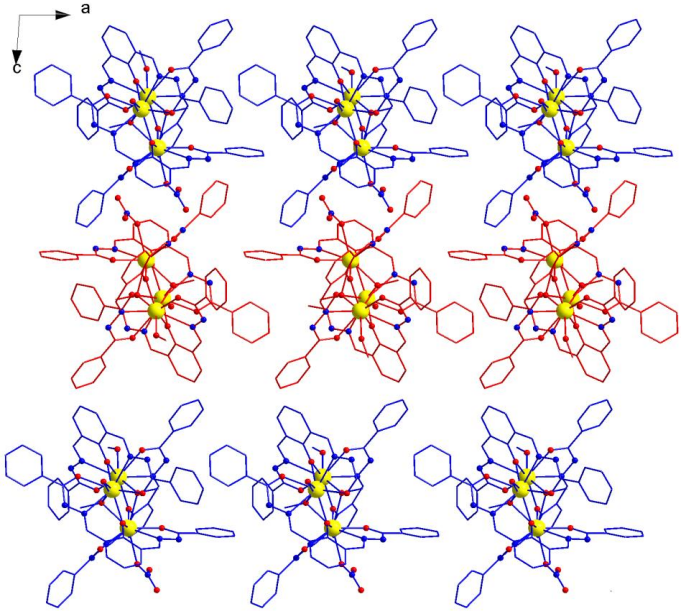


**Figure 4.24** Crystal packing diagram of complex **4-4** the along the crystallographic *b* axis showing the enantiomers Δ (blue) and Λ (red).

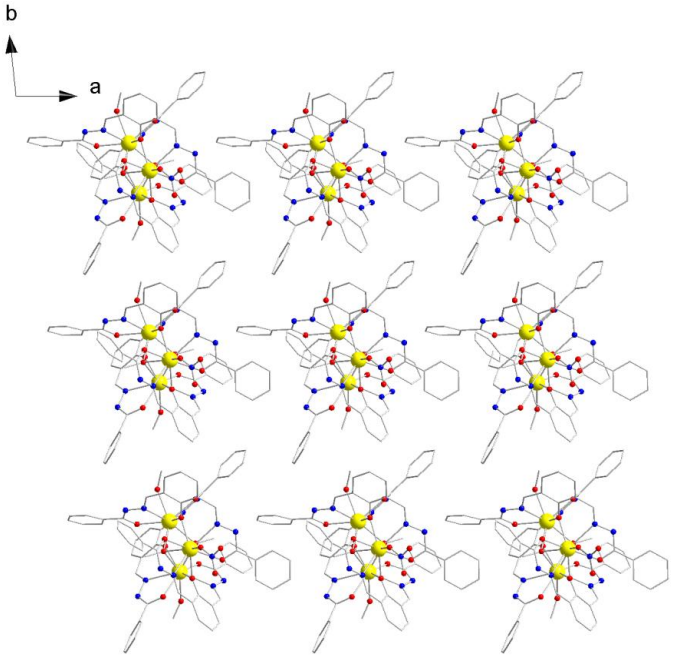


**Figure 4.25** Crystal packing diagram of complex **4-4** the along the crystallographic *c* axis.

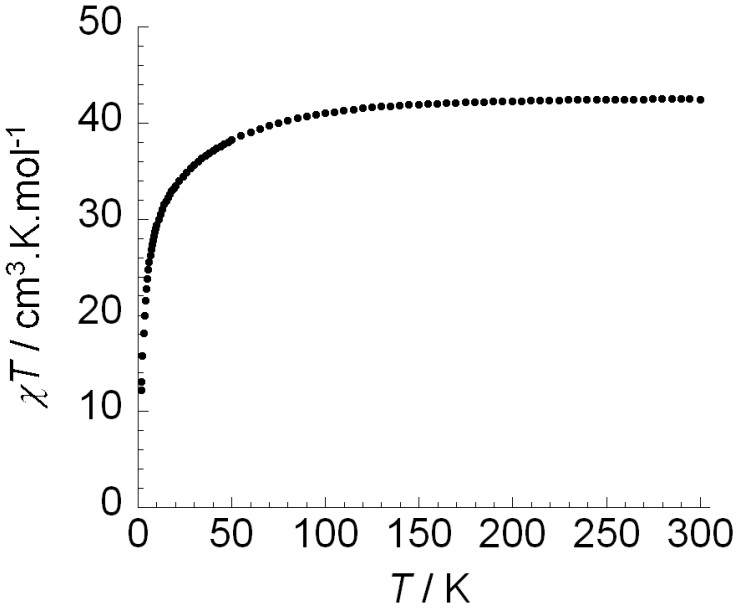


**Figure 4.26** Temperature dependence of the $\chi T$ product at 1000 Oe for complex **4-4** (with $\chi = M/H$ normalized per mol).

The magnetic susceptibility for complex **4-4** was measured in an applied dc field of 1000 Oe in the range of 1.8 K to 300 K on polycrystalline samples. The $\chi T$ *vs. T* plot is shown in Figure 4.26. At room temperature, the $\chi T$ value for **4-4** is 42.41 $cm^3.K.mol^{-1}$. It is close to the expected value of 42.51 $cm^3.K.mol^{-1}$ for three uncoupled $Dy^{III}$ ions ($S$ = 5/2, $L$ = 5, $^6H_{15/2}$, $g$ = 4/3). The $\chi T$ product remains relatively constant above 100 K and slightly decreases at lower temperature. The $\chi T$ drops dramatically under 50 K, reaching 12.19 $cm^3.K.mol^{-1}$ for **4-3** at 1.8 K. This behavior is generally indicative of weak intra-molecular antiferromagnetic coupling of the metal centers as well as the thermal depopulation of the Stark sub-levels and/or the presence of large anisotropy in the system.

Field dependence of the magnetization, *M*, exhibits similar behavior to that of complexes **4-1** and **4-3** which shows non-saturation at low temperatures (1.8 K) and high magnetic fields (up to 7 T) (Figure 4.27 (complex **4-4**)). Additionally, the reduced magnetization plot, *M vs. H/T*, (Figure 4.28 (complex **4-4**)) at different temperatures shows magnetization curves that are not superimposable on a single master curve. These two figures are indicative of the presence of significant magnetoanisotropy or low-lying excited states in the molecule.

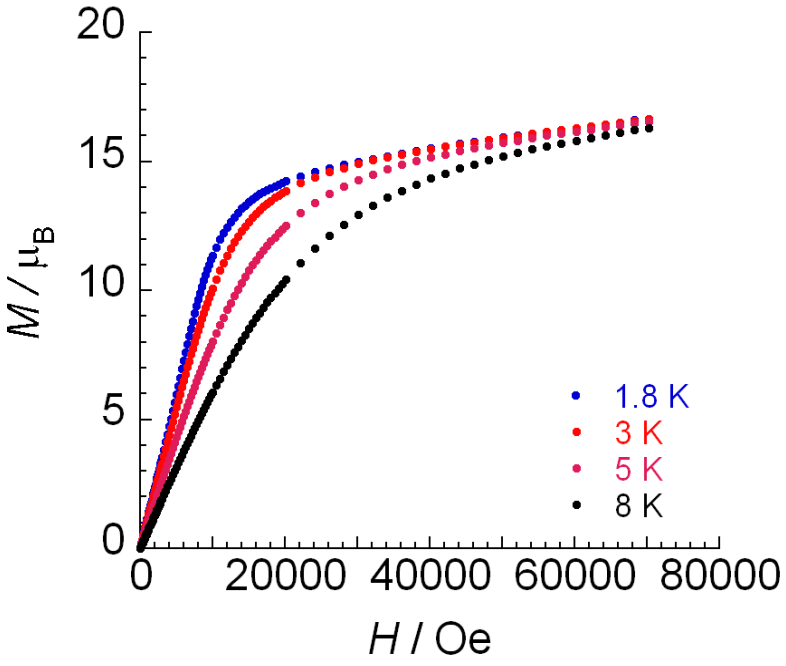


**Figure 4.27** The reduced magnetization plots for complex **4-4** measured at 1.8, 3, 5 and 8 K.

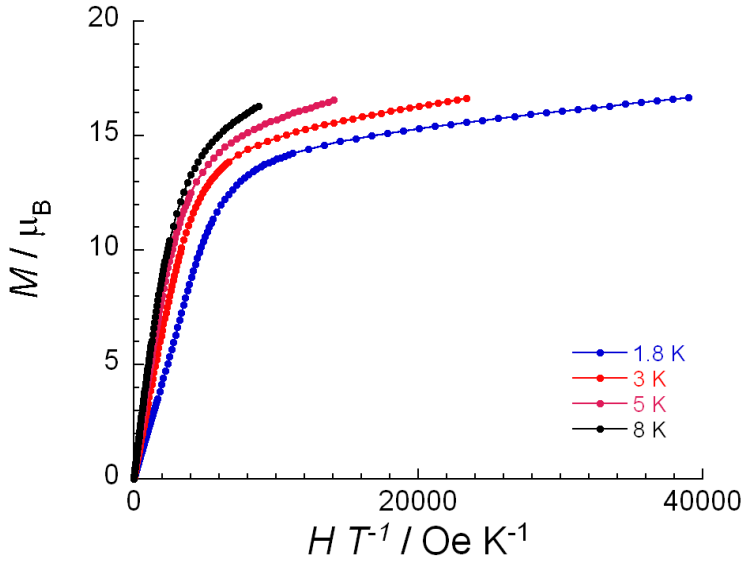


**Figure 4.28** The reduced magnetization plots for complex **4-4** measured at 1.8, 3, 5 and 8 K.

The dc susceptibility of complex **4-4** is still similar to that of complexes **4-2** and **4-3** due to the similar $Dy^{III}$ triangle core in all three complexes. However, SMMs properties are present in complex **4-4**. The ac measurements were performed on complex **4-4** in the temperature range 1.8-10 K with zero dc field and a 3 Oe ac field at frequencies between 50 and 1500 Hz (Figure 4.29 and 4.30) where an ac frequency dependent signal was observed. In the out-of-phase component $\chi''$ measurement, a tail of a peak is observed at very low temperature frequency ranging from 10- 1500 Hz; however, due to the lack of a maximum, it is difficult to quantify the energy barrier without a full peak.

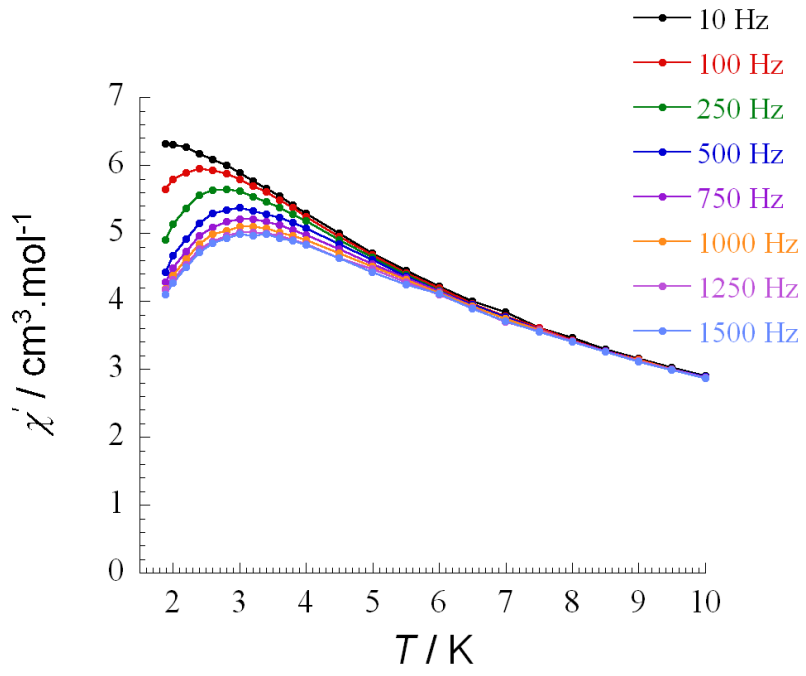


**Figure 4.29** In-phase susceptibility$\chi'$ *vs.* temperature *T* in the frequency range 10 - 1500 Hz for complex **4-4**.

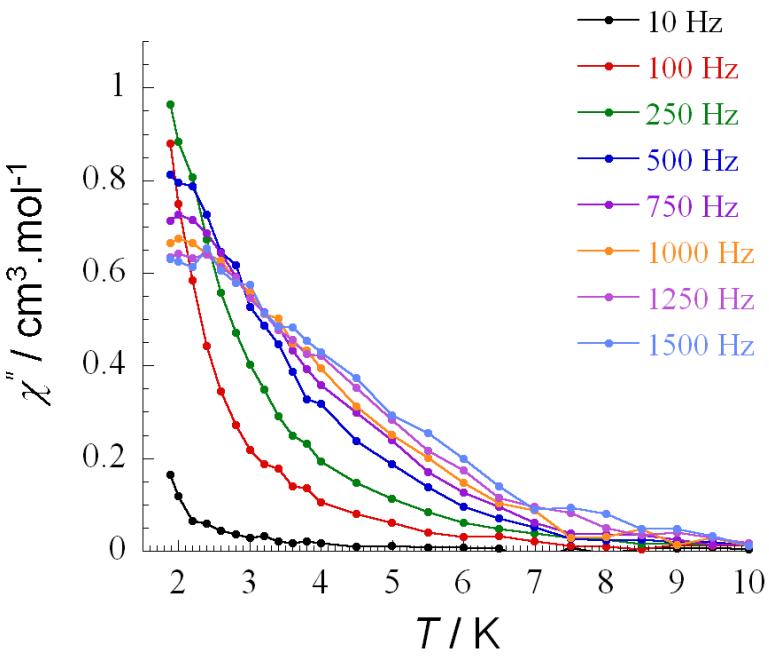


**Figure 4.30** Out-of-phase susceptibility $\chi''$ *vs*. temperature *T* in the frequency range 10 - 1500 Hz for complex **4-4**.

In order to figure out the energy barrier, we also checked the ac susceptibility as a function of frequency between 1-1500 Hz from 2-10 K (Figure 4.31 and 4.32).

Ac measurements below 3K revealed a temperature dependent signal with a clear out-of-phase ($\chi''$) peak. Such behavior is indicative of superparamagnet-like slow magnetization relaxation of a SMM. The peak values of the frequency of each temperature were obtained by Gaussian equation. From these data, the relaxation time can be deduced between 2 and 3 K.

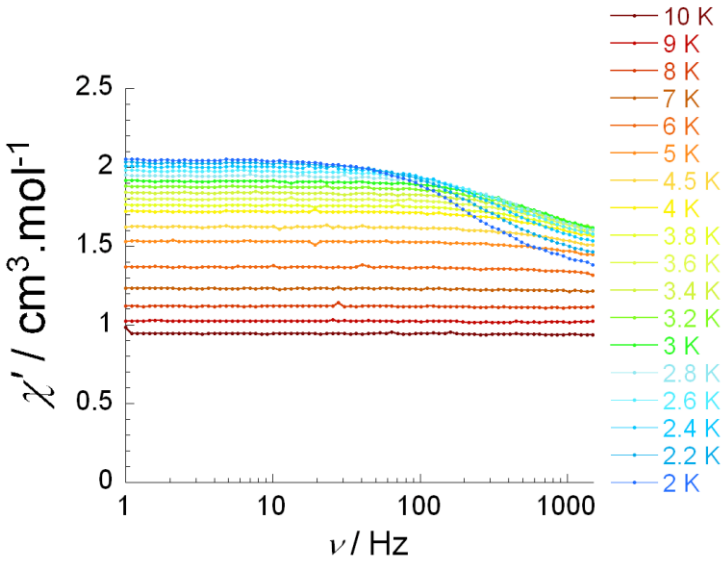


**Figure 4.31** In-phase susceptibility$\chi'$ *vs.* frequency ν in the temperature range 2-10 K for complex **4-4**.

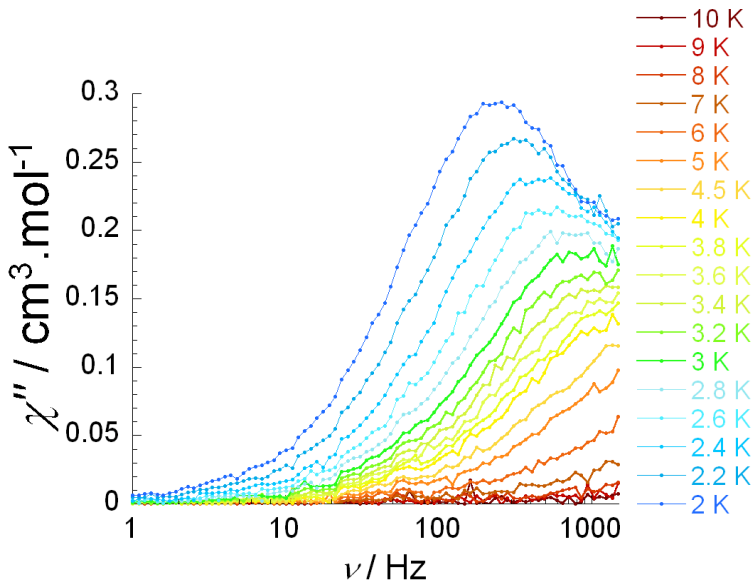


**Figure 4.32** Out-of-phase susceptibility$\chi'$ *vs.* frequency ν in the temperature range 2-10 K for complex **4-4**.

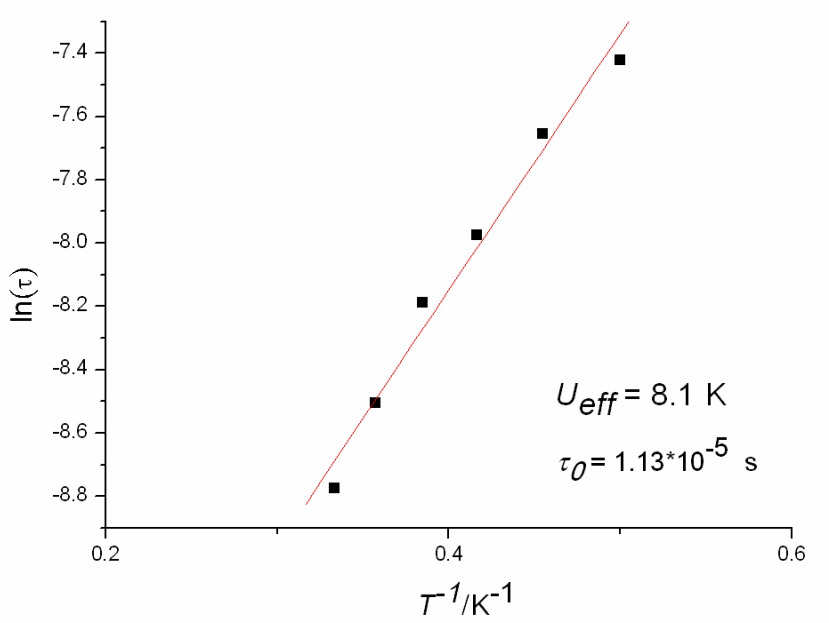


**Figure 4.33** Relaxation time of the magnetization ln($\tau$) *vs.* $T^{-1}$ (Arrhenius Plot using temperature-dependent ac data). The solid line corresponds to the fit.

The thermally activated relaxation follows Arrhenius-like behavior ($\tau = \tau_0 \exp(U_{eff}/kT)$) where the anisotropic energy barrier is calculated to be $U_{eff}$ = 8.1 K ($\tau_0$ = 1.13 × $10^{-5}$ s) (Figure 4.33). Moreover, we initially carried out ac measurements under various dc fields to determine the optimum field. The quantum tunneling of the magnetization (QTM) which is commonly observed in lanthanide systems might be reduced under an optimum dc field. The optimum fields were chosen as a function of the applied dc field where the minimum of the characteristic frequency was observed. The lowest frequency is shown in 200 Oe in complex **4-4** (Figure 4.34). However, the difference observed with and without a static field is very small which indicated no

obvious peak shifting from 0 – 600 Oe. In this case, higher energy barriers will not be obtained when the static field is applied.

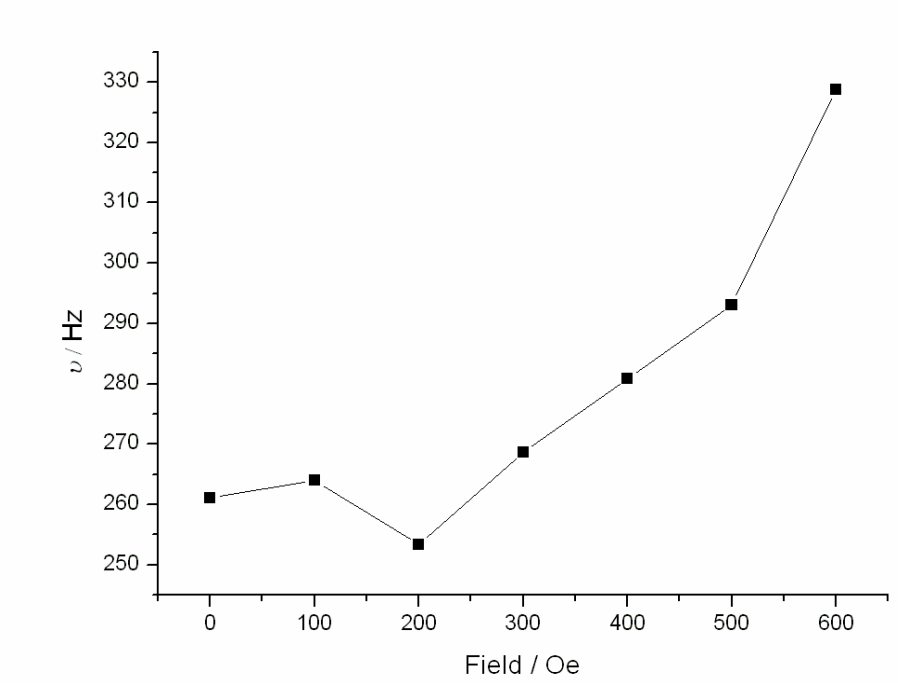


**Figure 4.34** Field dependence of the characteristic frequency (maximum of $\chi''$) as a function of the applied dc field for **4-4** at 2 K. Line is guide for the eyes.

## 4.4 Molecular structure and magnetism of $[Dy_3(\mu_3\text{-}OH)_2(\mu\text{-}OMe)(hmi)_2(MeOH)_4(H_2O)_2]\cdot Cl_2$ (4-5)

The record anisotropic energy barrier of lanthanide triangle complex is 7.15 K in the literature[34] which is similar to complex **4-4**. New triangle complexes should be synthesized for further research. $[Dy_3(\mu_3\text{-}OH)_2(\mu\text{-}OMe)(hmi)_2(MeOH)_4(H_2O)_2]\cdot Cl_2$

(complex **4-5**) was obtained through the reaction of $H_2$hmi (1 equiv.), triethylamine (2 equiv.) and $DyCl_3{\cdot}6H_2O$ (1.5 equiv.) in MeOH. $H_2$hmi ligand and similar reaction conditions have been used in dinuclear complexes (complex **3-6** and other analogue complexes), the counter ions ($DyCl_3{\cdot}6H_2O$) is key of triangle complex reaction. The structure of complex **4-5** is shown in Figure 4.35 with selected bond distances (Å) and angles (°) in Table 4.4.

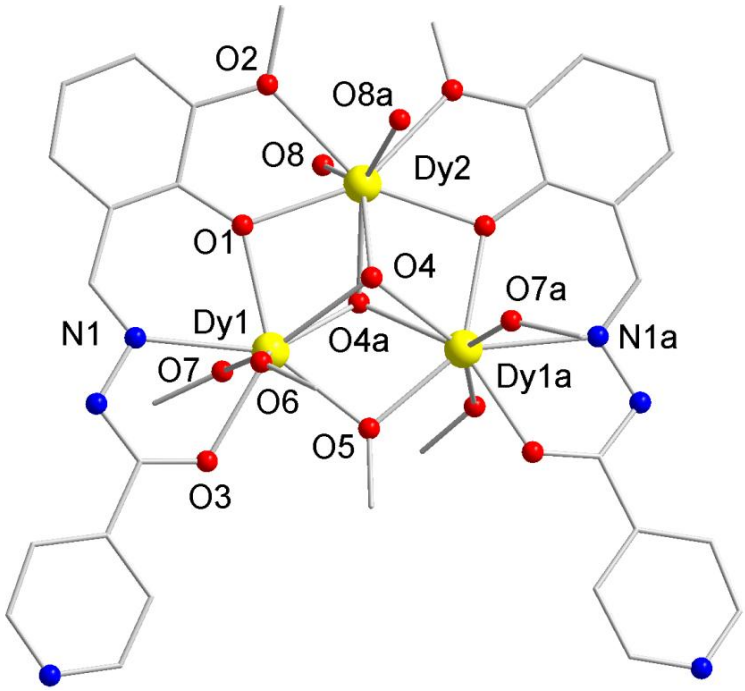


**Figure 4.35** Partially labeled molecular structure of mononuclear complex **4-5.** Yellow (Dy), Red (O), Blue (N) and Grey (C).

**Table 4.4** Selected bond distances (Å ) and angles (°) for complex **4-5**.

| | | | |
|---|---|---|---|
| Dy1-O1 | 2.350(4) | Dy1-O3 | 2.311(5) |
| Dy1-O4 | 2.427(4) | Dy1-O4a | 2.384(4) |
| Dy1-O5 | 2.274(4) | Dy1-O6 | 2.409(6) |
| Dy1-O7 | 2.391(6) | Dy1-N1 | 2.493(5) |
| Dy2-O1 | 2.355(4) | Dy2-O2 | 2.502(5) |
| Dy2-O4 | 2.305(4) | Dy2-O8 | 2.355(5) |
| Dy1---Dy1a | 3.5089(6) | Dy1---Dy2 | 3.5327(4) |
| Dy1-O1-Dy2 | 97.32(16) | Dy1-O4-Dy2 | 96.54(16) |
| Dy1-O4a-Dy2 | 97.76(14) | Dy1-O4-Dy1a | 93.66(15) |
| Dy1-O5-Dy1a | 101.0(3) | Dy1-Dy2-Dy1a | 59.555(11) |
| Dy1-Dy1a-Dy2 | 60.222(6) | | |

Complex **4-5** is mainly composed of a $Dy_3$ triangle in which the coordination environments of two of $Dy^{III}$ ions (Dy1 and Dy1a) are symmetrical. A two fold rotation axis passes through Dy2 and methoxide group (O5) in **4-5**. The central core is composed of three $Dy^{III}$ ions capped by two $\mu_3$-hydroxides (O4, O4a) above and below the $Dy_3$ triangular plane. The central core is reminiscent of aforementioned complex **4-4**. The distances of Dy1-O4, Dy1a-O4 and Dy2-O4 are 2.43, 2.38 and 2.31 Å where O4 is not at

the center of Dy triangle and the plane through Dy1, Dy1a and Dy2 is not a mirror plane. Each edge of the isosceles triangle is formed by two phenoxide bridges (Dy1-O1-Dy2 and Dy1a-O1a-Dy2) and one methoxide bridge (Dy1-O5-Dy1a) with angles of 97.3° and 96.5°, respectively. The triangle edges of Dy1-Dy2 and Dy1-Dy1a are 3.53 Å and 3.51 Å as well as the angles of Dy1-Dy2-Dy1a and Dy1-Dy1a-Dy2 are 59.6° and 60.2°, respectively. Two $hmi^{2-}$ ligands encapsulate equatorially the central core and the remaining coordination sphere is filled by two MeOH molecules for Dy1 and Dy1a and two $H_2O$ molecules for Dy2. The coordination environment of oxygen atoms of two terminal $H_2O$ molecules (O8 and O8a on Dy2) are symmetrical but the coordination environment of oxygen atoms of the two terminal MeOH molecules (O6 and O7 on Dy1 or O6a and O7a on Dy1a) are not. Overall the charges are balanced by two $Cl^-$ ions present in the crystal lattice. The charge for the molecule indicates that the ligand is in dianionic form with one deprotonated phenoxide (O1) and one deprotonated alkoxide (O3).

The packing arrangements along the *a*, *b* and *c* axes are in Figures 4.36, 4.37 and 4.38, respectively. Packing arrangements along *b* and *c* axes present are well isolated triangles. The triangles reverse in orientation at each layer along the *a* axis (Figure 4.36). The triangles in each layer are the same orientation and the planes of the triangles are also

toward the same direction along the c axis (Figure 4.38). Triangular metal complexes are of interest in regards to the field of quantum computation. Understanding the orientation of the molecules is important for the applications of quantum computation. The perfect orientation will be similar to the packing arrangement along the *c* axis with all molecules aligned in the same direction in order to avoid the cancellation of adjacent magnetic moments. Complex **4-5** only achieved the perfect orientation along the *c* axis and it will be ideal to engineer molecules by ligand and synthetic modifications in order to obtain the right packing arrangements along all axes.

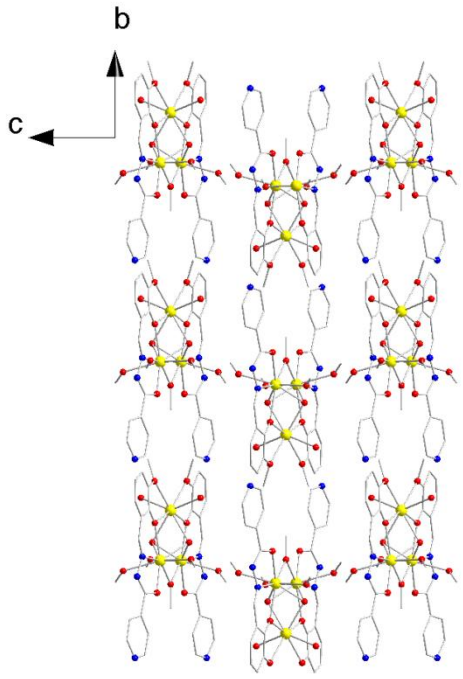


**Figure 4.36** Crystal packing diagram of complex **4-5** along the crystallographic *a* axis.

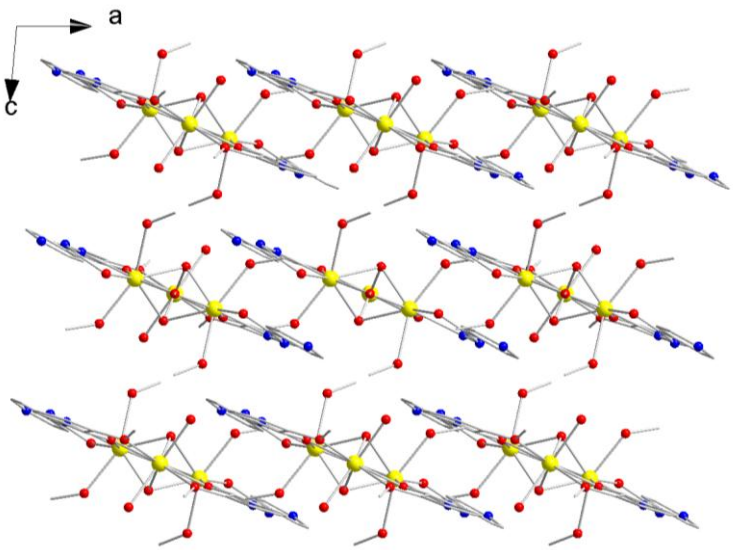


**Figure 4.37** Crystal packing diagram of complex **4-5** along the crystallographic *b* axis.

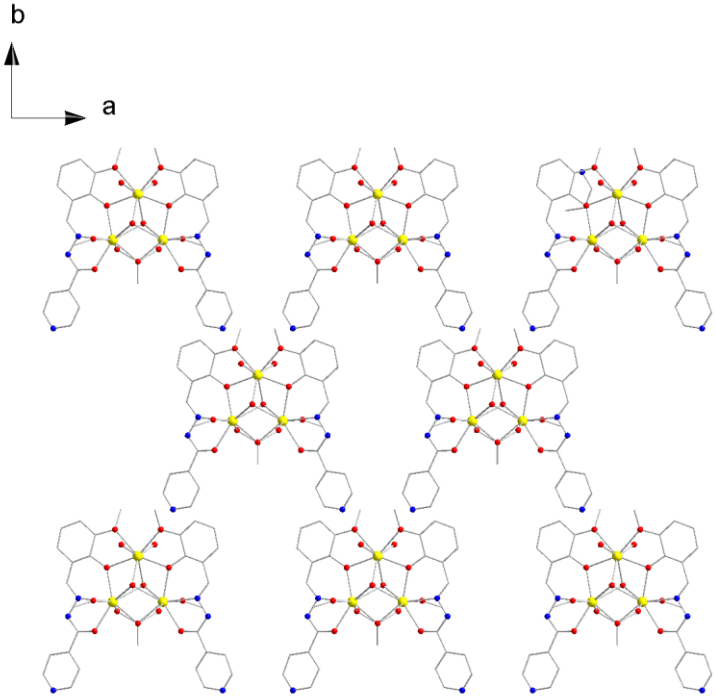


**Figure 4.38** Crystal packing diagram of complex **4-5** along the crystallographic *c* axis.

At room temperature, the $\chi T$ product of 40.2 $cm^3.K.mol^{-1}$ is in good agreement with the expected value (42.5 $cm^3.K.mol^{-1}$) for three $Dy^{III}$ metal ions ($S$ = 5/2, $L$ = 5, $^6H_{15/2}$ g =

4/3: $\chi T$ = 14.17 $cm^3.K.mol^{-1}$). When the temperature is lowered, the $\chi T$ product is roughly constant down to 150 K before exhibiting a slow decrease reaching a minimum value of 34.8 $cm^3K/mol$ at 1.8 K under 1000 Oe. The low temperature thermal decrease of the $\chi T$ product at 1000 Oe might reveal the presence of intramolecular antiferromagnetic interactions between Dy spin carriers. However, the behavior might also be due to the thermal depopulation of the Stark sub-levels and/or the presence of large anisotropy in the system. (Figure 4.39)

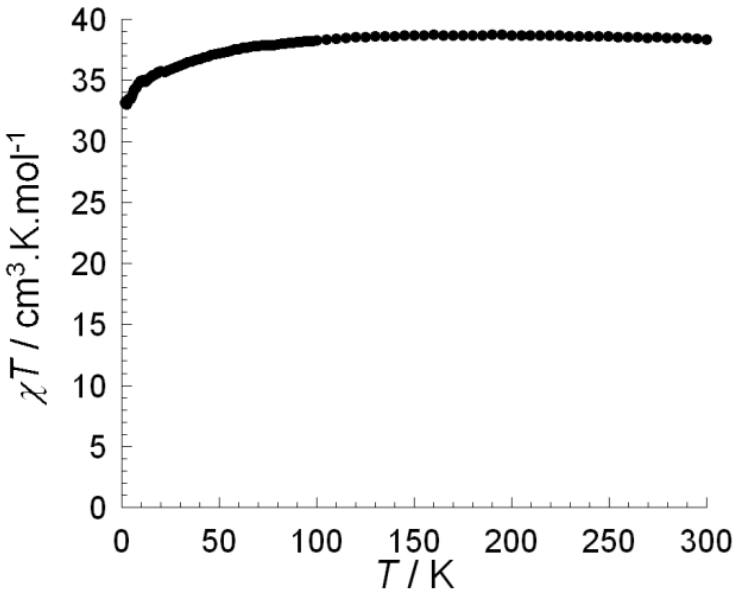


**Figure 4.39** Temperature dependence of the $\chi T$ product at 1000 Oe for complex **4-5** (with $\chi = M/H$ normalized per mol).

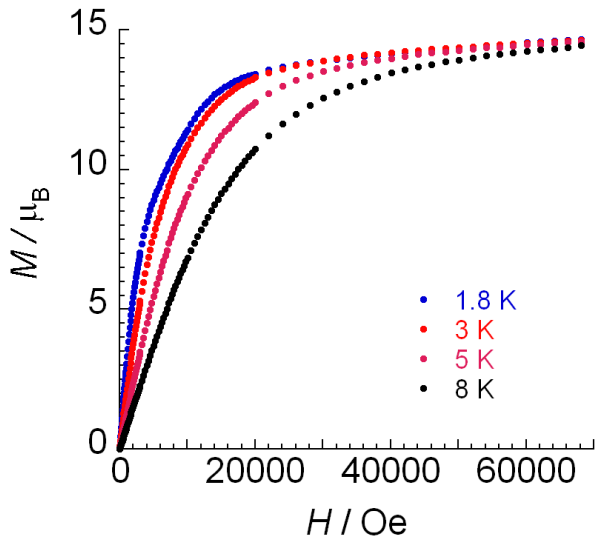


**Figure 4.40** Field dependence of the magnetization, *M*, at 1.8, 3, 5 and 8 K for complex **4-5**.

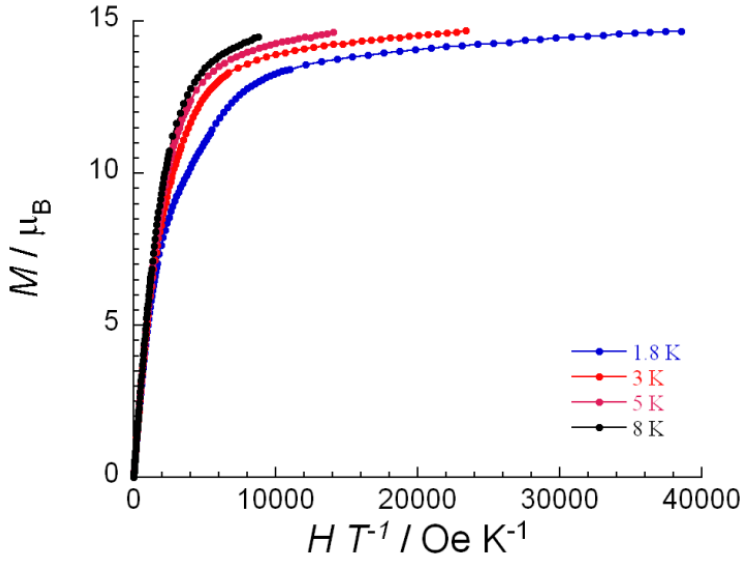


**Figure 4.41** The reduced magnetization plot for complex **4-5** measured at 1.8, 3, 5 and 8 K.

The field dependence of the magnetization below 8 K revealed a rapid increase of the magnetization at low fields and then a very slow linear increase without a clear saturation was observed. The magnetization at 1.8 K and 7 T is 15.4 $\mu_B$ which is close to the theoretical value of 15.7 $\mu_B$ for three $Dy^{III}$ ions (Figure 4.40). Additionally, the reduced magnetization plot, *M vs. H/T*, (Figure 4.41 (complex **4-5**)) at different temperatures shows magnetization curves that are not superimposable on a single master curve. The high field linear variation of the magnetization and the non-superimposable curves suggest the presence of significant magnetic anisotropy and also most likely low lying excited states.

The ac susceptibility of complex **4-5** was measured under zero dc field and a 3 Oe ac field over the temperature range 1.8-15 K between 1 and 1500 Hz. (Figure 4.42 and 4.43). The ac susceptibility was measured as a function of the frequency at different temperatures in zero dc field in order to follow the relaxation time. In the out-of-phase component $\chi''$ measurement, slow relaxation of the magnetization was observed based on the appearance of an out-of-phase signal below 15 K. The peak maximum values of the frequency of each temperature were obtained by Gaussian equation. Below 10 K, the clear relaxation time deviates from the Arrhenius behavior as expected when quantum

effect becomes relevant to describe the magnetization relaxation. Moreover, it seems that the purely quantum regime of relaxation is not observed even at 1.8 K. Above 10 K, the relaxation becomes thermally activated. Based on this data above 10 K, an estimation of the energy gap can be obtained at 80 K while the pre-exponential factor of the Arrhenius law ($\tau_0$) is about $9.2*10^{-7}$ s. (Figure 4.44)

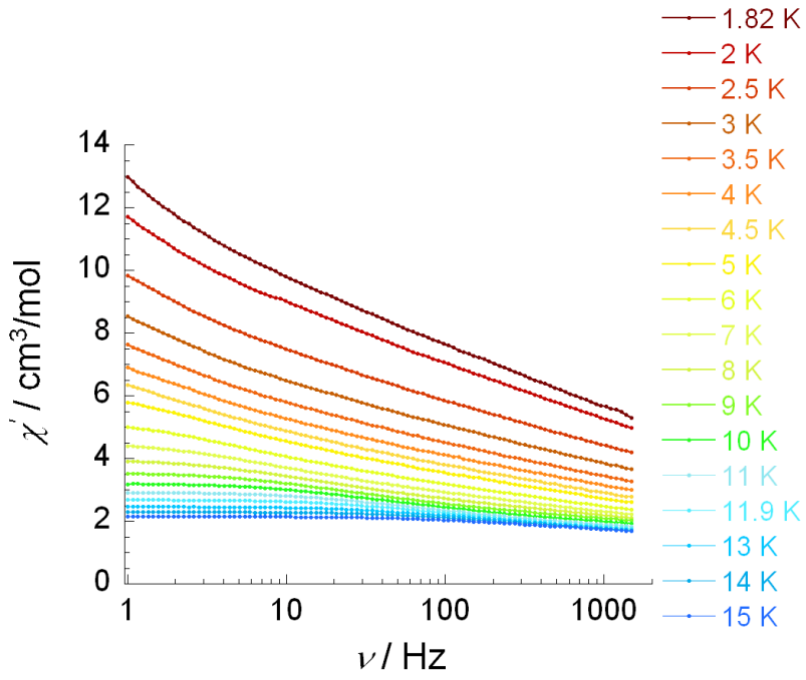


**Figure 4.42** In-phase susceptibility $\chi'$ *vs.* frequency $\nu$ over the temperature range 1.8-15 K for **4-5**.

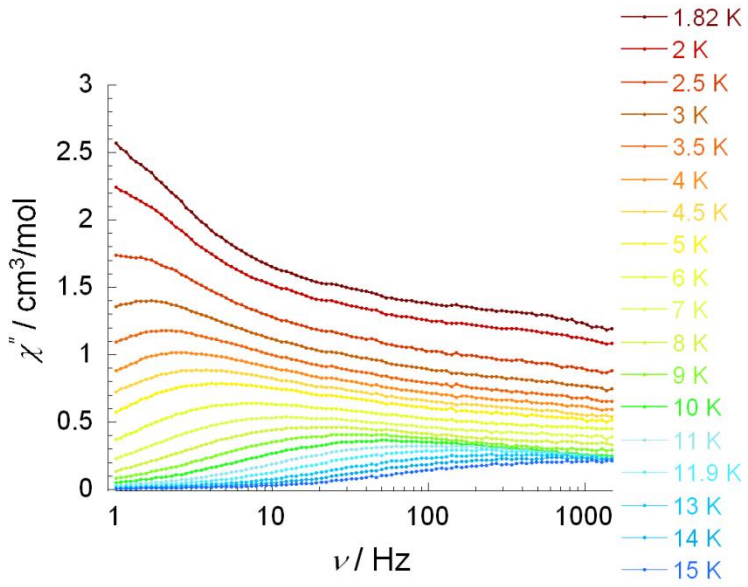


**Figure 4.43** Out-of-phase susceptibility $\chi'$ *vs.* frequency $\nu$ in the temperature range 1.8-15 K for **4-5**.

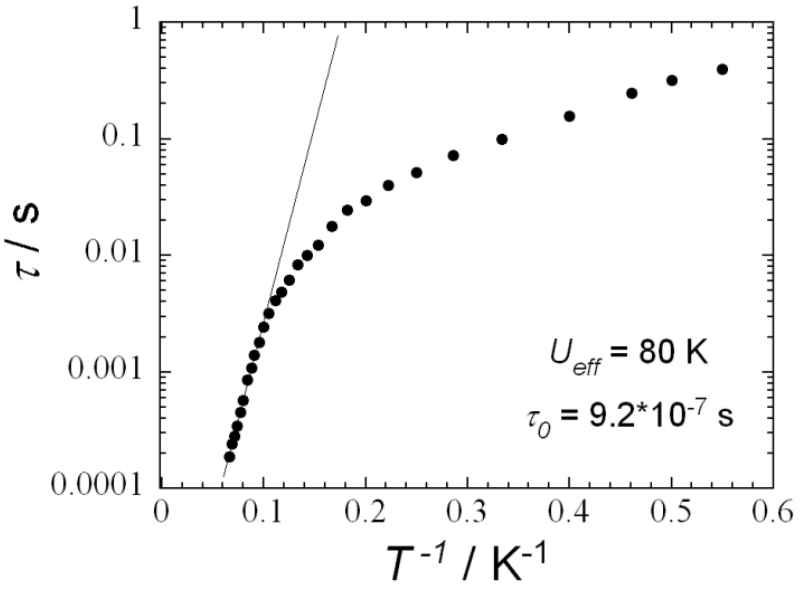


**Figure 4.44** Relaxation time of the magnetization $\tau$ *vs.* $T^{-1}$ (Arrhenius Plot using temperature-dependent ac data). The solid line corresponds to the fit.

# Conclusion

In this chapter, five trinuclear $Ln^{III}$ complexes were reported containing triangle metal cores which are very rare in lanthanide chemistry. To date, there are only five $Dy^{III}$ triangle complexes in the CCDC database. Two stereoisomers are present as a racemic mixture in complexes **4-1**, **4-2**, **4-3** and **4-4**. The Ln trinuclear cores of all five complexes are arranged close to equilateral triangle where the coordination environments of two $Dy^{III}$ ions are symmetric in complexes **4-1**, **4-2**, **4-3** and **4-5** but not in complex **4-4**. The angles of all triangles range from 59.55° to 60.45°. The intramolecular Dy---Dy distances of complexes **4-4** and **4-5** (around 3.5 Å ) are shorter than complexes **4-1** – **4-3** (around 3.5 Å ) which can result from the $\mu_3$-methoxide or hydroxide coordination in complexes **4-4** and **4-5**, respectively.

The dc magnetic susceptibilities for all five complexes were measured and the room temperature values are in good agreement with the expected values for three $Ln^{III}$ metal ions. The $\chi T$ *vs.* $T$ and $M$ *vs.* $H/T$ measurements are all similar due to the triangle arrangements of all complexes. There is no ac signal for complexes **4-1** to **4-3** but complexes **4-4** and **4-5** were shown to exhibit SMM behavior with $U_{eff}$ = 8.1 and 80 K, respectively, where complex **4-5** exhibited a record anisotropic energy barrier compared

to previously reported Dy triangle SMM. Except for one 3*d*-4*f* mixed metal complex,[45] all pure Dy triangle SMMs in this work and in the literature[34] have $\mu_3$-O centers which may play an important role in SMM properties. It may be advantageous to vary reaction conditions of complexes **4-1** – **4-3** in order to introduce a $\mu_3$-O center and pursue new molecules with SMM properties. Moreover, the anisotropic axes are impossible to predict from X-ray molecular structures of Dy complexes. *ab initio* calculations are necessary to determine the orientations of anisotropic axes. In the literature,[35b] ac susceptibility measurements of $Dy^{III}$ triangles have been interpreted within a non-colinear Ising model and/or resulted in a non-magnetic ground state. Therefore, understanding lowest magnetic states and the Zeeman splitting of complex **4-4** and **4-5** will also help in the investigation for their potential applications in quantum computation

[45] Aronica, C.; Pilet, G.; Chastanet, G.; Wernsdorfer, W.; Jacquot, J.-F.; Luneau, D. *Angew. Chem. Int. Ed.* **2006**, *45*, 4659

# Chapter 5

## Tetranuclear Lanthanide Complexes

Among the complexes presented so far, the polynuclear complexes based on $Dy^{III}$ ions showed the most promising magnetic behavior in terms of high-blocking temperature SMMs. One approach to increase the energy barrier, $U = |D| S^2$, is to increase the spin ground state ($S$) which can be achieved by increasing the number of ferromagnetically interacting metal ions. Additionally, coordination geometry, chelating and bridging groups are important factors to consider in the preparation of complexes that can potentially act as SMMs. For example, the coordination geometry of the metal center will affect the direction of the anisotropic axis and the bridging groups are related to the magnetic interactions between metal centers.

Four tetranuclear complexes will be discussed in detail with regards to their structural features in this chapter. With this in mind, we have introduced a novel *in situ* reaction where polynuclear complexes will be formed in fully and partially reacted ligands. All tetranuclear complexes have four octacoordinate lanthanide ions arranged in a defect dicubane (complexes **5-1**, **5-2** and **5-3**) or tetrahedral (complex **5-4**) fashion with some coordination sites occupied by counter ions depending on the reaction conditions.

Careful inspection of the structural arrangement indicated two possible super-exchange pathways via phenoxide and diaza groups. There are two super-exchange pathways (phenoxide and diaza groups) between the metal centers present in all four compounds. Complex **5-4** exists as two different isomers in the crystal structure where the resulting chirality is coordination-induced. SQUID measurements were carried out to investigate the dc and ac magnetic properties. Complexes **5-1** and **5-4** exhibit SMM properties with complex **5-1** possessing a high energy barrier of 170 K. In order to understand the relationship between geometries and magnetic properties, the anisotropic axes of all $Dy^{III}$ sites have been calculated and correlated to the SMM behavior. The detailed magnetic results will be discussed in this chapter.

## 5.1 Structure and magnetism of $[Ln_4(\mu_3\text{-}OH)_2(bmh)_2(msh)_4Cl_2]$ (Ln: Dy(5-1), Tb(5-2) and Ho(5-3)

In order to obtain multi-nuclear lanthanide complexes, a slightly different synthetic strategy containing 1,2-bis(2-hydroxy-3-methoxybenzylidene) hydrazone ($H_2$bmh) was employed. It can be noted that there are several rigid coordinating pockets to accommodate two lanthanide ions. Here we used the same strategy as was used to

synthesize complex **4-4** where the ligand is formed *in situ* with two *o*-vanillin molecules reacting with the N atoms of hydrazide. $[Ln_4(\mu_3\text{-}OH)_2(bmh)_2(msh)_4Cl_2]$ (Ln: Dy(**5-1**), Tb(**5-2**) and Ho(**5-3**)) was obtained through the reaction of *o*-vanillin (2 equiv.), $N_2H_4$ (4 equiv.), triethylamine (4 equiv) and $LnCl_3{\cdot}6H_2O$ (1 equiv.) (Ln: Dy(**5-1**), Tb(**5-2**) and Ho(**5-3**)) in DMF/$CH_2Cl_2$. As shown in Figure 5.1, there are two types of ligands (Hmsh and $H_2$bmh) formed *in situ* by the reaction of *o*-vanillin and hydrazine which is different from the other *in situ* reactions in chapters 4-1, 4-2 and 4-3. The Hmsh ligand is due to the partially reacted hydrazine with *o*-vanillin whereas the two nitrogen atoms of the hydrazine group on $H_2$bmh are both fully reacted with *o*-vanillin. The slight excess of hydrazine is essential for the formation of both ligands; when an excess of *o*-vanillin was used instead, we cannot obtain the product because the partial formation of the ligand which is critical for the structure synthesized will not be synthesized *in situ*. Moreover, the employed basic conditions promote the deprotonation of the ligands and the formation of bridging hydroxide anions from the hydrate of starting material ($DyCl_3{\cdot}6H_2O$). The molecular structure and the detailed core of complex **5-1** are shown in Figure 5.1 and Figure 5.2, respectively. The other two lanthanide complexes based on both lighter and heavier lanthanides ($Tb^{III}$ (**5-2**) and $Ho^{III}$ (**5-3**)) essentially exhibit planar isostructural tetranuclear cores. The selected bond

lengths and angles of complexes **5-1**, **5-2** and **5-3** are listed in Tables 5.1 and 5.2.

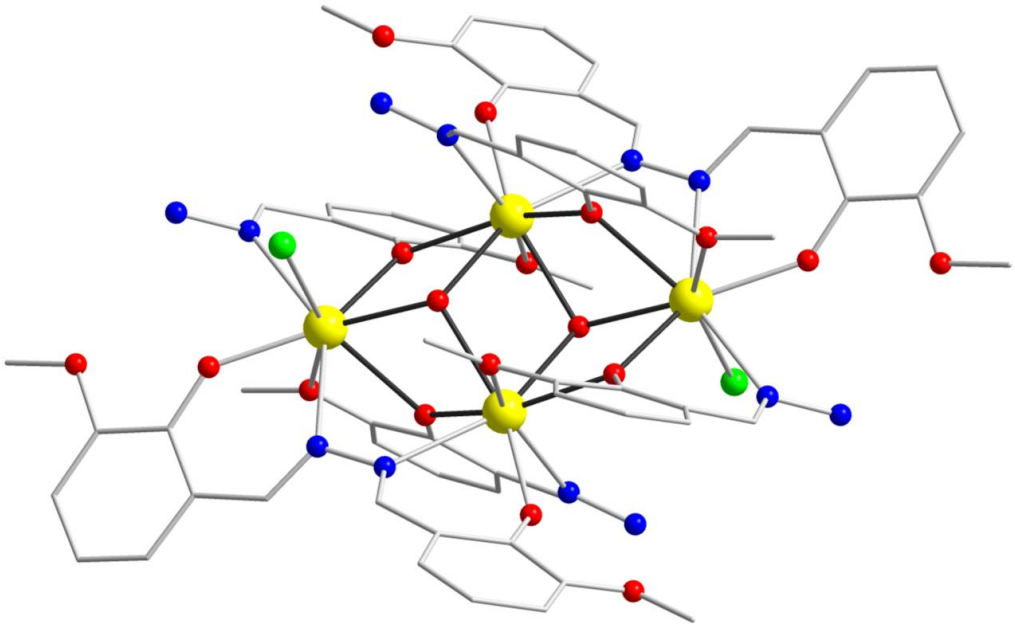

**Figure 5.1** Molecular X-ray structure of tetranuclear complex **5-1**. Yellow (Dy), Red (O), Blue (N), Grey (C), Green (Cl).

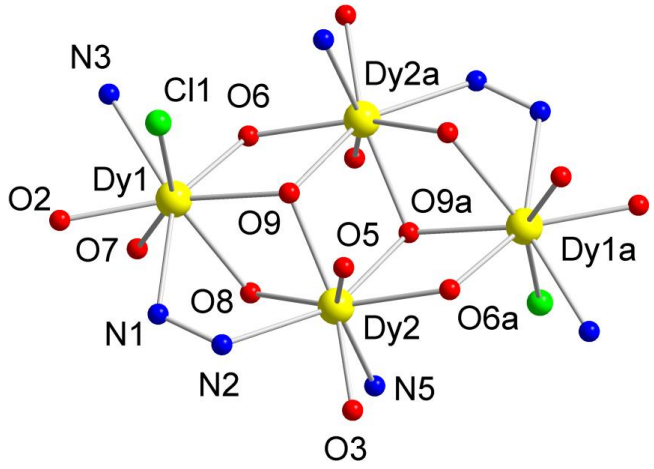


**Figure 5.2** Partially labled central symmetric core structure of complex **5-1**

All octa-coordinate $Dy^{III}$ ions are coplanar and linked together by a combination of

$\mu_3$-hydroxo (O9, O9a) and phenoxo (O6, O8, O6a and O8a) oxygen atoms. The two $\mu_3$-OH ligands are displaced above and below (0.92 Å) the Dy4 plane with Dy1-O9, Dy2-O9 and Dy2a-O9 bond lengths of 2.36, 2.45 and 2.30 Å as well as Dy1-O9-Dy2, Dy1-O9-Dy2a and Dy2-O9-Dy2 angles of 106.5, 107.7 and 105.7°, respectively. Four $\mu$-phenoxide O atoms between Dy1 and Dy2 are from the ligands with Dy1-O6, Dy1-O8, Dy2-O6a and Dy2-O8 of 2.30, 2.45, 2.31 and 2.34 Å and Dy1-O6-Dy2a and Dy1-O8-Dy2 of 114.8 and 106.3°, respectively. Moreover, two diaza groups from $bmh^{2-}$ ligands bridge Dy1, Dy2 and Dy1a, Dy2a with Dy1-N1 and Dy2-N2 distances of 2.51 and 2.56 Å, respectively. $Cl^-$ ion coordinated to Dy1 with a Dy1-Cl1 distance of 2.72 Å. The remaining coordination sites of Dy1 and Dy2 are filled by four $msh^{-1}$ and two $bmh^{-2}$ ligands. Such planar $Dy_4$ complexes are relatively rare in the literature with only three other examples currently reported.[46]

---

[46](a) Abbas, G.; Lan, Y.; Kostakis, G. E.; Wernsdorfer, W.; Anson, C. E.; Powell, A. K. *Inorg. Chem.* **2010**, *49*, 8067; (b) Zheng, Y. Z.; Lan, Y.; Anson, C. E.; Powell, A. K. *Inorg. Chem.* **2008**, *47*, 10813; (c) Yan, P.-F.; Lin, **P.-H.;** Habib, F.; Aharen, T.; Murugesu, M.; Deng, Z.-P.; Li, G.-M.; Sun, W.-B. *Inorg. Chem.*, **2011**, *50*, 7059.

**Table 5.1** Selected bond distances (Å ) for complexes **5-1** (Dy), **5-2** (Tb) and **5-3** (Ho).

| | | | |
|---|---|---|---|
| Dy1-O2 | 2.197(7) | Dy1-O6 | 2.297(6) |
| Dy1-O7 | 2.493(7) | Dy1-O8 | 2.448(6) |
| Dy1-O9 | 2.367(6) | Dy1-N1 | 2.565(8) |
| Dy1-N3 | 2.534(9) | Dy1-Cl1 | 2.724(3) |
| Dy2-O3 | 2.196(6) | Dy2-O5 | 2.592(6) |
| Dy2-O6a | 2.312(6) | Dy2-O8 | 2.344(6) |
| Dy2-O9 | 2.450(6) | Dy2-O9a | 2.306(6) |
| Dy2-N2 | 2.509(8) | Dy2-N5 | 2.454(8) |
| Dy1---Dy2 | 3.8834(6) | Dy1---Dy1a | 6.615(8) |
| Dy2---Dy2a | 3.7861(9) | Tb1-O2 | 2.211(12) |
| Tb1-O6 | 2.304(10) | Tb1-O7 | 2.508(10) |
| Tb1-O8 | 2.432(10) | Tb1-O9 | 2.384(10) |
| Tb1-N1 | 2.569(13) | Tb1-N3 | 2.539(14) |
| Tb1-Cl1 | 2.726(6) | Tb2-O3 | 2.196(10) |
| Tb2-O5 | 2.598(10) | Tb2-O6a | 2.319(9) |
| Tb2-O8 | 2.385(10) | Tb2-O9 | 2.456(10) |
| Tb2-O9a | 2.315(10) | Tb2-N2 | 2.529(13) |
| Tb2-N5 | 2.470(13) | Tb1---Tb2 | 3.894(5) |
| Tb1---Tb1a | 6.631(7) | Tb2---Tb2a | 3.799(2) |

| | | | |
|---|---|---|---|
| Ho1-O2 | 2.204(7) | Ho1-O6 | 2.293(6) |
| Ho1-O7 | 2.475(7) | Ho1-O8 | 2.431(6) |
| Ho1-O9 | 2.361(6) | Ho1-N1 | 2.547(8) |
| Ho1-N3 | 2.519(8) | Ho1-Cl1 | 2.706(3) |
| Ho2-O3 | 2.188(7) | Ho2-O5 | 2.591(7) |
| Ho2-O6a | 2.299(6) | Ho2-O8 | 2.344(6) |
| Ho2-O9 | 2.437(8) | Ho2-O9a | 2.283(6) |
| Ho2-N2 | 2.505(8) | Ho2-N5 | 2.437(8) |
| Ho1---Ho2 | 3.7150(18) | Ho1---Ho1a | 6.579(8) |
| Ho2---Ho2a | 3.758(2) | | |

**Table 5.2** Selected angles (°) for complexes **5-1** (Dy), **5-2** (Tb) and **5-3** (Ho).

| | | | |
|---|---|---|---|
| Dy1-O9-Dy2 | 106.2(2) | Dy1-O9-Dy2a | 107.4(2) |
| Dy2-O9-Dy2a | 105.4(2) | Dy1-O8-Dy2 | 102.5(2) |
| Dy1-O6-O2a | 114.8(3) | Dy1-Dy2-Dy1a | 120.453(13) |
| Dy2-Dy1-Dy2a | 59.547(13) | Dy1-Dy2-Dy2a | 62.153(15) |
| Dy1-Dy2a-Dy2 | 58.300(13) | Tb1-O9-Tb2 | 105.8(4) |
| Tb1-O9-Tb2a | 107.1(4) | Tb2-O9-Tb2a | 105.6(4) |
| Tb1-O8-Tb2 | 102.1(4) | Tb1-O6-Tb2a | 114.8(4) |
| Tb1-Tb2-Tb1a | 120.41(2) | Tb2-Tb1-Tb2a | 59.59(2) |

| | | | |
|---|---|---|---|
| Tb1-Tb2-Tb2a | 62.13(3) | Tb1-Tb2a-Tb2 | 58.28(2) |
| Ho1-O9-Ho2 | 106.2(2) | Ho1-O9-Ho2a | 106.9(2) |
| Ho2-O9-Ho2a | 105.2(2) | Ho1-O8-Ho2 | 102.2(2) |
| Ho1-O6-O2a | 114.4(3) | Ho1-Ho2-Ho1a | 120.56(3) |
| Ho2-Ho1-Ho2a | 59.44(3) | Ho1-Ho2-Ho2a | 62.20(4) |
| Ho1-Ho2a-Ho2 | 58.36(2) | | |

The Dy tetranuclear complexes are well isolated along *a* and *b* axes (Figure 5.3 and 5.4). Close inspection of the packing arrangement reveals stacking of the molecules along the *a* axis with intermolecular Dy···Dy distances of 11.86 Å and a zigzag arrangement of molecules along the *c* axis (Figure 5.5).

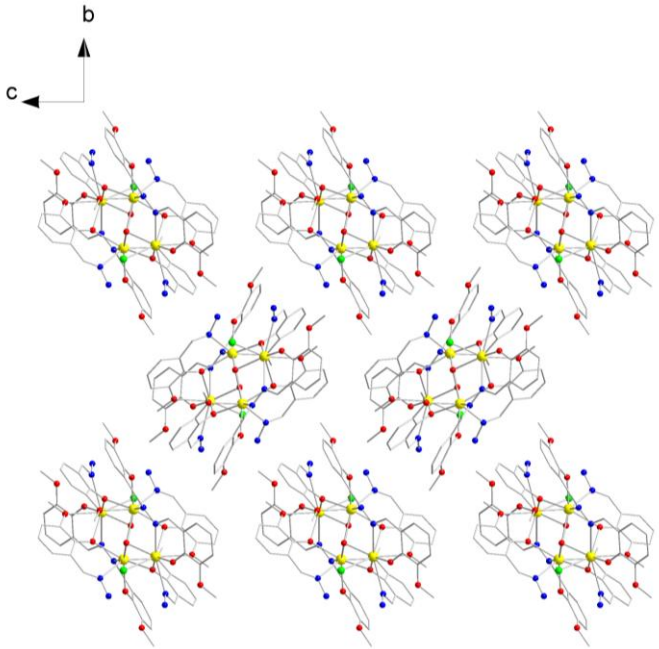


**Figure 5.3** Crystal packing diagram of complex **5-1** along the crystallographic *a* axis

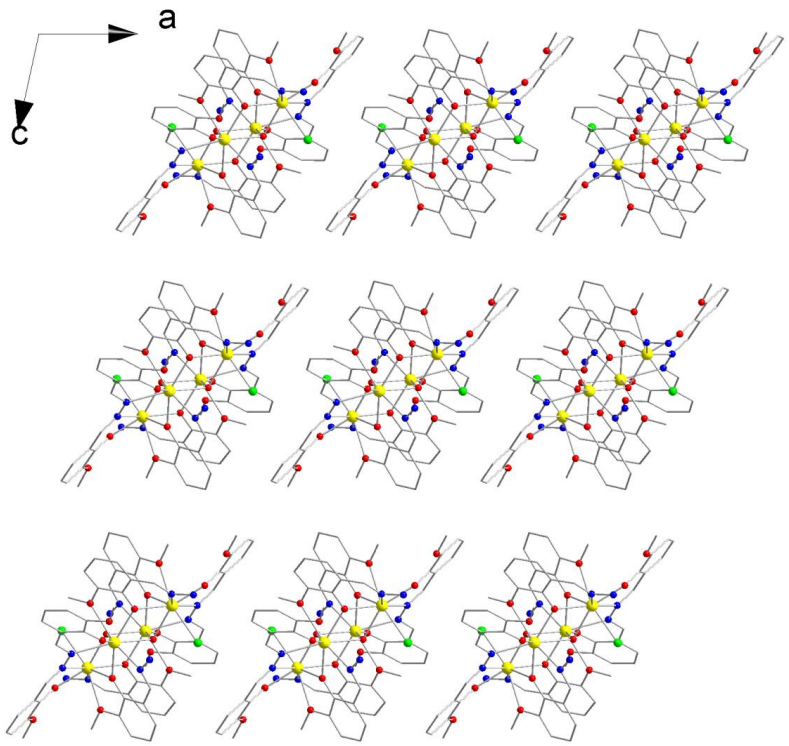


**Figure 5.4** Crystal packing diagram of complex **5-1** along the crystallographic *b* axis

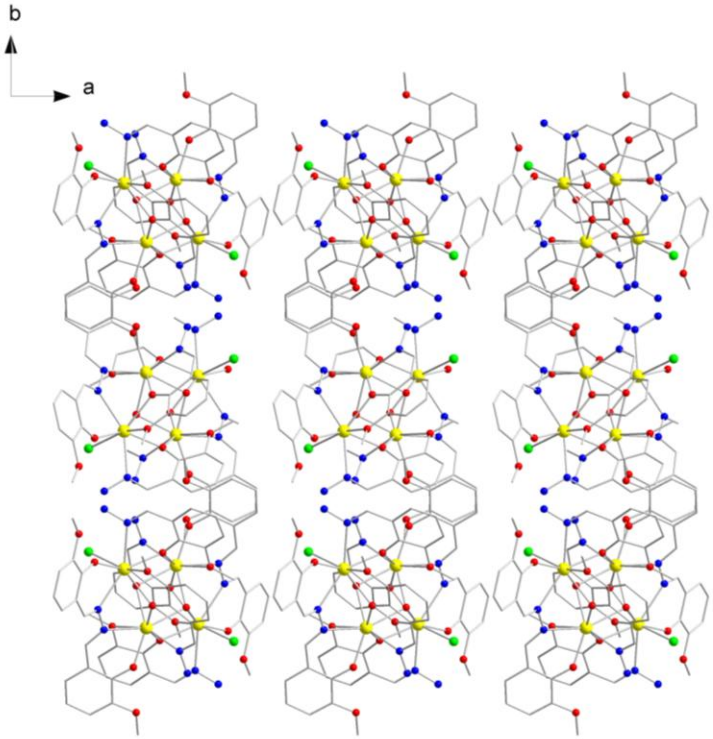


**Figure 5.5** Crystal packing diagram of complex **5-1** along the crystallographic *c* axis.

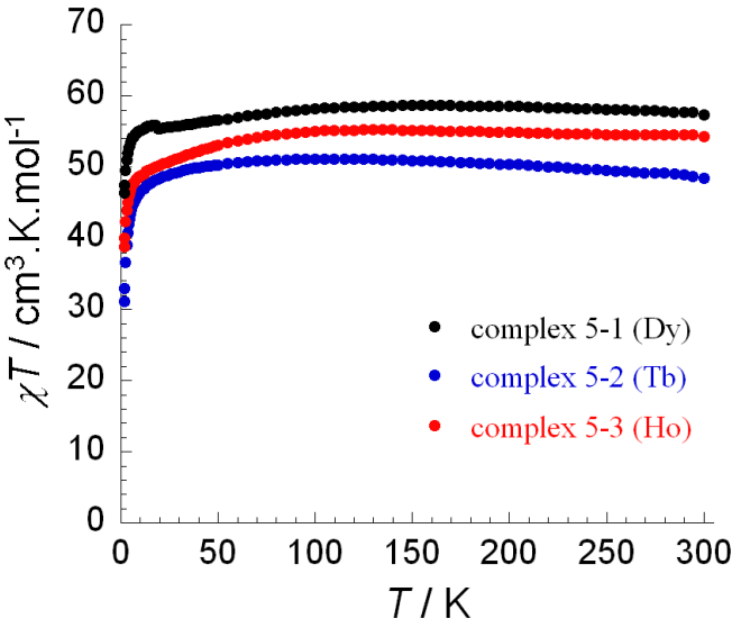


**Figure 5.6** Temperature dependence of the $\chi T$ product at 1000 Oe for complexes **5-1** (black), **5-2** (blue) and **5-3** (red) (with $\chi = M/H$ normalized per mol).

The magnetic susceptibility for complexes **5-1, 5-2** and **5-3** was measured in an applied dc field of 1000 Oe in the range of 1.8 K to 300 K on polycrystalline samples. The $\chi T$ *vs.* $T$ plot is shown in Figure 5.6. The dc magnetic susceptibility of complexes **5-1, 5-2** and **5-3** reveals a room-temperature $\chi T$ value of 56.6, 47.3 and 56.3 $cm^3.K.mol^{-1}$ per molecule which is close to the expected value of 56.6, 47.3 and 56.3 $cm^3.K.mol^{-1}$, respectively, (complex **5-1** : $Dy^{III}$, $S = 5/2$, $L = 5$, $^6H_{15/2}$, $g = 4/3$, complex **5-2** : $Tb^{III}$, $^7F_6$, $S = 3$, $L = 3$, $g = 3/2$, complex **5-3** : $Ho^{III}$, $^5I_8$, $S = 2$, $L = 6$, $g = 5/4$). The $\chi T$ product remains roughly constant with decreasing temperature down to 10 K, and then drops to a

minimum value of 49.4, 31.1 and 38.3 $cm^3.K.mol^{-1}$ for complexes **5-1**, **5-2** and **5-3** at 2 K, respectively. This behavior is generally indicative of weak intra-molecular antiferromagnetic coupling of the metal centers. The behavior may also be due to the thermal depopulation of the Stark sub-levels and/or the presence of large anisotropy in the system.

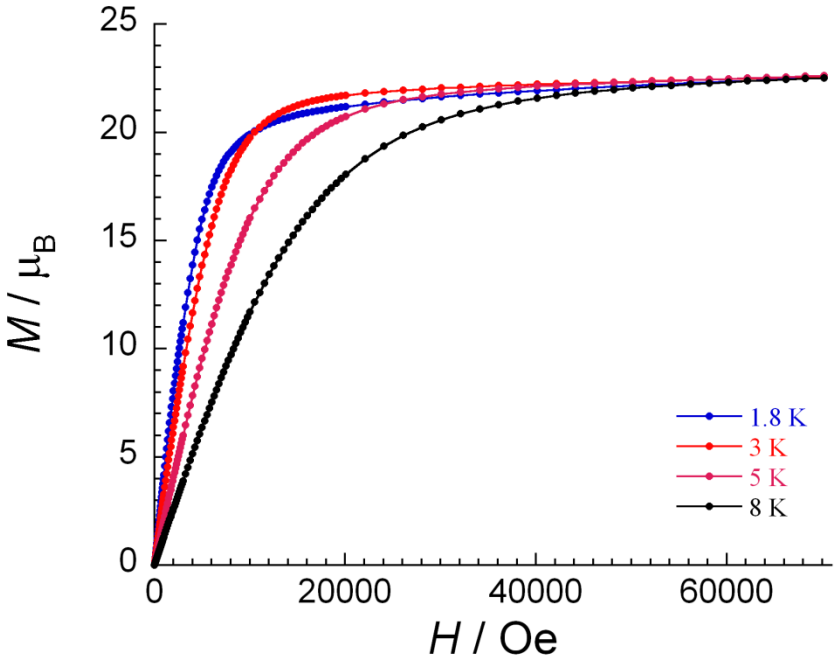


**Figure 5.7** Field dependence of the magnetization, *M*, at 1.8, 3, 5 and 8 K for complex **5-1**.

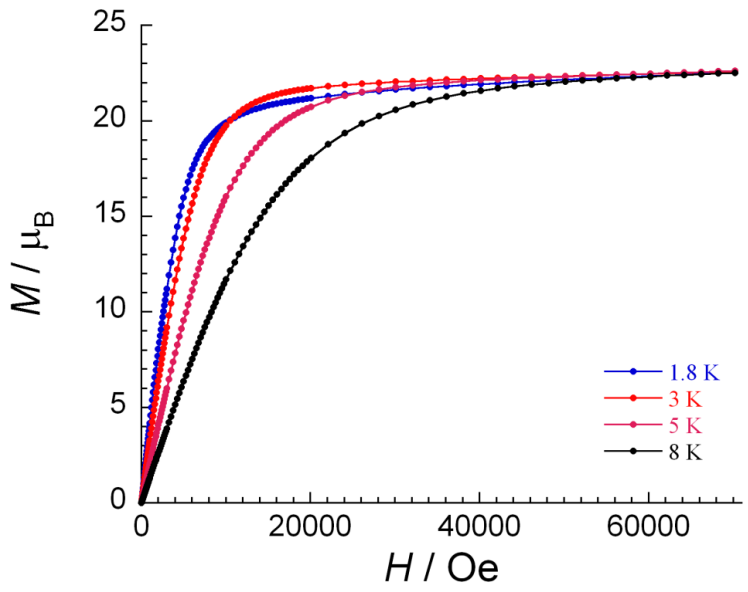


**Figure 5.8** Field dependence of the magnetization, *M*, at 1.8, 3, 5 and 8 K for complex **5-2**.

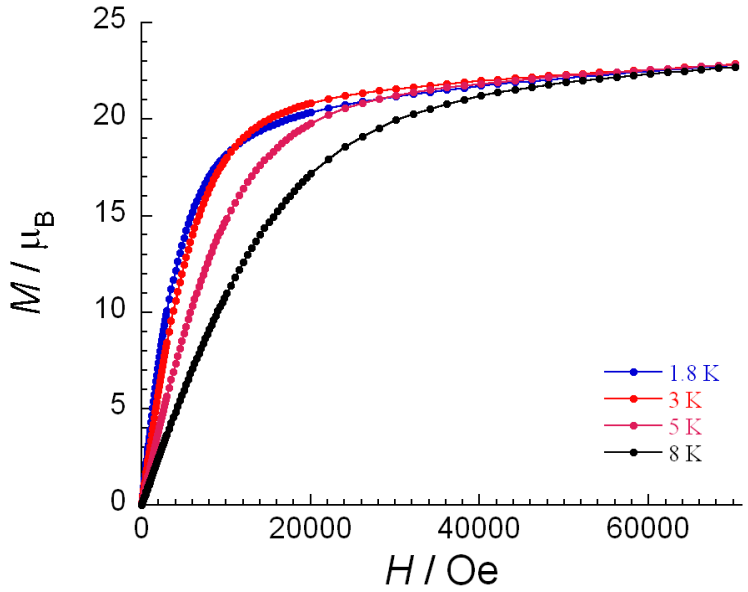


**Figure 5.9** Field dependence of the magnetization, *M*, at 1.8, 3, 5 and 8 K for complex **5-3**.

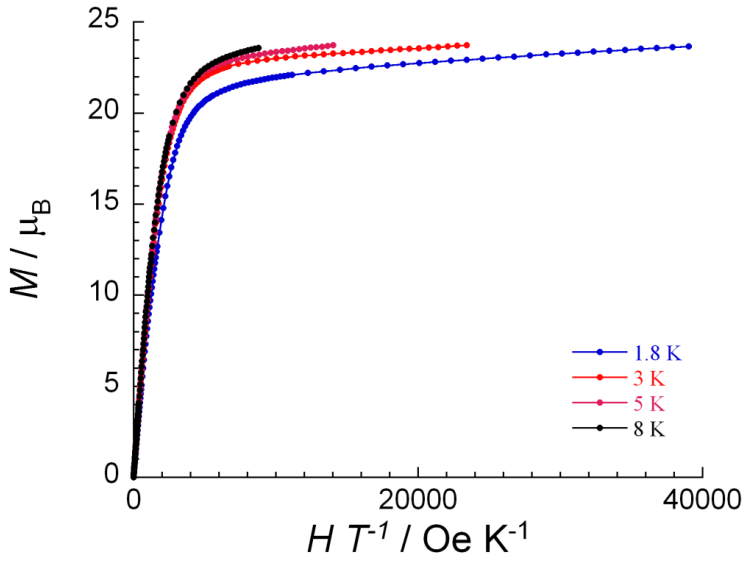


**Figure 5.10** The reduced magnetization plot for complex **5-1** measured at 1.8, 3, 5 and 8 K.

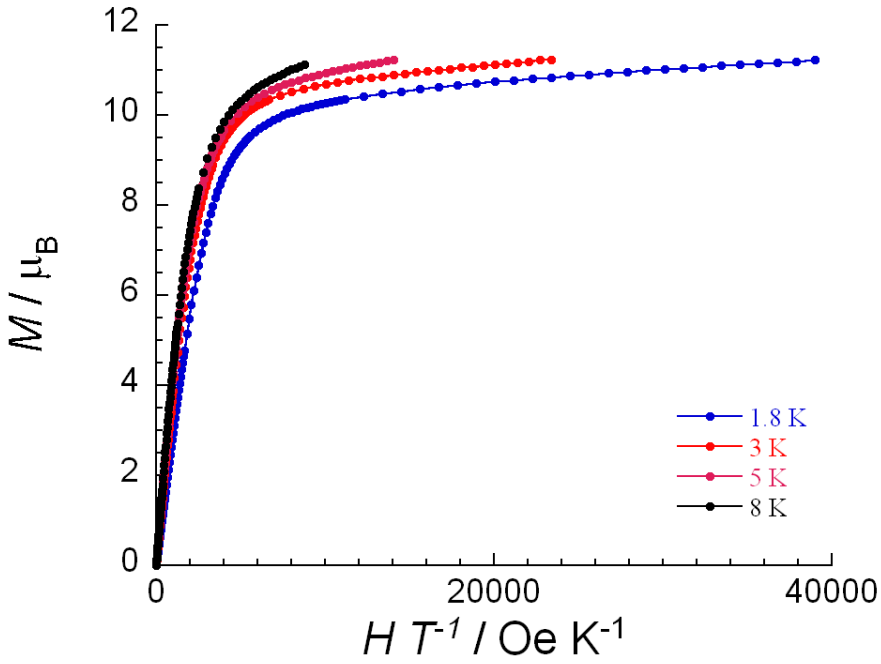


**Figure 5.11** The reduced magnetization plot for complex **5-2** measured at 1.8, 3, 5 and 8 K.

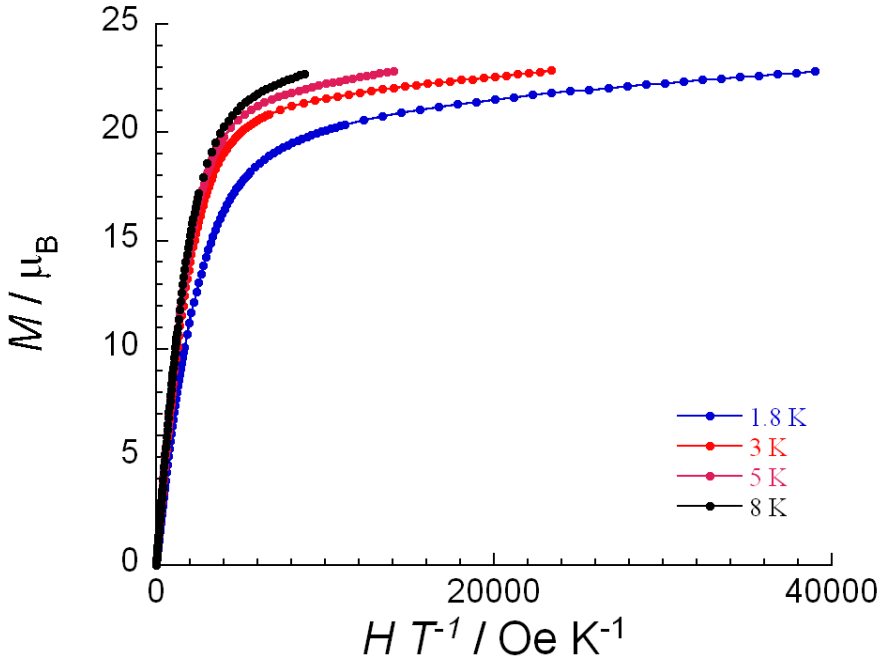


**Figure 5.12** The reduced magnetization plot for complex **5-3** measured at 1.8, 3, 5 and 8 K.

Furthermore, the field dependence of the magnetization below 8 K is not saturated even at 7 T (Figure 5.7, 5.8 and 5.9 for complexes **5-1**, **5-2** and **5-3**, respectively). Additionally, the reduced magnetization plot, *M vs. H/T*, (Figure 5.10, 5.11 and 5.12 for complexes **5-1**, **5-2** and **5-3**, respectively) in different temperatures shows magnetization curves that are not superimposable on a single mastercurve. These features are presumably due to the presence of large magneto-anisotropy in the $Ln^{III}$ system as well as weak intramolecular interactions between metal ions making the low lying exited states accessible even at 1.8 K.

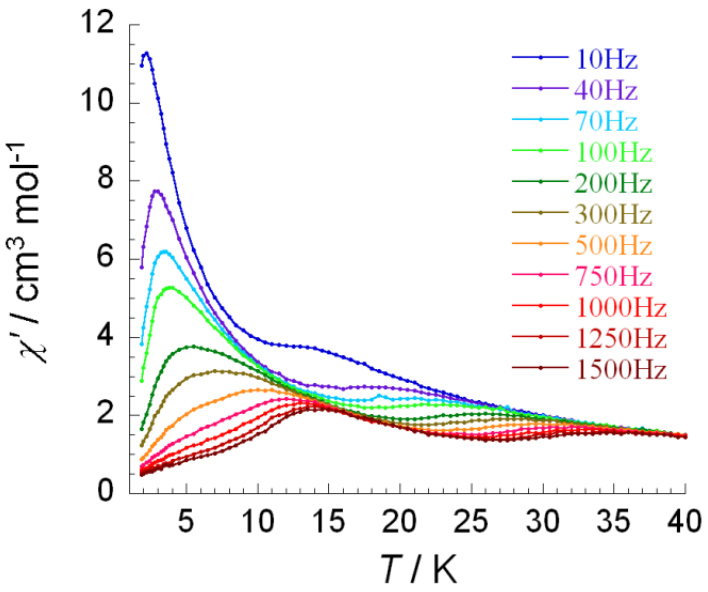


**Figure 5.13** In-phase susceptibility $\chi'$ *vs*. temperature *T* in the frequency range 10 - 1500 Hz under zero dc field for complex **5-1**.

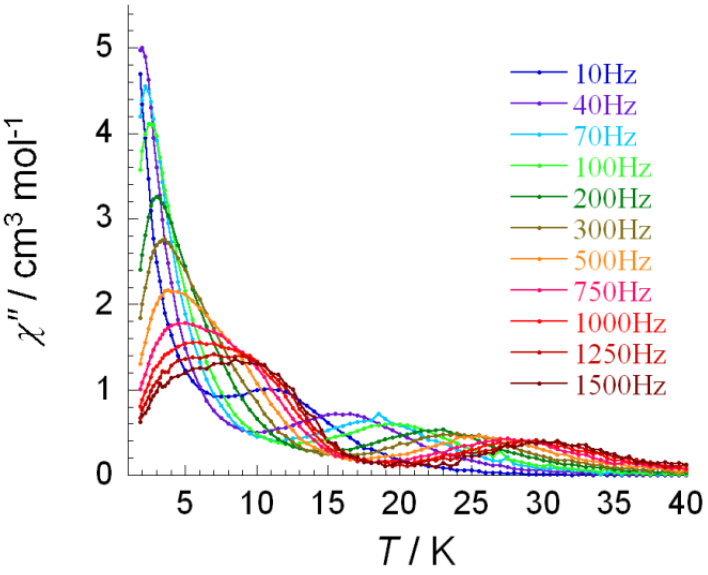


**Figure 5.14** Out-of-phase susceptibility $\chi''$ *vs*. temperature *T* in the frequency range 10 - 1500 Hz under zero dc field for complex **5-1**.

In order to investigate the possibility of SMM behavior, ac magnetic susceptibility measurements were carried out under zero dc field. Only complex **5-1** exhibited SMM properties as well as complexes **5-2** and **5-3** did not show such signals.

The temperature dependent ac susceptibility of **5-1** was measured under zero dc field. Out-of phase ($\chi$'') ac signals (Figure 5.14), indicating slow relaxation of magnetization, are observed with maxima at 30 and 9 K for 1500 Hz, indicating the presence of two modes of relaxation. These frequency-dependent signals are indicative of SMM behavior. The observation of slow relaxation of the magnetization at high temperatures is unique, as most reported SMMs exhibit relaxation below 10 K. Such unusual behavior in a weakly coupled molecular system is presumably due to the large intrinsic magnetic anisotropy of the $Ln^{III}$ ions. The relaxation times deduced from this data (Figure 5.15) are consistent with an activated behavior with effective energy barriers of $U_{eff}$=10 K (preexponential factor of $\tau_0 = 3*10^{-5}$ s) and $U_{eff}$=170 K ($\tau_0 = 4*10^{-7}$ s) for low- and high-temperature dynamics, respectively. The latter barrier of 170 K is a very high $U_{eff}$ value for polynuclear SMMs.

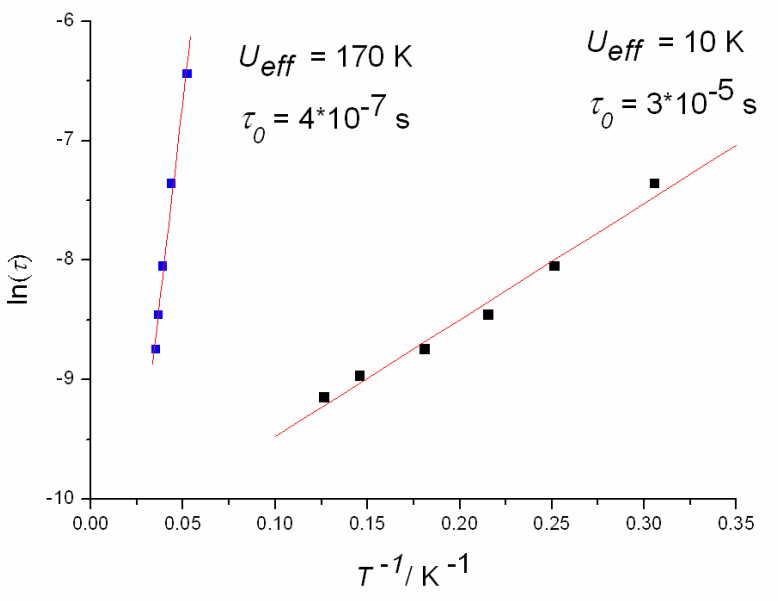


**Figure 5.15** Relaxation time of the magnetization ln($\tau$) *vs*. $T^{-1}$ (Arrhenius Plot using temperature-dependent ac data). The high and low temperature relaxation region are present in blue and black. The solid line corresponds to the fit.

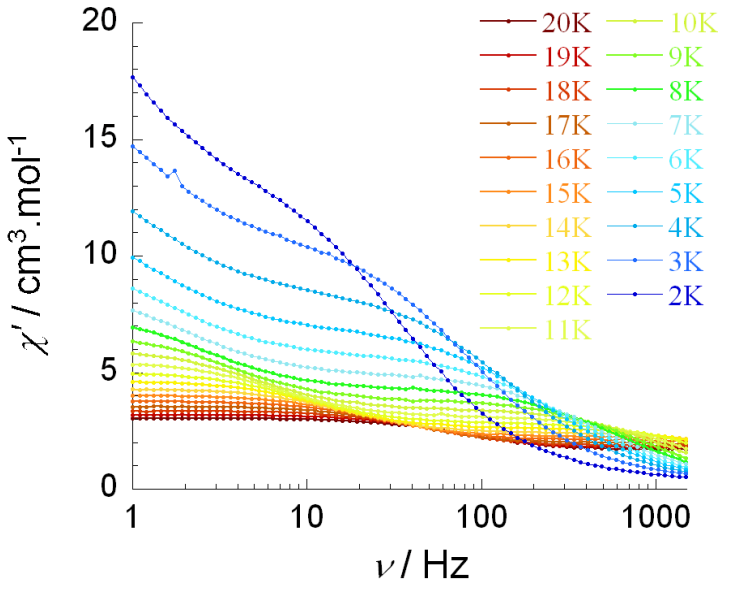


**Figure 5.16** In-phase susceptibility $\chi'$ *vs*. frequency $\upsilon$ in the temperature range 2 - 20 K under zero dc field for complex **5-1**.

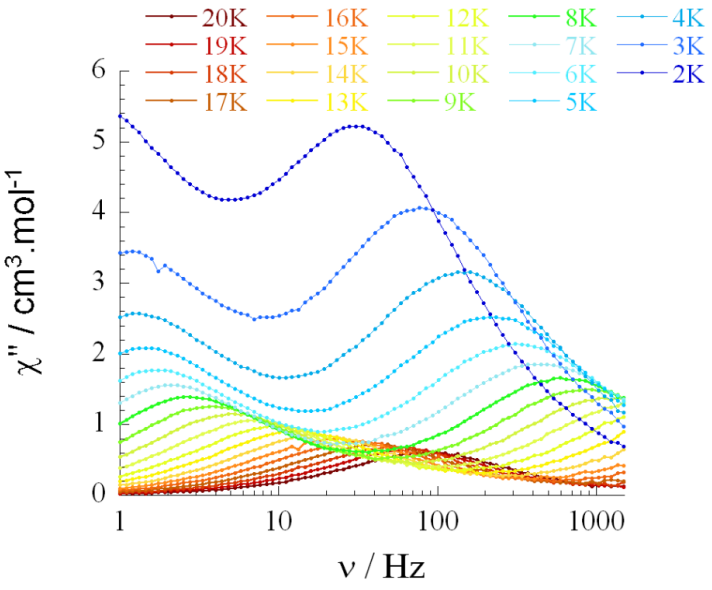


**Figure 5.17** Out-of-phase susceptibility *χ'' vs.* frequency *υ* in the temperature range 2 - 20 K under zero dc field for complex **5-1**.

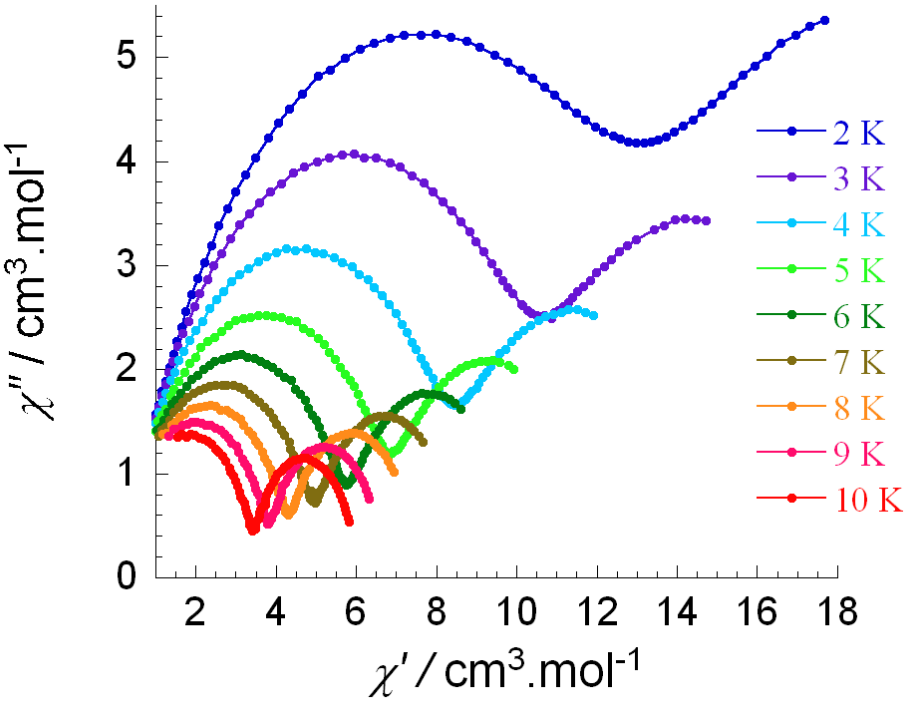


**Figure 5.18** Cole-Cole plot for complex **5-1** obtained using the ac susceptibility data.

In order to confirm the two relaxation modes of complex **5-1**, the ac susceptibility measurements were also obtained in function of frequency (Figure 5.16 and 5.17). Two individual peaks are present in out-of-phase $\chi''$ ac susceptibility measurement. Moreover, there are two individual semicircles at each temperature of Cole-Cole plot in the temperature range of 2-10 K (Figure 5.18) which is a very clear evidence of two relaxation modes presents in complex **5-1**.

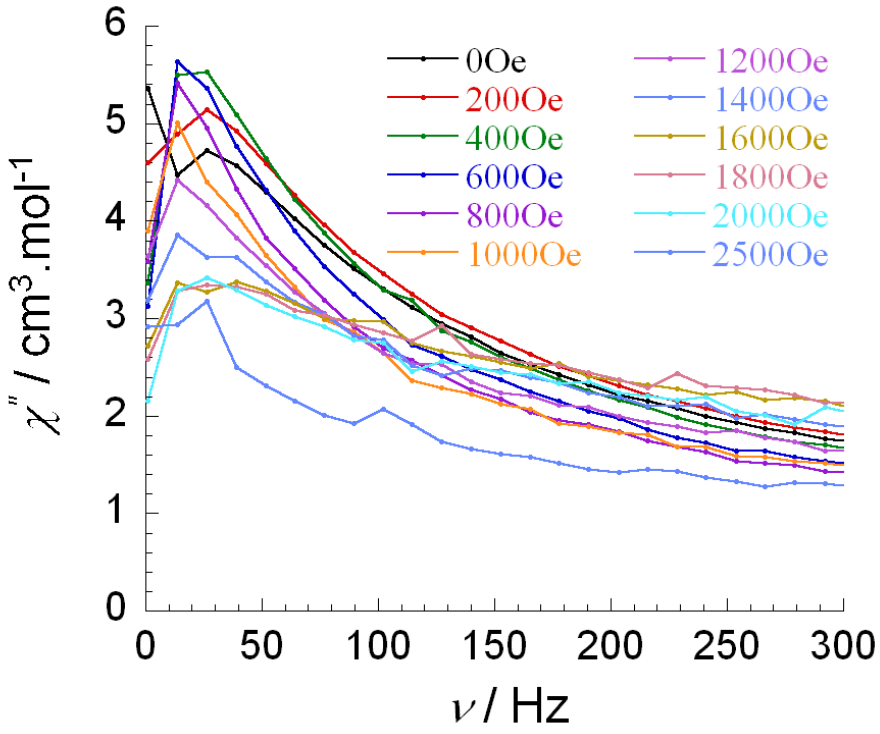


**Figure 5.19** Out-of-phase susceptibility $\chi''$ *vs.* frequency υ in the field range 0 - 2500 Oe under zero dc field for complex **5-1**.

To shortcut the quantum tunneling of the magnetization (QTM) which is commonly observed in lanthanide systems, ac measurements would be carried out under an optimum applied static dc field. However, there is no obvious peak shifting under the static dc fields from 0 – 2500 Oe. (Figure 5.19) In this case, higher energy barriers will not obtain when the static field is applied which indicates that the QTM is less efficient at zero field.

Low-temperature, single-crystal dc magnetization measurements of complex **5-1** were carried out on a micro-SQUID magnetometer between 0.04 and 7 K (Figure 5.20). Below 7 K, multi-step hysteresis loops were observed with an opening at a temperature of 7 K (Figure 5.21). The coercivities of the hysteresis loops increase with decreasing temperature and increasing field sweep rate, as expected for an SMM. This hysteresis loop opening temperature is one of highest ever observed for SMMs. The multi-steps seen in the loops are generally due to the resonant QTM. However, we are not able to determine the mechanism of the QTM in this stage.

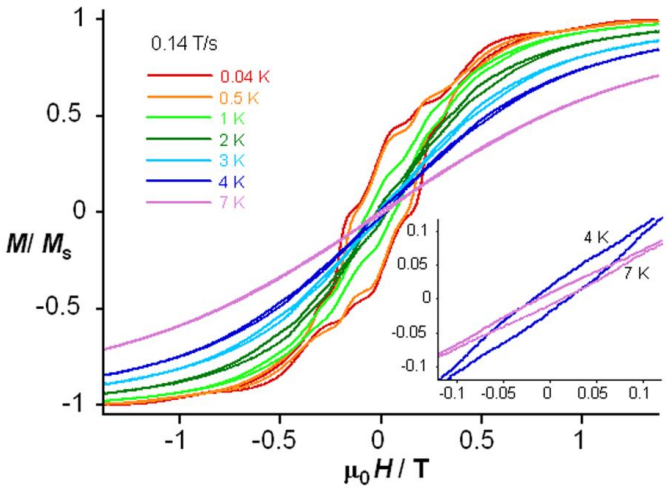


**Figure 5.20** Magnetization (*M*) *vs.* applied dc field sweeps at the indicated sweep rate and temperatures. Inset: Zoomed-in section of the hysteresis loops showing an opening at 7 K.

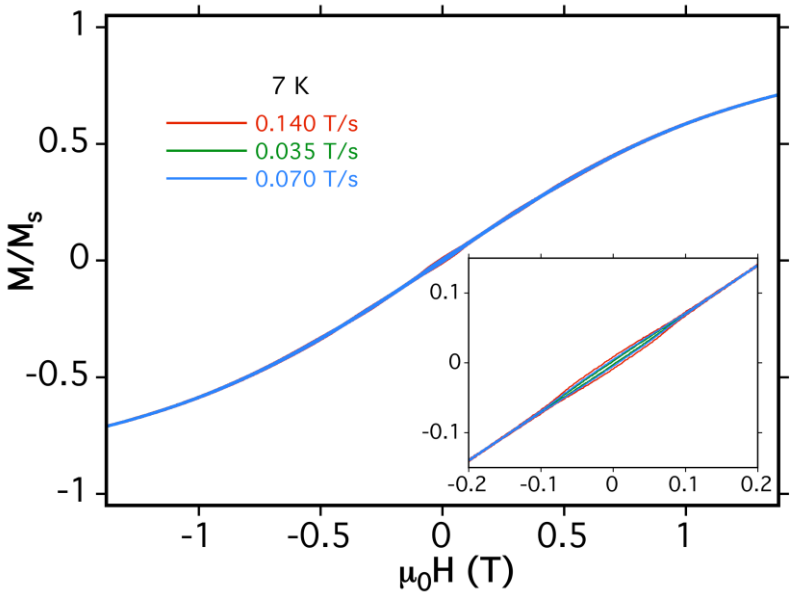


**Figure 5.21** Magnetization (*M*) *vs.* applied dc field sweeps at the indicated sweep rates and at 7 K. *M* is normalized to the magnetization value, *Ms*, at 1.4 T and 40 mK. Inset: Enlargement of the central part of the hysteresis loops.

To further investigate this property, *ab initio* calculations were carried out to determine the local anisotropy on each metal site. The calculated directions of the anisotropy axes at the four $Dy^{III}$ sites are shown in the inset of Figure 5.22. Anisotropy axes in **5-1** are parallel to each other for the opposite ions and point almost radially to each Dy site. The axis passing though the Dy1 and Dy2 ions makes an angle of 28.78 and 3.18° with the Dy4 plane. The corresponding $g$ factors for the lowest Kramers doublets on the dysprosium sites were calculated to be very anisotropic ($g_{\parallel}$=19.5 for Dy1, $g_{\parallel}$=19.2 for Dy2, and $g_{\perp}$ is negligible for both types of ions). From these large values of local axial $g$ factors, we may conclude that the exchange interaction between the lowest Kramers doublets on the dysprosium sites will be close to Ising type, which is similar to what was found in other dysprosium-only SMMs. Since the anisotropy axes on Dy1 and Dy2 are almost orthogonal, the exchange interaction between the lowest Kramers doublets of these ions is expected to be very small. *Ab initio* calculations also predict the first excited Kramers doublet on Dy1 and Dy2 lying 83 K and 199 K over the ground one, respectively. Since the exchange interaction between the dysprosium sites is much smaller than the obtained local excitation energies, the main contribution to the barrier of blockage of magnetization in complex **5-1** comes from the blockage of magnetizations of individual dysprosium ions. The two maxima of the out-of-phase ($\chi''$) ac signals can then

be naturally associated with two relaxation times (and two barriers of blocking of magnetization) corresponding to two types of dysprosium ions in complex **5-1**. The large difference of local excitation energies on Dy1 and Dy2 support this scenario.

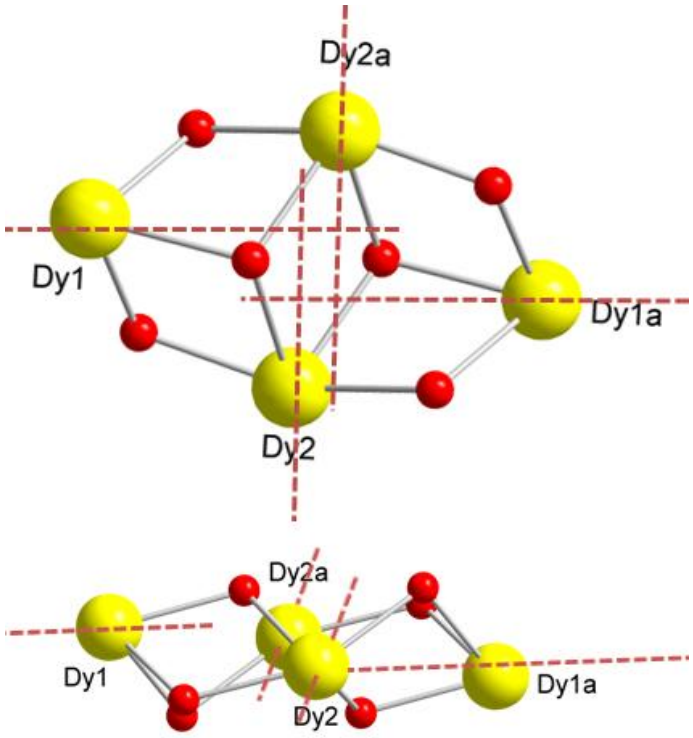


**Figure 5.22** Calculated magnetic anisotropic axis direction on each $Dy^{III}$ site

## 5.2 Structure and magnetism of $[Dy_4(\mu_4\text{-}O)(\mu\text{-}OMe)_2(beh)_2(esh)_4]\cdot 3MeOH$ (5-4)

In this section, we slightly modified the functional group of the ligand from section 5-1 where the methyl group is replaced by an ethyl group. $[Dy_4(\mu_4\text{-}O)(\mu\text{-}OMe)_2(beh)_2(esh)_4]\cdot 3MeOH$ (complex **5-4**) was obtained through the reaction of 3-ethoxysalicylaldehyde (2 equiv.), $N_2H_4$ (4 equiv.), triethylamine (4 equiv) and $DyCl_3\cdot 6H_2O$ (1 equiv.) in MeOH. The structure of complex **5-4** is shown in Figure 5.23. Two ligands, 1,2-bis(2-hydroxy-3-ethoxybenzylidene) hydrazone ($H_2$beh) and 3-ethoxysalicylaldehyde hydrazone (Hesh), which are formed *in situ* are similar to the ligands in section 5-1. Using MeOH instead of a DMF/$CH_2Cl_2$ mixture is key to obtain complex **5-4** where the molecular structure exhibited MeOH for co-solvent and $\mu$-OMe from deprotonated MeOH molecule.

**Table 5.3.** Selected bond distances (Å) for complex **5-4**.

| | | | |
|---|---|---|---|
| Dy1-O3 | 2.286(12) | Dy1-O5 | 2.379(13) |
| Dy1-O7 | 2.424(12) | Dy1-O8 | 2.608(13) |
| Dy1-O18 | 2.217(13) | Dy1-O19 | 2.291(11) |
| Dy1-N2 | 2.459(16) | Dy1-N3 | 2.642(17) |
| Dy2-O1 | 2.287(13) | Dy2-O9 | 2.450(12) |

| | | | |
|---|---|---|---|
| Dy2-O10 | 2.547(13) | Dy2-O11 | 2.440(13) |
| Dy2-O17 | 2.215(12) | Dy2-O19 | 2.304(12) |
| Dy2-N1 | 2.511(14) | Dy2-N9 | 2.577(17) |
| Dy3-O9 | 2.400(13) | Dy3-O9 | 2.400(13) |
| Dy3-O11 | 2.380(13) | Dy3-O13 | 2.262(13) |
| Dy3-O18 | 2.234(12) | Dy3-O19 | 2.285(11) |
| Dy3-N7 | 2.609(15) | Dy3-N7 | 2.521(16) |
| Dy4-O5 | 2.439(12) | Dy4-O6 | 2.578(13) |
| Dy4-O7 | 2.349(11) | Dy4-O15 | 2.248(12) |
| Dy4-O17 | 2.247(13) | Dy4-O19 | 2.299(12) |
| Dy4-N5 | 2.593(17) | Dy4-N12 | 2.479(16) |
| Dy1---Dy2 | 4.125(5) | Dy1---Dy3 | 3.6249(13) |
| Dy1---Dy4 | 3.4939(13) | Dy2---Dy3 | 3.4605(13) |
| Dy2---Dy4 | 3.5719(13) | Dy3---Dy4 | 4.140(2) |

**Table 5.4** Selected angles (°) for complex **5-4**.

| | | | |
|---|---|---|---|
| Dy1-O19-Dy2 | 127.7(5) | Dy1-O19-Dy3 | 104.8(4) |
| Dy1-O19-Dy4 | 99.1(5) | Dy2-O19-Dy3 | 97.9(5) |
| Dy2-O19-Dy4 | 101.8(4) | Dy3-O19-Dy4 | 129.2(5) |
| Dy1-O18-Dy3 | 109.1(5) | Dy1-O5-Dy4 | 93.0(4) |
| Dy1-O7-Dy4 | 94.1(4) | Dy2-O9-Dy3 | 91.0(4) |

| | | | |
|---|---|---|---|
| Dy2-O11-Dy3 | 91.8(4) | Dy2-O17-O4 | 106.4(5) |
| Dy1-Dy3-Dy2 | 91.16(3) | Dy1-Dy4-Dy2 | 71.42(3) |
| Dy1-Dy2-Dy3 | 56.28(2) | Dy1-Dy4-Dy3 | 55.92(2) |
| Dy1-Dy2-Dy4 | 53.41(2) | Dy1-Dy3-Dy4 | 52.98(2) |
| Dy2-Dy1-Dy3 | 52.57(2) | Dy2-Dy1-Dy4 | 55.17(2) |

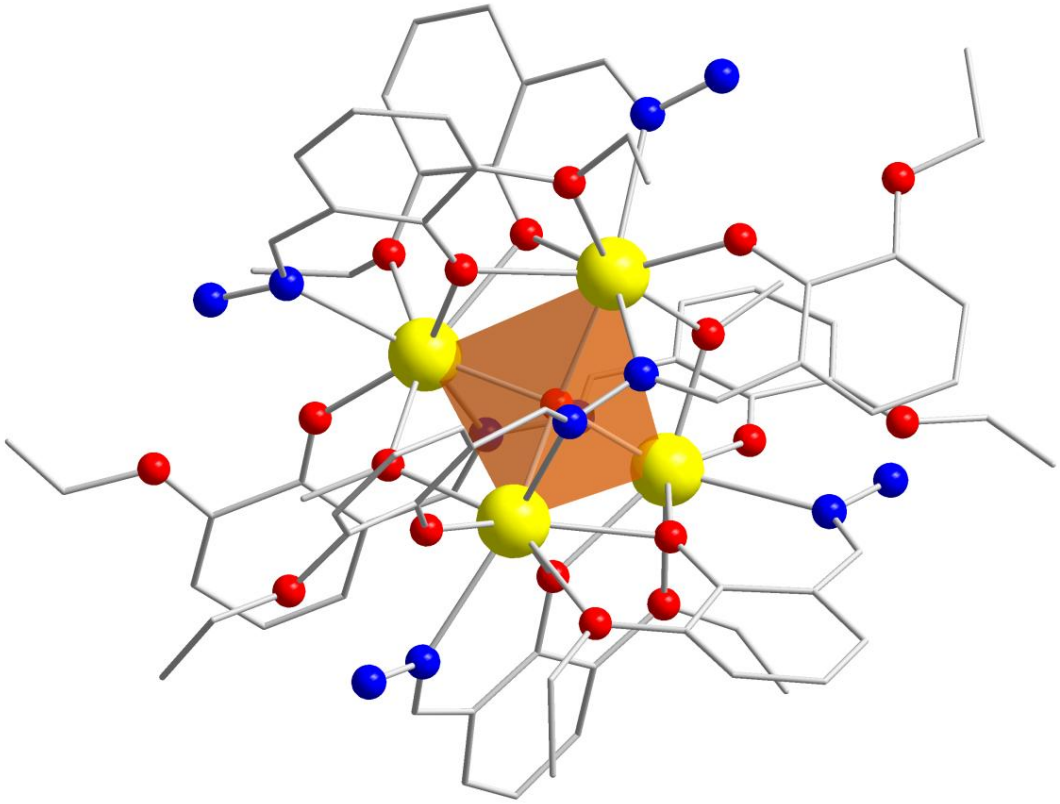

**Figure 5.23** Molecular X-ray structure of complex **5-4**. Yellow (Dy), Red (O), Blue (N), Grey (C).

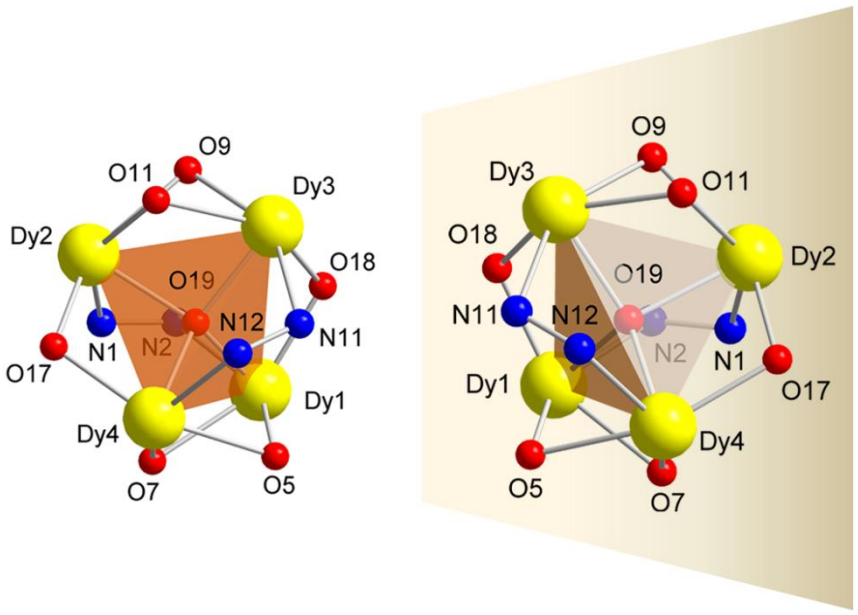


**Figure 5.24** The core structure detail of complex **5-4.** Fully labelled tetrahedral core emphasizing different bridging modes between $Dy^{III}$ ions of two isomers

Complex **5-4** consists of four $Dy^{III}$ ions arranged in a distorted tetrahedral fashion around the central $\mu_4$-O atom (O19) with Dy1–O19, Dy2–O19, Dy3–O19 and Dy4–O19 distances of 2.29, 2.30, 2.29 and 2.30 Å, respectively. Four of the edges are formed by two methoxide (O17, O18) and two diazine (N1N2, N11N12) bridges, while the remaining two edges are formed by four doubly bridged phenoxide oxygen atoms (O5, O7, O9 and O11). Within the core, the intramolecular Dy1---Dy2, Dy1---Dy3, Dy1---Dy4, Dy2---Dy3, Dy2---Dy4 and Dy3---Dy4 distances are in the range of 4.13, 3.62, 3.49, 3.46, 3.57 and 4.14 Å, respectively. The coordination environments of the octacoordinate $Dy^{III}$ ions are filled by two nitrogen donor atoms from the diaza group of

the ligand and by oxygen atoms from a combination of oxide, methoxide and phenoxide groups. Upon coordination, the fully formed $beh^{2-}$ ligand is locked in a conformation, thus preventing the free rotation about the N–N bridge. Therefore, conformational chirality is induced. The two stereoisomers exist as a racemic mixture of enantiomers with O19 as a chiral centre (Figure 5.24). It is noteworthy that similar $\mu_4$-O centred tetrahedral cores are common in transition-metal chemistry;[47] however, they are relatively rare in lanthanide chemistry. The handful of reported tetrahedral lanthanide molecules belong to the family of organometallic complexes, whereas no coordination complexes have been reported. This is mainly due to the presence of small ligands in organometallic complexes[48], which facilitate the formation of cluster complexes without

---

[47] a) Afrati, T.; Dendrinou-Samara, C.; Raptopoulou, C. P.; Terzis, A.; Tangoulis, V.; Kessissoglou, D. P. *Angew. Chem. Int. Ed.* **2002**, *41*, 2148; b) Jian, F.; Xiao, H.; Bai, Z.; Zhao, P. *J. Mater. Chem.* **2006**, *16*, 3746; c) Zaleski, C. M.; Weng, T.-C.; Dendrinou-Samara, C.; Alexiou, M.; Kanakaraki, P.; Hsieh, W.-Y.; Kampf, J.; Penner-Hahn, J. E.; Pecoraro, V. L.; Kessissoglou, D. P. *Inorg. Chem.* **2008**, *47*, 6127;

[48] Wang, J.; Li, S.; Zheng, C.; Li, A.; Hosmane, N. S.; Maguire, J. A.; Roesky, H. W.; Cummins, C. C.; Kaim, W. *Organometallics* **2004**, *23*, 4621.

significant coordination strain. On the other hand, the encapsulation of ligands generally employed in coordination chemistry induces ligand strain, which thus leads to smaller complexes. Complex **5-4** represents the first example of a tetrahedral Dy4 complex reported to date. Synthetically speaking, complex **5-4** can only be synthesized by in situ condensation reaction of 3-ethoxysalicylaldehyde and hydrazine in a 1:2 ratio. Because of the presence of excess hydrazine, two fully formed $beh^{2-}$ and four partially formed $esh^{-}$ ligands participate in the formation of this tetranuclear complex. When a fully formed $beh^{2-}$ ligand was employed prior to the complexation reaction, no crystals were isolated. The use of $Et_3N$ in the reaction mixture is critical for the formation of this large complex. The $Et_3N$ base helps deprotonate the $H_2$beh and Hesh chelates as well as promotes the formation of the $\mu_4$-O and $\mu$-OMe bridges from the $H_2O$/MeOH molecules introduced by the hydrated $DyCl_3$ and the employed solvent.

A close inspection of the packing arrangement reveals that two different Dy4 enantiomers are in different layers (layer a and layer b) along the crystallographic *a* and *c* axes (Figures 5.25 and 5.26), with the shortest Dy···Dy distance of 10.07 Å between adjacent molecules. A reverse arrangement of the molecules is shown between two layers (layer a, layer a' and layer b, layer b') of the same enantiomers. The Dy tetranuclear complexes are well isolated along *b* axis (Figure 5.27). All molecules are the same

enantiomers and orientated in the same direction.

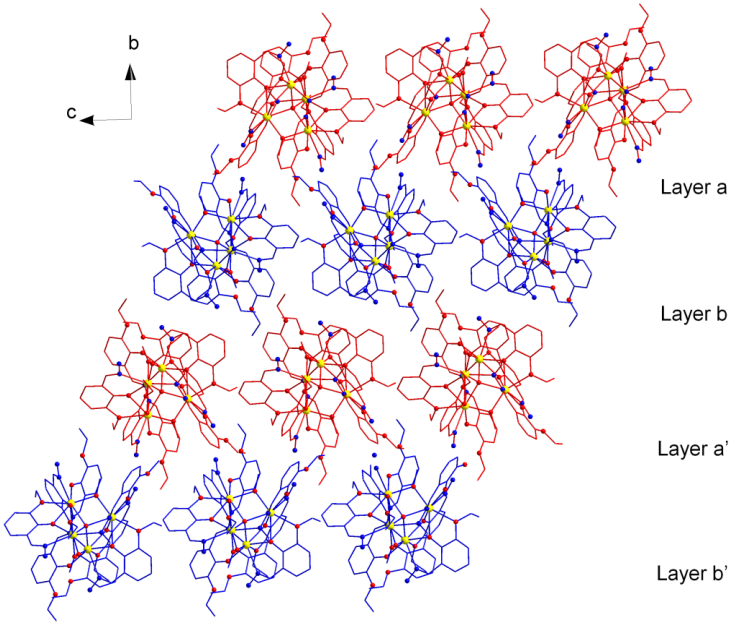


**Figure 5.25** Crystal packing diagram of complex **5-4** along the crystallographic *a* axis

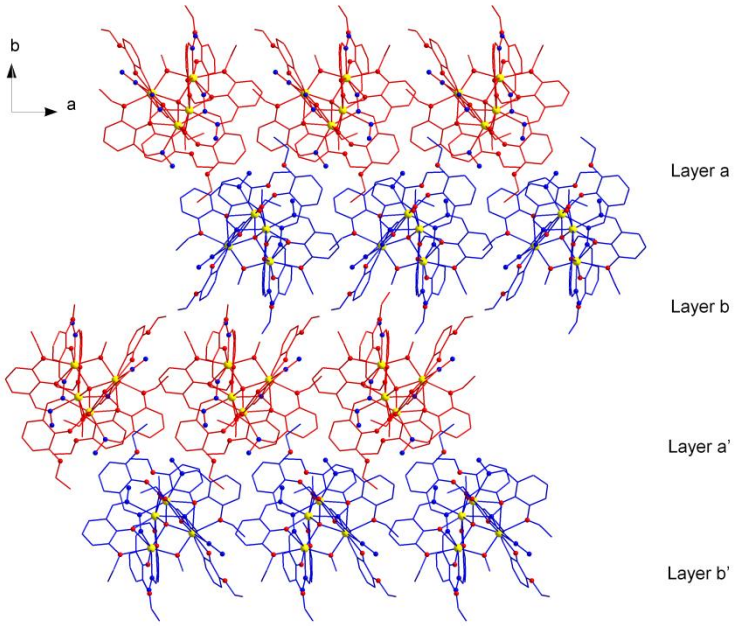


**Figure 5.26** Crystal packing diagram of complex **5-4** along the crystallographic *c* axis

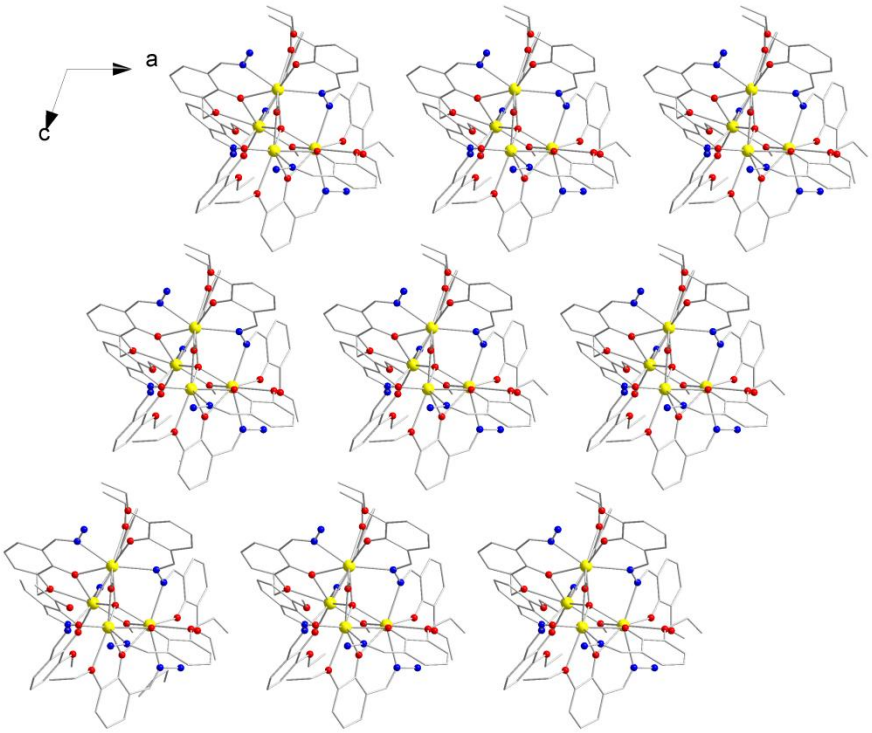


**Figure 5.27** Crystal packing diagram of complex **5-4** along the crystallographic *b* axis

The dc magnetic susceptibility of complex **1** was carried out on a freshly prepared sample at 1000 Oe between 2 and 300 K, plotted as $\chi T$ vs. $T$ (Figure 5.28). The observed paramagnetism arises from the 4f orbitals of the $Dy^{III}$ ion ($^6H_{15/2}$, $S$ = 5/2, $L$ = 5, $J$ = 15/2, $g$ = 4/3, $\chi T$ = 14.17 $cm^3.K.mol^{-1}$). The room temperature $\chi T$ value of 54.54 $cm^3.K.mol^{-1}$ is close to the expected value of 56.68 $cm^3.K.mol^{-1}$ for four noninteracting $Dy^{III}$ ions. As the temperature decreases, the $\chi T$ product of complex **5-4** remains constant down to 70 K. A negative deviation is clearly observed below 70 K, which suggests the presence of some intramolecular antiferromagnetic interactions between the $Dy^{III}$ ions. However, it should be noted that the thermal depopulation of Stark sublevels, crystal field effect and

strong spin-orbit coupling can also be partially or totally responsible for the rapid decrease in the $\chi T$ product. It is therefore difficult to establish, in a definitive manner, the nature of the intramolecule magnetic interactions by using SQUID measurements only. At lower temperatures, the $\chi T$ product further decreases to 12.26 $cm^3.K.mol^{-1}$ at 1.8 K for complex **5-4**.

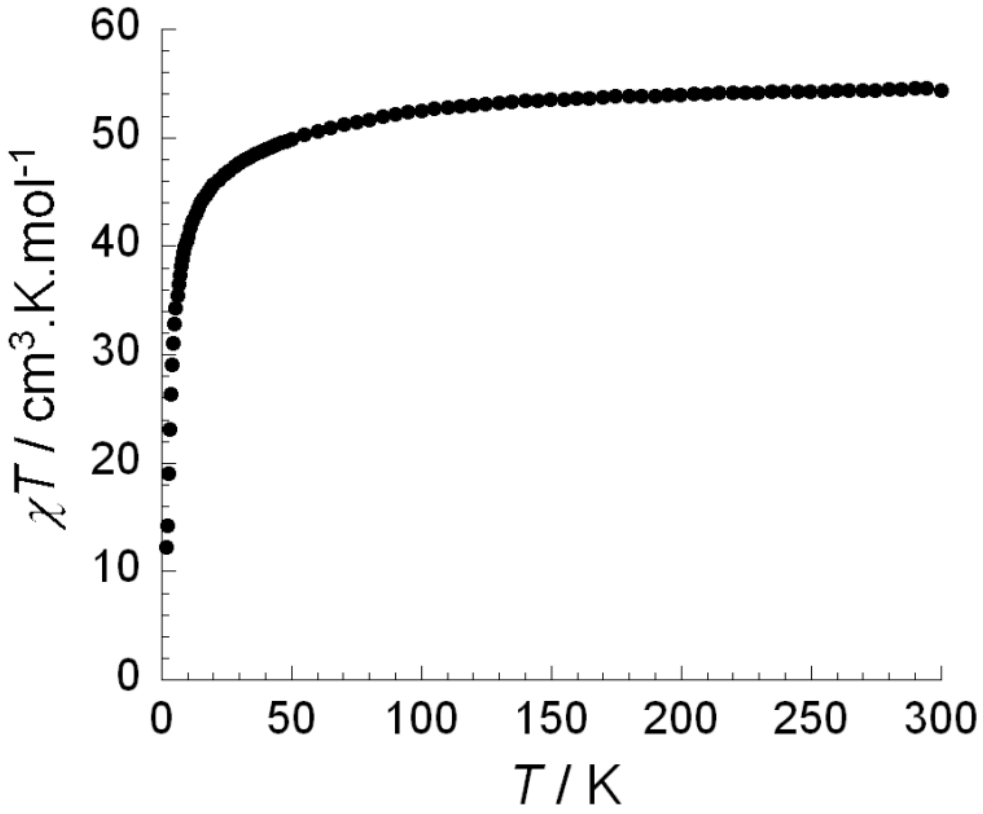


**Figure 5.28** Temperature dependence of the $\chi T$ product at 1000 Oe for complex **5-4** (with $\chi = M/H$ normalized per mol).

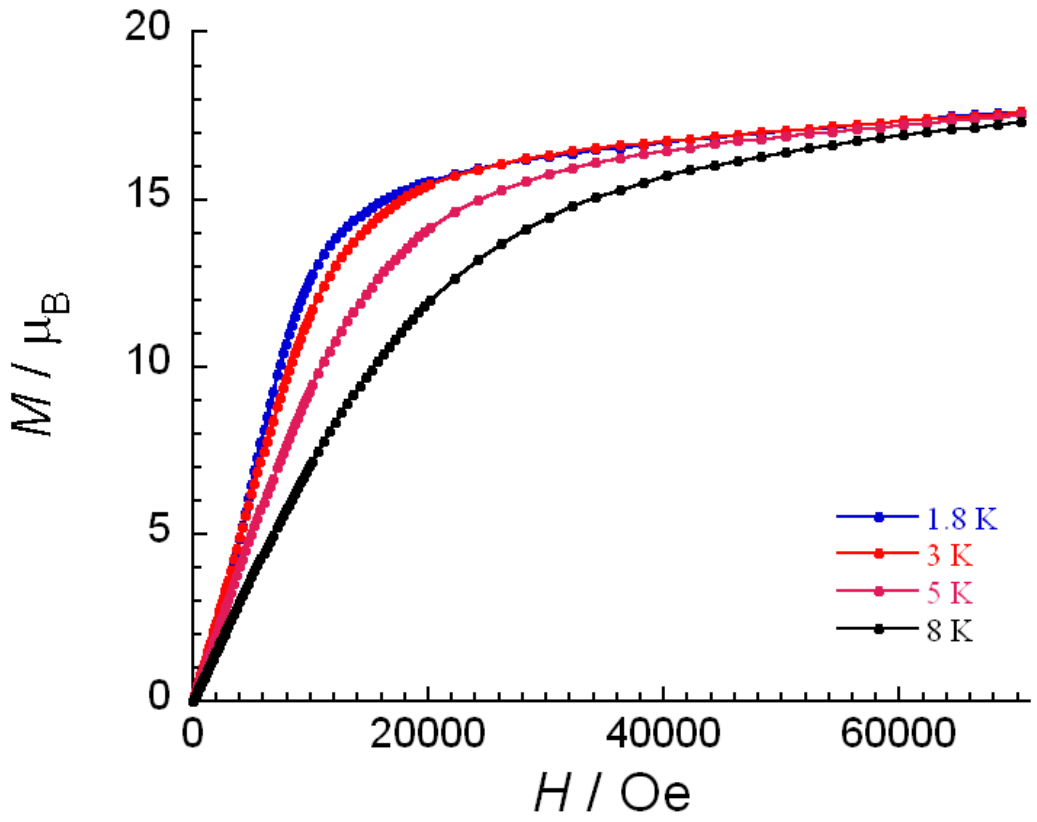


**Figure 5.29** Field dependence of the magnetization, *M*, at 1.8, 3, 5 and 8 K for complex **5-4**.

Field dependence of the magnetization, *M*, measurements shows non-saturation at low temperatures (1.8 K) and high magnetic fields (up to 7 T) (Figure 5.29). Additionally, the reduced magnetization plot, *M vs. H/T*, (Figure 5.30) at different temperatures shows magnetization curves that are not superimposable on a single mastercurve. These two figures are indicative of the presence of significant magnetoanisotropy or low-lying excited states in the molecule.

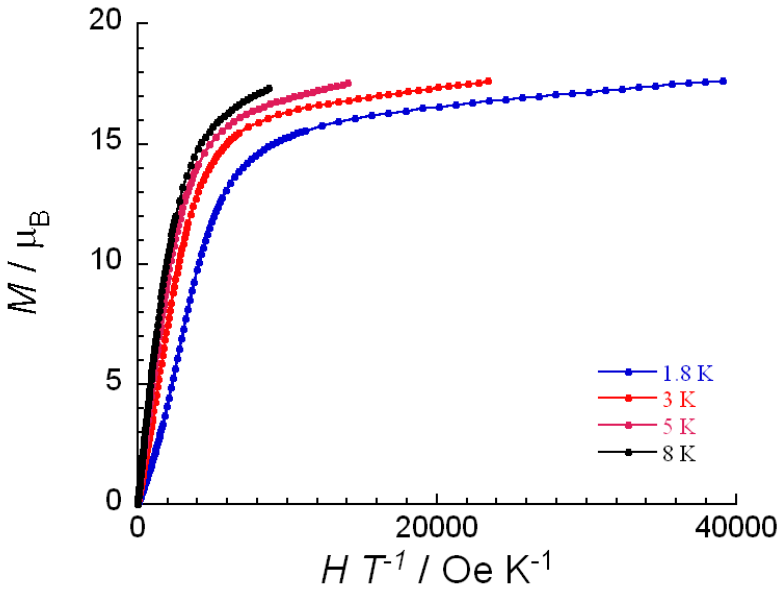


**Figure 5.30** The reduced magnetization plot for complex **5-4** measured at 1.8, 3, 5 and 8 K.

In order to investigate the possibility of SMM behavior, ac magnetic susceptibility measurements were carried out under zero dc field (Figure 5.31 and 5.32). A frequency dependent ac signal was observed below 15 K, which indicates slow relaxation of the magnetization of **5-4**, as expected for an SMM. Although a full frequency dependent peak was not observed, the maxima can be observed for a wide range of frequencies between 7 and 1.8 K. This range of data is sufficient to extract an energy barrier for complex **5-4**. The relaxation time deduced from this data is consistent with an activated behavior (Figure 5.33), with an energy gap of 24 K and a pre-exponential factor, $\tau_0$ of $8.2*10^{-8}$ s. Moreover, in order to shortcut the quantum tunneling of the magnetization

(QTM) which is commonly observed in lanthanide systems, ac measurements need to be carried out under an optimum dc field. However, there is no obvious peak shifting under the static dc fields from 0 – 2500 Oe at 2K (Figure 5.34). It is not necessary to measure the ac susceptibility with a static dc field.

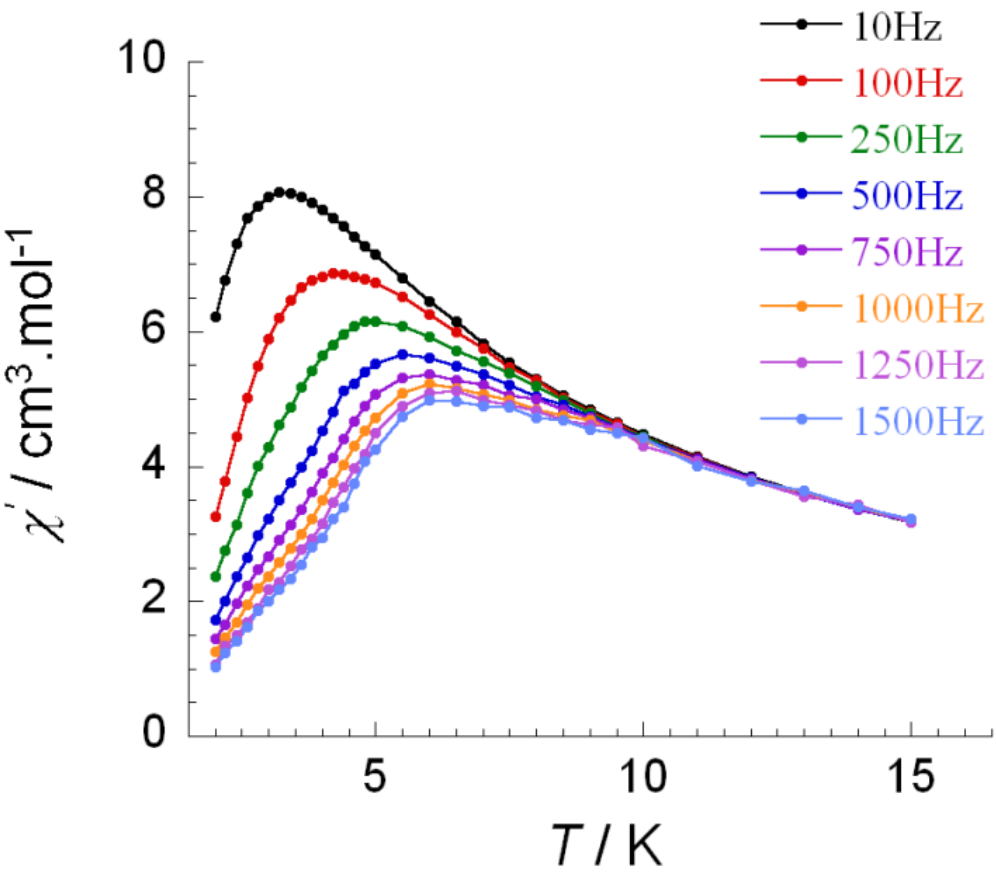


**Figure 5.31** In-phase susceptibility $\chi'$ *vs.* temperature $T$ in the frequencies range 10 - 1500 Hz under zero dc field for complex **5-4**.

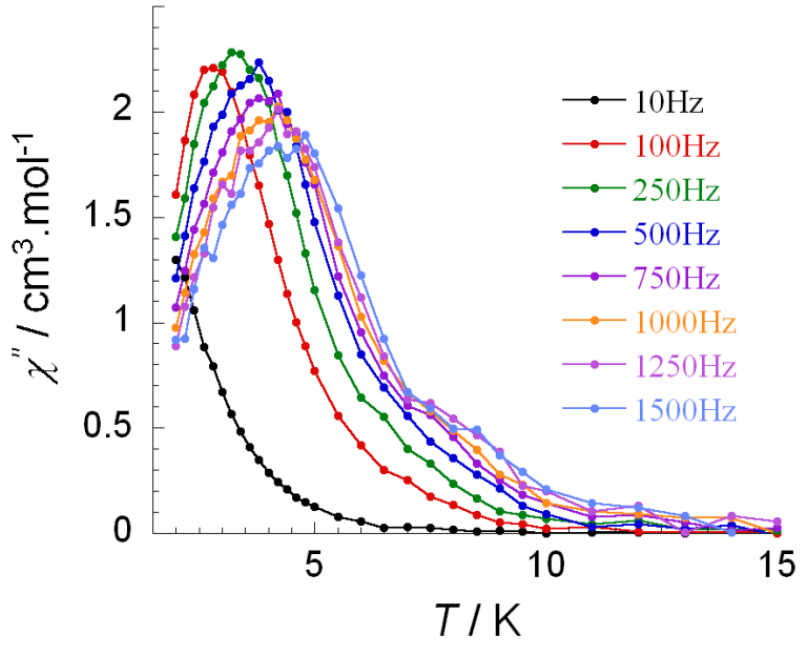


**Figure 5.32** Out-of-phase susceptibility $\chi''$ *vs.* temperature $T$ in the frequency range 10 - 1500 Hz under zero dc field for complex **5-4**.

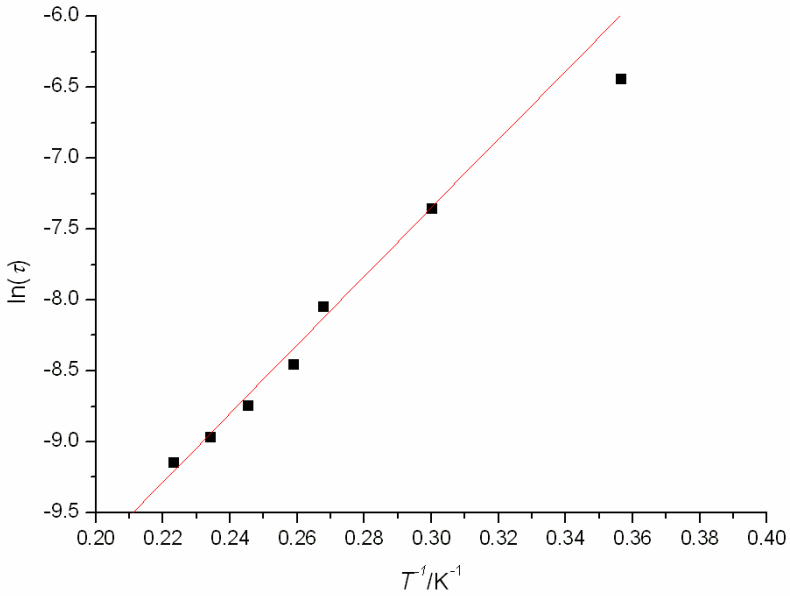


**Figure 5.33** Relaxation time of the magnetization ln($\tau$) *vs.* $T^{-1}$ (Arrhenius Plot using temperature-dependent ac data). The solid line corresponds to the fit.

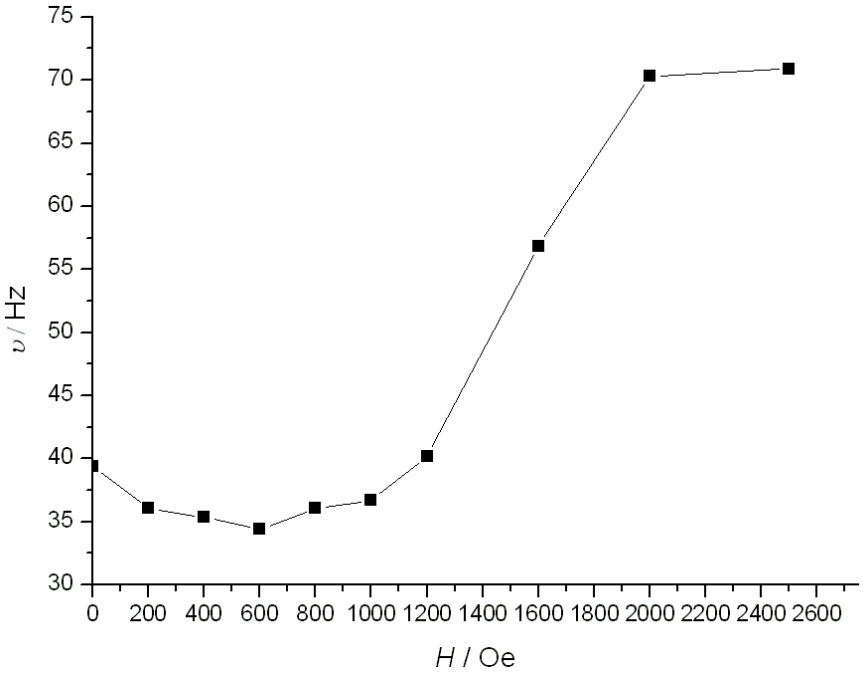


**Figure 5.34** Field dependence of the characteristic frequency (maximum of $\chi''$) as a function of the applied dc field for **5-4** at 2K. Line is guide for the eyes.

In order to investigate the low-temperature behavior, single-crystal dc magnetization measurements of complex **5-4** were carried out on a micro-SQUID magnetometer between 0.04 and 5 K (Figures 5.35 and 5.36). Temperature-dependent hysteresis loops with steps were observed with a large coercive field opening at very low temperatures ($H$c = 0.6 T at 0.04 K). The step at 0.5 T indicates the presence of resonant quantum tunnelling of the magnetization (QTM) and/or reversal of the magnetization of individual $Dy^{III}$ ions. The absence of a step at $H$ = 0 simply indicates that the QTM is less efficient at zero field. This shift of step position is most likely affected by the weak exchange

coupling present within the $Dy^{III}$ ions. This type of behavior is typical for lanthanide-based SMMs.

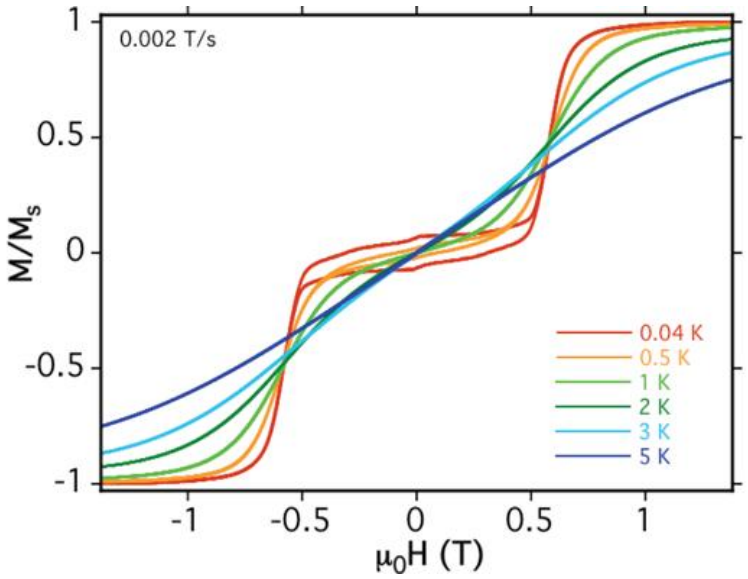


**Figure 5.35** Magnetization (*M*) *vs.* applied dc field sweeps at the sweep rate 0.002 T/s between 0.04-5 K.

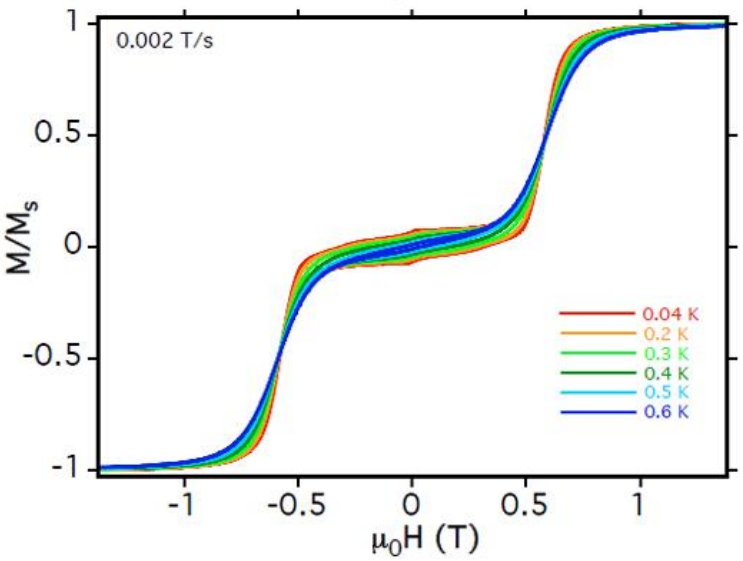


**Figure 5.36** Magnetization (*M*) *vs.* applied dc field sweeps at the sweep rate 0.002 T/s between 0.04-0.6 K.

As mentioned before, the slow relaxation of the magnetization originates mainly from the local anisotropy of the *4f* ions in pure lanthanide systems. Therefore, it is crucial to determine the direction of the local anisotropy axis on each $Dy^{III}$ site. At 300 K, the value of $\chi T$ is well approximated by the sum of the contributions of individual centers (Figure 5.37). The experimental susceptibility obtained is slightly higher than the calculated one at 300 K and experimental magnetic susceptibility is in good agreement with the calculated curves. The exchange coupling between magnetic ions was considered within the Lines approximation. For the simplicity of the model we have used a single exchange parameter to simulate all exchange interactions in the Dy4 system. The Lines parameter *J* of the exchange interaction between magnetic centers (dysprosium ions) was found to be $J$ = - 0.30 $cm^{-1}$. The simulation confirms the overall antiferromagnetic exchange coupling present between the $Dy^{III}$ ions, which can be correlated with the observed step in the hysteresis loop that occurs at 0.6 T. The *ab initio* calculated directions of the anisotropy axes for the four Dy sites are shown in Figure 5.38. The four anisotropic axes in complex **5-4** point in all different directions, which correlate with four crystallographically nonequivalent $Dy^{III}$ ions. The calculated *g* tensors on the $Dy^{III}$ sites which are also obtained for *ab initio* calculation are strongly anisotropic (Table 5.5), although less axial than in the previously investigated dysprosium complexes.

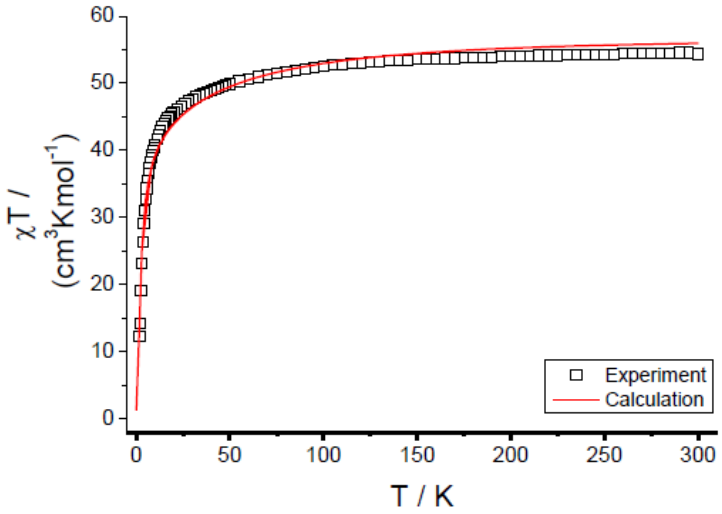


**Figure 5.37** A comparison between measured (empty squares) and calculated (red line) magnetic susceptibility for complex **5-4**.

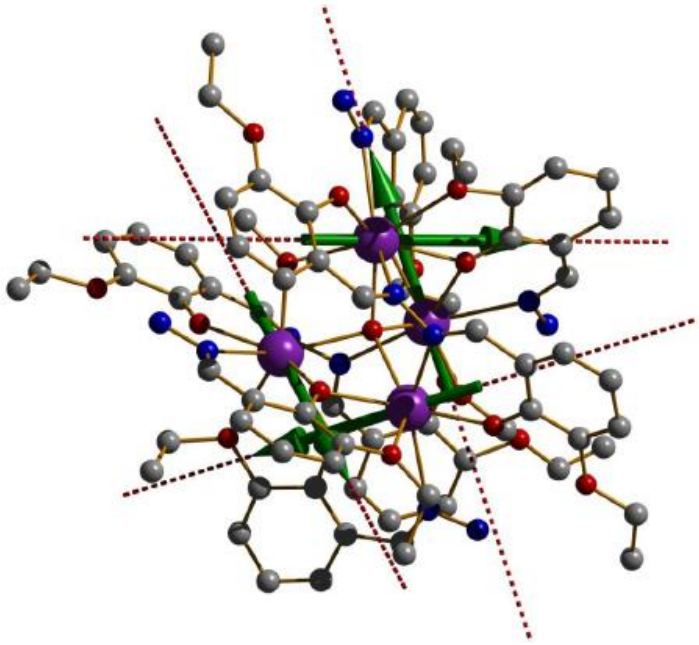

**Figure 5.38** Calculated magnetic axes corresponding to the lowest Kramers doublet. Green arrows show the orientation of the local magnetic moment in the ground state.

**Table 5.5** Main values of the *g*-tensor for the lowest two Kramers doublets.

| Kramers doublet | | Main value of *g* tensors | | | |
|---|---|---|---|---|---|
| | | Dy1 | Dy2 | Dy3 | Dy4 |
| 1 | $g_x$ | 0.1514 | 0.3235 | 0.1090 | 0.0766 |
| | $g_y$ | 0.4139 | 1.0767 | 0.2927 | 0.1558 |
| | $g_z$ | 18.4125 | 18.1889 | 18.5495 | 19.4623 |

# Conclusion

In this chapter, four tetranuclear $Ln^{III}$ complexes were reported to exhibit defect dicubane or tetrahedral metal cores. All of the ligands were formed *in situ* by Schiff-base reactions that allowed us to obtain unusual geometric complexes. With this synthetic stratagem, we were able to isolate defect-dicubane and tetrahedron core complexes with unique magnetic properties. Two stereoisomers are present as a racemic mixture of enantiomers in complex **5-4**.

Both complexes **5-1** and **5-4** exhibited SMM behavior; however, two relaxation processes can be seen for complex **5-1** in the ac susceptibility measurements. Complex **5-4** only exhibited one broad peak and a small shoulder in the out-of-phase ac plots. In

comparing the anisotropic energy barrier, the relaxation times of complex **5-1** are consistent with an activated behavior with effective energy barriers of $U_{eff}$ = 170 K for high-temperature dynamics which is much higher than complex **5-4**. The anisotropic axes of all $Dy^{III}$ sites in complexes **5-1** and **5-4** were estimated by *ab initio* calculations. Correlating the anisotropic axes to the result of ac susceptibility, it was apparent that the alignment of anisotropic axes is the key for synthesizing pure lanthanide SMMs with high energy barriers.

# Chapter 6

## Conclusion

In the present work, the synthesis, molecular structures and magnetic properties of multinuclear complexes have been discussed. The chapters are sequentially arranged in increasing nuclearity from mononuclear to tetranuclear $Ln^{III}$ complexes. A total of thirty lanthanide complexes were synthesized in an attempt to achieve high energy barrier SMMs. The molecular structures were characterized exclusively by single crystal X-ray crystallography and the magnetic properties were measured using a SQUID magnetometer.

In chapter 2, ten mononuclear $Ln^{III}$ complexes were reported to exhibit various coordination numbers. The rigid pockets created by the ligands we designed can form stable five- and six-membered rings when coordinated to metal ions. Various tautomeric forms of the ligands are present in the mononuclear complexes. Moreover, complex **2-10** is shown to have two lanthanide ions in the same molecule which are well-separated by coordinating to two isolated pockets. Complex **2-10** was shown to exhibit SMM behavior with $U_{eff}$ = 36 K under a static field of 1800 Oe.

In chapter 3, eleven dinuclear $Ln^{III}$ complexes were characterized structurally and magnetically. The dinuclear complexes were successfully synthesized with the same types of ligands by carefully tuning the reaction conditions. Additionally, in complexes **3-7** to **3-11**, the dinuclear units were linked by a pyridine moiety of the coordinating ligand, $H_2$hmi, forming 2-D network systems. Three complexes were shown to exhibit SMM behavior with $U_{eff}$ = 56, 71 and 130 K for complexes **3-6**, **3-9** and **3-11**, respectively. Complex **3-11** has one of the highest anisotropic energy barriers of dinuclear $Dy^{III}$ SMMs reported to date.

In chapter 4, five trinuclear $Ln^{III}$ complexes were reported. All complexes consisted of a triangular $Dy_3$ unit linked side-on *via* O bridges. Complexes **4-1**, **4-2**, **4-3** and **4-4** exist as two different isomers in their respective crystal structures. Ac signals were present in complexes **4-3**, **4-4** and **4-5**, but only complexes **4-4** and **4-5** behaved as SMMs with $U_{eff}$ = 8 and 80 K, respectively.

In chapter 5, four tetranuclear $Ln^{III}$ complexes were reported. The ligands were formed *in situ* by Schiff-base reaction of *o*-vanillin (complexes **5-1** to **5-3**) or 3-ethoxysalicylaldehyde (complex **5-4**) and hydrazine. Two different core geometries, defect-dicubane and tetrahedron, were observed. Complex **5-4** exists as two different isomers in the crystal structure where the resulting chirality is coordination-induced.

Complexes **5-1** and **5-4** were both shown to exhibit SMM behavior with two relaxation processes present in complex **5-1**. The energy barriers ($U_{eff}$) were calculated to be 170 and 24 K for complexes **5-1** and **5-4**, respectively. The anisotropic axes of all $Dy^{III}$ sites were also calculated and correlated to the SMM properties.

Due to the large anisotropy provided by spin orbital coupling from *4f* orbitals, lanthanide ions were shown to be good candidates in the synthesis of SMMs. Moreover, $Dy^{III}$ ions have shown SMM behavior whereas the $Eu^{III}$, $Gd^{III}$ and $Tb^{III}$ analogs did not. The two key components of SMMs are large spin ground state and large anisotropy. The spin ground state of $Eu^{III}$ is 0 while $Gd^{III}$ does not possess magnetic anisotropy due to its half-filled *f* orbitals. Therefore, these two elements are not good candidates for SMM synthesis. Moreover, the lack of SMM properties of $Tb^{III}$ complexes is due to the quantum tunneling at zero applied field which is commonly observed in metal ions with an integer spin. There are eight $Dy^{III}$ SMMs in this thesis where the energy barriers surpass what was previously achieved by transition-metal systems. Moreover, *ab initio* calculations indicated that the direction of the anisotropic axis is key in obtaining SMMs with high energy barriers. The presented results confirm the merit of a solely lanthanide approach to isolate higher anisotropic barrier SMMs. The large anisotropy provided by the $Dy^{III}$ ions with the careful choice of ligand was successful in SMM syntheses.

Multi-nuclear dysprosium complexes may have a chance to obtain record SMMs due to the introduction of more unpaired electrons and more anisotropy which are the two main requirements of SMMs. We are confident that the use of lanthanide metals in SMM chemistry will continue to pave the way towards even higher anisotropic barriers in the future.

In recent years the development of novel lanthanide-only SMMs introduces several questions that should be investigated: Why are large energy barriers seen for mononuclear lanthanide complexes? What is the correlation between the ligand field, the coordination geometry and the local anisotropy of the lanthanide ions? What is the role of the bridging groups between lanthanide centers where the interaction is weak due to the core nature of 4*f* orbitals? To understand these fundamental questions is as important as synthesizing new SMMs with high energy barriers. Our systems will have the potential to answer such important questions with the detailed magnetic measurements and *ab initio* calculations to be performed in the future.

Although the anisotropy of lanthanides is difficult to predict, molecules with low symmetry geometries may lead to strong anisotropy.[49] Mononuclear complexes can be

---

[49] Rinehart, J. D.; Long, J. R. *Chem. Sci.*, **2011**, *2*, 2078

simple, but useful, models in understanding the *f*-element electronic structure. Three rare geometries with diverse coordination environments of lanthanide complexes in chapter 2 will be good model candidates. Recently, Evans and Long have elegantly demonstrated that reduction introduces radical character into the bridging dinitrogen unit, drastically enhancing the magnetic properties of the molecules.[50] Even though the coupling between the lanthanide ions remains small through the super-exchange pathway, it is important to investigate analogous dinuclear systems with different types of bridging atoms. The rigid pockets of our ligand system that can coordinate the lanthanides will be a good premise on which to synthesize an entire series of analogues. Sulfur or tellurium can be selected instead of the phenoxide group of the ligand and the strength of the interaction can be further studied. We believe this may be the way forward in controlling the interactions between 4*f* ions and in further understanding the mechanism of SMMs.

An exciting new field in molecular magnetism is that of SMMs which holds the promise of revolutionizing molecular electronics, memory storage devices and quantum computing. The majority of reported SMMs have been prepared with transition-metal

---

[50] Rinehart, J. D.; Fang, M.; Evans, W. J.; Long, J. R. *J. Am. Chem. Soc.*, **2011**, *133*, 14236

ions although the recent application of a mixed transition-metal / lanthanide strategy has also yielded many structurally and magnetically interesting systems. There was a scarcity of lanthanide-only SMMs results when I started my PhD. research. My contribution to this project included synthesizing novel pure lanthanide complexes form mononuclear to tetranuclear lanthanide centers with seven, eight and nine coordination environments. Although only eight complexes exhibited SMM properties, the various geometries of the lanthanide centers are useful for further understanding the detailed magnetic behavior of lanthanide complexes. Complexes **3-9** and **5-1** also exhibited record anisotropic barriers when we published these discoveries.

During my fruitful graduate research, I have published 19 articles where 15 articles are directly related to lanthanide chemistry and/or SMMs. Two publications have been cited more than 100 times in the literature.

## Publication List in Reverse Date Order

1. Fatemah Habib, Jérôme Long, **Po-Heng Lin**, Ilia Korobkov, Liviu Ungur, Liviu F. Chibotaru, Muralee Murugesu,* "From Quadruply-Stranded Helicate to Mesocate Through Ligand Modification." *Chem. Sci.,* **2012**, *3,* 2158.

2. R. Thomas Baker*, John C. Gordon*, Charles W. Hamilton, Neil J. Henson, **Po-Heng Lin**, Muralee Murugesu, Brian L. Scott and Nathan C. Smythe, "Metal Complex-Catalyzed Ammonia-Borane Dehydrogenation. A Potential Route Towards B-N Containing Polymer Motifs Using Earth Abundant Metal Catalysts." *J. Am. Chem. Soc.*, **2012**, *134*, 5598..

3. Matthew Jeletic, **Po-Heng Lin**, Jennifer J. Le Roy, Ilia Korobkov, Muralee Murugesu,* "An Organometallic Sandwich Lanthanide Single-Molecule Magnet with an Unusual Multiple Relaxation Mechanism." *J. Am. Chem. Soc.*, **2011**, *133,* 19286. (Citations: 1)

4. **Po-Heng Lin**, Nathan C. Smythe, Serge Gorelsky, Steven Maguire, Neil J. Henson, Ilia Korobkov, Brian L. Scott, John C. Gordon, R. Tom Baker, Muralee Murugesu*, "Importance of Out-of-State Spin-Orbit Coupling for Slow Magnetic Relaxation in Mono-nuclear $Fe^{II}$ complexes." *J. Am. Chem. Soc.*, **2011**, *133,* 15806. (Citations: 5)

5. Titel Jurca, Ahmed Farghal, **Po-Heng Lin**, Ilia Korobkov, Muralee Murugesu*, Darrin S. Richeson,* "Inducing a Solution-Phase, Single-Molecule Magnet with a Single Metal Center through Peripheral Ligand Modifications." *J. Am. Chem. Soc.*, **2011**, *133*, 15814. (Citations: 6)

6. **Po-Heng Lin**, Wen-Bin Sun,* Mang-Fei Yu, Guang-Ming Li, and Peng-Fei Yan,* Muralee Murugesu,* "Unsymmetrical Coordination Environment Leading to Two Slow Relaxation Modes in $Dy_2$ Single-Molecule Magnets." *Chem. Commun.,* **2011**, *47*, 10993-10995. (Citations: 2)

7. Peng-Fei Yan, **Po-Heng Lin**, Fatemah Habib, Tomoko Aharen, Muralee Murugesu,* Zhao-Peng Deng, Guang-Ming Li, Wen-Bin Sun*, "A Planar Tetranuclear Dy(III) Single-Molecule Magnet and Its Sm(III), Gd(III) and Tb(III) Analogues Encapsulated By Salen-Type and β-Diketonate Ligands." *Inorg. Chem.,* **2011**, *50*, 7059-7065. (Citations: 3)

8. **Po-Heng Lin**, Sarah Eastman, Aman Bhatti, Melanie Brulotte, Tara J. Burchell, Ilia Korobkov, Gary Enright, Rodolphe Clérac and Muralee Murugesu*, "Polyalcohol Ligands in $Cu^{II}$ and $Fe^{III}$ Cluster Chemistry: Synthesis, Structures and Magnetic Properties of $\{Cu_{12}\}$ and $\{Fe_8\}$ Aggregates." *Inorg. Chim. Acta.*, **2011**, *375*, 187-192.

9. Fatemah Habib, **Po-Heng Lin**, Jérôme Long, Ilia Korobkov, Wolfgang Wernsdorfer

and Muralee Murugesu*, "Relaxing Together or Alone? : The Use of Magnetic Dilution to Elucidate the Slow Magnetic Relaxation Effects of a $Dy_2$ Single-Molecule Magnet." *J. Am. Chem. Soc.*, **2011**, *133*, 8830-8833. (Citations: 14)

10. Derek J. Reid, John E. W. Cull, Kimberley D. S. Chisholm, Alexandre Langlois, **Po-Heng Lin**, Jérôme Long, Olivier Lebel, Ilia Korobkov, Ruiyao Wang, James D. Wuest, Muralee Murugesu and Jennifer Scott*, "Synthesis, Structure and Magnetism of Homodinuclear Complexes of Co, Ni and Cu Supported by a Novel Bitriazine Scaffold." *Dalton Trans.*, **2011**, *40*, 5009-5017.
11. **Po-Heng Lin**, Ilia Korobkov, Wolfgang Wernsdorfer, Liviu Ungur, Liviu F. Chibotaru and Muralee Murugesu*, "A Rare $\mu_4$-O Centred $Dy_4$ Tetrahedra with Coordination-Induced Chirality and Single-Molecule Magnet Behaviour." *Eur. J. Inorg. Chem.*, **2011**, *2011*, 1535-1539. (Citations: 9)
12. Jérôme Long, Fatemah Habib, **Po-Heng Lin**, Ilia Korobkov, Gary Enright, Liviu Ungur, Wolfgang Wernsdorfer, Liviu F. Chibotaru and Muralee Murugesu*, "Single-Molecule Magnet Behavior for an Antiferromagnetically Superexchange-Coupled a Dinuclear Dysprosium(III) Complex." *J. Am. Chem. Soc.*, **2011**, *133*, 5319-5328. (Citations: 28)
13. **Po-Heng Lin**, Serge Gorelsky, Didier Savard, Tara J. Burchell, Wolfgang

Wernsdorfer, Rodolphe Clérac and Muralee Murugesu*, "Synthesis, Characterisation and Computational Studies on a Novel One-Dimensional Arrangement of Schiff-base $Mn_3$ Single-Molecule Magnet." *Dalton Trans*., **2010**, *39*, 7650-7658. (Citations: 2) (**CrystEngSelects** from across the RSC journals**)**

14. **Po-Heng Lin**, Mathieu Leclère, Jérôme Long, Tara J. Burchell, Ilia Korobkov, Rodolphe Clérac and Muralee Murugesu*, "Fluorescent Dialdehyde Ligand for the Encapsulation of Dinuclear Luminescent Lanthanide Complexes." *Dalton Trans*., **2010**, *39*, 5698-5704. (Citations: 3)
15. **Po-Heng Lin**, Tara J. Burchell, Liviu Ungur, Liviu Chibotaru, Wolfgang Wernsdorfer and Muralee Murugesu*, "A Polynuclear Lanthanide Single-Molecule Magnet with a Record Anisotropic Barrier." *Angew. Chem. Int. Ed.*, **2009**, *48*, 9489-9492. (Citations: 104)
16. Didier Savard, **Po-Heng Lin**, Tara J. Burchell, Wolfgang Wernsdorfer, Rodolphe Clérac and Muralee Murugesu*, "Two-Dimensional Networks of Lanthanide Cubane-Shaped Dumbbells." *Inorg. Chem.*, **2009**, *48*, 11748-11754. (Citations: 14)
17. Carolyn E. Burrow, Tara J. Burchell, **Po-Heng Lin**, Fatemah Habib, Wolfgang Wernsdorfer, Rodolphe Clérac and Muralee Murugesu*, "Salen-Based $[Zn_2Ln_3]$ Complexes with Fluorescence and Single Molecule Magnet Properties," *Inorg.*

*Chem.*, **2009**, *48*, 8051-8053. (Citations: 23)

18. **Po-Heng Lin**, Tara J. Burchell, Rodolphe Clérac* and Muralee Murugesu*, "Dinuclear Dysprosium(III) Single-Molecule Magnets with a Large Anisotropic Barrier." *Angew. Chem. Int. Ed.*, **2008**, *47*, 8848-8851. (Citations: 105)
19. M. N. Zhidkova, A. B. Ilyukhin, V. Yu. Kotov*, I. A. Stenina, **Po-Heng. Lin** and Muralee Murugesu, "Lead Bipyridyl Hexacyanoferrate Complex." *Russ. J. Inorg. Chem.*, DOI: 10.1134/S0036023611020318.

# Chapter 7

# Experimental

## 7.1 IR spectroscopy

Infrared analyses were obtained using a Nicolet Nexus 550 FT-IR spectrometer in the 4000-650 $cm^{-1}$ range. The spectra were recorded in the solid state by preparing KBr pellets.

## 7.2 X-ray crystallography

Crystals were grown from the solvent indicated in inorganic experimental section. A single crystal suitable for X-ray diffraction measurements was mounted on a glass fiber. Unit cell measurements and intensity data collections were performed on a Bruker-AXS SMART 1 k CCD diffractometer using graphite monochromatized Mo *K*αradiation (λ= 0.71073 Å). The data reduction included a correction for Lorentz and polarization effects, with an applied multi-scan absorption correction (SADABS). The crystal structure was solved and refined using the SHELXTL program suite. Direct methods yielded all non-hydrogen atoms which

were refined with anisotropic thermal parameters. All hydrogen atom positions were calculated geometrically and were riding on their respective atoms. The unit cell details will be present in next chapter.

## 7.3 Magnetic measurement

The magnetic susceptibility measurements were obtained with the use of a Quantum Design SQUID magnetometer MPMS-XL housed at the chemistry department, University of Ottawa. This magnetometer works between 1.8 and 400 K for dc applied fields ranging from -7 to 7 T. Measurements were performed on a polycrystalline samples. In order to prevent the loss of any solvent from the crystallization which will affected the sample weight and molecular weight, all samples are crushed from fresh crystals without drying in vacuum. We are confident using the molecular weight from X-ray structure for all the calculations of magnetic measurements. *M vs. H* measurements has been performed at 100 K to check for the presence of ferromagnetic impurities that has been found absent. ac susceptibility measurements have been measured with an oscillating ac field of 3 Oe and ac frequencies ranging from 1 to 1500 Hz. The magnetic data were corrected for the sample holder and the diamagnetic contributions. The micro-SQUID magnetic

measurements were obtained with the magnetometer housed at Institut Néel, CNRS & Université J. Fourier in France. Measurements were performed on single crystal samples.

## 7.4 Computational Details

The basis sets used for the calculations were taken from the ANO_RCC basis library included in MOLCAS program package. For magnetic electrons localized in the 4f orbitals of the metal sites the spin-orbit coupling and the crystal field are much stronger than the intramolecular exchange interaction, making these effects a priority in our study. The competition between the spin-orbit coupling, the crystal field, and the intrinsic multiconfigurational nature of the multi-electronic wave function of the 4*f* electrons can only be treated adequately by an explicitly correlated ab initio method. Therefore, we used a combined approach for studying magnetic properties of complexes which implies *ab initio* calculations of mononuclear lanthanide centers with a model description of the exchange interactions between the centers. This methodology has been already successfully applied for the calculation of the magnetic properties of other polynuclear complexes containing lanthanide and transition-metal ions.

The *ab initio* calculations on individual lanthanide fragments have been carried out with MOLCAS 7.4 program package. In this approach, the relativistic effects are treated in two steps, both based on Douglas-Kroll-Hess Hamiltonian. Scalar terms were included in the basis set generation and used to determine the spin-free wave functions and energies in the multiconfigurational self-consistent field (CASSCF) method. In the second step, spin_orbit interaction was taken into account within the restricted active space state interaction (RASSI) method, which uses the spin free multiconfigurational wave functions as input states. The obtained wave functions and energies of the molecular multiplets were used for the calculation of the anisotropic magnetic properties and the g tensors of the lowest states using a specially designed routine SINGLE-ANISO. As a result, the magnetic properties of a single magnetic ion are calculated by a fully *ab initio* approach, in which the spin_orbit coupling is considered nonperturbatively.

## 7.5 Ligand Synthesis

### 7.5.1 Preparation of (2-hydroxy-3-methoxyphenyl)methylene(isonicotino) hydrazine ($H_2$hmi)[29]

To a solution of isonicotinic acid hydrazide (0.02 mol, 2.75 g) in methanol (10

ml) was added a solution of *o*-vanillin (0.02 mol, 3.04 g) in methanol (10 ml). The mixture was stirred for 24 h at room temperature. The product, a yellow powder, was filtered, washed with cold methanol and dried *in vacuo* for 2 h. Yield = 95%. IR (KBr, $cm^{-1}$): 3449 (br), 3193(m), 2999 (m), 1682 (s), 1602 (m), 1563 (m), 1460 (m), 1411 (m), 1350 (w), 1286 (m), 1252 (br), 1158 (m), 1106 (s), 1079 (m), 1064, (m), 972 (s), 791 (s), 740 (m), 693 (m). NMR (DMSO-*d*6, 400 Mhz): 12.22 (s, 1H), 10.65 (s, 1H), 8.76 (d, 2H), 8.66 (s, 1H), 7.80 (d, 2H), 7.17 (d, 1H), 7.02 (d, 1H), 6.84 (t, 1H), 3.79 (s, 3H).

### 7.5.2 Preparation of (2-hydroxy-3-methoxyphenyl)methylenebenzohydrazine ($H_2$hmb)

To a solution of benzhydrazide (0.02 mol, 2.72 g) in methanol (10 ml) was added a solution of *o*-vanillin (0.02 mol, 3.04 g) in methanol (10 ml). The mixture was stirred for 24 h at room temperature. The product, a light yellow powder, was filtered, washed with cold methanol and dried *in vacuo* for 2 h. Yield = 85%. IR (KBr, $cm^{-1}$): 3421 (br), 3079(m), 1655(s), 1605(m), 1572(m), 1534(w), 1465(s), 1448(w), 1411(w), 1379(s), 1346(s), 1249(s), 1165(m), 1096(m), 1074(s), 1028(w), 972(m), 957(w), 953(m), 890(w), 873(w), 834(w), 804(s), 787(s), 775(m), 736(s),

717(s), 702(w).

### 7.5.3 Preparation of (2-hydroxy-3-methoxyphenyl)methylene(aceto) hydrazine ($H_2$hma)

To a solution of acetylhydrazide (0.02 mol, 1.48 g) in methanol (10 ml) was added a solution of *o*-vanillin (0.02 mol, 3.04 g) in methanol (10 ml). The mixture was stirred for 24 h at room temperature. The product, a light yellow powder, was filtered, washed with cold methanol and dried *in vacuo* for 2 h. Yield = 88%. IR (KBr, $cm^{-1}$): 3740 (br), 2943(m), 1742(w), 1680(s), 1607(s), 1576(s), 1534(w), 1513(w), 1467(s), 1433(s), 1393(s), 1351(s), 1334(s), 1255(s), 1190(w), 1169(m), 1152(m), 1199(s), 1078(s), 1030(s), 973(m), 956(w), 936(s), 870(m), 833(m), 782(s), 734(s), 700(w) and 663(w).

### 7.5.4 Preparation of (2-hydroxy-3-methoxyphenyl)methyleneformyl hydrazine ($H_2$hmf)

To a solution of formic acid hydrazide (0.02 mol, 1.20 g) in methanol (10 ml) was added a solution of *o*-vanillin (0.02 mol, 3.04 g) in methanol (10 ml). The mixture was stirred for 24 h at room temperature. The product, a light yellow powder, was filtered, washed with cold methanol and dried *in vacuo* for 2 h. Yield

= 88%. IR (KBr, $cm^{-1}$): 3447(br), 3079(m), 2950 (m), 1690(s), 1576(m), 1469(s), 1414(w), 1372(m), 1354(m), 1314(w), 1282(s), 1241(s), 1170(w), 1141(m), 1076(s), 1035(m), 966(m), 944(s), 834(m), 780(s), 744(s), 731(s) and 678(w).

### 7.5.5 Preparation of *N,N'*-bi(2-hydroxy-3-methoxybenzylidene)terephthalo hydrazide ($H_4$hmt)

A solution of terephthalic acid (0.5 g, 1.5 mmol) and MeOH (25 ml) was refluxed for 30 min. Thionyl chloride (9 ml) was added dropwise, and the mixture was maintained 10 hours under reflux. After being cooled to room temperature, the solvent was removed under reduced pressure. The mixture was extracted twice with ethyl ether (50 ml) and washed with a basic (potassium hydroxide) solution. The organic layers were dried over $MgSO_4$. The solvent was removed under reduced pressure to obtain white powder (dimethyl terephthalate). Yield = 82%. IR (KBr, $cm^{-1}$): 3421(br), 2960(m), 1723(s), 1540(w), 1499(m), 1434(s), 1404(m), 1383(w), 1278(s), 1258(s), 1194(m), 1108(s), 1018(s), 951(m), 879(m), 817(m) and 727(s).

A solution of dimethyl terephthalate (0.194 g, 1 mmol), $N_2H_2 \cdot H_2O$ (224 µl, 4 mmole) and MeOH (15 ml) was refluxed for 1 day. After being cooled to room temperature, the white product (terephthalohydrazide) was filtered, washed with

cold methanol and dried *in vacuo.* Yield = 68%. IR (KBr, $cm^{-1}$): 3317(s), 3027(w), 1724(m), 1694(w), 1616(s), 1562(w), 1534(s), 1488(s), 1431(m), 1404(w), 1378(w), 1338(s), 1281(s), 1193(m), 1106(s), 1016(m), 988(m), 958(w), 931(m), 874(w), 866(w), 825(w), 792(w), 737(w), 712(m) and 699(w).

To a solution of terephthalohydrazide (0.01 mol, 1.94 g) in methanol (10 ml) was added a solution of *o*-vanillin (0.02 mol, 3.04 g) in methanol (10 ml). The mixture was stirred for 24 h at room temperature. The product, a light yellow powder, was filtered, washed with cold methanol and dried *in vacuo* for 2 h. Yield = 75%. IR (KBr, $cm^{-1}$): 3425(br), 3037(w), 1718(m), 1650(s), 1604(m), 1572(m), 1463(m), 1433(w), 1403(w), 1380(w), 1359(w), 1326(w), 1277(s), 1246(s), 1197(w), 1148(w), 1106(m), 1076(m), 1017(m), 962(m), 896(w), 870(w), 828(w), 783(w), 737(m) and 716(m). $^1$H-NMR (DMSO-*d*6, 400 Mhz): $\delta$(ppm) 12.22 (s, 2H), 10.87 (s, 2H), 8.69 (d, $J$ = 5.3 Hz, 2H), 8.21 (m, 4H), 7.19(dd, $J$ = 7.8, 1.2 Hz, 2H) , 7.06 (dd, $J$ = 8.0, 1.2 Hz, 2H), 6.82 (t, $J$ = 8.0 Hz, 2H), 3.83 (s, 6H).

## 7.6 Inorganic Synthesis

### 7.6.1 Preparation of $[Tb(Hhmi)(NO_3)_2(MeOH)_2]$ (**2-1**)

A suspension of $Tb(NO_3)_3{\cdot}6H_2O$ (0.1162g, 0.25 mmol) and $H_2$hmi (0.068 g, 0.25 mmol) in MeOH (20 ml) was treated with pyridine (0.08 ml, 1 mmol). The

resulting pale yellow solution was stirred for a further 15 min, filtered, and the filtrate left undisturbed at room temperature. After two days, dark orange crystals suitable for X-ray were formed, collected by filtration, washed with MeOH and dried in vacuum. (Yield ~ 55%) Selected IR data for **2-1** (KBr, $cm^{-1}$): 3446(br), 3100(m), 1689(s), 1604(m), 1575(w), 1560(m), 1502(m), 1458(s), 1403(s), 1379(s), 1325(m), 1277(m), 1244(s), 1143(w), 1109(w), 1079(m),1034(m), 1003(m), 972(m), 894(m), 857(m), 778(m), 757(m) and 728(s).

### 7.6.2 Preparation of $[Ln(H_2hmi)(DMF)_2Cl_2]Cl \cdot 2(CH_3CN)$ (Ln: Tb(**2-2**) and Yb(**2-3**))

A solution of $Ln(NO_3)_3 \cdot 6H_2O$ (0.75 mmol, $Ln^{III}$=$Tb^{II}$ and $Yb^{III}$) in DMF (5 ml) was added slowly to a solution of $H_2hmi$ (0.135 g, 0.5 mmol) in MeCN (25 ml). The mixture was stirred for 5 min at room temperature and then filtered. After three days, X-ray-quality dark red needle crystals were formed, which were collected by filtration, washed with ether, and dried in vacuum. (Yield ~ 45%) The sample was maintained in contact with the mother liquor to prevent deterioration of the crystals, which have been identified crystallographically. Selected IR data for **2-2** (KBr, $cm^{-1}$): 3426(br), 1602(s), 1569(m), 1526(s), 1456(s), 1435(w), 1407(w), 1379(s), 1317(s),

1272(m), 1242(m), 1214(s), 1169(w), 1104(w), 1081(m), 1060(m), 1013(m), 960(m), 917(w), 850(m), 784(w), 739(m), 700(m) and 668(w). **2-3**: 3404(br), 1606(s), 1556(m), 1503(s), 1462(s), 1402(w), 1379(s), 1267(m), 1249(m), 1219(s), 1171(s), 1116(m), 1075(m), 1057(s), 1004(w), 908(m), 832(m), 793(w), 754(m) and 665(w).

### 7.6.3 Preparation of $[Dy(Hhmb)(DMF)_2Cl_2]$ (**2-4**·)

A solution of $DyCl_3 \cdot 6H_2O$ (0.942g, 0.25 mmol) in DMF (5 ml) was added slowly to a solution of $H_2hmb$ (0.068 g, 0.25 mmol) in DMF (5 ml). The mixture was stirred for 5 min at room temperature and then filtered. The filtrate was placed into a diethyl ether bath to help crystallization. After three days, X-ray-quality dark red needle crystals were formed, which were collected by filtration, washed with ether, and dried in vacuum. (Yield ~ 43%) The sample was maintained in contact with the mother liquor to prevent deterioration of the crystals, which have been identified crystallographically. Selected IR data for **2-4** (KBr, $cm^{-1}$): 3416(br), 3059(w), 2924(w), 1651(s), 1603(s), 1562(s), 1494(w), 1449(m), 1399(m), 1382(m), 1370(w), 1336(m), 1310(m), 1239(m), 1215(s), 1173(w), 1158(w), 1110(m), 1084(m), 1061(w), 1030(w), 972(w), 901(w), 868(w), 794(w), 747(m), 709(m) and 679(m).

### 7.6.4 Preparation of $[Ln(Hhmb)(bp)(NO_3)_2]\cdot MeCN$ (Ln: Tb(**2-5**), Dy(**2-6**) and Ho(**2-7**))

A solution of $Ln(NO_3)_3\cdot 6H_2O$ (0.25 mmol, $Ln^{III}$=$Tb^{III}$, $Dy^{III}$ and $Ho^{III}$) in MeOH (10 ml) was added slowly to a solution of $H_2$hmb (0.068 g, 0.25 mmol), 2,2'-Bipyridine (0.1171g, 0.75 mmol) in MeCN (20 ml). The mixture was stirred for 5 min at room temperature and then filtered. The filtrate was placed into a diethyl ether bath to help crystallization. After three days, X-ray-quality yellow cubic crystals were formed, which were collected by filtration, washed with ether, and dried in vacuum. (Yield ~ 53%) The sample was maintained in contact with the mother liquor to prevent deterioration of the crystals, which have been identified crystallographically. Selected IR data for **2-5**. **2-6** and **2-7** (KBr, $cm^{-1}$): 3436(br), 1607(s), 1565(s), 1546(m), 1494(s), 1477(w), 1462(m), 1450(w), 1437(m), 1395(m), 1385(s), 1286(s), 1239(s), 1217(s), 1160(w), 1110(m), 1082(m), 1063(w), 1028(m), 1015(m), 975(m), 899(m), 868(m), 815(m), 796(w), 761(s), 740(s), 707(m) and 687(s).

### 7.6.5 Preparation of $[Dy(Hhma)(DMF)_2Cl_2]$ (**2-8**)

A solution of $DyCl_3\cdot 6H_2O$ (0.047g, 0.125 mmol) in DMF (5 ml) was added

slowly to a solution of $H_2$hma (0.026 g, 0.125 mmol) and pyridine (0.08 ml, 1mmol) in THF (15 ml). The mixture was stirred for 5 min at room temperature and then filtered. The filtrate was placed into a diethyl ether bath to help crystallization. After three days, X-ray-quality dark red needle crystals were formed, which were collected by filtration, washed with ether, and dried in vacuum. (Yield ~ 33%) The sample was maintained in contact with the mother liquor to prevent deterioration of the crystals, which have been identified crystallographically. Selected IR data for **2-8** (KBr, $cm^{-1}$): .3425(br), 3162(m), 3037(s), 1652(s),1636(s), 1619(w), 1596(s), 1567(m), 1541(m), 1498(m), 1460(m), 1424(m), 1388(s), 1378(s), 1332(m), 1299(w), 1232(s), 1218(s), 1185(w), 1167(w), 1113(s), 1080(m), 1015(w), 973(w), 862(m), 734(m) and 678(m).

### 7.6.6 Preparation of $[Dy(hmf)(DETA)_2]Cl \cdot 2CH_2Cl_2 \cdot MeOH$ (**2-9**)

A solution of $DyCl_3 \cdot 6H_2O$ (0.094g, 0.25 mmol) in MeOH (5 ml) was added slowly to a solution of $H_2$hmf (0.049 g, 0.25 mmol) and diethyltriamine (0.108 ml, 1mmol) in $CH_2Cl_2$ (25 ml). The mixture was stirred for 5 min at room temperature and then filtered. The filtrate was placed into a diethyl ether bath to help crystallization. After three days, X-ray-quality dark red needle crystals were formed,

which were collected by filtration, washed with ether, and dried in vacuum. (Yield ~ 29%) The sample was maintained in contact with the mother liquor to prevent deterioration of the crystals, which have been identified crystallographically. Selected IR data for **2-9** (KBr, $cm^{-1}$): 3260(s), 2991(br), 1895(w), 1599(w), 1572(s), 1598(s), 1445(m), 1450(w), 1374(w), 1342(m), 1316(m), 1229(w), 1146(s), 1133(s), 1117(s), 1082(s), 1059(m), 1019(w), 1006(w), 984(m), 961(m), 892(s), 872(w), 834(w) and 766(s).

### 7.6.7 Preparation of $[Dy(H_2hmt)(NO_3)_4(DMF)_2]$ (**2-10**)

A solution of $Dy(NO_3)_3{\cdot}6H_2O$ (0.057 g, 0.125 mmol) in DMF (5 ml) was added slowly to a solution of $H_2hmt$ (0.058 g, 0.125 mmol) in THF (25 ml). The mixture was stirred for 5 min at room temperature and then filtered. After three days, X-ray-quality red plate crystals were formed, which were collected by filtration, washed with ether, and dried in vacuum. (Yield ~ 30%) The sample was maintained in contact with the mother liquor to prevent deterioration of the crystals, which have been identified crystallographically. Selected IR data for **2-10** (KBr, $cm^{-1}$): 3436(br), 1663(s), 1604(s), 1545(w), 1459(m), 1442(m), 1414(w), 1383(s), 1295(m), 1250(m), 1219(m), 1170(w), 1115(m), 1086(m), 1058(w), 1030(w), 979(w), 887(w), 859(w),

815(w), 742(m) and 718(w).

### 7.6.8 Preparation of $[Dy_2(Hhmb)_2(NO_3)_4]\cdot MeCN$ (**3-1**)

A suspension of $Dy(NO_3)_3\cdot 6H_2O$ (0.114 g, 0.25 mmol) and $H_2hmb$ (0.068 g, 0.25 mmol) in MeCN/MeOH (20 ml : 10 ml) was treated with pyridine (0.081 ml, 1 mmol). The resulting yellow solution was stirred for a further 15 min, filtered, and the filtrate left undisturbed at ambient temperature. After two days, X-ray quality pale yellow crystals were formed, collected by filtration, washed with a MeCN/MeOH mixture, and dried in vacuum. (Yield ~ 42%) Selected IR data for **3-1** (KBr, $cm^{-1}$): 3425(br), 1606(s), 1573(s), 1517(s), 1489(w), 1460(s), 1399(s), 1381(s), 1285(s), 1238(m), 1215(s), 1085(m), 1027(m), 960(m), 899(m), 851(m), 841(m), 778(m), 747(m), 734(w), 711(m), 686(w) and 668(w).

### 7.6.9 Preparation of $[Dy_2(Hhmb)_2(NO_3)_4(N_3)_2(MeOH)]\cdot 2MeOH$ (**3-2**)

A suspension of $Dy(NO_3)_3\cdot 6H_2O$ (0.114 g, 0.25 mmol), $H_2hmb$ (0.068 g, 0.25 mmol) and $NaN_3$ (0.049 g, 0.75 mmol) in MeOH (10 ml) was treated with pyridine (0.081 ml, 1 mmol). The resulting yellow solution was stirred for a further 5 min, filtered, and the filtrate left undisturbed at ambient temperature. After two days, X-ray quality pale yellow crystals were formed, collected by filtration, washed with

a MeOH mixture, and dried in vacuum. (Yield ~ 42%) Selected IR data for **3-2** (KBr, $cm^{-1}$): 3441(br), 2113(s), 2060(s), 1607(s), 1567(s), 1491(w), 1458(s), 1438(w), 1402(m), 1383(s),1296(s), 1240(m), 1218(s), 1167(m), 1106(w), 1086(m), 1061(w), 1026(m), 969(m), 904(m), 855(m), 812(w), 798(w), 780(w), 743(m) and 706(m).

### 7.6.10 Preparation of $[Dy_2(Hhma)_3(NO_3)_3 \cdot CH_3CN] \cdot 2MeOH$ (**3-3**)

A suspension of $Dy(NO_3)_3 \cdot 6H_2O$ (0.114 g, 0.25 mmol) and $H_2hma$ (0.052 g, 0.25 mmol) in MeOH/MeCN (5 ml : 25 ml) was treated with $Et_3N$ (0.033 ml, 0.25 mmol). The resulting pale yellow solution was stirred for a further 15 min, filtered, and the filtrate left undisturbed at room temperature. After two days, pale orange crystals suitable for X-ray were formed, collected by filtration, washed with MeOH and dried in vacuum. (Yield ~ 36%) Selected IR data for **3-3** (KBr, $cm^{-1}$): 3436(br), 3240(s), 3094(s), 2851(w), 1615(s), 1565(s), 1525(s), 1509(w), 1451(s), 1399(s), 1315(s), 1268(s), 1239(s), 1219(s), 1204(w), 1173(w), 1117(w), 1094(m), 1071(s), 1040(m), 1025(s), 1004(m), 977(m), 938(s), 846(m), 810(m), 792(s), 740(s) and 681(m).

### 7.6.11 Preparation of $[Ln_2(hmi)_2(NO_3)_2(MeOH)_4]$ (Ln: Eu(**3-4**) and Tb(**3-5**))

A suspension of $Ln(NO_3)_3{\cdot}6H_2O$ (0.37 mmol, $Ln^{III}$=$Eu^{III}$, $Tb^{III}$) and $H_2$hmi (0.068 g, 0.25 mmol) in MeOH (20 ml) was treated with $Et_3N$ (0.141 ml, 1 mmol). The resulting pale yellow solution was stirred for a further 15 min, filtered, and the filtrate left undisturbed at room temperature. After two days, pale orange crystals suitable for X-ray were formed, collected by filtration, washed with MeOH and dried in vacuum. (Yield ~ 35%) The sample remained in contact with the mother liquor to prevent deterioration of the crystals, which have been identified crystallographically as **3-4** and **3-5**. Selected IR data for **3-4** (KBr, $cm^{-1}$): 3405(br), 1616(w), 1603(s), 1572(m), 1519(s), 1459(s), 1436(w), 1408(s), 1381(s), 1370(w), 1268(m), 1242(m), 1217(s), 1099(w), 1079(m), 1059(m), 1015(m), 960(m), 917(w), 811(w), 846(m), 822(s), 784(w), 738(m), 697(m). **3-5** (KBr, $cm^{-1}$): 1603(s), 1572(m), 1562(w), 1521(s), 1456(s), 1435(w), 1410(w),1383(s), 1325(s), 1325(s), 1272(m), 1242(m), 1216(s), 1168(w), 1103(w), 1078(m), 1062(m), 1011(m), 958(m), 917(m), 847(m), 822(m), 783(m), 751(m), 739(m), 702(m), 668(w).

### 7.6.12 Preparation of $[Dy_2(hmi)_2(NO_3)_2(MeOH)_2]$ (**3-6**)

A suspension of $Dy(NO_3)_3{\cdot}6H_2O$ (0.168g, 0.37 mmol) and $H_2$hmi (0.068 g, 0.25 mmol) in MeOH (20 ml) was treated with $Et_3N$ (0.141 ml, 1 mmol). The

resulting pale yellow solution was stirred for a further 15 min, filtered, and the filtrate left undisturbed at room temperature. After two days, pale orange crystals suitable for X-ray were formed, collected by filtration, washed with MeOH and dried in vacuum. (Yield ~ 35%) Selected IR data for **3-6** (KBr, $cm^{-1}$): 3421(br), 1601(s), 1572(m), 1521(s), 1458(s), 1407(w), 1381(s), 1328(w), 1267(w), 1240(m), 1219(s), 1169(w), 1097(w), 1076(m), 1057(m), 1010(w), 959(m), 907(w), 845(m), 783(w), 741(s), 695(m).

### 7.6.13 Preparation of $[Ln_2(hmi)_2(NO_3)_2(MeOH)_2]_\infty \cdot MeCN$ (Ln: Eu (**3-7**), Tb(**3-8**) and Dy(**3-9**))

A suspension of $Ln(NO_3)_3 \cdot 6H_2O$ (0.25 mmol, $Ln^{III}=Eu^{III}$, $Tb^{III}$ and $Dy^{III}$) and $H_2hmi$ (0.068 g, 0.25 mmol) in MeCN/MeOH (15 ml : 5 ml) was treated with pyridine (0.081 ml, 1 mmol). The resulting yellow solution was stirred for a further 15 min, filtered, and the filtrate left undisturbed at ambient temperature. After two days, X-ray quality pale orange crystals were formed, collected by filtration, washed with a MeCN/MeOH mixture, and dried in vacuum. (Yield ~ 40%) The sample remained in contact with the mother liquor to prevent deterioration of the crystals, which have been identified crystallographically as the polymers **3-7**, **3-8** and **3-9**.

Selected IR data for **3-7** (KBr, $cm^{-1}$): 3403(br), 1605(s), 1570(m), 1549(w), 1522(s), 1457(s), 1383(s), 1312(m), 1266(w), 1241(m), 1215(m), 1172(w), 1079(m), 1059(w), 1038(w), 1012(m), 959(m), 910(w), 849(m), 789(w), 745(m), 706(m), 673(w). **3-8** (KBr, $cm^{-1}$): 3414(br), 1621(w), 1603(s), 1575(m), 1561(w), 1520(s), 1458(s), 1439(w), 1409(w), 1384(s), 1370(w), 1324(m), 1270(m), 1241(m), 1218(s), 1169(w), 1098(w), 1084(m), 1061(w), 1015(m), 963(m), 918(w), 885(w), 823(w), 786(w), 740(m), 698(m). **3-9** (KBr, $cm^{-1}$): 3415(br), 1610(s), 1572(m), 1522(s), 1459(s), 1383(s), 1307(m), 1263(m), 1244(m), 1221(m), 1077(m), 1013(w), 961(w), 914(w), 855(w), 789(w), 740(m), 704(m), 688(w).

### 7.6.14 Preparation of $[Gd_2(hmi)_2(NO_3)_2(H_2O)_2]_\infty \cdot MeOH$ (**3-10**)

A suspension of $Gd(NO_3)_3 \cdot 6H_2O$ (0.113g, 0.25 mmol) and $H_2hmi$ (0.068 g, 0.25 mmol) in MeCN/MeOH (15 ml : 5 ml) was treated with pyridine (0.081 ml, 1 mmol). The resulting yellow solution was stirred for a further 15 min, filtered, and the filtrate left undisturbed at ambient temperature. After two days, X-ray quality pale orange crystals were formed, collected by filtration, washed with a MeCN/MeOH mixture, and dried in vacuum. (Yield ~ 38%) The sample remained in contact with the mother liquor to prevent deterioration of the crystals, which have

been identified crystallographically as the polymers **3-10**. Selected IR data for **3-10** (KBr, $cm^{-1}$): 3435(br), 2596(w), 1603(s), 1575(m), 1557(w), 1522(s), 1458(s), 1439(w), 1407(w), 1380(s), 13324(m), 1271(m), 1239(m), 1218(s), 1167(w), 1103(w), 1082(m), 1059(w), 1016(m), 962(m), 919(w), 850(m), 819(w), 785(m), 742(s).

### 7.6.15 Preparation of $[Dy_2(hmi)_2(N_3)_2(MeOH)_2]_\infty \cdot 2MeOH$ (**3-11**)

A suspension of $DyCl_3 \cdot 6H_2O$ (0.091g, 0.25 mmol) and $H_2$hmi (0.068 g, 0.25 mmol) in MeOH (30 ml) was treated with $NaN_3$ (0.065 g, 1 mmol). The resulting yellow solution was stirred for a further 20 min, filtered, and the filtrate left undisturbed at ambient temperature. After two days, X-ray quality pale orange crystals were formed, collected by filtration, washed with MeOH and dried in vacuum. (Yield ~ 26%) The sample was maintained in contact with the mother liquor to prevent deterioration of the crystals, which have been identified crystallographically as the polymer **3-11**. Selected IR data for **3-11** (KBr, $cm^{-1}$): 3379(br), 2076(s), 1605(s), 1564(s), 1517(s), 1410(s), 1388(m), 1362(m), 1264(m), 1243(m), 1217(s), 1170(w), 1150(w), 1098(w), 1078(m), 1057(w), 1010(m), 959(m), 917(w), 845(m), 788(w), 746.55(m), 700(m).

### 7.6.16 Preparation of $3N(CH_3)_4[Ln_3(hmf)_6]\cdot 2CH_3OH\cdot H_2O$ (Ln: Dy(**4-1**), Tb(**4-2**))

A solution of $Ln(NO_3)_3\cdot 6H_2O$ (0.125 mmol, $Ln^{III}$=$Dy^{III}$ and $Tb^{III}$) in MeOH (2.5 ml) was added slowly to a solution of TMAOH (0.183 g, 1 mmol) , formic acid hydrazide (0.015g, 0.25 mmol) and o-vanillin (0.0380g, 0.25 mmol) in $CH_2Cl_2$(25 ml) and MeOH (2.5 ml). The mixture was stirred for 5 min at room temperature and then filtered. After three days, X-ray-quality pale yellow needle crystals were formed, which were collected by filtration, washed with ether, and dried in vacuum. (Yield ~ 22%) The sample was maintained in contact with the mother liquor to prevent deterioration of the crystals, which have been identified crystallographically. Selected IR data for **4-1** and **4-2** (KBr, $cm^{-1}$): 3426(br), 3012(w), 1639(m), 1607(s), 1486(s), 1463(w), 1443(m), 1384(m), 1343(m), 1259(w), 1233(w), 1207(w), 1106(w), 1082(w), 998(w), 950(s), 857(m) and 732(m).

### 7.6.17 Preparation of $3N(CH_3)_4[Dy_3(hef)_6]\cdot 2CH_3OH\cdot H_2O$ (**4-3**)

A solution of $Dy(NO_3)_3\cdot 6H_2O$ (0.057g, 0.125 mmol) in MeOH (2.5 ml) was added slowly in a solution of tetramethylammonium hydroxide (0.183 g, 1 mmol) , formic acid hydrazide (0.015g, 0.25 mmol) and 3-ethoxysalicylaldehyde (0.0415g,

0.25 mmol) in $CH_2Cl_2$(25 ml) and MeOH (2.5 ml). The mixture was stirred for 5 min at room temperature and then filtered. After four days, X-ray-quality pale orange crystals were formed, which were collected by filtration, washed with ether, and dried in vacuum. (Yield ~ 25%) The sample was maintained in contact with the mother liquor to prevent deterioration of the crystals, which have been identified crystallographically. Selected IR data for **4-3** (KBr, $cm^{-1}$): 3447(br), 2909(w), 1609(s), 1560(s), 1488(m), 1447(m), 1385(s), 1346(m), 1316(w), 1264(w), 1240(m), 1212(m), 1117(w), 1045(w), 1021(w), 990(w), 943(m), 900(w), 861(m) and 740(m).

### 7.6.18 Preparation of $[Dy_3(\mu_3\text{-}OMe)(hbb)_3(NO_3)(CH_3OH)_2]\cdot 3(NO_3)\cdot 5(CH_3OH)$ (**4-4**)

To a solution of $Dy(NO_3)_3\cdot 6H_2O$ (0.114 mg, 0.25 mmol) in MeOH (15 ml) was added to a solution of 2-hydroxyisophthaldehyde (0.019 g, 0.125 mmol), tetraethylammonium hydroxide (152 µl, 0.25 mmol) and benzhydrazide (0.034 g, 0.25 mmol) in MeOH (15 ml) while stirring. The resulting clear yellow solution was stirred for 30 s and then filtered. After 2–3 weeks, yellow needle-shaped crystals of complex **4-4** were isolated. Yield ≈ 17%. Selected IR data for **4-4** (KBr, $cm^{-1}$): 3410 (br.), 3027(w), 1620(s), 1572(s), 1491(w), 1435(m), 1379(s), 1313(m), 1236(m),

1189(w), 1143(w), 1078(m), 1043(w), 1024(m), 973(w), 902(w), 881(m), 838(w), 801(w), 765(m), 715(m) and 687(m).

### 7.6.19 Preparation of $[Dy_3(\mu_3\text{-}OH)_2(\mu\text{-}OMe)(hmi)_2(MeOH)_4(H_2O)_2]\cdot Cl_2$ (**4-5**)

A suspension of $DyCl_3\cdot 6H_2O$ (0.141 g, 0.37 mmol) and $H_2$hmi (0.068 g, 0.25 mmol) in MeOH (15 ml) was treated with $Et_3N$ (76 μL, 0.5 mmol). The resulting pale yellow solution was stirred for a further 15 min, filtered, and the filtrate left undisturbed at room temperature. After two days, X-ray-quality light yellow crystals were formed from ether bath, which were collected by filtration, washed with MeOH, and dried in vacuum. The sample was maintained in contact with the mother liquor to prevent deterioration of the crystals, which have been identified crystallographically as **4-5**. Selected IR data for **4-5** (KBr, $cm^{-1}$): 3374(br), 1628(w), 1605(s), 1564(m), 1548(m), 1518(w), 1499(w), 1456(s), 1414(m), 1399(m), 1316(w), 1299(m), 1222(s), 1169(w), 1104(w), 1081(m), 1008(m), 958(w), 903(w), 851(w), 785(w), 767(m), 696(m).

### 7.6.20 Preparation of $[Ln_4(\mu_3\text{-}OH)_2(bmh)_2(msh)_4Cl_2]$ (Ln: Dy(**5-1**), Tb(**5-2**) and Ho(**5-3**))

A suspension of $LnCl_3 \cdot 6H_2O$ (0.125 mmol, $Ln^{III}$=$Dy^{III}$, $Tb^{III}$ and $Ho^{III}$) and o-vanillin (0.038g, 0.25 mmol) in DMF/$CH_2Cl_2$ (5 ml/25 ml) was treated with $Et_3N$ (76 μL, 0.5 mmol). The solution was stirred for 1 min, and then $N_2H_4 \cdot H_2O$ (26 μL, 0.5 mmol) was added. The resulting pale-yellow solution was stirred for a further 15 min and then filtered, and the filtrate was left undisturbed. After 2 days, rectangular, X-ray-quality orange-yellow crystals of the tetranuclear complexes were formed ~ 19.1% yield. The sample was maintained in contact with the mother liquor to prevent deterioration of the crystals, which were identified crystallographically as **5-1**, **5-2** and **5-3**. Selected IR data for **5-1**, **5-2** and 5-3 (KBr, $cm^{-1}$): 3441(br), 1647(m), 1603(2), 1576(w), 1537(m), 1465(s), 1381(w), 1332(w), 1298(w), 1238(s), 1217(m), 1170(m), 993(w), 965(w), 851(w), 778(w), 731 (m).

### 7.6.21 Preparation of $[Dy_4(\mu_4\text{-}O)(\mu\text{-}OMe)_2(beh)_2(esh)_4] \cdot 3MeOH$ (**5-4**)

To a solution of 3-ethoxysalicylaldehyde (41.4 mg, 0.25 mmol) in MeOH (30 ml) was added $DyCl_3 \cdot 6H_2O$ (47.1 mg, 0.125 mmol), $Et_3N$ (76 μL, 0.5 mmol) and then $N_2H_4 \cdot H_2O$ (26 μL, 0.5 mmol) while stirring. The resulting clear yellow solution was stirred for 30 s and then filtered. After 2–3 weeks, yellow needle-shaped crystals of complex **5-4** were isolated. Yield ≈ 19.1%. Selected IR data for **5-4** (KBr, $cm^{-1}$):

3431 (br.), 3234 (w), 1610 (s), 1543 (m), 1460 (s), 1383 (w), 1321 (m), 1217 (s), 1109 (m), 1067 (m), 1015 (w), 886 (w), 850 (w), 778 (w), 731 (s).

# Chapter 8

## Crystal structure data

The crystal data and refinement parameters are listed in this chapter. All information is extracted from the cif files of complexes.

| Complex | **2-1** | **2-2** | **2-3** | **2-4** |
|---|---|---|---|---|
| Formula | $C_{16}H_{20}N_5O_{11}Tb$ | $C_{24}H_{33}Cl_3N_7O_5Tb$ | $C_{24}H_{33}Cl_3N_7O_5Yb$ | $C_{21}H_{27}Cl_2DyN_4O_5$ |
| FW, g mol$^{-1}$ | 617.29 | 764.84 | 778.96 | 648.87 |
| crystal system | Triclinic | Monoclinic | Monoclinic | Triclinic |
| space group | P-1 | P2(1) | P2(1) | P-1 |
| *T*, K | 203(2) | 203(2) | 203(2) | 201(2) |
| $\lambda$ , Å | 0.71073 | 0.71073 | 0.71073 | 0.71073 |
| *a* , Å | 7.8472(7) | 9.617(2) | 9.5942(9) | 7.170(3) |
| *b* , Å | 10.3110(9) | 14.189(3) | 14.0484(13) | 10.079(4) |
| *c* , Å | 14.5880(12) | 12.082(3) | 12.1092(11) | 18.934(8) |
| $\alpha$ , ° | 109.8720(10) | 90.00 | 90.00 | 87.847(5) |
| $\beta$ , ° | 95.9570(10) | 103.412(3) | 103.1450(10)° | 85.655(5) |
| $\gamma$ , ° | 95.3360(10) | 90.00 | 90.00 | 70.035(5) |
| *V*, Å$^3$ | 1093.64(16) | 1603.6(7) | 1589.4(3) | 1282.3(9) |
| *Z* | 2 | 2 | 2 | 2 |
| $\rho_{calcd}$, g cm$^{-3}$ | 1.875 | 1.584 | 1.628 | 1.681 |
| μ (Mo, Kα), mm$^{-1}$ | 3.301 | 2.498 | 3.238 | 3.159 |
| *F*(000) | 608 | 764 | 774 | 642 |
| measd/indep | 9918/5052 | 9912/5410 | 12895/5955 | 9193/9206 |
| ($R_{int}$) reflns | 0.0293 | 0.0484 | 0.0556 | 0.0660 |
| $^a$*R*1(*I* > 2 σ (*I*)) | 0.0459 | 0.0437 | 0.0464 | 0.0723 |
| $^b$*wR*2 (*I* > 2 σ (*I*)) | 0.1167 | 0.1003 | 0.0961 | 0.1964 |
| GOF on $F^2$ | 1.125 | 1.012 | 1.007 | 1.035 |

| Complex | **2-5** | **2-6** | **2-7** | **2-8** |
|---|---|---|---|---|
| Formula | $C_{26}H_{21}N_8O_9Tb$ | $C_{27}H_{24}DyN_7O_9$ | $C_{26}H_{21}HoN_8O_9$ | $C_{16}H_{25}Cl_2Dy\ N_4O_5$ |
| FW, g mol$^{-1}$ | 748.43 | 753.03 | 754.44 | 586.80 |
| crystal system | Triclinic | Triclinic | Triclinic | Monoclinic |
| space group | P-1 | P-1 | P-1 | P2(1)/c |
| *T*, K | 201(2) | 202(2) | 201(2) | 203(2) |
| $\lambda$ , Å | 0.71073 | 0.71073 | 0.71073 | 0.71073 |
| *a* , Å | 10.1282(12) | 10.1183(14) | 10.1053(17) | 12.383(3) |
| *b* , Å | 11.4528(14) | 11.4426(15) | 11.459(2) | 12.692(3) |
| *c* , Å | 12.9816(16) | 12.9654(17) | 12.946(2) | 14.823(3) |
| $\alpha$ , ° | 91.871(2) | 92.066(2) | 92.221(2) | 90.00 |
| $\beta$ , ° | 101.862(2) | 101.925(2) | 101.939(2) | 105.503(2) |
| $\gamma$ , ° | 93.410(2) | 93.249(2) | 93.293(2) | 90.00 |
| *V*, Å$^3$ | 1469.5(3) | 1464.6(3) | 1462.3(4) | 2244.9 |
| *Z* | 2 | 2 | 2 | 4 |
| $\rho_{calcd}$, g cm$^{-3}$ | 1.691 | 1.708 | 1.713 | 1.736 |
| μ (Mo, Kα), mm$^{-1}$ | 2.472 | 2.616 | 2.771 | 3.599 |
| *F*(000) | 740 | 746 | 744 | 1156 |
| measd/indep | 13375/5932 | 13409/5958 | 13330/5922 | 21575/4265 |
| ($R_{int}$) reflns | 0.0528 | 0.0596 | 0.0522 | 0.0299 |
| $^a$*R*1($I > 2\ \sigma\ (I)$) | 0.0487 | 0.0491 | 0.0560 | 0.0341 |
| $^b$*wR*2 ($I > 2\ \sigma\ (I)$) | 0.1258 | 0.0822 | 0.1504 | 0.0953 |
| GOF on $F^2$ | 1.020 | 1.046 | 1.045 | 1.193 |

| Complex | **2-9** | **2-10** | **3-1** | **3-2** |
|---|---|---|---|---|
| Formula | $C_{25.50}H_{39}Cl_4DyN_6O_4$ | $C_{42}H_{62}Dy_2N_{14}O_{24}$ | $C_{32}H_{29}Dy_2N_9O_{18}$ | $C_{33}H_{38}Dy_2N_{12}O_{15}$ |
| FW, g mol$^{-1}$ | 797.93 | 1472.06 | 1152.64 | 1167.75 |
| crystal system | Monoclinic | Triclinic | Triclinic | Triclinic |
| space group | P2(1)/n | P-1 | P-1 | P-1 |
| *T*, K | 200(2) | 203(2) | 202(2) | 200(2) |
| $\lambda$ , Å | 0.71073 | 0.71073 | 0.71073 | 0.71073 |
| *a* , Å | 16.8391(10) | 9.5597(18) | 9.446(2) | 10.7687(2) |
| *b* , Å | 10.6560(6) | 10.0626(19) | 10.607(2) | 11.3482(2) |
| *c* , Å | 20.1530(12) | 16.895(3) | 11.265(3) | 19.6302(6) |
| $\alpha$ , ° | 90.00 | 78.919(3) | 65.179(3) | 92.274(2) |
| $\beta$ , ° | 114.3310(10) | 80.042(3) | 84.097(3) | 96.614(2) |
| $\gamma$ , ° | 90.00 | 64.022(3) | 86.408(3) | 118.0070(10) |
| *V*, Å$^3$ | 3295.0(3) | 1426.5(5) | 1018.7(4) | 2091.82(8) |
| *Z* | 4 | 1 | 1 | 2 |
| $\rho_{calcd}$, g cm$^{-3}$ | 1.608 | 1.714 | 1.879 | 1.854 |
| μ (Mo, Kα), mm$^{-1}$ | 2.632 | 2.690 | 3.725 | 3.626 |
| *F*(000) | 1600 | 736 | 560 | 1144 |
| measd/indep | 32296/5584 | 14934/5414 | 8765/3823 | 10267/ |
| ($R_{int}$) reflns | 0.0778 | 0.0253 | 0.0752 | 0.0233 |
| $^a$*R*1(*I* > 2 σ (*I*)) | 0.0378 | 0.0332 | 0.0594 | 0.0270 |
| $^b$*wR*2 (*I* > 2 σ (*I*)) | 0.0996 | 0.0940 | 0.1541 | 0.0774 |
| GOF on $F^2$ | 1.054 | 1.164 | 1.058 | 1.013 |

| Complex | **3-3** | **3-4** | **3-5** | **3-6** |
|---|---|---|---|---|
| Formula | $C_{34}H_{44}Dy_2N_{10}O_{20}$ | $C_{32}H_{38}Eu_2N_8O_{16}$ | $C_{32}H_{38}$ $Tb_2N_8O_{16}$ | $C_{30}H_{30}Dy_2N_8O_{14}$ |
| FW, g $mol^{-1}$ | 1237.79 | 1094.62 | 1104.51 | 1051.62 |
| crystal system | Triclinic | Monoclinic | Monoclinic | Monoclinic |
| space group | P-1 | P2(1)/c | P2(1)/c | P2(1)/c |
| *T*, K | 202(2) | 201(2) | 202(2) | 203(2) |
| $\lambda$ , Å | 0.71073 | 0.71073 | 0.71073 | 0.71073 |
| *a* , Å | 11.145(2) | 9.7676(7) | 9.7446(13) | 9.6976(10) |
| *b* , Å | 12.407(2) | 11.3061(9) | 11.2229(15) | 10.5912(10) |
| *c* , Å | 17.813(3) | 17.5592(13) | 17.484(2) | 17.2186(17) |
| $\alpha$ , ° | 81.334(2) | 90.00 | 90.00 | 90.00 |
| $\beta$ , ° | 75.852(2) | 96.9150(10) | 96.788(2) | 95.4300(10) |
| $\gamma$ , ° | 84.688(2) | 90.00 | 90.00 | 90.00 |
| *V*, $Å^3$ | 2357.2(7) | 1925.0(3) | 1898.7(4) | 1760.6(3) |
| *Z* | 2 | 2 | 2 | 2 |
| $\rho_{calcd}$, g $cm^{-3}$ | 1.744 | 1.888 | 1.932 | 1.984 |
| μ (Mo, Kα), $mm^{-1}$ | 3.230 | 3.3111 | 3.778 | 4.291 |
| *F*(000) | 1220 | 1080 | 1080 | 1020 |
| measd/indep | 22243/8280 | 17871/3921 | 15840/3457 | 17911/4212 |
| ($R_{int}$) reflns | 0.1230 | 0.0564 | 0.1037 | 0.0401 |
| [a]*R*1(*I* > 2 σ (*I*)) | 0.0768 | 0.0403 | 0.0566 | 0.0315 |
| [b]*wR*2 (*I* > 2 σ (*I*)) | 0.2143 | 0.1069 | 0.1581 | 0.0784 |
| GOF on $F^2$ | 1.014 | 1.082 | 1.065 | 1.066 |

| Complex | **3-7** | **3-8** | **3-9** | **3-10** |
|---|---|---|---|---|
| Formula | $C_{32}H_{33}Eu_2N_9O_{14}$ | $C_{32}H_{33}Tb_2N_9O_{14}$ | $C_{32}H_{33}Dy_2N_9O_{14}$ | $C_{29}H_{30}Gd_2N_8O_{15}$ |
| FW, g mol$^{-1}$ | 2143.19 | 1085.51 | 1082.67 | 1045.11 |
| crystal system | Orthorhombic | Orthorhonmbic | Orthorhombic | Orthorhombic |
| space group | Pbca | Pbca | Pbca | Pbca |
| *T*, K | 201(2) | 201(2) | 203(2) | 296(2) |
| $\lambda$ , Å | 0.71073 | 0.71073 | 0.71073 | 0.71073 |
| *a* , Å | 14.6306(15) | 14.5250(17) | 18.496(3) | 14.8208(10) |
| *b* , Å | 14.3139(14) | 14.2910(17) | 14.486(2) | 14.1687(11) |
| *c* , Å | 18.5437(19) | 18.492(2) | 14.326(2) | 18.3907(13) |
| $\alpha$ , ° | 90.00 | 90.00 | 90.00 | 90.00 |
| $\beta$ , ° | 90.00 | 90.00 | 90.00 | 90.00 |
| $\gamma$ , ° | 90.00 | 90.00 | 90.00 | 90.00 |
| *V*, Å$^3$ | 3883.4(7) | 3838.8(8) | 3838.3(10) | 3861.9(5) |
| *Z* | 2 | 2 | 2 | 4 |
| $\rho_{calcd}$, g cm$^{-3}$ | 1.833 | 1.878 | 1.891 | 1.798 |
| μ (Mo, Kα), mm$^{-1}$ | 3.278 | 3.732 | 3.941 | 3.480 |
| *F*(000) | 2104 | 2120 | 2128 | 2032 |
| measd/indep | 32319/3959 | 31844/3905 | 30478/3906 | 44987/4744 |
| ($R_{int}$) reflns | 0.0621 | 0.0809 | 0.0611 | 0.0521 |
| $^a$*R*1($I > 2\sigma(I)$) | 0.0369 | 0.0402 | 0.0350 | 0.0411 |
| $^b$*wR*2 ($I > 2\sigma(I)$) | 0.0923 | 0.0968 | 0.0937 | 0.1388 |
| GOF on $F^2$ | 1.075 | 1.059 | 1.090 | 1.032 |

| Complex | **3-11** | **4-1** | **4-2** | **4-3** |
|---|---|---|---|---|
| Formula | $C_{32}H_{38}Dy_2N_{12}O_{10}$ | $C_{70}H_{97}Dy_3N_{15}O_{22}$ | $C_{69}H_{104}N_{15}O_{22}Tb_3$ | $C_{144}H_{208}Dy_6N_{30}O_{44}$ |
| FW, g mol$^{-1}$ | 1075.74 | 1988.13 | 1972.43 | 4038.40 |
| crystal system | Orthorhombic | Monoclinic | Monoclinic | Monoclinic |
| space group | Pbca | C2/c | C2/c | C2/c |
| *T*, K | 200(2) | 202(2) | 205(2) | 203(2) |
| $\lambda$ , Å | 0.71073 | 0.71073 | 0.71073 | 0.71073 |
| *a* , Å | 14.845(5) | 23.694(12) | 23.436(3) | 23.773(5) |
| *b* , Å | 14.134(5) | 26.995(13) | 27.273(4) | 27.012(5) |
| *c* , Å | 17.958(6) | 12.804(6) | 12.5888(18) | 14.270(3) |
| $\alpha$ , ° | 90.00 | 90.00 | 90.00 | 90.00 |
| $\beta$ , ° | 90.00 | 95.872(6) | 95.384 | 95.889(3) |
| $\gamma$ , ° | 90.00 | 90.00 | 90.00 | 90.00 |
| *V*, Å$^3$ | 3768.0(2) | 8147(7) | 8011(2) | 9115(3) |
| *Z* | 8 | 4 | 4 | 2 |
| $\rho_{calcd}$, g cm$^{-3}$ | 1.896 | 1.621 | 1.635 | 1.471 |
| μ (Mo, Kα), mm$^{-1}$ | 4.008 | 1.621 | 2.700 | 2.506 |
| *F*(000) | 2104 | 3984 | 3976 | 4060 |
| measd/indep | 17736/2289 | 38547/7196 | 29145/7604 | 37378/ 7637 |
| ($R_{int}$) reflns | 0.1776 | 0.0827 | 0.0854 | 0.0623 |
| [a]*R*1($I > 2\sigma(I)$) | 0.0569 | 0.0689 | 0.0662 | 0.0630 |
| [b]*wR*2 ($I > 2\sigma(I)$) | 0.1198 | 0.1421 | 0.1693 | 0.1670 |
| GOF on $F^2$ | 1.084 | 1.233 | 1.135 | 1.069 |

| Complex | **4-4** | **4-5** | **5-1** | **5-2** |
|---|---|---|---|---|
| Formula | $C_{75}H_{85}Dy_3N_{16}O_{30}$ | $C_{33}H_{47}Cl_2Dy_3N_6O_{15}$ | $C_{64}H_{64}Cl_2Dy_4N_{12}O_{18}$ | $C_{64}H_{64}Cl_2N_{12}O_{18}Tb_4$ |
| FW, g mol$^{-1}$ | 2178.09 | 1326.17 | 2010.17 | 1995.85 |
| crystal system | Triclinic | Monoclinic | Monoclinic | Monoclinic |
| space group | P-1 | C2/c | P2(1)/c | P2(1)/c |
| *T*, K | 202(2) | 200(2) | 200(2) | 199(2) |
| $\lambda$ , Å | 0.71073 | 0.71073 | 0.71073 | 0.71073 |
| *a* , Å | 13.285(2) | 16.1616(7) | 11.8651(9) | 11.849(3) |
| *b* , Å | 13.362(2) | 24.2577(11) | 20.3761(16) | 20.399(4) |
| *c* , Å | 25.248(4) | 14.1200(6) | 14.5767(11) | 14.603(3) |
| $\alpha$ , ° | 95.490(2) | 90.00 | 90.00 | 90.00 |
| $\beta$ , ° | 93.724(2) | 95.065(2) | 102.3160(10) | 102.470(3) |
| $\gamma$ , ° | 95.741(2) | 90.00 | 90.00 | 90.00 |
| *V*, Å$^3$ | 4426.1(12) | 5514.0(4) | 3443.0(5) | 3446.3(13) |
| *Z* | 2 | 4 | 2 | 2 |
| $\rho_{calcd}$, g cm$^{-3}$ | 1.634 | 1.597 | 1.939 | 1.923 |
| μ (Mo, Kα), mm$^{-1}$ | 2.594 | 4.176 | 4.447 | 4.210 |
| *F*(000) | 2170 | 2556 | 1948 | 1940 |
| measd/indep | 40687/18000 | 41635/6762 | 36039/7062 | 31533/5841 |
| ($R_{int}$) reflns | 0.0708 | 0.0238 | 0.0994 | 0.2454 |
| [a]*R*1($I > 2\sigma(I)$) | 0.0554 | 0.0472 | 0.0491 | 0.0626 |
| [b]*wR*2 ($I > 2\sigma(I)$) | 0.1579 | 0.1402 | 0.1296 | 0.1640 |
| GOF on $F^2$ | 1.039 | 1.011 | 1.040 | 1.002 |

| Complex | **5-3** | **5-4** |
|---|---|---|
| Formula | $C_{64}H_{66}Cl_2Ho_4N_{12}O_{18}$ | $C_{77}H_{98}Dy_4N_{12}O_{22}$ |
| FW, g mol$^{-1}$ | 2021.91 | 2193.67 |
| crystal system | Monoclinic | Monoclinic |
| space group | P2(1)/c | P2(1)/n |
| *T*, K | 200(2) | 200(2) |
| $\lambda$ , Å | 0.71073 | 0.71073 |
| *a* , Å | 11.862(5) | 13.1664(14) |
| *b* , Å | 20.291(13) | 46.467(5) |
| *c* , Å | 14.539(7) | 14.0254(15) |
| $\alpha$ , ° | 90.00 | 90.00 |
| $\beta$ , ° | 102.18(4) | 109.157(2) |
| $\gamma$ , ° | 90.00 | 90.00 |
| *V*, Å$^3$ | 3421(3) | 8105.5(15) |
| *Z* | 2 | 4 |
| $\rho_{calcd}$, g cm$^{-3}$ | 1.963 | 1.798 |
| μ (Mo, Kα), mm$^{-1}$ | 4.733 | 3.726 |
| *F*(000) | 1960 | 4336 |
| measd/indep | 35679/6235 | 36464/9182 |
| ($R_{int}$) reflns | 0.0812 | 0.1218 |
| $^a$*R*1(*I* > 2 σ (*I*)) | 0.0448 | 0.0761 |
| $^b$*wR*2 (*I* > 2 σ (*I*)) | 0.1156 | 0.2218 |
| GOF on $F^2$ | 1.044 | 1.085 |